Wang, Jinghua (2016). A hybrid model for large scale simulation of unsteady nonlinear waves. (Unpublished Doctoral thesis, City University London)

Original citation: Wang, Jinghua (2016). A hybrid model for large scale simulation of unsteady nonlinear waves. (Unpublished Doctoral thesis, City University London)

Permanent City Research Online URL: http://openaccess.city.ac.uk/14575/

CITY UNIVERSITY
LONDON

A HYBRID MODEL FOR LARGE SCALE SIMULATION OF UNSTEADY NONLINEAR WAVES

By

Jinghua Wang

B. Eng.

Supervisor

Prof. Qingwei Ma

A thesis submitted to

City University London

for the degree of

Doctor of Philosophy

School of Mathematics, Computer Science and Engineering

City University London

March, 2016

CONTENTS

LIST OF FIGURES 5

LIST OF TABLES 8

ACKNOWLEDGEMENTS 9

DECLARATION 10

ABSTRACT 11

LIST OF SYMBOLS AND TECHNICAL TERMS 12

1 INTRODUCTION 18

2 LITERATURE REVIEW 22

- 2.1 Steady wave models 22
  - 2.1.1 Linear wave model 23
  - 2.1.2 Stokes wave model 23
  - 2.1.3 Shallow water wave models 24
  - 2.1.4 Suitability of steady wave models 25
- 2.2 Unsteady wave models 26
  - 2.2.1 Second order wave models 26
  - 2.2.2 Shallow water wave models 29
  - 2.2.3 Nonlinear Schrödinger equations 32
  - 2.2.4 Fully nonlinear models 36
  - 2.2.5 Potential-NS models 41
- 2.3 Existing problems, objectives and main contribution 42
- 2.4 Outline of the thesis 44

3 MATHEMATICAL FORMULATIONS AND PREVIOUS WORKS 45

- 3.1 The fundamental equations 45
- 3.2 The Enhanced Nonlinear Schrödinger equation 46
  - 3.2.1 Governing equation for the free surface envelope 47
  - 3.2.2 Solution to the free surface and velocity potential 49
- 3.3 The Higher Order Dysthe equation 49
  - 3.3.1 Governing equation for the free surface envelope 49
  - 3.3.2 The fifth order ENLSE based on Hilbert transform 50
- 3.4 The Spectral Boundary Integral method 51
  - 3.4.1 The prognostic equations 51
  - 3.4.2 The boundary integral equation 52
  - 3.4.3 Numerical implementation 54
  - 3.4.4 Schemes for estimating V_3 and V_4 55

3.4.5 Quasi SBI 57
3.5 Discussion 58
4 THE FIFTH ORDER ENLSE BASED ON FOURIER TRANSFORM 59
4.1 The governing equation for the free surface envelope 59
4.2 Numerical implementation 60
4.3 Validation of the ENLSE-5F 61
4.4 Discussion 64
5 THE ENHANCED SPECTRAL BOUNDARY INTEGRAL METHOD 66
5.1 Techniques for de-singularity 66
5.1.1 Weak-singular integral in V_4 66
5.1.2 Weak-singular integral in V_3 67
5.1.3 Effectiveness of the de-singular techniques for evaluating V_3 and V_4 68
5.2 Techniques for Anti-Aliasing (TAA) 75
5.2.1 Anti-aliasing Techniques 76
5.2.2 Comparisons of different anti-aliasing techniques 82
5.3 Techniques for determining the critical surface slope 84
5.3.1 Estimation of magnitude of D_c 85
5.3.2 Values of D_c determined by numerical tests 85
5.4 Overall efficiency of the ESBI 89
5.5 Discussion 93
6 THE HYBRID MODEL 94
6.1 Relationship between η and A 95
6.1.1 Transformation from A to η and ϕ 95
6.1.2 Transformation from η to A 96
6.2 Methodology for the timing control 97
6.3 Effects of Tol_1 and Tol_2 by numerical simulations 99
6.3.1 Investigation on effects of Tol_2 101
6.3.2 Investigation on effects of Tol_1 103
6.4 Validation of the hybrid model 105
6.4.1 Two dimensional simulations 105
6.4.2 Three dimensional simulations 108
6.5 Discussion 113
7 NUMERICAL SIMULATION OF ROGUE WAVES IN RANDOM SEAS 114
7.1 Techniques to embed rogue waves 114
7.1.1 Basic formulations 114
7.1.2 Validations based on linear theory 116

    7.1.3 Discussion 121
  7.2 Discussions on the overall performance of the hybrid model 122
    7.2.1 Different rogue wave height 122
    7.2.2 Different numbers of rogue waves on temporal scale 126
    7.2.3 Different numbers of rogue waves on space scale 131
  7.3 Discussion 136
8 CONCLUSIONS AND RECOMMENDATIONS 137
  8.1 Conclusions 137
  8.2 Recommendations 138
APPENDIX A 141
APPENDIX B 146
APPENDIX C 148
APPENDIX D 149
APPENDIX E 152
REFERENCES 153

LIST OF FIGURES

Figure 3.0.1 Sketch of the problem 45

Figure 3.2.1 Sketch of the envelope 47

Figure 3.4.1 Flow chart for the numerical implementation of Spectral Boundary Integral Method..55

Figure 3.4.2 The flow chart of the numerical scheme for solving the boundary integral equation 57

Figure 4.2.1 Flow chart for the numerical implementation of ENLSE-5F..........................61

Figure 4.3.1 Profiles of Ψ_2 and Ψ_3 62

Figure 4.3.2 Envelopes of the numerical simulations 63

Figure 4.3.3 Profiles of the free surface 64

Figure 5.1.1 The local polar coordinates for the elements near the singular point.............67

Figure 5.1.2 Profiles of V_3 and V_4 70

Figure 5.1.3 Relative error of the profiles of V_3(a) and V_4(b) 71

Figure 5.1.4 Profiles of the free surfaces..73

Figure 5.1.5 Variation of the phase shift of wave profiles with time 74

Figure 5.1.6 Results for the case with a domain of $2L \times 2L$ and $\varepsilon = 0.2985$ 75

Figure 5.1.7 Resolution and CPU ratio to achieve $Err_1 < 2.5\%$ for different values of steepness 75

Figure 5.2.1 Illustration of TAA1..78

Figure 5.2.2 Illustration of TAA2..79

Figure 5.2.3 Profiles of $\mathrm{V}_4^{(2)}$ 80

Figure 5.2.4 Illustration of TAA3..81

Figure 5.2.5 Aliasing error against different resolutions for different steepness 83

Figure 5.2.6 Resolution and CPU ratio to achieve $Error\{V_3 + V_4\} < 1E - 6$ for different values of steepness..83

Figure 5.3.1 Ratio of CPU time taken by Scheme 1 to that of Scheme 2 for $\mathrm{Err}_1\{\varphi\} < 2.5\%$ 84

Figure 5.3.2 Wave profiles at different instants (a) and numerical error against maximum gradient (b) for $p_0 = 0.25$ 87

Figure 5.3.3 Numerical error against maximum gradient for different pressure amplitude 87

Figure 5.3.4 Results for Benjamin-Feir instability 88

Figure 5.3.5 Results for horse-shoe wave pattern 88

Figure 5.4.1 Evolution of perturbation components of $\boldsymbol{K} = (3/2, 4/3)$ 90

Figure 5.4.2 Free surface profiles at different section for $\varepsilon = 0.3$ at $T/T_0 = 18$ 91

Figure 5.4.3 Convergent rate of Fructus method and ESBI for $\varepsilon = 0.1$, 0.2 and 0.3 92

Figure 5.4.4 CPU time ratio against steepness at error less than 0.2% 92

Figure 5.4.5 Profiles corresponding to different errors for $\varepsilon = 0.3$ at $T/T_0 = 18$ 93

Figure 6.1.1 Flow chart of estimating the envelope A by iterations 97

Figure 6.2.1 Flow chart of the numerical scheme for hybrid model 99

Figure 6.3.1 Err_η against Tol_2 102

Figure 6.3.2 Err_η against Tol_1 104

Figure 6.4.1 Free surface at the end of the simulation. 105

Figure 6.4.2 The exchange between the models 106

Figure 6.4.3 Free surface at different instant. 107

Figure 6.4.4 The exchange between the models 108

Figure 6.4.5 The Profiles of free surface at $T/T_0 = 7.4$ for focusing wave 109

Figure 6.4.6 The exchange between the models for focusing wave 109

Figure 6.4.7 Evolution of perturbation components and peak wave components crescent wave 110

Figure 6.4.8 The exchange between the models for crescent wave 111

Figure 6.4.9 Free surface elevation at $T/T_0 = 250$ 112

Figure 6.4.10 Probability distribution of the free surface elevation at $T/T_0 = 200$ 112

Figure 7.1.1 Free surface and observed spectra based on the JONSWAP spectrum. 118

Figure 7.1.2 Observed spectra based on the JONSWAP spectrum 118

Figure 7.1.3 Free surface and observed spectra based on the Gaussian distribution. 119

Figure 7.1.4 Free surface and observed spectra based on the CNW 120

Figure 7.1.5 Free surface and observed spectra for multiple rogue waves tests. 121

Figure 7.2.1 Err_η and CPU ratio (CPU time of ESBI/CPU time of hybrid model) for the cases with different rogue wave heights 123

Figure 7.2.2 The exchange between models for the cases with different rogue wave heights 126

Figure 7.2.3 The profiles of the rogue wave with height of $4Hs$for the cases with different rogue wave heights 126

Figure 7.2.4 Err_{η} and CPU ratio (CPU time of ESBI/CPU time of hybrid model) : different rogue wave number on temporal scale 127

Figure 7.2.5 Maximum wave elevations with indicator which model is used for the cases of different numbers of rogue waves in time domain 129

Figure 7.2.6 The profiles of the rogue waves for the cases of different numbers of rogue waves in time domain 130

Figure 7.2.7 Err_{η} and CPU ratio (CPU time of ESBI/CPU time of hybrid model) for the cases of different amount of rogue waves on spatial scale 131

Figure 7.2.8 Maximum wave elevations with indicator which model is used for the cases of different numbers of rogue waves in spatial domain 134

Figure 7.2.9 The profiles of the rogue waves for the cases of different numbers of rogue waves in spatial domain 135

LIST OF TABLES

Table 3.4.1 Schemes of the boundary integral solver 56
Table 5.1.1 Phase shift with different experimental conditions...71
Table 6.0.1 Short summary of the three models 94

ACKNOWLEDGEMENTS

I would like to show my gratitude to all the people who have spent their precious time and offered me kind helps during my postgraduate study. Without their supports, this thesis cannot be made possible.

Firstly, I must express the sincerest appreciation to my supervisor, Prof. Qingwei Ma, who is the most influential person throughout my postgraduate study. He has inspired me in so many ways, and I've learnt a lot from our numerous discussions. I am so impressed by his profound knowledge and keen enthusiasm for researches and patience for educating his students. He has taught me valuable research skills that benefit not only my study, but also my careers in the future. He always encourages and pushes me to overcome one challenge after another, which enables me to know better about myself, dig my potential and gain confidence again and again. I will always remember his rigorous style of supervising, which will endeavor me to make further progress as a researcher.

I am also indebted to Dr. Shiqiang Yan, who has given me so much enlightening ideas and useful suggestions during my study. He also generously offered me his numerical code, without which my research won't be that smooth.

I am thankful to Prof. Huajun Li, who had supervised me during my master study at Ocean University of China and introduced me to Prof. Ma. I would also like to show my thanks to Prof. Bingchen Liang and Prof. Dongyoung Lee, who also provided kind helps during my PhD study.

Thanks to all my friends, with whom I have spent a very joyful and meaningful four-year, and that I will never forget.

I also appreciate the sponsorship provided by China Scholarship Council for the first 48 months and the last 4 months by Prof. Qingwei Ma during my study.

Last but not least, I am grateful to the most important persons in my life - my parents, who are always standing behind me and encouraging me. Without their unconditional love and support, I cannot go this far. Thanks to my sister, my brother in law and my niece, who cheer me up and brighten my life during my PhD study. Additionally, I give my special thanks to my beloved Miss Xin Zhao. Although we lived at a different cities and only met once a month. She always showed up at the moment when I need her during my hard time. We both cherish the limited time being together, and I believe it will become a priceless memory in our future life.

DECLARATION

No portion of the work referred to in the thesis has been submitted in support of an application for other degree or qualification of this or any other university or other institute of learning.

I grant powers of discretion to the City University Library to allow this thesis to be copied in whole or in part without any reference to me. This permission covers only single copies made for study purpose subject to normal condition of acknowledgement.

ABSTRACT

A hybrid model for simulating rogue waves in random seas on a large time and space scale is proposed in this thesis. It is formed by combining the derived fifth order Enhanced Nonlinear Schrödinger Equation based on Fourier transform (ENLSE-5F), the fully nonlinear Enhanced Spectral Boundary Integral (ESBI) method and its simplified version. The numerical techniques and algorithm for coupling three models on time scale are provided. Using them, and the switch between the three models during the computation is triggered automatically according to wave nonlinearities. Numerical tests are carried out and the results indicate that this hybrid model could simulate rogue waves both accurately and efficiently. In some cases showed, the hybrid model is more than 10 times faster than just using the ESBI method.

LIST OF SYMBOLS AND TECHNICAL TERMS

T_0	Peak period, characteristic period, Stokes wave period
L_0	Peak wave length, characteristic wave length
k_0	Peak wave number, characteristic wave number
b	Draught of the cylinder
h	Water depth
U_r	Ursell number
a	Wave amplitude
k	Wave number
ε	Wave steepness
η	Free surface elevation
Δ	Laplacian
ϕ	Velocity potential
p	Pressure on free surface
$\boldsymbol{X}$	Horizontal coordinates
X	Transversal coordinate
Y	Longitudinal coordinate
Z	Vertical coordinate
T	Time coordinate
ω_0	Peak circular frequency
ρ	Density of water
g	Gravitational acceleration
$F\{\}$	Fourier transform
$F^{-1}\{\}$	Inverse Fourier transform
$\boldsymbol{K}$	Variable wave number corresponding to $\boldsymbol{X}$
κ	Transversal wave number corresponding to X
ζ	Longitudinal wave number corresponding to Y
a_j	Wave amplitude of the jth component
$\boldsymbol{k_j}$	Wave number of the jth component
ω_j	Circular frequency of the jth component
φ_j	Phase of the jth component

i	Imaginary unit
A	Envelope of the free surface elevation
B	Envelope of the velocity potential
A_j	The jth harmonic coefficients for free surface elevation
B_j	The jth harmonic coefficients for velocity potential
$\bar{\eta}$	Free surface deflection due to wave radiation stress
$\bar{\phi}$	Mean flow due to wave radiation stress
$c.c.$	Complex conjugate
θ	Phase of the harmonic
$\mathscr{w}$	Circular frequency of envelope
$\boldsymbol{k_0}$	Directional peak wave number
Ψ_1	Nonlinear part of the ENLSE-4
Υ_1	Nonlinear part excluding the mean flow term of the ENLSE-4
Ψ_2	Nonlinear part of the ENLSE-5H
Υ_2	Nonlinear part excluding the Hilbert transform terms and Υ_1 of the ENLSE-5H
$\mathcal{H}\{\,\}$	Hilbert transform of first kind
$\mathcal{P}\{\,\}$	Hilbert transform of second kind
$\tilde{\phi}$	Velocity potential at free surface
V	Vertical velocity at free surface
$\boldsymbol{M}$	Vector form of the variables for free surface and velocity potential
$\mathcal{A}$	Matrix form of the circular frequency
$\boldsymbol{R}$	Vector form of the pressure term on free surface boundaries
$\boldsymbol{N}$	Vector form of the nonlinear parts of the free surface boundary conditions
$\mathit{\Omega}$	Variable circular frequency
K	Module of variable wave number
ΔT	Time step
α_j, β_j	Six-stage embedded fifth order Runge-Kutta coefficients
$\mathcal{K}_j$	Runge-Kutta increment at each stage
Err_T, Tol_T	Relative error between the fourth order and fifth order Runge-Kutta solutions and the tolerance
ΔT_{opt}	Optimised time step size
S	Area of the instantaneous free surface

r	Distance between the source and field point
$\boldsymbol{R}$	Vector pointing from source to field point
R	Module of $\boldsymbol{R}$
$\boldsymbol{n}$	Unit normal vector on free surface pointing outside
S_0	projection of S to the horizontal plane
D	Difference of the free surface between source and field point over their horizontal distance
V_j	The jth order convolution of the vertical velocity
Γ_1	Kernel of the integration part of V_3
Υ_1	Kernel of the integration part of V_4
$V_4^{(1)}$	The third order convolution part of V_4
$V_{4,I}{}'$	The integration part of V_4 up to the fifth order
V^{Iter}, V^{Iter+1}	The values of the velocity V at two successive iterations
Err_B, Tol_B	Relative error between V^{Iter} and V^{Iter+1}, and the tolerance
$\Delta\boldsymbol{X}$	Spatial step size
$V_3^{(1)}$	The fourth order convolution part of V_3
$V_3^{(2)}$	The sixth order convolution part of V_3
$V_{3,C}$	The whole convolution part of V_3
$V_{3,I}$	The integration part of V_3 up to the eighth order
$V_4^{(2)}$	The fifth order convolution part of V_4
$V_4^{(3)}$	The seventh order convolution part of V_4
$V_{4,C}$	The whole convolution part of V_4
$V_{4,I}$	The integration part of V_4 up to the ninth order
Γ_2, Υ_2	New kernel of the integration part of V_3 and V_4 respectively after further expansion
D_c	Critical value of D
$\lvert D\rvert_{max}$	Maximum value of the module of D
Ψ_3	Nonlinear part of the ENLSE-5F
$A^{(4)}, A^{(5)}$	Fourth and fifth order Runge-Kutta solution to the ENLSE-5F
Err_{AT}	Error between $A^{(4)}$ and $A^{(5)}$
X_c	Location of the centre of the envelope
$S(k,\theta)$	Directional wave spectrum
$G_1(\theta)$	Spreading function

σ	Area surround the singular point
$\tilde{f}(\boldsymbol{X}')$	Integrand of $V_{4,I}$ in Cartesian coordinates
$f(R,\theta)$	Integrand of $V_{4,I}$ in polar coordinates
$\rho(\theta),\delta$	Radius of the area S and σ respectively
$\tilde{g}(\boldsymbol{X}')$	Integrand of $V_{3,I}$ in Cartesian coordinates
$g(R,\theta)$	Integrand of $V_{3,I}$ in polar coordinates
V_{30},V_{40}	Maxima of V_3 and V_4 corresponding to the resolution $2^{10}\times2^{10}$
$Error\{V_3\},Error\{V_4\}$	Error of V_3 and V_4 between by using a specific resolution and benchmark
$Err_1\{\varphi\}$	Total phase shift error
$Err_2\{\varphi\}$	Mean phase shift error
$\Delta\varphi$	Total phase shift in radians
N_{to}	Total number of wave periods of simulation
I	Magnitude of the order
$V_{3,C}^{(N=2^n)},V_{4,C}^{(N=2^n)}$	Convolution parts of V_3 and V_4 with resolution of $2^n\times2^n$
$V_{3,C}^{(N=2^9)},V_{4,C}^{(N=2^9)}$	Convolution parts of V_3 and V_4 computed by using a resolution of $2^9\times2^9$
$Error\{V_3+V_4\}$	The total aliasing error of V_3 and V_4
$V_3^{(3)}$	The eighth order convolution part of V_3
$Error_1\{V\},Error_c$	The error due to ignoring the $V_{3,I}$ and $V_{4,I}$ for irregular waves and the tolerance
$Error_2\{V\}$	The error due to ignoring the $V_{3,I}$ and $V_{4,I}$ for regular wave
$V^{(scheme\ 3)}$	The profile of the velocity V calculated by using Scheme 3 at an instant
$V^{(scheme\ 2)}$	The profile of the velocity V calculated by using Scheme 2 at an instant
$Error_3\{V\}$	Relative error of Scheme 2
p_0	Amplitude of the pressure
C	Wave phase speed
$\delta\eta$	Free surface of the side-bands
$\lvert F\{\eta\}\rvert_{(\boldsymbol{K}=(3/2,4/3),T)}$	The value of the spectrum at a time T corresponding to the first disturbed term with $\boldsymbol{K}=(3/2,4/3)$
$\lvert F\{\eta\}\rvert_{(\boldsymbol{K}=(1,0),T=0)}$	The value of the spectrum at a time T corresponding to the carrier wave
Ψ_ϵ	The ratio between $\lvert F\{\eta\}\rvert_{(\boldsymbol{K}=(3/2,4/3),T)}$ and $\lvert F\{\eta\}\rvert_{(\boldsymbol{K}=(1,0),T=0)}$
$\eta^{(N=2^n)}$	the solution obtained by using a method with resolution $2^n\times2^n$ at $T/T_0=18$ for horse shoe wave pattern test
η_B	Benchmark solution for horse shoe wave pattern test

$Error_2\{\eta\}$	Error of the free surface by using resolution $2^n \times 2^n$
s	The order of the convergent rate
η_1, η_2, η_3	The first, second and third harmonics of the free surface elevation
$\eta^{(Iter)}$	The approximated surface by iterations
Err_A, Tol_A	The error of the envelope between the target and approximated one, and tolerance
Err_1, Tol_1	Error of the nonlinear part of the ENLSE-5H and the tolerance
Err_2, Tol_2	Error of the vertical velocity of QSBI and the tolerance
$FLAG$	Notation of which model is being employed
$S_J(k)$	JONSWAP wave number spectrum
H_s	Dimensionless significant wave height
α_J	JONSWAP spectrum coefficient
γ	The peak enhancement factor for JONSWAP spectrum
ς	Slope parameter of the JONSWAP spectrum
$S_W(k)$	Wallops wavenumber spectrum
α_W	Wallops spectrum coefficient
m	Width parameter of Wallops spectrum
L_d	Domain length
k_{max}	Cut-off wavenumber
η_0	Benchmark free surface solution obtained by using resolution 2^7 per peak wave length and $Tol_T = 1E - 7$
Err_η	Error of the free surface at the end of the simulation by using the ESBI
$G_2(\theta)$	Spreading function
$\dot{\eta}(X, T)$	Free surface of rogue waves embedded in random background by using Kriebel & Alsina's (2000) approach in two dimensions
η_T	Free surface of focusing part
η_R	Free surface of the random part
$\varphi_{Rj}, \theta_{Tj}$	Random phase and focusing phase
X_f, T_f	Focusing location and time
a_{Rj}, a_{Tj}	Amplitude of the random and focusing part
P_R, P_T	Energy ratio of random and focusing part
Δk	Wave number increment
θ_j	Phase by using Wang, et al.'s (2015) approach

$\ddot{\eta}(X,T)$	Free surface of rogue waves embedded in random background by using Wang, et al.'s (2015) approach
$\dot{\eta}'(X,T)$	Free surface of multiple rogue waves embedded in random background by using Kriebel & Alsina's (2000) approach
a'_{Rj}, a'_{Tjm}	Amplitude of the random and focusing part for the mth rogue wave
P_{Tm}	Energy percentage for the mth rogue wave
$\varphi'_{Rj}, \varphi'_{Tjm}$	Random phase and focusing phase for the mth rogue wave
X_{fm}	Focusing location for the mth rogue wave
θ'_j	Phase by using Wang, et al.'s (2015) approach

Significant wave height	Mean value of the 1/3 highest waves in a sea state
Rogue wave	Waves of height higher than two times the significant wave height
Exceedance probability	Probability of a particular variable, e.g., wave height, exceeding a prescribed value
Inviscous, irrotational	Assumption for potential flow, where the viscosity effects and cross products of velocity are neglected
Wave crest and trough	Highest and lowest points in an individual wave
Velocity potential	The gradient of velocity potential equals to velocity
Wave number	The number of waves per unit length
Wave steepness	Wave number times amplitude, i.e., *ka*
Order	Unless specified, the 'Order' is in terms of wave steepness
FFT	Fast Fourier Transform
Aliasing	Effect causing different wave signals to become indistinguishable

1 INTRODUCTION

Marine industry has went through an explosive growth in recently years. This is due to the fast growing voyage activities, increasing demands on submarine hydrocarbon resources, urgent requirements on coastal protection infrastructures, and recently emerging renewable energy devices. In order to accomplish such tasks, engineering projects on different purposes have been designed and constructed, which always require very costly investments. To make sure the structures can withstand and survive in the hostile ocean environment, engineers must pay great attentions to the factors such as gust, ice, wave, current, tide, seaquake and biological adhesion etc., as well as corrosion and fatigue problems of structure itself. Among all these effects, ocean waves are very common, but extremely crucial to the safety of the structures.

Ocean surface waves are generated due to different physics, for example, tide by gravitational forces from the moon and sun, tsunami by seaquake or landslides, and swell by wind-water resonance, and so on. The restoring force is the gravity of the earth except the capillary waves, which is restored by surface tension. Among all, the wind generated gravity waves is the main subject in this study due to that it is the most common problem associated with engineering practice. Over the last two centuries, researchers spent their entire life to investigate the surface waves mathematically and experimentally. Thanks to the efforts and contributions from the pioneers, significant progress has been made in solving this ancient fluid problem with free surface boundary conditions. However, the early analytical studies mainly focus on steady wave problems with small steepness on a linear or weakly nonlinear scenario. However, waves in reality exhibit randomness and feature complex physics, such as wave-wave interactions, waves interact with seabed, wind and current, etc., which involves strong nonlinearities and leads to significant change of wave profiles in space and time.

Not until World War II, researches on random waves went through a fast development, when the energy balance equation was first proposed and later being extended into wind wave models based on the wave action balance equation and still be widely adopted today (Cavaleri, et al., 2007). However, the wind wave models assume that the phase of each wave component is averaged so that only statistical information can be obtained, such as peak period and significant wave height. However, the information of phase is also very important, without which the surface profiles cannot be obtained, so that the wave dynamics cannot be estimated. Phase-resolved models did not become popular until vital breakthrough in computer sciences, which made it possible for computer to handle heavy and complicated computations. This big leap significantly accelerates the process of scientific researches and extends people's understanding of ocean wave physics.

It is not until the resent decades, rogue waves start to draw great attention, which have been overlooked in the past due to their rare in-situ observations. However, the probabilities of the rogue wave occurrence are higher than expected based on the traditional statistical theories (Kharif, et al., 2009), and marine accidents associated with rogue waves have been increasingly reported recently (Liu, 2007; Nikolkina & Didenkulova, 2012). The rogue wave is commonly defined as the wave with maximum wave height exceeding 2 times of significant wave height (H_s) and/or the maximum wave amplitude exceeding 1.25 H_s (Skourup, et al., 1996), where the significant wave height is defined as the mean value of the 1/3 highest waves in a sea state (or 4 times the standard deviation). They might be caused by many factors, such as the energy focusing due to the seabed geometry, wind-wave interaction, wave-current interaction, modulation instability, etc. A good review about the rogue waves could be found in the book by Kharif, et al. (2009) and the recent review by Adcock & Taylor (2014). However, the reasons of rogue waves still remain unknown so far (Kharif, et al., 2009). Due to that rogue waves always feature large steepness and their shapes can be highly asymmetry, it is recognized as a big threat to marine structures, which often cost huge loss. In order to make sure the marine structures are able to withstand the high loads caused by the violent rogue waves, it is necessary to study the dynamics of rogue waves in the random seas.

The most distinguishing feature of rogue wave is its transience, which means that it can happen and disappear very rapidly (Kharif, et al., 2009). Due to that reason, it cannot be modeled by using steady wave theories, e.g., Stokes waves (Stokes, 1847), cnoidal waves (Korteweg & DE Vries, 1895) or solitary wave (Boussinesq, 1871), which describe such waves with permanent profiles not evolving in time. Furthermore, due to the sudden appearance of rogue waves and the persistently changing sea state, the statistical stationarity condition also breaks down (Kharif, et al., 2009). Therefore, studies must be carried out in time domain in order to explore the physics of rogue waves.

Meanwhile, rogue waves are also associated with large steepness and strong nonlinearity. As pointed out by Kriebel (1990; 1992), Onorato, et al. (2006) and Phillips (1981), the linear and second order wave theories significantly underestimate the rogue wave dynamics, thus third or higher order theories should be incorporated (Phillips, 1981), which also has been confirmed by numerical simulations (Gibson & Swan, 2007; Ning, et al., 2009). In addition, the nonlinearities of rogue waves are so strong that sometimes breaking occurs. In order to deal with this problem, which cannot be handled by using the potential theories, other techniques should be introduced. Thanks to the fast development in computing science, which made it more and more efficient to study the waves by solving the Navier-Stokes (NS) equations numerically. The problems with free surface by solving the NS equations were discussed by pioneers such as Harlow and Welch (Harlow & Welch, 1965) and Hirt and Nichols (Hirt & Nichols, 1981).

On top of that, the studies on rogue waves have already been carried out extensively on multiple scales. Great attentions have been paid to the local effects, such as rogue wave interaction with wind (Touboul, et al., 2006; Yan & Ma, 2011), current (Touboul, et al., 2007; Yan, et al., 2010) and structures (Clauss, et al., 2005; Yan, 2006), etc. Such researches significantly contributed to our understanding of the local effects of rogue waves over a short window of time. However, the formation of rogue waves in random seas still cannot be fully explained based on our knowledge so far (Kharif, et al., 2009). In order to capture higher order nonlinear effects or the spatial-temporal spectrum evolution, which are associated with the occurrence of rogue waves, simulations of wave field in large and long time scale are needed (Xiao, 2013).

The statistical studies have suggested that the rogue waves usually have exceedance probabilities ranging from 10^{-3} to 10^{-5} (Adcock & Taylor, 2014). Unquestionably, it may take long duration to observe an occurrence of the rogue wave directly from random sea simulation either physically or numerically. For example, within the range of real observation, one may need to record $10^{3} \sim 10^{5}$ individual waves to collect reliable statistics, e.g. at least 3000 waves based on Rayleigh distribution (Kharif, et al., 2009). Most importantly, in such a way, the occurrence of the rogue waves is random and unpredictable. It may appear after sufficient long evolution due to nonlinearity, thus the duration of the numerical simulation should be long enough to cover the life span of one random sea state. Duration shorter than this may not well represent the evolution of random seas. Since the real sea state averagely lasts for 3 hours (Goda, 2010), and a typical peak period $T_0 \approx 10s$ in North Sea (Ducrozet, et al., 2007; Hasselmann, et al., 1973), the duration of the simulation should last as long as approximately $1000T_0$.

In addition, traditional statistical model only looks at the surface time history at a fixed location. While rogue waves can occur at arbitrary position during the nonlinear evolution, so that area-based statistics should be considered (Wu, 2004). According to Forristall's study on the air gap under the deck of a platform (Forristall, 2005), the maximum crest height in the whole working area ($50\text{m} \times 50\text{m}$) is almost 20% higher than the one expected at a single point. Meanwhile, researchers are aware that higher crests appear in radar images comparing with single point observed time history (Forristall, 2005). This further addresses the importance for developing a statistical model describing wave probability over a specific area, instead of just looking at a fixed location (Kharif, et al., 2009). Such work had been carried out by Piterbarg (2012) through his asymptotic distribution model over large multi-dimensional domain. Nevertheless, instead of directly using such statistical model, random sea can be simulated numerically so that the free surface can be obtained at every time step, which can later be used for statistics. Due to the fact that the location of rogue waves are unpredictable, the domain should be large enough to account for possible locations where rogue waves may occur. According to Wu (Wu, 2004), a large scale domain should cover $10^{2\sim3}$ km^2 in 3D (three-dimensional) situations in order to study the regional wave statistical conditions of spreading short-crest waves. Heuristically, for long-crest waves, i.e., in 2D situations, the corresponding domain size could be re-scaled to $\sqrt{10^{2\sim3}} \approx 10\sim32$ km. Furthermore, for a typical peak wave length in North sea, say $L_0 \approx 156m$ (Ducrozet, et al., 2007; Hasselmann, et al., 1973), the size of the large scale domain is equivalent to $64\sim205L_0$, for example, a domain of $128L_0$ used in (Ducrozet, et al., 2007) .

As aforementioned, the random sea dynamics, involving rogue wave occurrence, is very important for engineering practices, and numerical simulations must be carried out on a large spatial and time scales. In order to complete this task, an accurate and efficient hybrid numerical model will be proposed here .

2 LITERATURE REVIEW

Based on the physical characteristics of the waves, the subject could be divided into two main categories: steady waves and unsteady waves. The former denotes waves with permanent profiles over spatial and temporal scale and the latter represents waves with deformations such as dispersion, resonant interaction, modulation instability, overturning and breaking etc. Both of the categories could be studied by using potential theories except for breaking, which is beyond the theoretical limitation of the potential theories, therefore other approaches should be introduced. To simulate breaking waves, numerical models based on the Navier-Stokes (NS) equation are suggested, such as mesh-based method with specific surface tracking technique, e.g., Marker and Cell (MAC), Volume of Fluid(VOF), Level-Set (LS), Constrained Interpolation Profile (CIP), Particle-in-Cell(PIC), and meshless method, e.g., Moving Partial Semi-implicit (MPS), Smooth Particles Hydrodynamics (SPH), Meshless Local Petro-Galerkin (MLPG). Among them, VOF, SPH and MLPG are most frequently cited in the literatures for modelling free surface waves (Ma, 2008a; Ma & Zhou, 2009; Zhao, et al., 2010; Cui, et al., 2011; Dao, et al., 2011; Cui, et al., 2012; Zhao & Hu, 2012; Ransley, et al., 2013; Rudman & Cleary, 2013), in which impressive results could be found. The NS models could handle wave breaking, nevertheless, it is very computationally expensive. So that these models mainly focus on the local scale effects, such as wave-structure interactions, etc., and the computational domain is small. Therefore it is hardly adopted in the literatures beyond the local scale and will not be further discussed.

For regular waves, breaking occurs when the wave steepness exceeds 0.44 (Le Méhauté, 1976). Due to the complex physics involved in wave breaking, only non-breaking waves based on potential theories are discussed in this study. For reader’s own interest, an introduction and the difficulties involved in modelling breaking waves can be found in (Cokelet, 1977a). Next, a review on the potential wave models will be given.

2.1 Steady wave models

The steady wave model is often used to study the wave pattern, which is stationary to a moving frame. Early studies were mainly analytical solution based on some perturbation methods, which assumed the wave steepness is small. Numerical techniques were later introduced to improve the accuracy since computer programming became popular within researches. In this section, some well-known steady wave (i.e., unchanged wave shape) theories will be briefly reviewed, i.e., the linear wave model, Stokes wave model, shallow water wave models (cnoidal and solitary wave). The waves described by all the theories are symmetrical about a vertical line through crest or trough.

2.1.1 Linear wave model

The study on steady wave problems started from 19th century, while linear theories were dominating. A notable contribution were made by a number of British mathematicians, such as Airy (1845), Rayleigh (1876), Kelvin (1887) and Lamb (1916) etc., who systematically investigated the behavior of linear waves. They had provided an approach to describe the motion of the free surface, which formed the basis of the potential theory. By assuming the fluid is inviscous and irrotational, the Laplace equation is suggested to govern the body of the fluid. Two surface boundary conditions were also imposed, i.e., the kinematic and dynamic boundary conditions, to provide constrains for the problem. This system has soon become popular and hereafter widely used as the theoretical framework to study the wave dynamics. The linear theories assume that the wave amplitude is small, so that the nonlinear terms existing in both the surface boundary conditions are insignificant which can be neglected. The linearized system can be easily solved and the solution is straightforward, which will be discussed in section 3.1 thus details are omitted for simplicity.

In addition, the linear theory can also be used for dealing with some highly interesting unsteady problems, e.g., waves on sloping beaches, diffraction around a break water, wave pattern due to ship motion, leading waves due to sudden disturbance, and waves due to oscillating pressure, etc. The background and history of linear wave theories, as well as the applications, can be found in books by Johnson (1997), Mei (1983) and Stoker (2011). For short, linear wave theories have been successfully employed for modelling steady and unsteady waves of small amplitudes.

2.1.2 Stokes wave model

However, wave profile in reality is asymmetric and exhibits a sharper peak and flatter trough in deep and finite water depth, which could not be explained by linear wave theories. Before long, Stokes (1847) came up with the remarkable Stokes wave theory and unveiled the reason of asymmetric wave profile. In addition, the fifth order Stokes wave solution is limited in situations when the wave steepness is small. In order to apply the Stokes wave theory for large steepness waves, Chappelear (1961) developed a numerical technique which could be applied to desired order and was later improved by Dean (1965). Accurate numerical solutions for Stokes waves were also obtained by Schwartz (1974), Cokelet (1977b), Schwartz & Vanden-

Broeck (1979) and Rienecker & Fenton (1981). Subsequently, Fenton (1988) came up with a fully nonlinear numerical solver and improved the accuracy of Stokes wave theory to the breaking limit, which could be applied for general situations both in deep and finite water depth.

2.1.3 Shallow water wave models

Although the Stokes waves were successfully applied in deep and finite water, it still cannot explain the observation of the solitary wave without troughs in shallow water (Russell, 1845). The contribution to the study on shallow water waves is attributed to Boussinesq (1871), who derived the Boussinesq equation and obtained the solitary wave solution analytically, and also the independent work by Rayleigh (1876). Not until 1895, systematic study on shallow water waves were carried out by Korteweg & de Vries (1895), who obtained the famous KdV equation and the corresponding periodical cnoidal wave solution, as well as the solitary wave solution. Meanwhile, to improve the accuracy for higher amplitude solitary waves, McCowan (1891), Long (1956), Laitone (1960), Grimshaw (1971) had suggested higher order solutions. Subsequently, Fenton (1972) carried the solitary wave solution to the ninth order. However, the accuracy of the analytical solitary wave solution also depends on the magnitude of the wave steepness, and it is only accurate when the steepness is relatively small. To overcome this problem, more accurate fully nonlinear solutions for gravity solitary waves were obtained by Longuet-Higgins & Fenton (1974), Byatt-Smith & Longuet-Higgins (1976), Witting (1975) and Hunter & Vanden-Broeck (1983). A review of some of these methods can be found in (Miles, 1980). Similar to the method by Hunter & Vanden-Broeck (1983), Tanaka (1986) introduced a new variable to stretch the region near the steep crest, which significantly improved the accuracy for calculating large steepness solitary waves. It can also effectively solve the singularity problem at the peak of the crest when study the stability of solitary waves. This method has been recently improved by Clamond & Dutykh (2013) through using FFT algorithm, which significantly accelerated the computation.

Moreover, for periodical waves, the Stokes wave theory breaks down in shallow water limit due to that the convergence of the Fourier expansion in shallow water is very slow. In comparison with Stokes waves, shallow water periodical waves exhibit a sharper peak and long flatter trough. As mentioned above, the first order approximation to the periodical steady wave solution in shallow water, i.e., the cnoidal wave, was already obtained by Korteweg & de Vries (1895) based on the KdV equation. In order to improve the accuracy of the cnoidal wave solution, Laitone (1960) obtained the second order approximation. Later, Monkmeyer (1970) extended this solution to the fifth order, which however, is in terms of the velocity potential and not straight forward for practical use. Subsequently, Fenton (1979) derived the fifth order cnoidal wave solution which is a direct function of time and position and easy to be adopted in practice. Numerical techniques were later introduced to improve the accuracy of cnoidal waves by Fenton & Gardiner-Garden (1982), and more recently by Xu, et al. (2012), to arbitrary order.

2.1.4 Suitability of steady wave models

Based on the previous works, Dean (1974) and Le Méhauté (1976) had discussed the applicability of the theoretical models aforementioned, i.e., the linear wave model, first to fifth order Stokes waves, first order cnoidal waves and first order solitary wave, for steady wave problems and suggested the boundaries between each models in terms of the wave steepness and water depth. Additionally, the fifth order Stokes wave (Fenton, 1985), the fifth order cnoidal wave (Fenton, 1979) and the highest solitary wave (Hunter & Vanden-Broeck, 1983) were compared and their suitability was discussed by Fenton (1990). By using these guidance, researchers are able to determine which model should be employed according to the wave steepness and water depth for steady wave problems. These guidance restricts each wave model in a specific circumstances, beyond which the wave model becomes inaccurate.

As pointed out by Stoker (2011), the two basic nonlinear steady theories, i.e., the Stokes waves (short waves) and the shallow water waves (long waves such as solitary and cnoidal waves), are not uniformly valid in the complete range of water depth. In addition, the recently discovered spike waves in deep water by Lukomsky, et al. (2002a; 2002b), which have sharper crests in comparison with Stokes waves, cannot be explained by the steady wave models aforementioned. In order to develop a universal theory which is accurate for arbitrary depth and also able to model spike waves, Clamond (2003) suggested a renormalized cnoidal wave theory, by introducing Fourier-Padé approximation. According to Clamond (2003), all the types of waves aforementioned, i.e., the Stokes waves, cnoidal waves, solitary wave, as well as the newly discovered spike waves, can be represented by the renormalized cnoidal wave theory accurately.

Although these models aforementioned are improved by introducing new techniques either theoretically or numerically, they are only applicable for solving steady wave problems. However, waves in reality is a stochastic process and the random sea is unsteady without permanent profile. It consists of a wide spectrum of wave components with different frequencies, wavenumbers and amplitudes. The evolution of random sea involves very complicated physics such as linear dispersion of different components and the nonlinear wave-wave interactions. These non-stationary features are very important and cannot be modelled by using the steady models aforementioned. Therefore, steady wave models will not be further discussed in this thesis, except for the linear wave model, which will be adopted to convert the spectrum to free surface elevation.

2.2 Unsteady wave models

It was not until 1967, Benjamin & Feir (1967) found that waves were not able to remain permanent profiles when they tried to generate a uniform wave train in the flume. This phenomenon cannot be explained by using the Stokes wave theory alone. Soon after, they carried out the analysis to third order and realized that this phenomenon was due to the energy exchange between the carrier wave and its side-bands. Their discovery of the side-band instability emphasized the importance about studying the unsteady wave problems, in which the nonlinear effects cannot be neglected. Since the nonlinearities are very important for studying harsh random seas, the hybrid model should couple on the basis of nonlinear wave models. Therefore, a brief introduction will be given on the unsteady wave models.

2.2.1 Second order wave models

The second order wave theories consider the nonlinear wave-wave or wave-structure interactions one order higher than the linear models and are often applied in theoretical study of nonlinear waves. The study based on the second order wave models mainly looks at wave characteristics that cannot be explained by using the linear theory, which evidences that the linear wave model is inaccurate in some circumstances.

The second order effects (in terms of wave spectrum, which is fourth order in terms of wave steepness) were firstly considered in the modelling of wind waves on global scale. Hasselmann (1962) introduced the second order (in terms of wave spectrum) correction to the wind wave model to describe the evolution of the wave spectrum in order to involve the nonlinear effects. This soon became very popular in studying the wind wave models, which are based on the wave energy or action conservation equation. It was the first time when the wind wave model was applied to realistic ocean wave simulation by Komen, et al. (1996). The most frequently quoted and studied models include WAM, WAVEWATCH, SWAN and so on. A review on the wind wave models could be found in the book by Lavrenov (2003) and a more recent detailed introduction about the state of art on global wave modelling could be found in reference (Cavaleri, et al., 2007). However, those models only deal with the evolution of the wave spectrum, the phase is assumed to be averaged and cannot be derived during simulation. Without knowing the phase of each wave component, the free surface spatial distribution or time history is impossible to be determined. Thus it is difficult to judge whether rogue waves occur or not, let alone to study the wave kinematics. Besides, the resolution for numerical computation by using these models is too coarse, i.e. $0.5^o \approx 55km$ on a global scale and $1km$ near coastal areas (Cavaleri, et al., 2007), which is always larger than the wave length of interest (hundreds meters). So that the wind wave models will not be further discussed.

Meanwhile, the second order wave theories are widely used in the wave statistical models. It was Longuet-Higgins (1963), who came up with the second order statistic model to investigate the probability distribution of free surface elevation in deep sea. Further and more recent studies of wave statistics based on the second order theories can be found in (Forristall, 2000; Toffoli, et al., 2006). In addition, Janssen (2009) derived general expressions for the second order wavenumber and frequency spectrum, as well as the skewness and the kurtosis of the sea surface. It is reported that in deep water, the second order effects on the wavenumber spectrum are relatively small. However, in shallow water where waves are more nonlinear, the second-order effects are relatively large and reveal the observed second harmonics and infra-gravity waves in the coastal zone. This also evidenced the investigation by Longuet-Higgins & Stewart (1962; 1964), who addressed the radiation stresses in water waves to account for 'set-up' due to storm surge, and the study by Dalzell (1999) on the wave set-down in finite water depth. Although it has been pointed out that the skewness and kurtosis are related to the probability of the rogue wave occurrence (Kharif, et al., 2009), one still cannot obtain the deterministic information, such as the rogue wave free surface profile based on the statistical models. Furthermore, due to the sudden appearance of rogue waves and the persistently changing sea state, the statistical stationarity condition also breaks down (Kharif, et al., 2009). Thus, the statistical models will not be considered in this thesis.

Another application of the second order wave theory is mainly focused on wave-structure interactions, since great attentions are paid to the second order effects on the wave diffraction and reflection, wave forces and responses of the structures, etc. Kriebel (1990; 1992) investigated the interaction of second order Stokes waves with a large vertical circular cylinder. It is reported that the second order terms significantly alter the wave envelopes around the cylinder as a result of nonlinear diffraction. Sometimes the maximum wave crest run-up on the cylinder exceeds the linear prediction by up to 50%. Thus second order effects cannot be neglected and should be incorporated.

There are two approaches to study the second order effects of wave-structure interactions: One is based on frequency domain method and the other is based on time domain method. The frequency domain method is semi-analytic and does not require large amount of CPU time and computer memory. Such approaches can deal with bodies with arbitrary shape to the second order by using Fourier decomposition. Credits belong to Lighthill (1979), Molin (1979) and

Rahman (1984), who firstly considered and extended the second order theories for investigating wave forces on circular cylinder structures in deep, finite and shallow water depth respectively. Similar methods were also developed by Sharma & Dean (1979), Wu (1991) and Chau & Eatock-Taylor (1992). Furthermore, Huang and Eatock-Taylor (1996) developed a complete semi-analytical solution for second order diffraction of monochromatic waves by a truncated vertical cylinder. A particular solution to the second order diffraction potential, exactly satisfying the inhomogeneous free surface condition, was derived. It is reported that the approximate solution possesses excellent accuracy for the total second order heave force over a wide range of conditions. When $k_0b > 1.2$ (where k_0, b are the incident wavenumber and the draught of the cylinder respectively), the accuracy for total second-order surge force and pitch moment is also satisfactory. Later, Eatock-Taylor & Huang (1997) extended this exact theory for second order wave diffraction by a vertical cylinder to the case of bichromatic incident waves. Other applications can be found in many publications, e.g., WAMIT(R) (Lee & Newman, 2006) for structures interact with bichromatic and bidirectional waves, wave-structure interactions in spreading seas (Sharma & Dean, 1981), second order monochromatic water wave diffraction by an array of fixed cylinders (Malenica, et al., 1999), waves interacting with truncated vertical floating cylinders (Kashiwagi & Ohwatari, 2002), and extreme waves interacting with multi-column structures in random seas (Grice, et al., 2015), etc.

There are also works based on the time domain method. The advantage of the time domain method over the frequency domain method is that it can easily capture more transient effect if the motion is not periodic. The time domain method is usually solved by using the Boundary Element Method (BEM) through two schemes. One is based on Green function (Beck & Liapis, 1987) and the other is based on Rankine source (Isaacson & Cheung, 1991; 1992). The drawback by using these approaches is that they both requires large amount of memory. To overcome this challenge, Wang & Wu (2007) proposed a Finite Element Method (FEM) to analyze interactions of water waves and a group of cylinders. By using the FEM, more complicated shapes, other than circular cylinders can also be simulated. More interesting applications of the time domain method can also be found in references, e.g., the study on second order wave forces acting on stationary vessels in regular and irregular waves (Pinkster, 1980), and a complete second order solution for two dimensional wave motion forced by a sinusoidally moving generic wave maker (Solisz & Hudspeth, 1993), etc.

Considering the free motion of the waves, since the explicit expression of free surface is given by Sharma & Dean (1979), Forristall (2000) and Toffoli, et al. (2006), the extra terms in these second order wave models are the additional second order correction parts comparing with the linear wave models. Although the second order wave models consider the interaction between every two wave components, they are only accurate for small and moderate steepness waves. However, the random sea always involves strong nonlinear wave-wave interactions of large steepness waves and wide spectrum. In that case, the results given by second order theory will be inaccurate as nonlinear effects higher than the second order cannot be neglected.

As pointed out by Onorato, et al. (2006), for long-crested waves and for large values of the Benjamin-Feir index, the second order theory is not adequate to describe the tails of the probability density function of wave crests and wave heights. The probability of finding an extreme wave can be underestimated by more than one order of magnitude if second order theory is considered. In addition, according to Phillips (1981), who examined interaction between two gravity wave trains with arbitrary wavenumbers and only found bound harmonics with amplitudes remaining forever small, no continuing energy transfer exists to the second order. It means the second order model cannot well describe the energy transfer between different components, i.e., the so called resonant interactions, thus third or higher order theories should be incorporated (Phillips, 1981). This also has been confirmed by numerical simulations that the second order wave theory is inadequate for modelling extreme waves (Gibson & Swan, 2007; Ning, et al., 2009). In other words, the second order theories can well describe the wave characteristics, but only in a short window of time and in local areas. On large time and spatial scale, effects of third or higher orders cannot be neglected. Furthermore, to deal with infinitesimal steepness waves, the second order wave models cost more computational efforts compared with linear wave models due to their additional estimation of the second order terms. For moderate and large steepness waves involving strong nonlinearities, the second order theories are inaccurate as aforementioned. Thus the second order model will not be considered for simulating random waves for general purposes in this study.

2.2.2 Shallow water wave models

In fact, the investigations of nonlinear shallow water waves has a long history which could be traced back to Scott Russell's observation of a solitary wave phenomenon in a channel (Russell, 1845), and Airy's study on long waves of tides in 1845 (Airy, 1845). Scholar Scott Russell observed a particular type of waves which he named as the "solitary wave" in his experiment (Russell, 1845). The solitary wave has an extremely long wave length moving with a permanent shape, which could not be explained. Later on in 1845, Airy's study "Tides and Waves" (Airy, 1845) concluded that long waves must necessarily change their form as they advance, which contradicts with the observation of Russell. It was not until 1871, Boussinesq's derivation of his famous Boussinesq equation (Boussinesq, 1871) with the discussion of its solutions, and in 1876, Rayleigh's independent reproduction of this equation (Rayleigh, 1876), unveiled the mystery. It is a shame that the both of their studies of the weakly nonlinear, weakly dispersive wave system were often overlooked by the contemporaries according to Miles (1981) and Vastano & Mungall (1976).

A systematic study of nonlinear shallow water waves was carried out by Korteweg & de Vries (1895), who were inspired by Rayleigh but had never read the papers by Boussinesq. They obtained the well-known KdV equation, which has a relatively simpler form compared with the Boussinesq equation, and subsequently solved the equation for the solitary wave solution and the periodic cnoidal wave solution. It is worth noting that Ursell's contribution attributes to his explanation of the effect of the Ursell parameter $U_r = aL_0^2/h^3$ on the derivation of the shallow water governing equations using the Lagrangian scheme (Ursell, 1953). According to Airy's theory, finite amplitude progressive long wave cannot propagate without changing its form. While on the other hand, Rayleigh claimed that the solitary wave is a long wave with small amplitude travelling without change of form. The inapplicability of Airy's theory to solitary wave constitutes a paradox, which is then solved by Ursell through the introduction of Ursell parameter. When $U_r = O(1)$, the effect of the nonlinearity and the dispersion is balanced and it brings the Boussinesq equation coincides with Rayleigh’s conclusion; While $U_r \gg O(1)$, Airy's theory stands and the progressive long wave cannot propagate without changing its form.

In order to extend the shallow water equations, such as the KdV and Boussinesq equation, for studying the unsteady wave problems, new techniques were introduced to improve these models. Mei & Le Méhauté (1966) extended Boussinesq equation to cases with uneven bottom. Peregrine (1967) also extended the shallow water wave theory to variable depth situation and introduced the Peregrine system. Kadomtsev & Petviashvili (1970) came up with the KP equation to study the transverse instability of shallow water waves. Kakutani (1971) and Mei (1983) considered the effect of the uneven bottom on the gravity waves and derived the perturbed KdV equation.

Meanwhile, in order to consider higher order effects, Dingemans (1973) was the first to derive the higher order Boussinesq equation up to $O((k_0h)^4)$, by retaining more terms in the polynomial velocity expansion, though it has been pointed out by Madsen & Schäffer (1998) that singularities are involved thus it is difficult to be used in numerical simulation. Benjamin, et al. (1972) systematically discussed the linear dispersion properties based on the KdV equations, and they found that the numerical stability and dispersion were improved by including third derivative terms in the leading part. Following this idea, Mei (1983) straightforwardly reproduced the derivation of the shallow water governing equations through perturbation method and proposed four different versions of the KdV equations.

A milestone was laid when the numerical model based on low order Boussinesq equation is developed for commercial use, and soon became very popular in coastal engineering (Abbott, et al., 1984). Subsequently, attention was shifted to model nonlinear irregular waves and researchers spent lots of efforts to extend the practical range of application of these equation (McCowan, 1987; Rygg, 1988; Kirby & Vengayil, 1988). Later, the improvements on these shallow water equations mainly focused on two aspects: a) on linear dispersion characteristics and b) on nonlinear properties. In order to enhance the linear operator, Madsen, et al. (1991) and Nwogu (1993) borrowed the ideas of Witting (1984), and introduced a new technique incorporating Padé approximants. This resulted in extraordinarily good linear characteristic. Later, these works were extended to uneven bottom (Madsen & Sørensen, 1992) and larger depth $k_0h \approx 6$ (Schäffer & Madsen, 1995). On the other hand, in order to improve the nonlinear properties, Wei & Kirby (1995) and Wei, et al. (1995) made a breakthrough on Boussinesq type equation, who had allowed for the fully nonlinearities in its derivation. A Stokes type analysis by Wei & Kirby (1995) showed that a significant improvement of nonlinearity was achieved for $k_0h < 1.25$, while it gave poor nonlinearity for $k_0h > 1.5$. Further improvements and discussions on the nonlinear properties of shallow water equations are proposed by Zou (1999; 2000), Agnon, et al. (1999), Kennedy, et al. (2001), Wu (2001), Madsen, et al. (2002) and etc.

Based on the improved formulations, new features are also involved, and applications of KdV and Boussinesq models for water wave simulations are extensive. Kennedy, et al. (2000) and Chen, et al. (2000) explored the wave transformations, such as shoaling, breaking and run-up, in surf zone based on the extended Boussinesq equations in two and three dimensions respectively. Pelinovsky & Sergeeva (2006) also successfully applied the KdV equation to simulate random waves. Chen (2006) employed the Boussinesq equation to model wave-current interactions over porous sea beds. Nwogu & Demirbilek (2004) investigated the wave-ship interactions in a confined waterway based on the Boussinesq numerical model.

In spite of versatile versions of the KdV and Boussinesq equations, the applications of them are still limited to shallow or finite water (Madsen & Fuhrman, 2010). It has been pointed out by Grue, et al. (2008) that the KdV equation has limited capacity in resolving dispersion compared with the fully nonlinear approach when applied to model the propagation of long waves, such as tsunami. This was further confirmed by Wang & Ma (2015b) that the dispersion will not be accurately modeled by using the Boussinesq equation (Shi, et al., 2012) in relatively deep water for generating focusing waves, and the suitability of the Boussinesq equation (Shi, et al., 2012) depends on the Vertical Asymmetry Factor (VAF) of the focusing waves. Although various techniques are proposed to overcome the limitation on water depth, such as the higher order fully nonlinear Boussinesq model by Madsen, et al. (2003) and the multi-layered Boussinesq model by Lynett & Liu (2004), their computational efficiency are very expensive. In that case, fully nonlinear methods based on fast algorithms are preferred as they don't have such limitations on water depth, neither on wave steepness. Due to the limitations on water depth, these models are not considered for simulating random waves in deep sea in this study. For more details, one can refer the review about the shallow water equations by Madsen & Fuhrman (2010).

2.2.3 Nonlinear Schrödinger equations

It is also worth of noting that the third order wave model developed by Benjamin & Feir (1967) in order to investigate the modulation instability, unveiled the importance to study the nonlinear wave-wave interactions. Later, McLean, et al. (1981) and McLean (1982a; 1982b) extended this theory to 3D situations. Meanwhile, Whitham (1965) explored the nonlinear effect on dispersive waves up to the third order via the average Lagrangian method from another point of view. The details about the average Lagrangian approach could be found in (Whitham, 1974). In order to study the modulation instability of gravity waves in finite water depth, Whitham (1967) came up with the third order formulations for arbitrary depth, and concluded that the wave train will remain unstable unless the characteristic water depth $k_0 h \leq 1.363$. Subsequently, Benjamin & Hasselmann (1967) validated this conclusion by using very similar method as Benjamin & Feir (1967). Both of their studies are further confirmed by Phillips's investigations (Phillips, 1960; 1981) on resonant interactions. Before long, Chu & Mei (1970; 1971) found that the initial wave envelope tends to disintegrate into multiple groups of waves each of which approaches a stable permanent solitary envelope through their third order wave model. By using this method, if the initial condition of the wave train is specified, the maximum amplitude of the wave train could be obtained. They also concluded that the final amplitude of the envelope depends on the initial distribution of the amplitude and the modulation wave number over space. A recent and detailed review about the modulation instability and the related studies can be found in the annual review by Dias & Kharif (1999). More recently, the near-resonant interactions described by Benjamin & Feir (1967) was also considered in the statistical models for random waves, such as the investigations on the statistics of crest (Gibson, et al., 2007) and kurtosis of deep water waves (Fedele, 2015). Such third order wave theories are very important that they contributed to our understanding of unsteady waves.

The nonlinear Schrödinger equation (NLSE) is an effective tool to study the dynamics of the gravity water waves in deep and finite water depth. The third order weakly nonlinear equation was first derived from the Zakharov equation (Zakharov, 1968), which is referred as the cubic NLSE (short as CNLSE) in this thesis. The details of deriving the Zakharov equation and the CNLSE could also be found in (Johnson, 1997). Subsequently, Benny & Roskes (1969), Hasimoto & Ono (1972), Davey & Stewartson (1974) also came up with the similar equations by using perturbation method. Whitham also talked about the derivation of the CNLSE in his book (Whitham, 1974) by using the average Lagrangian method. Later, new features were introduced to the CNLSE to study the physics of nonlinear waves. For example, Johnson (1976) derived a Schrödinger type equation which describes the slow modulation of free surface waves over an arbitrary shear. It has been shown in this work that the equation can be evaluated for no-shear thus agrees with the work of Hasimoto & Ono (1972) in finite water and Davey & Stewartson (1974) in deep water. Meanwhile, this equation can also by simplified to the KdV equation (Korteweg & de Vries, 1895) after the coefficients being approximated for arbitrary shear. Stewartson (1977) also suggested an equation which describes the interactions between the surface waves and the current, who shows that uniform wave train could be significantly modified if its group velocity equals to the phase velocity of the long wave representing the current. Such improvements on the CNLSE for arbitrary depth also include the works of the parametric form of the formulation by Mei (1983) and Brinch-Neilsen & Jonsson (1986), etc.

The early studies based on the CNLSE mainly focus on the modulation instability (Benjamin & Feir, 1967). Researchers have devoted to solve the CNLSE analytically by using the Inverse Scattering Transform(IST) technique, e.g., Zakharov & Shabat (1972) and Ma (1979), who gave the plane wave solution to the CNLSE, as the prototype of rogue waves. Further analytical studies can be found in (Yuen & Lake, 1982; Peregrine, 1983). More recently, Osborne (2001) explored the rogue wave behaviour based on the analytical solutions to the CNLSE, in which various forms of analytical rogue wave solutions are discussed. Adcock & Taylor (2009) also studied the evolution of a Gaussian wave group in deep water by proposing an approximated analytical model based on the CNLSE, and qualitative agreement is obtained with numerical results based on the fully nonlinear model. This work is later being extended to finite water situations by Adcock & Yan (2010). Meanwhile, some researchers derived the spectral transport equations based on the CNLSE, e.g., Longuet-Higgins (1976) had reformulated CNLSE and Alber (1978) took advantages of the Davey & Stewartson system (Davey & Stewartson, 1974), to investigate the nonlinear energy transfer within the peak of a narrow spectrum. Furthermore, Lake at al. (1977) were the first to investigate the later stage of the wave packet evolution through numerical simulation based on the CNLSE and found that the modulation to the nonlinear wave train periodically increases and decreases, which makes the wave train exhibit the Fermi-Pasta-Ulam(FPU) recurrence phenomenon. Subsequently, Yuen & Ferguson (1978) carried out long time numerical simulations of the Benjamin-Feir instability with different initial conditions via solving the CNLSE and found a critical value of spectrum width which splits the evolution into simple evolution and complex evolution.

Based on the studies previously, Dysthe (1979) extended this theory to the fourth order (third order in steepness + first order in bandwidth) and derived the Dysthe equation, which is one order higher than the CNLSE. By using the Dysthe equation, Lo & Mei (1985) carried out a group of numerical simulations of modulation instability and good agreement is obtained, which was the first time that the Dysthe equation being solved numerically in literatures. However, the Dysthe equation is still subject to the limitation on the spectrum width, which is of order equivalent to the wave surface steepness and both must be small. In order to improve the applicability of the Dysthe equation for wider spectrum, Trulsen & Dysthe (1996) modified the assumption on the spectral width and derived an equation for broader band width. Subsequently, by using this equation, they investigated the evolution of the spectrum and found no permanent shift of the spectral peak in two dimensional situation. However, in three dimension cases, permanent downshift is observed (Trulsen & Dysthe, 1997), which was further confirmed in the laboratory (Trulsen, et al., 1999). Later, in order to further minimum the effect of the limitation on spectrum width, Trulsen, et al. (2000) corrected the linear terms to the exact linear operator, and named this model as the fourth order Enhanced Nonlinear Schrödinger Equation (short as ENLSE-4 hereafter).

Meanwhile, due to that it was very slow to solve the Zakharov equation numerically, simplified versions were proposed. For example, another parallel study was carried out by Stiassnie (1984), who applied the narrow spectrum assumption to the Zakharov equation and derived the same equation as Dysthe (1979), which indicates that the Zakharov equation does not subject to the narrow spectrum limitation and the Dysthe equation is only one special case of it. However, it was found that the equation obtained by Stiassnie is slightly different from that by Janssen (1983). This argument between Janssen (1983) and Stiassnie (1984) was later pointed out and resolved by Hogan (1985), who proved that Stiassnie made a mistake during the derivation. Later, Kit & Shemer (2002) obtained two fourth order evolution equations in terms of the amplitude of the free surface elevation and velocity potential, based on a spatial version of the Zahharov equation, which further illustrated the feasibility of extension to higher orders. In order to involve more nonlinear terms, Debsarma & Das (2005) used the same technique as Stiassnie (1984) and obtained a fifth order (third order in steepness + second order in bandwidth) equation called the Higher Order Dysthe Equation in terms of Hilbert transform. Similarly, by introducing Trulsen's approach (Trulsen, et al., 2000), the linear operation of this equation could be enhanced and it is referred as the fifth order Enhanced Nonlinear Schrödinger Equation based on Hilbert transform (short as ENLSE-5H) in this thesis.

One should note that the CNLSE (Zakharov, 1968), the Dysthe equation (Dysthe, 1979; Stiassnie, 1984) and Higher Order Dysthe Equation (Debsarma & Das, 2005), can be derived from the Zakharov equation (Zakharov, 1968), where the Zakharov equation is a third order equation in steepness. By assuming bandwidth being the same order with steepness, various versions of Schödinger type equations can be obtained, e.g., CNLSE of third order, Dysthe equation of fourth order (third order in steepness + first order in bandwidth) and Higher Order Dysthe Equation of fifth order (third order in steepness + second order in bandwidth). To avoid confusion, the order of bandwidth will not be mentioned and readers should be aware that the order of bandwidth is involved in naming the Schödinger type equations.

More recent developments and applications of the NLSE theory include irregular waves modelling in finite water depth by Trulsen, et al. (2001), higher order formulation for finite and shallow water depth by Slunyaev (2005), statistics of rogue waves in random sea (Schober & Calini, 2008), coupled Dysthe equation for interactions between two directional wave systems (Gramstad & Trulsen, 2011), variable coefficients fifth order nonlinear Schrödinger type equation for arbitrary water depth (Grimshaw & Annenkov, 2011), a NLSE for two dimensional surface water waves on finite depth with non-zero constant vorticity (Thomas, et al., 2012), numerical techniques for solving the Zakharov equation (Nwatchok, et al., 2011), Hamiltonian form of CNLSE for arbitrary depth (Gramstad & Trulsen, 2011; Craig, et al., 2012) and Akhmediev-Peregrine breather solution to the CNLSE in deep water (Vitanov, et al., 2013), etc.

Applications of Schrödinger type equations in large scale simulations are extensive. Onorato, et al. (2011) brought the effects of current into the CNLSE and showed that rogue waves can be triggered naturally when a stable wave train enters a region of an opposing current flow, based on a numerical simulation in a domain of 60 peak wave lengths lasting for 60 peak periods. Dysthe, et al. (2003) studied the evolution of the gravity wave spectra starting from narrow bandwidth based on both the CNLSE and the ENLSE-4 in a domain covering 100×100 peak wave lengths for 150 peak periods. According to them, a power law behavior $\mathrm{k}^{-2.5}$ for angularly integrated spectrum was observed, which was confirmed by the study carried out by Onorato, et al. (2002). In addition, Shemer, et al. (2010) studied the probability of rogue waves in a NWT of 77 peak wave lengths long during 100 peak periods based on both the CNLSE and the Dysthe equation for random wave simulations. Such similar large scale studies can also be found in (Dysthe, et al., 2005; Zhang, et al., 2007; Onorato, et al., 2001), etc.

Although versatile versions of NLSE have been suggested, they are only accurate when both wave steepness and local bandwidth are small. Henderson, et al. (1999) simulated traveling waves based on the CNLSE and fully nonlinear Higher-Order BEM, and concluded that there was excellent agreement between the results of these two models only for waves with small initial steepness ($\varepsilon < 0.056$). Clamond, et al. (2006) investigated the evolution of the envelope soliton of initial steepness $\varepsilon = 0.091$ using the ENLSE-4 and their fully nonlinear approach separately. Through comparing the free surface profiles, they concluded that the former was only valid for a limited period at the beginning of the simulation before rogue waves are formed, which indicates that the ENLSE-4 is inaccurate when wave steepness becomes large, i.e., $\varepsilon \geq 0.21$. Toffoli, et al. (2010) have simulated random directional wave field based on the modified Dysthe equation by Trulsen & Dysthe (1996) and the HOS method. Through comparing the results obtained from these two models, they found discrepancies between them within the first 20 peak periods when the experimental initial steepness reached $\varepsilon = 0.16$. Slunyaev, et al. (2013) have compared the analytical solution of the CNLSE with the numerical results of the Dysthe equation and the fully nonlinear Euler equations. They concluded that the CNLSE is not accurate for simulating waves evolving into its breaking limit, i.e., $\varepsilon \geq 0.42$. Hu, et al. (2015) compared the breather solution to the CNLSE with numerical results based on the NS solver, in which it is found that the analytical solution for $\varepsilon = 0.22$ provides good agreement only within the first 20 peak periods.

It should be noted that for numerical study, the ENLSE-4 is exact to model linear dispersion for small steepness waves, so that it is preferred rather than using CNLSE and the Dysthe equation. Meanwhile, the Higher Order Dysthe Equation is one order higher than the Dysthe equation, so that more nonlinear terms are involved and it is more accurate for modelling nonlinear waves. Thus, the ENLSE-4 and Higher Order Dysthe Equation will be considered further in the following study, and neither the CNLSE nor the Dysthe equation will be discussed again.

2.2.4 Fully nonlinear models

To simulate large steepness waves, the study on the unsteady gravity surface waves in a fully nonlinear sense was firstly attempted by Longuet-Higgins & Cokelet (1976), who introduced the Boundary Element Method (BEM) and successfully simulated the two-dimensional (2D) overturning waves in deep water. Subsequently, Vinje & Brevig (1981), Baker, et al. (1982) and (New, et al., 1985) adopted similar methods for cases in finite water depth. These authors investigated various types of breakers, which significantly contributed to our understanding of breaking wave dynamics. In order to extend the BEM for more general cases rather than breaking waves, the algorithm of BEM was later improved by Grilli, et al. (1989), Dold (1992), Grilli & Subramanya (1996), Grilli & Horrillo (1997) and Henderson, et al. (1999). These models can accommodate both arbitrary waves and complex bottom topography, as well as surface-piercing moving boundaries such as wave-makers. The simulations are carried out in physical space domain, where incident waves can be generated at one extremity and reflected, absorbed or radiated at the other extremity. For these reasons, they are often referred as the Numerical Wave Tank (NWT). However, the studies aforementioned are still limited to two dimensional problems. It was not until Boo, et al. (1994), who firstly tried to simulate non-breaking irregular waves in three dimensions by using a high order BEM. Subsequently, Ferrant (1996) and Celebi, et al. (1998) introduced new features to three dimensional NWT based on BEM for strong nonlinear wave problems, such as wave generation, wave-body interactions. Later, Xü & Yue (1992) and Xue, et al. (2001) investigated three dimensional overturning waves based on a quadratic BEM in infinite water depth and finite depth over a bottom obstacle. To address for the accuracy of modelling strong nonlinear three dimensional waves, Grilli, et al. (2001) proposed an accurate three dimensional BEM for modelling waves propagating over complex bottom topography. This NWT is based on a high-order BEM with third order spatial discretization, ensuring local continuity of the inter-element slopes. Arbitrary waves can be generated and absorbing condition can be specified on lateral boundaries. Moreover, the numerical models based on the BEM were extended to practical applications. Tong (1997) studied the bubble-structure interactions with unsteady free surface motion based on the BEM numerical simulations. Guyenne, et al. (2000) had performed a numerical simulation in NWT base on BEM to investigate wave impact on a vertical wall. Brandini & Grilli (2001a; 2001b) and Fochesato, et al. (2007) successfully generated rogue waves in spreading seas by using directional focusing wave approach based on BEM. Grilli, et al. (2002) and Enet (2006) developed a numerical BEM model to investigate the mechanism of tsunami generation by submarine landslide. The ship waves were modelled by Sung & Grill (2005; 2006; 2008) through imposing a moving pressure disturbance on the free surface.

Meanwhile, Wu & Eatock-Taylor (1994; 1995) introduced the Finite Element Method (FEM) to study the interaction between waves and structures in two dimensional cases. Further 2D studies based on FEM were also carried out by Westhuis & Andonowati (1998), Clauss & Steinhagen (1999), Wang & Khoo (2005) and Sriram, et al. (2006). This method was later extended to 3D cases by Wu, et al. (1995) in a circular wave tank. Then the NWT based on

FEM was further developed to deal with 3D problems in rectangular tank with waves generated by a wave maker or motion of a tank by Wu, et al. (1996; 1998), Ma, et al. (1997) and Ma (1998). Subsequently, the FEM was successfully used to model wave-structure interactions, e.g., interactions between waves and multi-bodies by Ma, et al. (2001a; 2001b), waves generated by a moving vertical cylinder by Hu, et al. (2002) and Wang & Wu (2006), and wave loads on oscillating cylinder by Wang, et al. (2007).

However, a drawback of the FEM is that the complex unstructured mesh needs to be regenerated at every time step to follow the motion of waves and bodies, which costs the majority of CPU time. Efforts have been made to reduce the CPU time on meshing (Heinze, 2003; Turnbull, et al., 2003; Wu & Hu, 2004). However, these methods are either still slow or restricted to cases for bodies with special shapes. In order to overcome this meshing problem, Yan (2006) and Ma & Yan (2006) proposed a new mesh strategy and came up with the Quasi Arbitrary Lagrangian-Eulerian Finite Element Method (QALE-FEM), which significantly improved the computational efficiency of the conventional FEM. This method was later successfully used to solve gravity surface wave problems, e.g., interactions between waves and floating structures (Yan, 2006), rogue wave generation by directional focusing technique (Yan & Ma, 2009), 3D overturning waves (Yan & Ma, 2010), wave-current interactions (Yan, et al., 2010), dynamics of rogue wave enhanced by wind (Yan & Ma, 2011), tsunami wave impacts (Yan, et al., 2013) and wave dynamics in moon-pool (Yan & Ma, 2014).

A detailed introduction about the fully nonlinear models aforementioned, i.e., the BEM, FEM and QALE-FEM, can be found in the review by Tsai & Yue (1996), chapter 3 and 5 in the book by Ma (2010). Although it was pointed out that the FEM cost less computer memory than the BEM by Wu & Eatock-Taylor (1994), which was further confirmed by Ma & Yan (2009), it should be noted that those methods are still relatively expensive. Meanwhile, the FFT based method is more computational efficient for simulating free motion of surface waves. One of such method relies on the perturbation expansion of the velocity potential at the free surface. For example, West, et al. (1978) and Dommermuth & Yue (1987) suggested the Higher-Order Spectral (HOS) method to simulate propagating waves. However, this method assumes that the Taylor expansion of the velocity potential at free surface is convergent. It is very accurate when the waves to be studied are not steep ($\varepsilon = k_0 a < 0.35$) (Dommermuth & Yue, 1987). Meanwhile, some researchers also focused on the expansions of the Dirichlet-Neumann operator, which expresses the normal surface particle velocity in terms of the velocity potential at the surface. For example, Craig & Sulem (1993) derived a limited series expansion of the Dirichlet-Neumann operator in two dimensions, which was later extend to three dimensions by

Nicholls (1998) and Bateman, et al. (2001). The evaluation of the higher order terms in Dirichlet-Neumann operator is highly recursive, which, according to Gibbs & Taylor (2005), can effectively reduce the number of FFT operations. This method was named as Spectral Continuation (SC) method (Nicholls, 1998) and was investigated in a comparative study by Schäffer (2008), who pointed out that the SC method is identical to the HOS method considering the Dirichlet-Neumann operator expansions alone. Taking both accuracy and efficiency into account, the expansion to the velocity potential or the Dirichlet-Neumann operator is always truncated to limited order, e.g., fifth order in the study by Nicholls (1998) by using the SC method and third order in the study by Wu, et al. (2005) by using the HOS method. As a consequence, the HOS or SC method is incapable to capture the higher order nonlinearities when wave steepness is large and nonlinearities are strong. Thus, they are only accurate when wave steepness is moderate and the nonlinearities are weak. Although the difficulty encountered for very steep waves was analyzed by Nicholls & Reitich (2001a; 2001b), who revolved the problem by introducing a sigma transformation of the vertical coordinate, the transformed system is very complicated and computationally demanding to solve (Schäffer, 2008). However, the HOS method is still very popular for simulating nonlinear waves, and other new features are continuously introduced, which include presence of atmospheric forcing (Dommermuth & Yue, 1988), variable finite depth (Liu & Yue, 1998), fixed and moving submerged bodies (Liu, et al., 1992; Zhu, et al., 1999), variable current (Wu, 2004), and effects of energy dissipation (Wu, et al., 2006). For readers' own interests, one can refer to the review by Tsai & Yue (1996), chapter 4 in the book by Ma (2010) and chapter 15 in the book by Mei, et al. (2005) for more details.

In order to simulate non-breaking waves accurately and not subject to limitation on wave steepness, an efficient numerical model based on boundary integral equations and FFT was proposed by Clamond & Grue (2001), which was later extended to the 3D applications by Fructus, et al. (2005). This method expands the Dirichlet-Neumann operator as a sum of global convolution terms and local integrals with kernels that decay quickly in space. The global terms are computed very quickly via FFT while the local terms are evaluated by numerical integration with truncated integrating range. Subsequently, new features were introduced to extend this method for more general situations, such as techniques for wave generation and for absorption by imposing a moving oscillating pressure at free surface (Clamond, et al., 2005), techniques for modelling waves interacting with surface piercing cylinder (Grue, 2005) and waves propagating over variable and moving bottom topography (Fructus & Grue, 2007). Furthermore, in order to improve the computational efficiency, Grue (2010) expanded the integral kernels and derived the convolution form up to the seventh order, and neglected the integration parts. This approach significantly accelerated the numerical simulation. Moreover, this method has been applied to investigate the dynamics of 3D horse shoe wave patterns (Fructus, et al., 2005), simulate long time evolution of short wave group in two dimensions (Clamond, et al., 2006), study the deformation of the tsunami moving into a shallow strait and formation of undular bores and solitary waves (Grue, et al., 2008), and model the motion of 3D interfacial waves (Grue, 2015).

The method by Fructus, et al. (2005), named as the Spectral Boundary Integral (SBI) method, was subsequently improved by Wang & Ma (2015a). Three new numerical techniques were introduced and the computational efficiency was significantly improved (35 times faster in some cases). The newly improved SBI method is then named as the Enhanced Spectral Boundary Integral (ESBI) method. Meanwhile, as pointed out by Wang & Ma (2015), the solution to the vertical velocity could be truncated to the third order convolutions and higher order terms can be neglected. As a result, the computational efficiency will be further improved. However, for large steepness waves, the results will be inaccurate because higher order nonlinear terms are important and cannot be neglected during estimating the vertical velocity. Nevertheless, it is still accurate for modelling small and moderate steepness waves. Thus it is named as the Quasi Spectral Boundary Integral (QSBI) method.

Since the FFT based fully nonlinear models are very computational efficient, they have been successfully applied to simulate random seas on large scale. Impressive results are obtained, such as the investigation of rogue waves in random background based on the HOS method by Wu, et al. (2005) (128×128 peak wave lengths taking up to 160 peak periods), Ducrozet, et al. (2007) (42×42 peak wave lengths taking up to 250 peak periods), and Xiao, et al. (2013) (128×128 peak wave lengths taking up to 150 peak periods), as well as the short wave group simulation based on the SBI method by Clamond, et al. (2006) (128 peak wave lengths taking up to 2000 peak periods).

Although the fully nonlinear models are more accurate than the weakly nonlinear models for dealing with strong nonlinear waves, one should note that they are relatively more computational expensive. It was reported, for example, by Ducrozet et al. (2007) that a 3D random sea simulation covering 42×42 peak wave lengths and lasts for 250 peak wave periods costs 10 CPU days on a 3 GHz-Xeon single processor PC by using the fifth order High-order Spectrial method! It is far longer than a sea state ($\approx 3hrs$). That demonstrates that the existing fully nonlinear models are not sufficiently efficient for use in design where a large number of parameter studies may be necessary.

Among the FFT based methods, the SBI doesn’t suffer the limitation on wave steepness, compared with the HOS and SC method. Furthermore, the improved method, i.e., ESBI and QSBI, is computationally efficient than the original SBI method. Therefore, the ESBI and QSBI will be adopted to propose the hybrid model for large scale random wave simulations in this thesis.

2.2.5 Potential-NS models

Although this study mainly focuses on nonbreaking waves, the Potential-NS model coupling the NS model and potential model is briefly reviewed in order to demonstrate the uniqueness of the current hybrid model. Such Potential-NS models are proposed to simulate wave breaking or wave-structure interaction while considering viscous effects. The main idea is that the local area where viscosity is dominating is modeled by using the NS equation, while domain with weak viscous effects is modelled by the potential model. The mainstream for coupling the NS model with the potential model includes: (a) domain decomposition method and (b) velocity decomposition method.

The domain decomposition method divides the domain into two subspaces and the local physics such as wave breaking and vorticity are located at the subdomain governed by the NS model. The solution of the potential model provides the boundary condition for the NS model. Sitanggang & Lynett (2009) developed a Potential-NS model coupling the higher order Boussinesq equation with Reynolds-Averaged NS (RANS) equation, for simulating wave propagating from deep water to shoreline, involving the breaking waves. Narayanaswamy, et al. (2010) had also suggested a Potential-NS model coupling the higher order Boussinesq equation with the SPH method to study the coastal waves while considering the breaking effects. Clauss, et al. (2005) studied the wave-structure interaction through coupling the FNPT solver based on FEM and NS solver based on VOF method, and validated the model by comparing with laboratory results. Sriram, et al. (2012) had developed a novel algorithm to couple the FNPT solver based on QALE-FEM and NS solver based on IMLPG_R to study the breaking waves. Yan and Ma (2011) presented an improved pressure model combining the FNPT solver based on QALE-FEM and NS solver based on commercial software StarCD to study the dynamics of rogue waves under the action of winds.

On the other hand, the velocity decomposition method splits the velocity into the potential part and the viscous part and only considers the viscous velocity around the structure. The domain of the potential and NS model is overlapped and the velocity of the whole domain of potential model will be corrected with the viscous velocity at each time step. Grilli (2008) and Harris & Grilli (2010; 2012) had developed a Potential-NS model to study the wave induced sediment transport. The velocity and pressure are decomposed into a potential part and a viscous part and the viscous part is obtained by solving a complementary equation. Subsequently, Janssen, et al. (2010) proposed a new approach coupling the FNPT with the NS based Lattice-Boltzmann model to study the wave breaking problems. Later, Rosemurgy, et al. (2012) studied the ship motion based on their new model coupling the Free Surface Green Function and RANS equation. Luquet, et al. (2007), Ferrant, et al. (2008), and Monroy, et al. (2011) proposed a new spectral wave explicit NS equation approach called SWENSE, which couples the FNPT solver based on the HOS method and RANS solver based on VOF method. They had successfully employed this coupled method to model waves interacting with tension-leg platform and ship body in regular or irregular seas. Other applications about the velocity decomposition method could be found in (Ferrant, et al., 2003; Gentaz, et al., 2004; Luquet, et al., 2004; Luquet, et al., 2005; Monroy, et al., 2009).

The Potential-NS models aforementioned are proved to be more computational efficient than the NS model in the applications for simulating breaking waves and wave-structure interactions. Although they are successfully applied to those situations, the location where the viscous effects cannot be neglected should be specified and foreknown to the user. In fact, it is worth of noting that the coupling is carried out on spatial scale, and once the size of the viscosity-dominating area is determined, it cannot be changed. However, in reality, the location of rogue waves cannot be predicted in random sea. So that it is difficult to specify the viscosity-dominating area when these Potential-NS models are adopted. Therefore, the Potential-NS model coupling the potential model and NS model on spatial scale is impractical for the purpose of simulating rogue waves in random sea and will not be further discussed in this thesis.

2.3 Existing problems, objectives and main contribution

After the numerical models are reviewed and compared, it is found that the NLSE and FFT based fully nonlinear models are suitable for the present study. As aforementioned, the Schrödinger type equations are very computationally efficient, however, they should only be employed when steepness and local bandwidth are small. While rogue waves are often referred as waves with strong nonlinearities, high steepness. Thus, the Schrödinger type equations cannot give accurate results when used to study rogue waves independently on large scale over long time. Otherwise, when the wave steepness is large and nonlinearities are strong, the FFT based fully nonlinear models should be adopted. But they are relatively time consuming compared with the weakly nonlinear models.

Thus in this thesis, a numerical scheme to couple the Schrödinger type equation and fully nonlinear model based on FFT will be proposed in order to simulate rogue waves in random sea both efficiently and accurately. In summary, this thesis mainly includes three tasks:

I) Among the Schrödinger type equations, as discussed in section 2.2.3, the Higher Order Dysthe Equation suggested by Debsarma & Das (2005) is found more accurate dealing with relatively stronger nonlinear sea states, so that it is selected in this study. However, there is still some difficulties in the numerical coupling implementation for this equation due to the existence of the Hilbert transform, thus it will be reformulated in terms of Fourier transform and the ENLSE-5F (short for fifth order Enhanced Nonlinear Schrödinger Equation based on Fourier transform) is proposed, which will be discussed in chapter 4.

II) Meanwhile, among the FFT based fully nonlinear models, both the HOS and the SC methods become less accurate when dealing with large steepness waves with strong nonlinearities, while there is no such limitation for the SBI method. Therefore, the SBI method will be chosen to be coupled. Nevertheless, the computational efficiency will be further improved by introducing three numerical techniques and the ESBI is proposed, which will be explained in chapter 5, and QSBI will also be suggested.

III) Based on I) and II), the hybrid model will be proposed and tested by introducing new numerical techniques coupling the ENLSE-5F, QSBI and ESBI on time scale, which is discussed in chapter 6 in details. Then the hybrid model will be further validated by simulating rogue waves in random seas in chapter 7.

The model will be based on potential theory, which assumes the fluid is irrotational and inviscid. Thus only non-breaking waves are considered in this research. In addition, due to the application of the Fast Fourier Transform (FFT), periodical boundary condition is required in the simulation. However, following other studies on large scale random sea simulations (Ducrozet, et al., 2007; Wu, 2004; Xiao, et al., 2013; Onorato, et al., 2001), the random sea states are usually reconstructed by assuming periodical boundary condition. In addition, the effects of the sea bed is another factor on the occurrence of rogue waves but not the subject of the present research, as only waves in deep water are simulated.

The main contribution of this thesis is to suggest a hybrid model, which couples the Schrödinger equation and fully nonlinear model based on FFT, in order to simulate gravity waves both accurately and efficiently. The hybrid model is able to switch between the Schrödinger equation and fully nonlinear model automatically according to the intensity of the nonlinearities, while maintain dramatic computational speed and accuracy. In other words, when the steepness becomes large, the waves exhibit strong nonlinearities and fully nonlinear method is adopted; While the sea state relaxes and wave steepness becomes moderate, the Schrödinger equation is employed. This hybrid model fills the gap between the weakly nonlinear theory, i.e., the Schrödinger type equation, and the fully nonlinear theory, i.e., the SBI method. And more importantly, the idea for this hybrid model can also be extended to couple other weakly nonlinear models with fully nonlinear models, e.g., hybrid model coupling the Boussinesq equation and SBI for shallow water situations. But this work will be left for future study.

2.4 Outline of the thesis

In chapter 2, review on the analytical and numerical wave models is carried out. Two models, i.e., the Spectral Boundary Integral (SBI) method and the Higher Order Dysthe equation, are selected to form the hybrid model based on the review by comparing the advantages and disadvantages of the existing numerical models. Basic equations of the chosen wave models will be presented in chapter 3. Chapter 4 shows the reformulation of the fifth order Enhance Nonlinear Schrödinger Equation based on Hilbert transform (short as ENLSE-5H) and the fifth order Enhanced Nonlinear Schrödinger Equation based on Fourier transform (short as ENLSE-5F) is suggested. Next, the Enhanced Spectral Boundary Integral (ESBI) method is introduced in order to improve the computational efficiency of the original SBI method in chapter 5. Based on that, the hybrid model is proposed coupling the ENLSE-5F, the QSBI and ESBI in chapter 6. In order to explore the dynamics of rogue waves in random seas, techniques for embedding large waves in random background is discussed and an improved approach is proposed in chapter 7, in which the hybrid model is further validated. At last, the conclusions and recommendations for future work is given in chapter 8.

3 MATHEMATICAL FORMULATIONS AND PREVIOUS WORKS

In this chapter, the basic equations will be presented for NLSE and the SBI model. The main work is based on the studies by Trulsen, et al. (2000), Debsarma & Das (2005) for the developments of the NLSE, and Fructus, et al. (2005) for the SBI.

The sketch of the problem is displayed in Figure 3.0.1, in which the fluid domain is described in the three dimensional Cartesian coordinate system. The free surface is denoted by η and the mean level of the water is Z=0. The water depth is infinite in -Z direction. For two dimensional problems, i.e., long crest waves, Y axis will be hided.

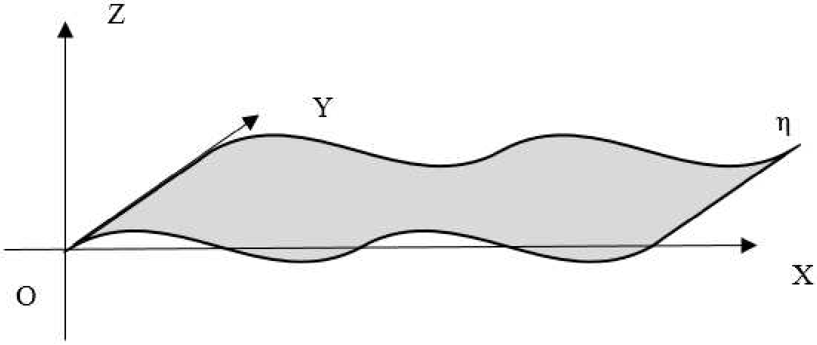

Figure 3.0.1 Sketch of the problem

3.1 The fundamental equations

Under the framework of potential theory, the governing equation together with all boundary conditions are given as

$$\Delta\phi = 0 \tag{3.1.1}$$

$$\frac{\partial \eta}{\partial T} + \nabla\phi \cdot \nabla\eta - \frac{\partial \phi}{\partial Z} = 0, \quad on \quad Z = \eta \tag{3.1.2}$$

$$\frac{\partial \phi}{\partial T} + \eta + \frac{1}{2}\left(\nabla\phi \cdot \nabla\phi + {\frac{\partial \phi}{\partial Z}}^{2}\right) + p = 0, \quad on \quad Z = \eta \tag{3.1.3}$$

$$\frac{\partial \phi}{\partial Z} = 0, \quad Z \to -\infty \tag{3.1.4}$$

where Δ is the Laplacian and $\nabla = \frac{\partial}{\partial \boldsymbol{X}} = \frac{\partial}{\partial X}\vec{\imath} + \frac{\partial}{\partial Y}\vec{\jmath}$ is the horizontal gradient operator, and η is the elevation of the free surface, ϕ is the velocity potential, p is the pressure on the free surface and $p = 0$ if it is not specified. Among the variables in the equations above, η, $\boldsymbol{X} = (X, Y)$ and Z have been non-dimensionalized by multiplying the peak wave number k_0, ϕ by multiplying $\sqrt{k_0^3/g}$, p by multiplying $k_0/(\rho g)$ and T by multiplying ω_0, where $\omega_0 = \sqrt{gk_0}$ is the peak circular frequency, ρ is the density of water and g is the gravitational acceleration.

In order to derive the equations for numerical simulation, the Fourier transform $F\{\ \}$ and the inverse transform $F^{-1}\{\ \}$ are introduced and defined as

$$\hat{\eta}(\boldsymbol{K}, T) = F\{\eta\} = \int_{-\infty}^{\infty} \eta(\boldsymbol{X}, T) e^{-i\boldsymbol{K}\cdot\boldsymbol{X}} d\boldsymbol{X} \tag{3.1.5}$$

$$\eta(\boldsymbol{X}, T) = F^{-1}\{\hat{\eta}\} = \frac{1}{4\pi^2}\int_{-\infty}^{\infty} \hat{\eta}(\boldsymbol{K}, T) e^{i\boldsymbol{K}\cdot\boldsymbol{X}} d\boldsymbol{K} \tag{3.1.6}$$

where the wave number $\boldsymbol{K} = (\kappa, \zeta)$. Fast Fourier Transform (FFT) is adopted to perform the Fourier and inverse transform (IFFT) numerically.

Assuming the wave steepness is small, the nonlinear terms in Eq.(3.1.2) and (3.1.3) are of one order smaller than the linear terms and thus can be neglected. In that case, the system regresses into a linear problem and the solution could be given by (Dean, 1974)

$$\eta(\boldsymbol{X}, T) = \sum_{j=1}^{\infty} a_j \cos\left(\boldsymbol{k_j} \cdot \boldsymbol{X} - \omega_j T + \varphi_j\right) \tag{3.1.7}$$

$$\phi(\boldsymbol{X}, Z, T) = \sum_{j=1}^{\infty} \frac{a_j}{\omega_j} e^{k_j Z} \sin\left(\boldsymbol{k_j} \cdot \boldsymbol{X} - \omega_j T + \varphi_j\right) \tag{3.1.8}$$

where a_j, $\boldsymbol{k_j}$, ω_j and φ_j are the amplitude, wave number, circular frequency and random phase of the jth component respectively, and the dispersion relation is given by $\omega_j = \sqrt{|\boldsymbol{k_j}|}$. The linear wave model assumes that the free surface and the velocity potential are the summation of independent components and the nonlinear interaction is neglected.

3.2 The Enhanced Nonlinear Schrödinger equation

In this section, the formulations of the ENLSEs will be presented. In the first subsection, the ENLSE-4 in terms of the free surface envelope A is derived, which is ready to be solved numerically based on FFT. The second subsection gives the solution to the free surface and velocity potential in terms of the velocity envelope.

3.2.1 Governing equation for the free surface envelope

As the NLSE has been studied extensively, the basic equations are only given here for completeness without the details of derivation. The surface elevation and the velocity potential could be written in the form of the summation of harmonics by introducing the concept of envelope (same dimensionless variables as Eq.(3.1.1)-(3.1.4) are employed)

$$\eta = \bar{\eta} + \frac{1}{2}\left(Ae^{i\theta} + A_2e^{2i\theta} + A_3e^{3i\theta} + \cdots + c.c.\right) \tag{3.2.1}$$

$$\phi = \bar{\phi} + \frac{1}{2}\left[Be^{i\theta+Z} + B_2e^{2(i\theta+Z)} + B_3e^{3(i\theta+Z)} + \cdots + c.c.\right] \tag{3.2.2}$$

where A and B are complex envelops of the first harmonic of surface elevation and velocity potential respectively, A_j and B_j are the jth harmonic coefficients, $\bar{\eta}$ and $\bar{\phi}$ are real functions representing the surface deflection and mean flow, $c.c.$ is the complex conjugate, and $\theta = X - T$ with X being the main propagating direction. An example of the sketch of the free surface envelope A is shown in Figure 3.2.1.

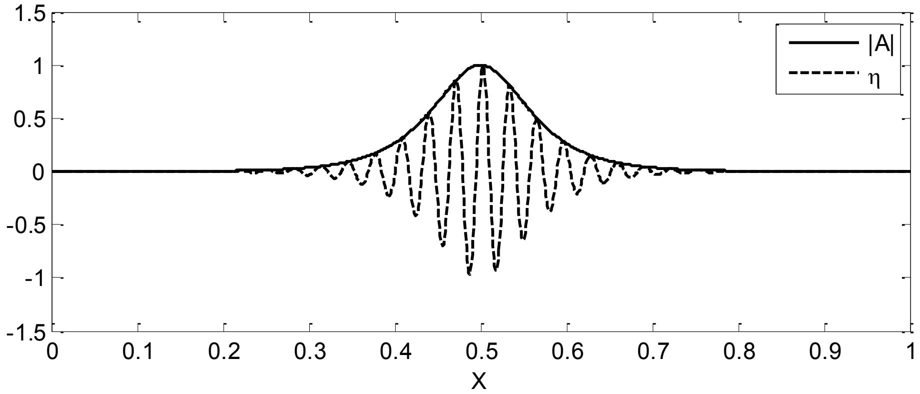

Figure 3.2.1 Sketch of the envelope

Subject to the assumption that steepness $\varepsilon \ll 1$ and spectrum width is of order $O(\varepsilon)$, one can introduce the slow modulation variables εX, εY, εZ and εT, and assume A and B are slowly modulated by such variables. By using the perturbation approach to the fourth order $O(\varepsilon^4)$, one is able to obtain the Dysthe equation of the first kind (Dysthe, 1979; Stiassnie, 1984), which is in terms of B. One can also obtain the Dysthe equation of the second kind (Mei, 1983) in term of wave envelope A, which is employed in this thesis

$$\begin{aligned}\frac{\partial A}{\partial T}+\frac{1}{2}\frac{\partial A}{\partial X}+\frac{i}{8}\frac{\partial^2 A}{\partial X^2}-\frac{i}{4}\frac{\partial^2 A}{\partial Y^2}-\frac{1}{16}\frac{\partial^3 A}{\partial X^3}+\frac{3}{8}\frac{\partial^3 A}{\partial X\partial Y^2}\\ =-\frac{i}{2}|A|^2A-\frac{3}{2}|A|^2\frac{\partial A}{\partial X}-\frac{A^2}{4}\frac{\partial A^*}{\partial X}-iA\frac{\partial\bar{\phi}}{\partial X}\end{aligned} \tag{3.2.3}$$

$$\frac{\partial\bar{\phi}}{\partial Z}=\frac{1}{2}\frac{\partial|A|^2}{\partial X},\ \ Z=0 \tag{3.2.4}$$

$$\Delta\bar{\phi}=0,\ \ Z\le 0 \tag{3.2.5}$$

$$\frac{\partial\bar{\phi}}{\partial Z}=0,\ \ Z=-\infty \tag{3.2.6}$$

where the superscript $*$ denotes its complex conjugate. The first and second kind of Dysthe equations could be transformed to each other via variables substitution (Hogan, 1985) and keep the appearance to the same order. The order of the equation is defined in the way that

$$\begin{gathered}A^I\sim O(\varepsilon^I),\ \bar{\phi}\sim O(\varepsilon^2)\\ \frac{\partial}{\partial T}\sim O(\varepsilon),\ \frac{\partial}{\partial Z}\sim O(\varepsilon)\ \text{and}\ \frac{\partial^I}{\partial X^I},\frac{\partial^I}{\partial Y^I}\sim O(\varepsilon^I)\end{gathered} \tag{3.2.7}$$

Trulsen, et al. (2000) later pointed out that the linear operators could be replaced by the exact linear solution, and proposed the following form

$$\frac{\partial A}{\partial T}+F^{-1}\{i(\omega-1)F\{A\}\}=-\frac{i}{2}|A|^2A-\frac{3}{2}|A|^2\frac{\partial A}{\partial X}-\frac{A^2}{4}\frac{\partial A^*}{\partial X}-iA\frac{\partial\bar{\phi}}{\partial X} \tag{3.2.8}$$

where $\omega=\sqrt{|\boldsymbol{k_0}+\boldsymbol{K}|}$ and $\boldsymbol{k_0}=(1,0)$ is the peak wave number. Note that the mean wave direction has been assumed pointing to the positive X-axis. The linear terms on the left hand side now become the exact representation of linear propagation and no longer subject to the narrow spectrum assumption, while the nonlinear part is still bandwidth-limited. The nonlinear terms on the right hand remain the same. The method based on Eq.(3.2.8) is named as ENLSE-4 in this thesis for convenience. The term $\bar{\phi}$ needs to be determined before the equations can be solved numerically, which is given by Wang & Ma (2015),

$$\bar{\phi}=F^{-1}\left\{\frac{i}{2}\frac{\kappa}{K}F\{|A|^2\}\right\} \tag{3.2.9}$$

substitute which into Eq.(3.2.8), one has the other form of the ENLSE-4

$$\frac{\partial A}{\partial T}+F^{-1}\{i(\omega-1)F\{A\}\}=\Psi_1 \tag{3.2.10}$$

where

$$\Psi_1=\Upsilon_1+\frac{i}{2}AF^{-1}\left\{\frac{\kappa^2}{K}F\{|A|^2\}\right\} \tag{3.2.11}$$

$$\Upsilon_1=-\frac{i}{2}|A|^2A-\frac{3}{2}|A|^2\frac{\partial A}{\partial X}-\frac{1}{4}A^2\frac{\partial A^*}{\partial X} \tag{3.2.12}$$

Eq. (3.2.10) is equivalent to the equation of first kind in terms of B derived by Clamond, et al. (2006), and is easy to be solved numerically if the initial condition $A(\boldsymbol{X}, T = 0)$ is given.

3.2.2 Solution to the free surface and velocity potential

Trulsen & Dysthe (1996) have given the coefficients for each harmonic of the surface elevation and velocity potential, corresponding to the first kind of NLSE in terms of B, which follow as

$$\begin{aligned} A = iB + \frac{1}{2}\frac{\partial B}{\partial X} + \frac{i}{8}\frac{\partial^2 B}{\partial X^2} - \frac{i}{4}\frac{\partial^2 B}{\partial Y^2} - \frac{1}{16}\frac{\partial^3 B}{\partial X^3} - \frac{3}{8}\frac{\partial^3 B}{\partial X \partial Y^2} - \frac{5i}{128}\frac{\partial^4 B}{\partial X^4} \\ + \frac{15i}{32}\frac{\partial^4 B}{\partial^2 X \partial Y^2} - \frac{3i}{32}\frac{\partial^4 B}{\partial Y^4} + \frac{i}{8}|B|^2 B \end{aligned} \tag{3.2.13}$$

$$A_2 = -\frac{1}{2}B^2 + iB\frac{\partial B}{\partial X} + \frac{1}{8}B\frac{\partial^2 B}{\partial X^2} + \frac{3}{8}\left(\frac{\partial B}{\partial X}\right)^2 - \frac{1}{4}B\frac{\partial^2 B}{\partial Y^2} + \frac{3}{4}\left(\frac{\partial B}{\partial Y}\right)^2 \tag{3.2.14}$$

$$A_3 = -\frac{3i}{8}B^3 \tag{3.2.15}$$

$$B_2 = \frac{i}{2}B\frac{\partial^2 B}{\partial Y^2} - \frac{i}{2}\left(\frac{\partial B}{\partial Y}\right)^2 \tag{3.2.16}$$

$$\bar{\eta} = -\frac{\partial \bar{\phi}}{\partial T} - \frac{1}{16}\frac{\partial^2 |B|^2}{\partial X^2} - \frac{1}{8}\frac{\partial^2 |B|^2}{\partial Y^2} \tag{3.2.17}$$

and $B_3 = 0$. By using Eq.(3.2.13)-(3.2.17) together with Eq.(3.2.1) and (3.2.2), one is able to obtain η and ϕ once B is known. However, this is not very straightforward because that A is easier to be estimated based on Eq.(3.2.10) rather than B. This problem will be discussed and solved in chapter 6.

3.3 The Higher Order Dysthe equation

Zakharov (1968) had pointed out that the CNLSE could be derived from the Zakharov equation with narrow spectrum assumption. Later, Stiassinie (1984) found that the Dysthe equation could also be derived from Zakharov equation by expanding the nonlinear terms to the specific order. Based on the same idea, Debsarma & Das (2005) made one step further and obtained the Higher Order Dysthe equation in terms of the Hilbert transform.

3.3.1 Governing equation for the free surface envelope

The Higher Order Dysthe equation by Debsarma & Das (2005) follows as

$$
\begin{aligned}
&\left[\frac{\partial}{\partial T}+\frac{1}{2}\frac{\partial}{\partial X}+\frac{i}{8}\left(\frac{\partial^2}{\partial X^2}-2\frac{\partial^2}{\partial Y^2}\right)-\frac{1}{16}\left(\frac{\partial^3}{\partial X^3}-6\frac{\partial^3}{\partial X\partial Y^2}\right)\right.\\
&\qquad -\frac{i}{128}\left(5\frac{\partial^4}{\partial X^4}-60\frac{\partial^2}{\partial X^2\partial Y^2}+12\frac{\partial^4}{\partial Y^4}\right)\\
&\qquad +\frac{1}{256}\left(7\frac{\partial^5}{\partial X^5}-140\frac{\partial^5}{\partial X^3\partial Y^2}+84\frac{\partial^5}{\partial X\partial Y^4}\right)\\
&\qquad \left.+\frac{i}{1024}\left(21\frac{\partial^6}{\partial X^6}-630\frac{\partial^6}{\partial X^4\partial Y^2}+756\frac{\partial^6}{\partial X^2\partial Y^4}-56\frac{\partial^6}{\partial Y^6}\right)\right]A\\
&\qquad =\Psi_2
\end{aligned}
\tag{3.3.1}
$$

where

$$
\begin{aligned}
\Psi_2 = \Upsilon_1+\Upsilon_2 &-\frac{i}{2}A\mathcal{H}\left\{\frac{\partial|A|^2}{\partial X}\right\}-\frac{1}{2}\frac{\partial A}{\partial X}\mathcal{H}\left\{\frac{\partial|A|^2}{\partial X}\right\}-\frac{1}{4}A\frac{\partial}{\partial X}\mathcal{H}\left\{A\frac{\partial A^*}{\partial X}\right\}\\
&-\frac{1}{2}A\frac{\partial}{\partial X}\mathcal{H}\left\{A^*\frac{\partial A}{\partial X}\right\}+\frac{i}{8}A\frac{\partial^2}{\partial X^2}\mathcal{P}\left\{\frac{\partial|A|^2}{\partial X}\right\}-\frac{1}{2}\frac{\partial A}{\partial Y}\mathcal{H}\left\{\frac{\partial|A|^2}{\partial Y}\right\}\\
&-\frac{1}{2}A\frac{\partial}{\partial Y}\mathcal{H}\left\{A^*\frac{\partial A}{\partial Y}\right\}
\end{aligned}
\tag{3.3.2}
$$

$$
\begin{aligned}
\Upsilon_2 = \frac{5i}{8}|A|^2\frac{\partial^2 A}{\partial X^2}+\frac{9i}{16}A^*\left(\frac{\partial A}{\partial X}\right)^2+\frac{i}{8}A\frac{\partial A}{\partial X}\frac{\partial A^*}{\partial X}-\frac{i}{8}A^2\frac{\partial^2 A^*}{\partial X^2}+\frac{5i}{8}A^*\left(\frac{\partial A}{\partial Y}\right)^2\\
-\frac{i}{4}A\frac{\partial A}{\partial Y}\frac{\partial A^*}{\partial Y}-\frac{i}{4}A^2\frac{\partial^2 A^*}{\partial Y^2}
\end{aligned}
\tag{3.3.3}
$$

and the Hilbert transforms are given by

$$
\mathcal{H}\{A(\boldsymbol{X})\}=\frac{1}{2\pi}\int_{-\infty}^{\infty}A(\boldsymbol{X}')\frac{X'-X}{|\boldsymbol{X}'-\boldsymbol{X}|^3}d\boldsymbol{X}' \tag{3.3.4}
$$

$$
\mathcal{P}\{A(\boldsymbol{X})\}=\frac{1}{2\pi}\int_{-\infty}^{\infty}A(\boldsymbol{X}')\frac{X'-X}{|\boldsymbol{X}'-\boldsymbol{X}|^2}d\boldsymbol{X}' \tag{3.3.5}
$$

3.3.2 The fifth order ENLSE based on Hilbert transform

By introducing Trulsen's technique, the linear operator of Eq. (3.3.1) could be replaced with the exact linear solution, and it is referred as the fifth order Enhanced Nonlinear Schrödinger Equation based on Hilbert transform (ENLSE-5H). For completeness, the formulation of the ENLSE-5H follows as

$$
\frac{\partial A}{\partial T}+F^{-1}\{i(\omega-1)F\{A\}\}=\Psi_2 \tag{3.3.6}
$$

In order to estimate the Hilbert transform, i.e., the Cauchy integral, involved in Ψ_2, numerical integration should be used. The difficulties with performing the numerical integration for these Cauchy integrals exist in two aspects. Firstly, the range of the integration is from $-\infty$ to ∞, although it could be optimized to a limited range, a large number of numerical tests should be carried out in order to determine this range and the tests may be needed for different cases as the range may depend on the specific value of envelope. Secondly, the integrals are weakly singular at $\boldsymbol{X}' = \boldsymbol{X}$ and so they require de-singularity technique. Although the techniques can be developed, they need extra computational effort. In order to eliminate the difficulties, an equivalent formulation will be suggested, which will be discussed in chapter 4.

3.4 The Spectral Boundary Integral method

The following content is a brief introduction to the work by Fructus, et al. (2005), i.e., the original SBI method. The formulations are presented in this section, as well as the numerical procedures for solving the equations. Schemes for estimating the vertical velocity is also proposed. Finally, the QSBI method is suggested.

3.4.1 The prognostic equations

The boundary conditions, i.e. Eq.(3.1.2) and (3.1.3), could be reformulated as

$$\frac{\partial\eta}{\partial T} - V = 0 \tag{3.4.1}$$

$$\frac{\partial\tilde{\phi}}{\partial T} + \eta + \frac{1}{2}\left(\left|\nabla\tilde{\phi}\right|^2 - \frac{\left(V + \nabla\eta\cdot\nabla\tilde{\phi}\right)^2}{1+|\nabla\eta|^2}\right) + p = 0 \tag{3.4.2}$$

after introducing $V = \frac{\partial\phi}{\partial n}\sqrt{1+|\nabla\eta|^2}$ and the velocity potential at free surface $\tilde{\phi}$. This is always referred as the Dirichlet to Neumann operation. Applying Fourier transform to both the boundary conditions leading to the skew-symmetric prognostic equation

$$\frac{\partial\boldsymbol{M}}{\partial T} + \mathcal{A}\boldsymbol{M} + \boldsymbol{R} = \boldsymbol{N} \tag{3.4.3}$$

where

$$\boldsymbol{M} = \begin{pmatrix} KF\{\eta\} \\ K\Omega F\{\tilde{\phi}\} \end{pmatrix}, \mathcal{A} = \begin{bmatrix} 0 & -\Omega \\ \Omega & 0 \end{bmatrix}, \boldsymbol{R} = \begin{pmatrix} 0 \\ K\Omega F\{p\} \end{pmatrix}$$
$$\text{and } \boldsymbol{N} = \begin{pmatrix} K\left(F\{V\} - KF\{\tilde{\phi}\}\right) \\ K\Omega F\left\{\frac{1}{2}\left[\frac{\left(V+\nabla\eta\cdot\nabla\tilde{\phi}\right)^2}{1+|\nabla\eta|^2} - \left|\nabla\tilde{\phi}\right|^2\right]\right\} \end{pmatrix} \tag{3.4.4}$$

and the circular frequency $\Omega = \sqrt{K}$, module of the wave number $K = |\boldsymbol{K}| = \sqrt{\kappa^2 + \zeta^2}$. Then the solution is given as

$$\boldsymbol{M}(T = \Delta T) = e^{-\mathcal{A}\Delta T}\int_0^T e^{\mathcal{A}\Delta T}(\boldsymbol{N} - \boldsymbol{R})dT + e^{-\mathcal{A}\Delta T}\boldsymbol{M}(T = 0) \tag{3.4.5}$$

where

$$e^{\mathcal{A}\Delta T} = \begin{bmatrix} \cos\Omega\Delta T & -\sin\Omega\Delta T \\ \sin\Omega\Delta T & \cos\Omega\Delta T \end{bmatrix} \tag{3.4.6}$$

According to Clamond, et al. (2007), this time integrator is linearly stable and exact. The six-stage embedded fifth order (in terms of time step size) Runge-Kutta method is adopted to solve the equation numerically. The solution can be written as

$$
\begin{aligned}
\boldsymbol{M}^{(4)} &= e^{-\mathcal{A}\Delta T}\left[\boldsymbol{M}(T=0) + \sum_{j=1}^{6} \alpha_j \mathcal{K}_j\right] \\
\boldsymbol{M}^{(5)} &= e^{-\mathcal{A}\Delta T}\left[\boldsymbol{M}(T=0) + \sum_{j=1}^{6} \beta_j \mathcal{K}_j\right]
\end{aligned}
\tag{3.4.7}
$$

where coefficients α_j and β_j can be found in (Dormand & Pince, 1980), and $\mathcal{K}_j$ is the Runge-Kutta increment at each stage. The superscripts (4) and (5) represent the fourth order and fifth order (in terms of time step size) solution of the Runge-Kutta time integrator respectively. The time step size is self-adaptive which is determined by imposing the following condition

$$
Err_T = \frac{\int\left[\left|\eta^{(5)} - \eta^{(4)}\right| + \left|\tilde{\phi}^{(5)} - \tilde{\phi}^{(4)}\right|\right] d\boldsymbol{X}}{\int\left[\left|\eta^{(5)}\right| + \left|\tilde{\phi}^{(5)}\right|\right] d\boldsymbol{X}} < Tol_T \tag{3.4.8}
$$

where Err_T is the relative error between the fourth order and fifth order solutions and Tol_T is the tolerance. Using the equation, one can obtain the optimised time step size ΔT_{opt} as a function of Err_T, as suggested in (Clamond, et al., 2007).

3.4.2 The boundary integral equation

On the other hand, the boundary integrals of Green's theorem follow as

$$
\iint_S \frac{1}{r}\frac{\partial \phi'}{\partial n'} dS' = 2\pi\tilde{\phi} + \iint_S \tilde{\phi}' \frac{\partial}{\partial n'}\frac{1}{r} dS' \tag{3.4.9}
$$

where S is the area of the instantaneous free surface, the variables with the prime indicate those at source point $(\boldsymbol{X}', Z')$, the variables without the prime are those at field point $(\boldsymbol{X}, Z)$, $r = \sqrt{R^2 + (Z' - Z)^2}$ and $R = |\boldsymbol{R}| = |\boldsymbol{X}' - \boldsymbol{X}|$, S' denotes the segment of $S(\boldsymbol{X}', Z')$. Using $dS' = \sqrt{1 + |\nabla\eta|^2} d\boldsymbol{X}'$, the above integral can be written as

$$
\int_{S_0} \frac{V'}{r} d\boldsymbol{X}' = 2\pi\tilde{\phi} + \int_{S_0} \tilde{\phi}' \sqrt{1 + |\nabla'\eta'|^2} \frac{\partial}{\partial n'}\frac{1}{r} d\boldsymbol{X}' \tag{3.4.10}
$$

where S_0 is the projection of S' to the horizontal plane. Then a new variable $D = \frac{\eta' - \eta}{R}$ is introduced and the equation above is reformulated as

$$\int_{S_0} \frac{V'}{R} d\boldsymbol{X}' = 2\pi\tilde{\phi} + \int_{S_0} (\eta' - \eta)\nabla'\tilde{\phi}' \cdot \nabla' \frac{1}{R} d\boldsymbol{X}'$$
$$- \int_{S_0} \tilde{\phi}' \left[\frac{1}{(1 + D^2)^{3/2}} - 1\right] \nabla' \cdot \left[(\eta' - \eta)\nabla' \frac{1}{R}\right] d\boldsymbol{X}' \tag{3.4.11}$$
$$- \int_{S_0} \frac{V'}{R} \left(\frac{1}{\sqrt{1 + D^2}} - 1\right) d\boldsymbol{X}'$$

Then the velocity V can be split into four parts, i.e., $V = V_1 + V_2 + V_3 + V_4$. Each part is given by

$$V_1 = F^{-1}\left\{KF\{\tilde{\phi}\}\right\} \tag{3.4.12}$$

$$V_2 = -F^{-1}\{KF\{\eta V_1\}\} - \nabla \cdot \left(\eta \nabla \tilde{\phi}\right) \tag{3.4.13}$$

$$V_3 = V'_{3,I} = F^{-1}\left\{\frac{K}{2\pi} F\left\{\int_{S_0} \tilde{\phi}' \nabla' \cdot \left[(\eta' - \eta)\nabla' \frac{1}{R}\right] \Gamma_1(\mathrm{D}) d\boldsymbol{X}'\right\}\right\}$$
$$= F^{-1}\left\{\frac{K}{2\pi} F\left\{\int_{S_0} \tilde{\phi}' \frac{(\eta' - \eta) - \boldsymbol{R} \cdot \nabla'\eta'}{R^3} \Gamma_1(\mathrm{D}) d\boldsymbol{X}'\right\}\right\} \tag{3.4.14}$$

$$V_4 = F^{-1}\left\{\frac{K}{2\pi} F\left\{\int_{S_0} \frac{V'}{R}\left(1 - \frac{1}{\sqrt{1 + D^2}}\right) d\boldsymbol{X}'\right\}\right\} \tag{3.4.15}$$

where V_1 and V_2 could be estimated directly by applying the Fourier and the inverse transforms and

$$\Gamma_1(\mathrm{D}) = 1 - \frac{1}{(1 + D^2)^{3/2}} \tag{3.4.16}$$

Fructus, et al. (2005) has rewritten the kernel of V_4, and the dominant part could be expanded into the third order convolutions, say

$$V_4 = V_4^{(1)} + V'_{4,I}$$
$$= F^{-1}\left\{-\frac{K}{2}\left[KF\{\eta^2 V\} - 2F\left\{\eta F^{-1}\{KF\{\eta V\}\}\right\} + F\left\{\eta^2 F^{-1}\{KF\{V\}\}\right\}\right]\right\} \tag{3.4.17}$$
$$+ F^{-1}\left\{\frac{K}{2\pi} F\left\{\int \frac{V'}{R} \Upsilon_1(D) d\boldsymbol{X}'\right\}\right\}$$

where

$$\Upsilon_1(D) = 1 - \frac{1}{\sqrt{1 + D^2}} - \frac{1}{2}D^2 \tag{3.4.18}$$

$V_4^{(1)}$ denotes the third order convolutions in the first curly-bracket term and ${V_{4,I}}'$ represents the remaining integration part in the second curly-bracket term on the right of Eq.(3.4.17). Note that the determination of V_1, V_2 and V_3 is explicit while the determination of V_4 is implicit and needs iterations.

During iteration for finding V_4, the initial value of V_4 is firstly estimated by letting $V = V_1 + V_2$ and assuming

$$Err_B = \frac{\int |V^{Iter} - V^{Iter+1}| d\boldsymbol{X}}{\int |V^{Iter+1}| d\boldsymbol{X}} < Tol_B \tag{3.4.19}$$

with V^{Iter} and V^{Iter+1} being the values of the velocity V at the two successive iterations.

The calculation of the convolutions is very fast owing to the algorithm of FFT. Otherwise, the remaining integration part of V_4 and the whole expression of V_3 are estimated through numerical integration, which is the most time consuming step of the current numerical scheme.

In addition, the numerical integration is estimated at nodes $\boldsymbol{X} + \frac{1}{2}\Delta\boldsymbol{X}$ and shifted back to regular points through Fourier interpolation in order to avoid explicit singularity for calculating the integrand. It is found that the resolution needs to be well refined in order to obtain accurate results by using this method. Grue (2010) made one step further, expanded the kernels of V_3 and V_4 and wrote the dominant parts into the convolutions up to the sixth and seventh order respectively. Both the remaining integration parts of V_3 and V_4 are neglected. The numerical scheme is significantly accelerated due to the most time consuming parts are excluded. However, it is found the expansion is based on the assumption that the gradient parameter $D \ll 1$. Thus the integration parts are important to the accuracy of the estimation to V_3 and V_4 and could not be neglected in local areas where the wave surface are steep.

3.4.3 Numerical implementation

The flow chart in Figure 3.4.1 illustrates the whole numerical scheme and procedure of the spectral boundary integral method. In this figure, the gradient of the free surface $\nabla\eta$ and the velocity potential $\nabla\tilde{\phi}$ are estimated by Fourier and its inverse transform

$$\nabla\eta = F^{-1}\{i\boldsymbol{K}F\{\eta\}\} \quad and \quad \nabla\tilde{\phi} = F^{-1}\left\{i\boldsymbol{K}F\{\tilde{\phi}\}\right\} \tag{3.4.20}$$

It is noted that the most time consuming parts are the boundary integral modules involved in Equation (3.4.14) and (3.4.15). Robust numerical techniques to significantly accelerate the procedure will be developed and explained in chapter 5.

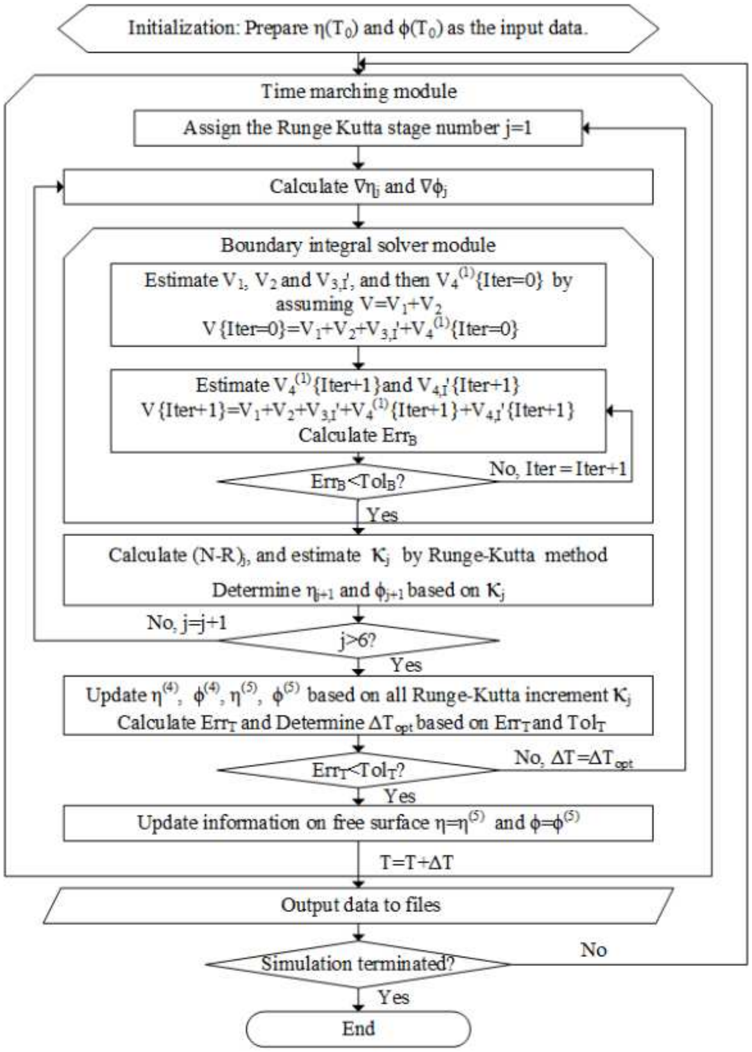

Figure 3.4.1 Flow chart for the numerical implementation of Spectral Boundary Integral Method

3.4.4 Schemes for estimating V_3 and V_4

Fructus, et al. (2005) had expanded the expression of V_4, and replaced the main part with convolutions to the third order as indicated above. Grue (2010) brought the expressions of both V_3 and V_4 to convolutions of the sixth and seventh order respectively. Based on that, the expansion procedures are repeated and the equivalent but slightly different results are obtained, given by (refer to APPENDIX A for details)

$$V_3 = V_{3,C} + V_{3,I} = \underbrace{V_3^{(1)}}_{4th} + \underbrace{V_3^{(2)}}_{6th} + \underbrace{V_{3,I}}_{integration} \tag{3.4.21}$$

$$V_4 = V_{4,C} + V_{4,I} = \underbrace{V_4^{(1)}}_{3rd} + \underbrace{V_4^{(2)}}_{5th} + \underbrace{V_4^{(3)}}_{7th} + \underbrace{V_{4,I}}_{integration} \tag{3.4.22}$$

$$V_{3,I} = F^{-1}\left\{\frac{K}{2\pi}F\left\{\iint \tilde{\phi}'\frac{(\eta' - \eta) - \boldsymbol{R}\cdot\nabla'\eta'}{R^3}\Gamma_2(\mathrm{D})d\boldsymbol{X}'\right\}\right\} \tag{3.4.23}$$

$$V_{4,I} = F^{-1}\left\{\frac{K}{2\pi}F\left\{\iint \frac{V'}{R}\Upsilon_2(D)d\boldsymbol{X}'\right\}\right\} \tag{3.4.24}$$

where

$$\Gamma_2(\mathrm{D}) = 1 - \frac{1}{(1+D^2)^{3/2}} - \frac{3}{2}D^2 + \frac{15}{8}D^4 \tag{3.4.25}$$

$$\Upsilon_2(D) = 1 - \frac{1}{\sqrt{1+D^2}} - \frac{1}{2}D^2 + \frac{3}{8}D^4 - \frac{5}{16}D^6 \tag{3.4.26}$$

$V_{3,C} = V_3^{(1)} + V_3^{(2)}$ and $V_{4,C} = V_4^{(1)} + V_4^{(2)} + V_4^{(3)}$ are convolution parts and the order of each convolution is labelled at the bottom of each term. The order of the convolution is defined in this way, for example, $F\{V\eta^{I-1}\} \sim O(\varepsilon^I)$, as the Ith order. When the steepness is small, the order of the integration parts $V_{3,I}$ and $V_{4,I}$ are insignificant compared with the convolution parts, and so can be neglected. Generally, three approaches of estimating V_3 and V_4 are suggested, as summarized in Table 3.4.1.

Table 3.4.1 Schemes of the boundary integral solver

Scheme 1	$V_3 = V_{3,I}{}'$	$V_4 = V_4^{(1)} + V_{4,I}{}'$
Scheme 2	$V_3 = V_{3,C}$	$V_4 = V_{4,C}$
Scheme 3	$V_3 = V_{3,C} + V_{3,I}$	$V_4 = V_{4,C} + V_{4,I}$

In Scheme 1, V_3 is estimated with integration. V_4 is expanded to third order convolution plus integration term. In Scheme 2, V_3 and V_4 are expanded to the sixth and seventh order convolutions respectively, but ignoring both $V_{3,I}$ and $V_{4,I}$. Scheme 3 is the same as Scheme 2, except the integration parts are included.

It is understood that Scheme 1 and Scheme 3 are equivalent. However, Scheme 3 requires more computational efforts over Scheme 1 on calculating the convolution parts, thus this scheme is only used as benchmark to quantify the difference between Scheme 1 and Scheme 2. In addition, Scheme 2 is the most efficient but is only valid when D is not too large. Assume there exist a critical value D_c, under which the velocity can be solved by Scheme 2; otherwise by Scheme 1, the boundary integral solver module in Figure 3.4.1 can be replaced by the flow chart in Figure 3.4.2.

It is noted here that the evaluation of integration parts in Schemes 1 and 3 necessitate the computation of the integrals which have a singular integrand. A better numerical technique for evaluating the integrals will be suggested in chapter 5. In addition, Fructus, et al. (2005) applied Scheme 1 to Stokes waves while Grue (2010) employed Scheme 2 to simulate 3D wave fields, as indicated above. One of main contributions of this thesis is to suggest mixing the two schemes and more importantly to develop a technique for quantitatively determining the critical value D_c, so that the computation can automatically switch to Scheme 1 or Scheme 2 according to the instantaneous value of $|D|_{max}$, significantly accelerating the computation of wave fields. The details about this will be presented in chapter 5.

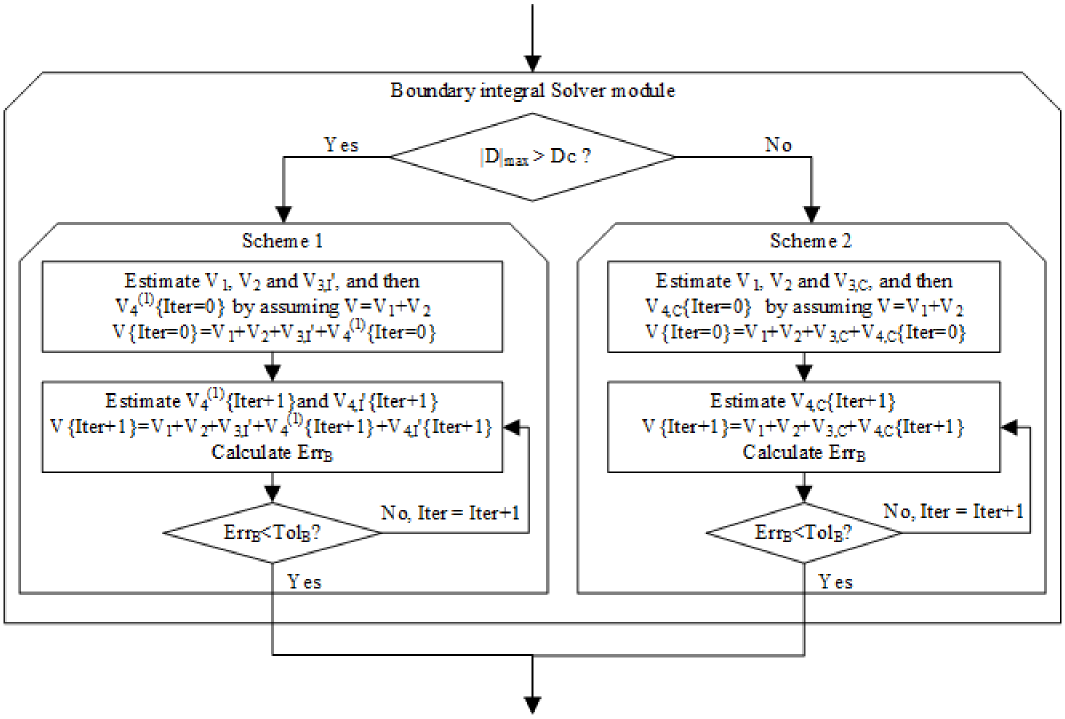

Figure 3.4.2 The flow chart of the numerical scheme for solving the boundary integral equation

3.4.5 Quasi SBI

In addition to Table 3.4.1, another computational efficient method may be formed, in which only the third order convolution terms, neglecting the integration terms in the vertical velocity, i.e.,

$$V = V_1 + V_2 + V_4^{(1)} \tag{3.4.27}$$

are considered. The difference between this approximate approach and the SBI lies in the vertical velocity estimation. All others, including the prognostic equation and full nonlinear free surface conditions, are the same as the SBI. It is expected that this approximate approach will be as accurate as the SBI when the waves are not strongly nonlinear. This approximate approach will be referred as the Quasi Spectral Boundary Integral (QSBI) method in this thesis for convenience. The QSBI is also solved by using the embedded fifth order Runge-Kutta method with adaptive time step, as illustrated in section 3.4.1 and Figure 3.4.1. The QSBI will be formed as a part of the hybrid method, which will be discussed in chapter 6.

3.5 Discussion

Before the ENLSE-5H and the SBI are coupled, it is found that there are a few impediments. As aforementioned, it is not convenient to perform the Hilbert transform while solving the ENLSE-5H numerically. Therefore, it needs to be reformulated in order to make the numerical procedure simplified. This will be discussed in chapter 4. Meanwhile, for the SBI method, the singularity problem need to be well treated. The question that whether the integration parts should be neglected and how to effectively deal with the aliasing when higher order convolution parts are involved in the calculation of the vertical velocity, needs to be answered. Thus, to guarantee both efficiency and accuracy of the SBI method, new techniques should be introduced, which will be discussed in chapter 5.

4 THE FIFTH ORDER ENLSE BASED ON FOURIER TRANSFORM

The fifth order ENLSE based on Fourier transform (ENLSE-5F for short) is proposed in this chapter. This part demonstrates the derivation of the ENLSE-5F from the ENLSE-5H based on the work by Wang & Ma (2015).

4.1 The governing equation for the free surface envelope

Before the new equation is presented, the substitutions are introduced as (Wang, et al., 2015)

$$F\{\mathcal{H}\{A(\boldsymbol{X})\}\} = \frac{i\kappa}{K}F\{A(\boldsymbol{X})\} \tag{4.1.1}$$

$$F\{\mathcal{P}\{A(\boldsymbol{X})\}\} = \frac{i\kappa}{K^2}F\{A(\boldsymbol{X})\} \tag{4.1.2}$$

By using the substitution above, the Hilbert transform involved in Eq.(3.3.6) is now able to be replaced by the Fourier transform. Using Eqs. (4.1.1) and (4.1.2), Eqs. (3.3.2) and (3.3.6) are then replaced by

$$\frac{\partial A}{\partial T} + F^{-1}\{i(\omega - 1)F\{A\}\} = \Psi_3 \tag{4.1.3}$$

where

$$\begin{aligned}\Psi_3 = {} & \Upsilon_1 + \Upsilon_2 + \frac{i}{2}AF^{-1}\left\{\frac{\kappa^2}{K}F\{|A|^2\}\right\} + \frac{1}{2}\frac{\partial A}{\partial X}F^{-1}\left\{\frac{\kappa^2}{K}F\{|A|^2\}\right\} \\ & + \frac{1}{4}AF^{-1}\left\{\frac{\kappa^2}{K}F\left\{A\frac{\partial A^*}{\partial X}\right\}\right\} + \frac{1}{2}AF^{-1}\left\{\frac{\kappa^2}{K}F\left\{A^*\frac{\partial A}{\partial X}\right\}\right\} \\ & + \frac{i}{8}AF^{-1}\left\{\frac{\kappa^4}{K^2}F\{|A|^2\}\right\} + \frac{1}{2}\frac{\partial A}{\partial Y}F^{-1}\left\{\frac{\kappa\zeta}{K}F\{|A|^2\}\right\} \\ & + \frac{1}{2}AF^{-1}\left\{\frac{\kappa\zeta}{K}F\left\{A^*\frac{\partial A}{\partial Y}\right\}\right\}\end{aligned} \tag{4.1.4}$$

The new form (Eqs.(4.1.3) and (4.1.4)) is referred as the fifth order Enhanced Nonlinear Schrödinger Equation based on Fourier transform, shortened as ENLSE-5F.

Through comparing Ψ_2 and Ψ_3, it is found that the difference between the ENLSE-5H and ENLSE-5F is that the terms involving the Hilbert transform are now replaced with these in terms of the Fourier transform. The benefit of this substitution is that it is much easier to perform the Fourier transform than the Hilbert transform. In the ENLSE-5F, there are no difficulties associated with ENLSE-5H described in section 3.3. Another benefit of using the ENLSE-5F is that it is also solved by FFT technique, same as for the SBI methods. If the ENLSE-5H would be coupled with them, extra FFT analysis must be performed after numerically estimating the Hilbert transform, which needs extra computational time. Nevertheless, it requires performing FFT twice for each corresponding term in Eq.(4.1.4), so that further investigations are needed in order to compare the computational efficiency with estimating Ψ_2 by using numerical integration. Furthermore, the periodical boundary condition needs to be imposed in the new formulation. However, following other studies on large scale random sea simulations (Onorato, et al., 2001; Wu, 2004; Ducrozet, et al., 2007; Xiao, et al., 2013), the random sea states are usually reconstructed by assuming periodical boundary condition.

In addition, comparing the nonlinear part of the ENLSE-4, i.e., Eq.(3.2.11) and that of ENLSE-5F, i.e., Eq.(4.1.4), it is found that, apart from Υ_1 and $\frac{i}{2} A F^{-1}\left\{\frac{\kappa^2}{K} F\{|A|^2\}\right\}$, there are also Υ_2 and the rest parts in terms of the Fourier transform of order $O(\varepsilon^5)$ in Eq.(4.1.4). That means that the nonlinear effects in the ENLSE-5F are one order higher than the ENLSE-4.

4.2 Numerical implementation

As shown above, the ENLSE-5F, i.e., Eqs.(4.1.3) and (4.1.4), will be adopted in the hybrid model and solved by using the embedded fifth order Runge-Kutta method with adaptive time step. This procedure is similar with the numerical implementation for solving the SBI, as shown in Figure 3.4.1. The solution by using the six-stage embedded fifth order Runge-Kutta method can be written as

$$\begin{aligned} A^{(4)} &= A(T=0) + \sum_{j=1}^{6} \alpha_j \mathcal{K}_{Aj} \\ A^{(5)} &= A(T=0) + \sum_{j=1}^{6} \beta_j \mathcal{K}_{Aj} \end{aligned} \tag{4.2.1}$$

where coefficients α_j and β_j can be found in (Dormand & Pince, 1980), and $\mathcal{K}_{Aj}$ is the Runge-Kutta increment at each stage. The superscripts (4) and (5) represent the fourth order and fifth order solution of the Runge-Kutta time integrator respectively. The time step size is self-adaptive which is determined by imposing the following condition

$$Err_{AT} = \frac{\int \left|A^{(5)} - A^{(4)}\right| d\boldsymbol{X}}{\int |A^{(5)}| d\boldsymbol{X}} < Tol_T \tag{4.2.2}$$

where Err_{AT} is the relative error between the fourth order and fifth order solutions and Tol_T is the tolerance, which can be the same with the SBI. Using the equation, one can obtain the optimised time step size ΔT_{opt} as a function of Err_T, as suggested in (Clamond, et al., 2007). Based on that aforementioned, the numerical implementation for solving the ENLSE-5F is summarized in Figure 4.2.1.

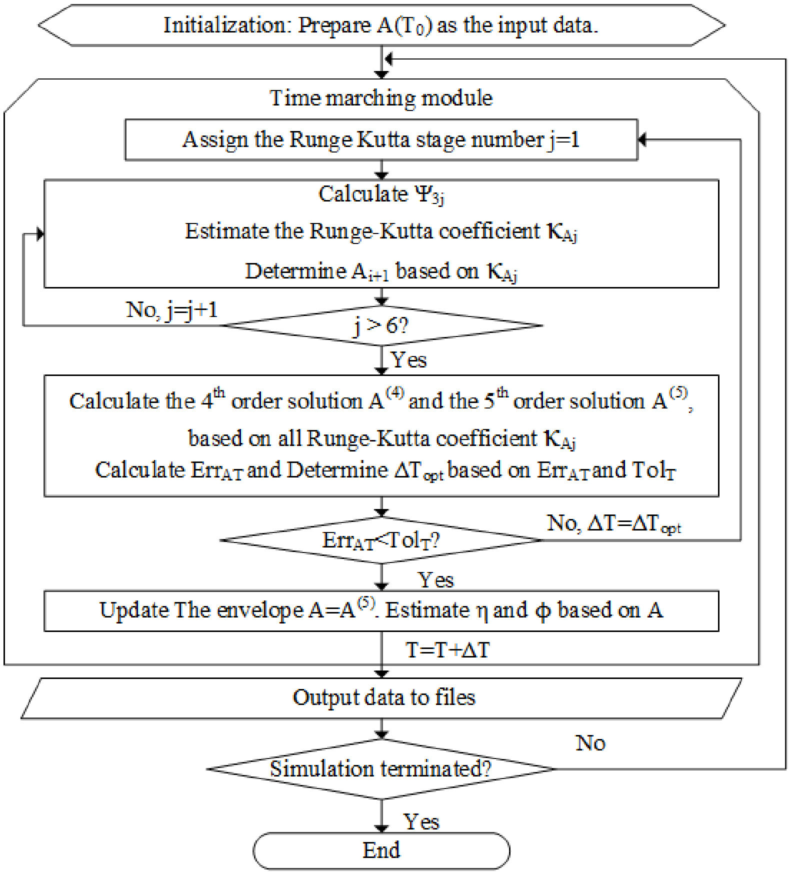

Figure 4.2.1 Flow chart for the numerical implementation of ENLSE-5F

4.3 Validation of the ENLSE-5F

In order to illustrate that the newly derived ENLSE-5F is equivalent to the original ENLSE-5H, a numerical test is carried out, in which the initial condition

$$A = 0.1 + 0.01e^{iX/16} \tag{4.3.1}$$

is considered. The domain covers 16 peak wave lengths. In order to resolve the singularity problems involved in Ψ_2 in Eq.(3.3.6), the method suggested by Fructus, et al. (2005) is employed. According to Wang & Ma (2015a), by using this method, the resolution in physical space must be very high in order to obtain satisfactory results. Thus, the domain is resolved into 8192 points. The profiles for both Ψ_2 and Ψ_3 are shown in Figure 4.3.1, and the maximum error between them is about 1.7%. It indicates that the derived ENLSE-5F is an equivalent formulation of the ENLSE-5H.

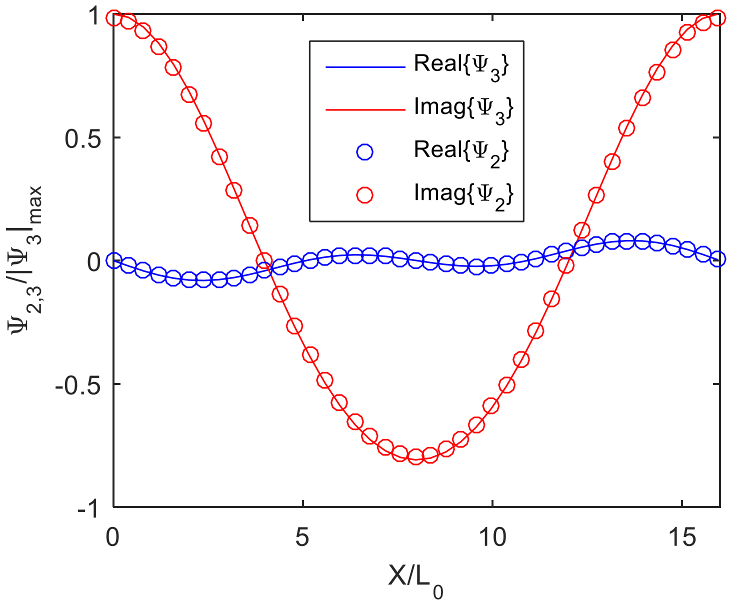

Figure 4.3.1 Profiles of Ψ_2 and Ψ_3

In order to validate the ENLSE-5F model for large domain simulations, the experiment by (Clamond, et al., 2006) is repeated by using ENLSE-5F. The results obtained from the ENLSE-5F is compared with that in (Clamond, et al., 2006), where the domain covers 128 wave lengths and resolved into 4096 points. The initial condition is given by

$$A = 0.0908\,\mathrm{sech}[0.0334(X - X_c)] \tag{4.3.2}$$

and the simulation lasts for 500 peak periods. A back and forth simulation is performed to validate the numerical scheme, and the error of the energy and free surface distribution between the initial and final stage is about 6×10^{-7} and 1×10^{-4} respectively, which implies that the calculation is very accurate. The envelopes obtained by using the ENLSE-5F and that in (Clamond, et al., 2006) are shown in Figure 4.3.2 for comparisons. Large waves occur repetitively, which leads to spectrum width changing correspondingly. This phenomenon is called Fermi-Pasta-Ulam recurrence (Yuen & Ferguson, 1978). It shows that in the first 300 peak periods, the results obtained from ENLSE-5F is visually the same with that obtained by using the ENLSE-4 and the fully nonlinear method in (Clamond, et al., 2006). However, all three models give inconsistent results at $T/T_0 = 500$, while the envelope of ENLSE-5F is more resemble to that by using the fully nonlinear model in (Clamond, et al., 2006), compared with the envelope obtained by using the ENLSE-4. The error between the maximum envelope of the ENLSE-5F and the fully nonlinear model at $T/T_0 = 500$ is about 3.85%, while that between the ENLSE-4 and the fully nonlinear model is about 56%! It indicates that the ENLSE-5F is more accurate for describing the evolution of the envelope, compared with the ENLSE-4, which is due to the effects of additional nonlinear terms.

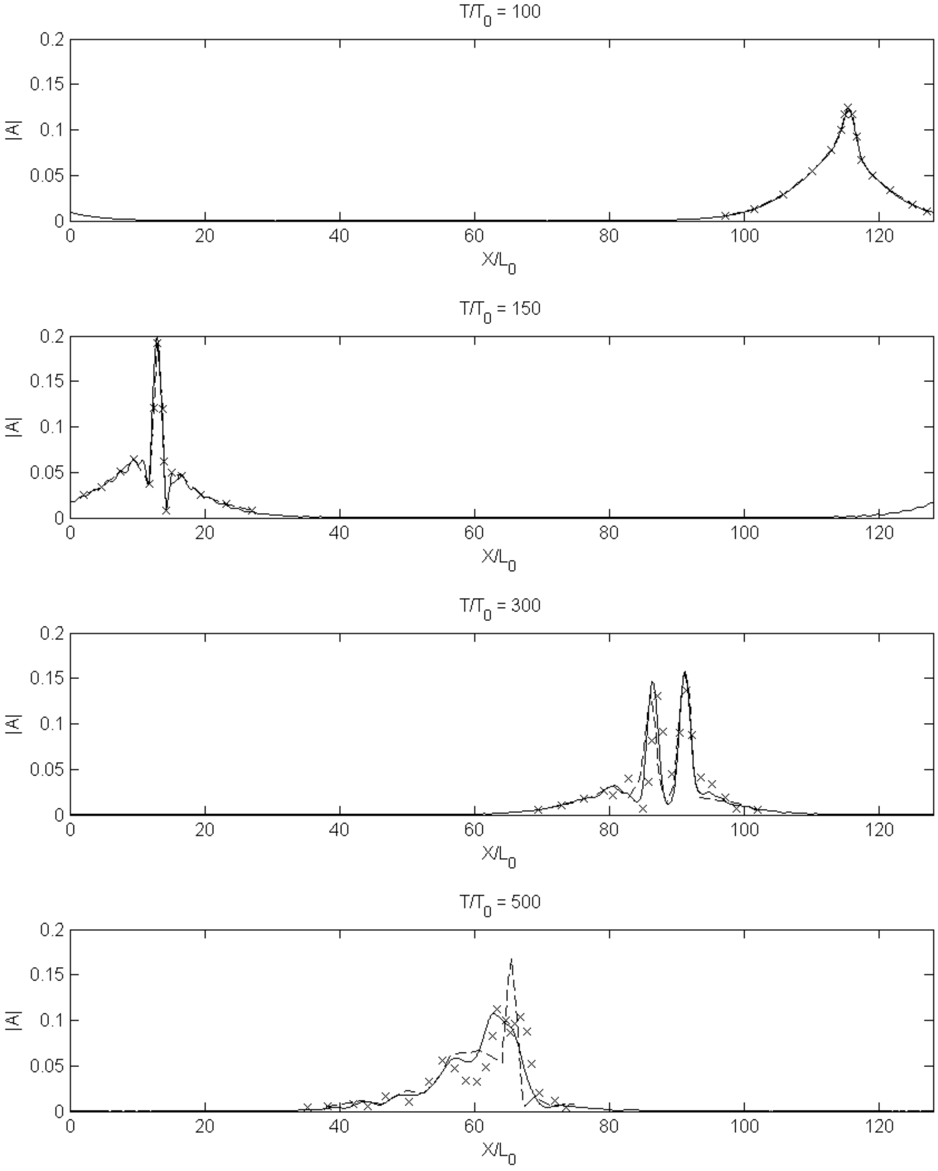

Figure 4.3.2 Envelopes of the numerical simulations. '—': ENLSE-5F; 'x': Fully nonlinear model in (Clamond, et al., 2006); '---': ENLSE-4 in (Clamond, et al., 2006)

Furthermore, in order to validate the ENLSE-5F model for three dimensional (3D) problems, the numerical tests for directional focusing wave described by Bateman et al. (2001) is simulated here with the same setups. The domain covers $14L_0 \times 14L_0$, i.e., $(-7L_0, -7L_0) \sim (7L_0, 7L_0)$, and is resolved into 256×256 collocation points. A focusing wave of steepness $\varepsilon = 0.3602$ is generated at the center of the domain, i.e., $\boldsymbol{X}_f = (0,0)$, at $T/T_0 = 7.4$. The following directional spectrum is adopted

$$S(k,\theta) = S_J(k)G_1(\theta) \tag{4.3.3}$$

where $S_J(k)$ is the JONSWAP spectrum given in Eq.(6.3.1), $\gamma = 1.7$ and the spreading function is

$$G_1(\theta) = \begin{cases} 1.788\cos^7\left(\frac{\theta}{2}\right), & |\theta| \le \frac{\pi}{2} \\ 0, & |\theta| > \frac{\pi}{2} \end{cases} \tag{4.3.4}$$

The simulation lasts for 10 peak periods. A back and forth simulation is also performed in this case to examine the numerical scheme, and the error of the energy and free surface distribution between the initial and final stage is about 3×10^{-7} and 2×10^{-6} respectively. The profiles of the free surface along $Y/L_0 = 0$ at the focusing time for both the ENLSE-5F and results in (Bateman, et al., 2001) are shown in Figure 4.3.3, and the error of the maximum surface elevation is about 4.33%, which means that the ENLSE-5F successfully captured the occurrence of the focusing wave. It indicates that the ENLSE-5F can be used for three dimensional simulations.

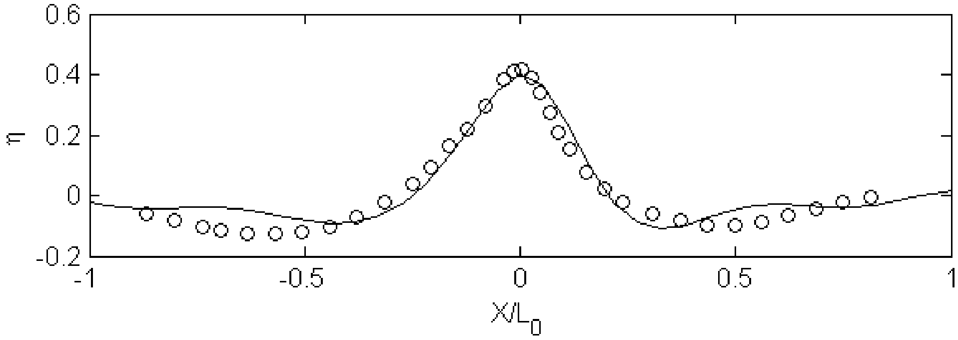

Figure 4.3.3 Profiles of the free surface. '—': ENLSE-5F; 'o': Fully nonlinear model in (Bateman, et al., 2001)

4.4 Discussion

In this chapter, the fifth order Enhanced Nonlinear Schrödinger Equation based on Fourier transform, i.e., ENLSE-5F, is derived. The numerical procedures for solving the ENLSE-5F is also presented. Compared with its counterpart, i.e., the ENLSE-5H, this equation is easier to be solved numerically, due to that the Fourier transform is performed by using FFT and is consistent with the numerical implementation of SBI. Although it can only be applied to periodical boundary problems due to the requirement of the FFT, this equation is still applicable to large scale random sea simulations for engineering purposes as explained above. In addition, numerical tests are carried out in order to validate the ENLSE-5F for simulating both two and three dimensional waves. The comparison between the numerical results obtained by using the ENLSE-5F with that in literature indicates that the ENLSE-5F can be used for simulating gravity waves in both two and three dimensions.

5 THE ENHANCED SPECTRAL BOUNDARY INTEGRAL METHOD

In this chapter, the SBI method will be enhanced by introducing three numerical techniques. It proves that the enhanced SBI method (ESBI for short) is more computationally efficient compared with the method originally suggested by Fructus, et al. (2005) when considering the same level of accuracy. The most part of contents in the chapter has been published in external source (Wang & Ma, 2015a).

5.1 Techniques for de-singularity

As mentioned in section 3.4.2, the integrals in Eq.(3.4.14), (3.4.17), (3.4.23) and (3.4.24) have singular integrands. Singularity is an inherited problem for all methods based on the boundary integrals dealing with gravity water waves, from when they were introduced by Longuet-Higgins & Cokelet (1976) in their study on the 2D overturning waves. In their paper, the normal velocity ϕ_n appeared in $\int \phi_n \ln s \, ds$, where s is the arc-length on the boundary, was expanded at $s = 0$ and $s^i \ln s$ was integrated analytically. Grilli, et al. (1989) dealt with the singular integrals by using so called 'singularity extraction' method for their boundary element method applying to 3D wave problems. In the approach, they introduced the polar coordinates and then transformed the principle integration to a regular integration.

For the SBI Method, Fructus, et al. (2005) suggested evaluating the integrands at nodes $\boldsymbol{X} + \frac{1}{2}\Delta\boldsymbol{X}$, and shifting back to regular nodes through Fourier interpolation. This method is equivalent to evaluating the integrations without considering the elements around the singular points so that the contributions to the integration coming from this area are neglected. The smaller the neglected area is, the more accurate the numerical integration is. In other words, to achieve high accuracy of results, the number of elements splitting the free surface has to be large. This can decelerate the computational process. In this section, an alternative technique is suggested to evaluate the singular integrals for the the spectral boundary integral method.

5.1.1 Weak-singular integral in V_4

Similar to the strategy by Grilli, et al. (1989), the integration part of V_4 around the singular point can be written as

$$\lim_{\sigma\to 0}\int_{S-\sigma}\frac{V'\Upsilon_i}{R}d\boldsymbol{X}' = \lim_{\sigma\to 0}\int_{S-\sigma}\frac{\tilde{f}(\boldsymbol{X}')}{R}d\boldsymbol{X}' \tag{5.1.1}$$

where Υ_i is given by Eq.(3.4.18) or (3.4.26), σ is an area surrounding the singular point. Using the local polar coordinates illustrated in Figure 5.1.1, the right hand side of Eq.(5.1.1) can be given as

$$\lim_{\sigma\to 0}\int_{S-\sigma}\frac{\tilde{f}(\boldsymbol{X}')}{R}d\boldsymbol{X}' = \lim_{\delta\to 0}\int_0^{2\pi}\int_{\delta}^{\rho(\theta)} f(R,\theta)dRd\theta = \int_0^{2\pi}\int_0^{\rho(\theta)} f(R,\theta)dRd\theta \tag{5.1.2}$$

where $\rho(\theta)$ and δ are the radius of the area S and σ respectively, and

$$\tilde{f}(\boldsymbol{X}') = f(R,\theta) = V'\Upsilon_i \tag{5.1.3}$$

with $D \to \frac{\partial\eta}{\partial X}cos\theta + \frac{\partial\eta}{\partial Y}sin\theta$ for $R \to 0$. The expression in Eq.(5.1.3) is not singular $R \to 0$. For each value of θ from 0 to 2π, one can assume $f(R,\theta)$ vary linearly along R. Thus a two point trapezium rule is enough for evaluation.

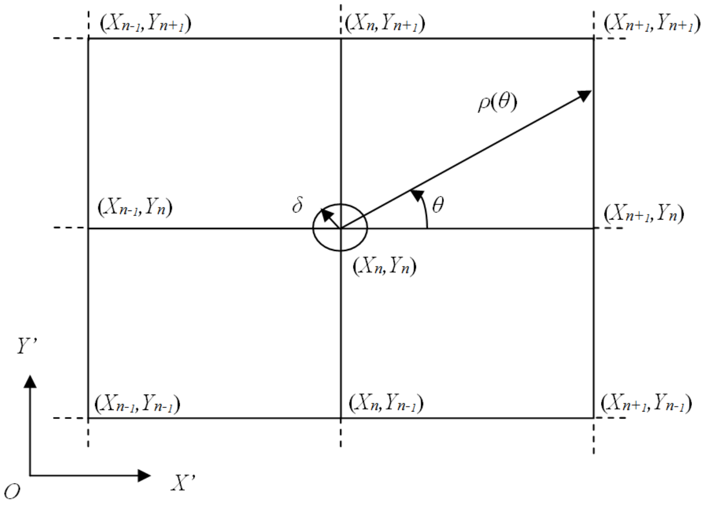

Figure 5.1.1 The local polar coordinates for the elements near the singular point

5.1.2 Weak-singular integral in V_3

Following the same strategy, the weak-singular integral around the singular point in the expression of V_3 is written as

$$\lim_{\sigma\to 0}\int_{S-\sigma}\frac{\tilde{g}(\boldsymbol{X}')}{R^2}d\boldsymbol{X}' = \lim_{\sigma\to 0}\int_{S-\sigma}\frac{g(R,\theta)}{R}dRd\theta \tag{5.1.4}$$

where

$$g(R,\theta) = \tilde{g}(\boldsymbol{X}') = \tilde{\phi}'\left(D - \frac{\boldsymbol{R}\cdot\nabla'\eta'}{R}\right)\Gamma_{\mathrm{i}} \tag{5.1.5}$$

and Γ_i is defined by Equation (3.4.16) or (3.4.25). Note that when $R \to 0, \frac{\boldsymbol{R}\cdot\nabla'\eta'}{R} - D \to 0$, that means $g(R = 0, \theta) = 0$. Thus, in order to evaluate the integral numerically, $g(R, \theta)$ is approximated with the first order Taylor series

$$g(R,\theta) = g(0,\theta) + \frac{\partial g}{\partial R}(0,\theta)R + \mathrm{O}(R^2) \tag{5.1.6}$$

Then one has

$$\int_0^{2\pi}\int_0^{\rho(\theta)} \frac{g(R,\theta)}{R} dRd\theta = \int_0^{2\pi}\int_0^{\rho(\theta)} \frac{\partial g}{\partial R}(0,\theta)dRd\theta \tag{5.1.7}$$

which provides a solution for converting the weak-singular integration to a regular integration, as there is no singularity in $\frac{\partial g}{\partial R}(0, \theta)$.

5.1.3 Effectiveness of the de-singular techniques for evaluating V_3 and V_4

In order to show how effective the above de-singular techniques are, the cases for Stokes waves presented in (Fructus, et al., 2005) are tested in this section. To model the case, the initial free surface elevation and velocity potential on the free surface are calculated by using the Fenton's numerical solver (Fenton, 1988) up to seventh order with the wave steepness of $\varepsilon = 2\pi a/L = 0.2985$ ($L = 2\pi$ is the wave length) in a spatial domain of $2L \times 2L$. In addition, numerical tests indicate that any value of $Tol_B \leq 10^{-5}$ in Eq.(3.4.19) leads to almost the same results and so the value of Tol_B is taken as 10^{-5} hereafter.

Since the specific values of V_3 and V_4 are time-dependent, the effectiveness of the de-singularity technique will be examined using the profiles of V_3 and V_4 at the first time step. These profiles obtained by the methods with or without the de-singularity technique are shown in Figure 5.1.2 for different numbers of elements represented by the resolution. The profiles are normalized by V_{30} and V_{40}, which are the maxima of V_3 and V_4 corresponding to the resolution $2^{10}\times2^{10}$. The results for the case without the de-singularity technique are obtained by using the same method as in (Fructus, et al., 2005), that is, the singularity is avoided by evaluating the integrands of V_3 and V_4 at a shifted point $(\boldsymbol{X} + \frac{1}{2}\Delta\boldsymbol{X})$. As the de-singularity techniques are relevant only to the integration parts in V_3 and V_4, the results plotted are only these parts in V_3 and V_4. As can be seen from Figure 5.1.2, without the de-singularity technique, the peak values of both V_3 and V_4 are significantly under-estimated when the resolution is not sufficiently high. With increase of the resolution, the profiles of V_3 and V_4 gradually coincide with each other. Specifically, at the resolution of $2^9\times2^9$, the difference between them becomes negligible. This demonstrates that the approach proposed in (Fructus, et al., 2005) can give accurate results but requires higher resolution. In order to shed more light on the performance of the techniques, their errors are analyzed using the following equations

$$Error\{V_3\} = \frac{\int \left|V_3 - V_3^{(N=2^{10})}\right| dX}{\int \left|V_3^{(N=2^{10})}\right| dX}, \quad Error\{V_4\} = \frac{\int \left|V_4 - V_4^{(N=2^{10})}\right| dX}{\int \left|V_4^{(N=2^{10})}\right| dX} \tag{5.1.8}$$

where $V_3^{(N=2^{10})}$ and $V_4^{(N=2^{10})}$ are the values of V_3 and V_4 calculated using resolution of $2^{10}\times2^{10}$, and the integrations are made over the whole projected free surface. The errors against the different resolutions are shown in Figure 5.1.3. It can be seen that the error corresponding to the results obtained by using the de-singularity technique for the resolution of $2^6\times2^6$ is as small as that obtained without the de-singularity technique for the resolution of $2^{10}\times2^{10}$, while the error from the method without the de-singularity technique for the resolution of $2^6\times2^6$ is more than 6 times larger than the latter. This further demonstrates that the de-singularity technique help achieving the similar results with much low resolution or achieving the results with higher accuracy by using the same resolution, compared to the approach suggested in (Fructus, et al., 2005).

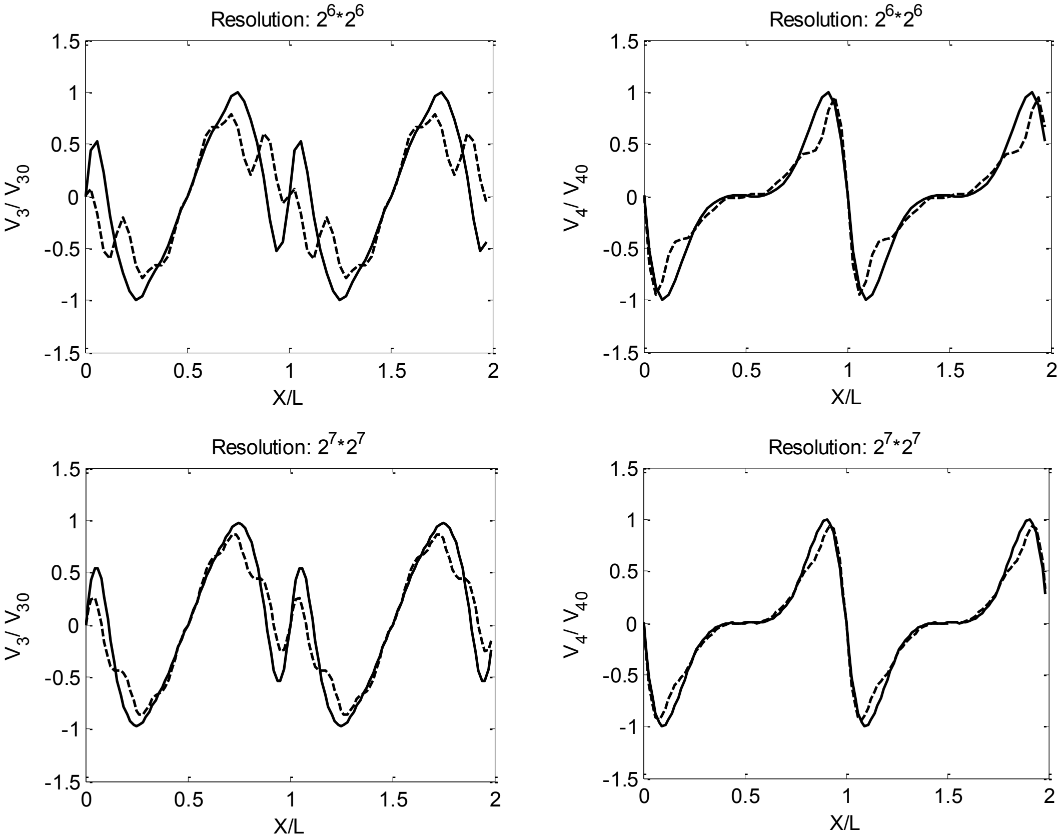

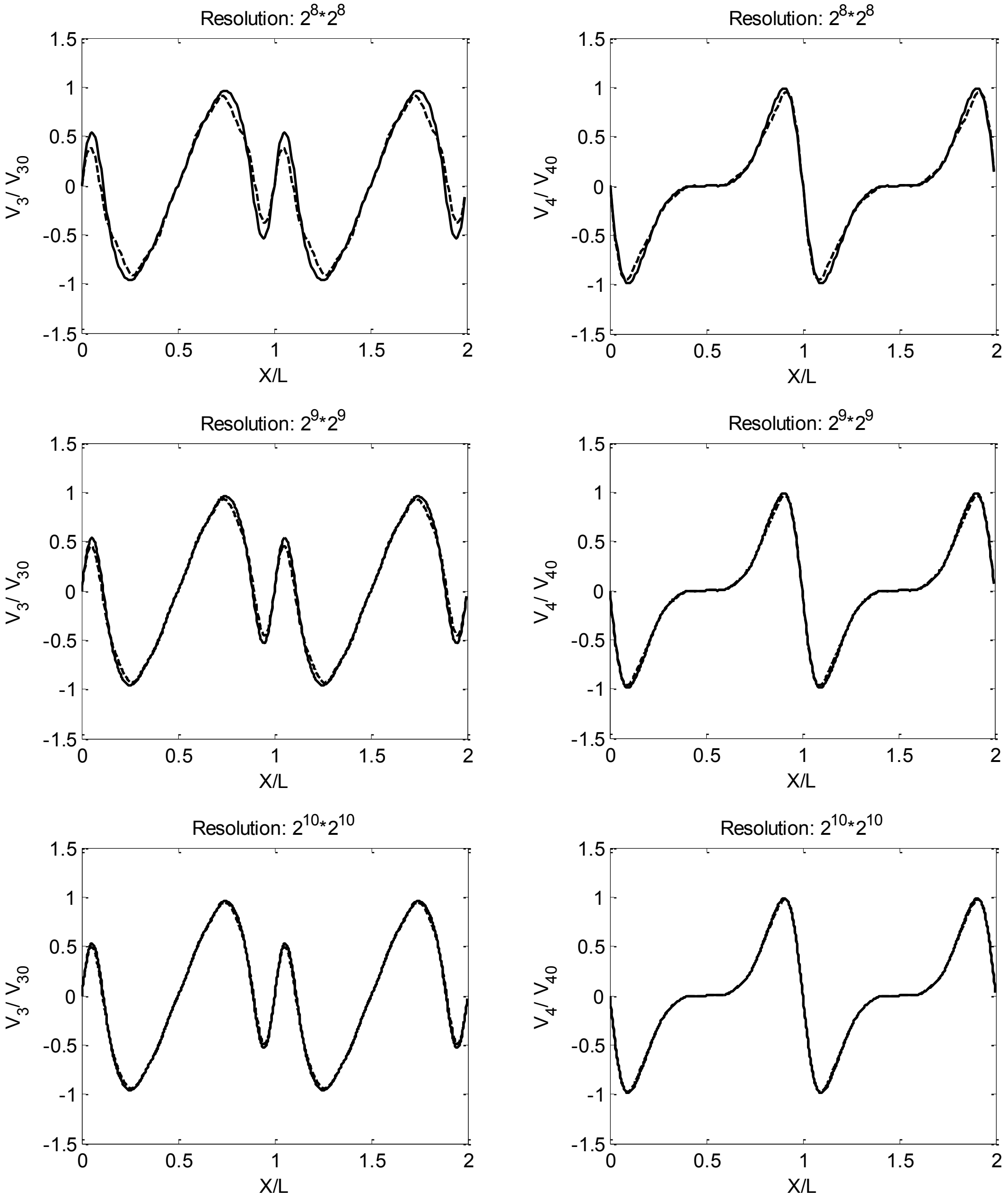

Figure 5.1.2 Profiles of V_3 and V_4

Solid: with de-singularity technique; Dash: without de-singularity technique

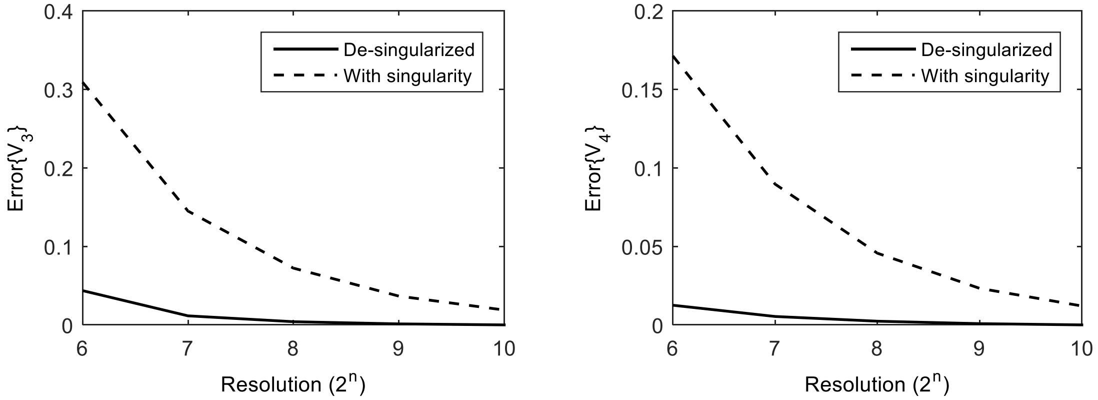

(a) (b)

Figure 5.1.3 Relative error of the profiles of V_3(a) and V_4(b)

Table 5.1.1 Phase shift with different experimental conditions

Phase shift (degree)	$Tol_T = 1E - 6$			$Tol_T = 1E - 7$			$Tol_T = 1E - 8$		
	o	×	√	o	×	√	o	×	√
$2L \times 2L$ domain	-	19.52	4.33	-	19.60	4.26	18	19.61	4.25
$4L \times 2L$ domain	-	19.56	4.29	-	19.60	4.25	-	19.61	4.25
$8L \times 2L$ domain	-	19.58	4.26	-	19.61	4.25	-	19.61	4.25

Note: 'o' result from *(Fructus, et al., 2005)*; '×' without de-singularity technique; '√' with de-singularity technique

Next, the overall effects of the de-singularity technique on wave propagation of a long period will be examined. The same waves for Figure 5.1.2 and Figure 5.1.3 are considered but simulated in different sizes ($2L \times 2L$, $4L \times 2L$ and $8L \times 2L$) of the spatial domain. To simulate these cases, the resolution used is $2^6 \times 2^6$, $2^7 \times 2^6$ and $2^8 \times 2^6$, (i.e., the number of elements per wave length is the same), respectively. The wave profiles after the simulation of $1000T_0$ (T_0 is the wave period output by the Fenton's numerical solver (Fenton, 1988), which is 6.0095 in this case) are plotted in Figure 5.1.4. If there would be no error, the profiles after the propagation of $1000T_0$ should coincide with the initial profile (the dotted line in the figure). One can see from this figure that the profile obtained without the de-singularity technique has a large phase shift (about 20 degree), while that obtained with the de-singularity technique has only a small phase shift (about 4 degree). The phase shift is gradually accumulated during the simulation. The variation of the phase shift with time is depicted in Figure 5.1.5 for different sizes of spatial domain. It clearly shows that the phase shift varies linearly with time and eventual values are almost the same for different domains. In addition, the effects of Tol_T used in Eq.(3.4.8) are also shown in this figure and in Table 5.1.1. All the information confirms that $Tol_T = 1E - 7$ is sufficiently small to give consistent results.

To further examine the effectiveness of the new de-singularity technique quantitatively, the errors defined in two different ways are introduced below:

a) The total phase shift error

$$Err_1\{\varphi\} = 100\frac{|\Delta\varphi|}{2\pi} \tag{5.1.9}$$

b) The mean phase shift error per wave period

$$Err_2\{\varphi\} = \frac{Err_1}{N_{to}} \tag{5.1.10}$$

where $\Delta\varphi$ is the total phase shift in radians over the whole period of simulation and N_{to} is the total number of wave periods of simulation, which is 1000 in this case. The errors of the same case as in Figure 5.1.4(a) for the domain size of $2L \times 2L$ but obtained using different resolutions are plotted in Figure 5.1.6(a), where the number of horizontal axis represents the power (n) of 2^n (the same employed hereafter). In addition, the CPU time against different errors for running all the simulations up to $1000T_0$ on a workstation equipped with the Intel Xeon E5-2630 v2 (Intel Corporation, Santa Clara, CA, USA) of 2.6GHz processor are depicted in Figure 5.1.6 (b). All figures involving the CPU time appears in this chapter are based on the same workstation. The results clearly show that for the case with the wave steepness of $\varepsilon = 0.2985$, use of the de-singularity technique allows considerably lower resolution or requires much less CPU time to achieve the same level of accuracy, compared without use of the de-singularity technique. For example, to achieve the results with an error of about 2.5% in terms of $Err_1\{\varphi\}$ needs the resolution of $2^5 \times 2^5$ and the CPU time of 2×10^3 seconds with use of the de-singularity technique; otherwise, it needs the resolution of $2^7 \times 2^7$ and the CPU time of about 10^4 seconds.

The ratio of the minimum resolutions and corresponding CPU time needed to achieve the error less than 2.5% by the methods with and without use of the de-singularity technique are shown in Figure 5.1.7. The ratio in this figure is calculated in the way that the value of the method without the de-singularity technique is divided by that of the method with the de-singularity technique. The figure demonstrates that the minimum resolution and corresponding CPU time used by the two methods with and without the de-singularity technique are almost the same for the cases with small wave steepness. However, for the cases with larger wave steepness (specifically, $\varepsilon \geq 0.2$), the method with use of the de-singularity technique needs much less resolution and CPU time than the one without use of the de-singularity technique. For example, for the case of $\varepsilon = 0.36$, the CPU time required by the method with use of the de-singularity technique is only 1% of that without it to yield the results at the said error level. All the above information evidences that the de-singularity technique is particularly effective for modelling strong nonlinear waves in terms of the resolution and so the CPU time required. The CPU time recorded for each simulation may not reflect the real physical time accurately, because parallel computation is employed. This can explain the slightly decreasing of CPU ratio for $\varepsilon \geq 0.3$ in Figure 5.1.7 (b).

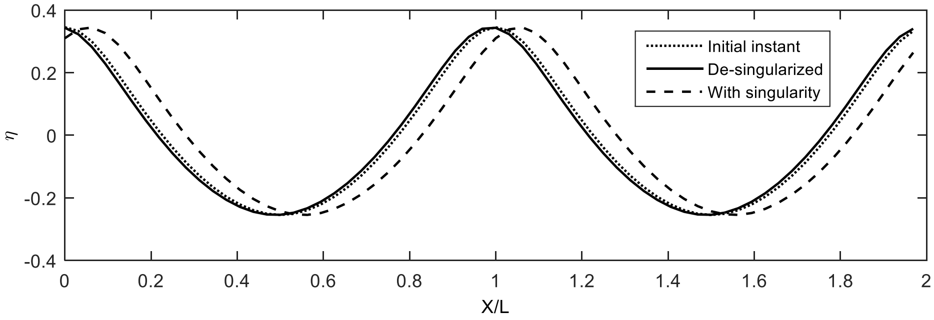

(a) Domain size: $2L \times 2L$

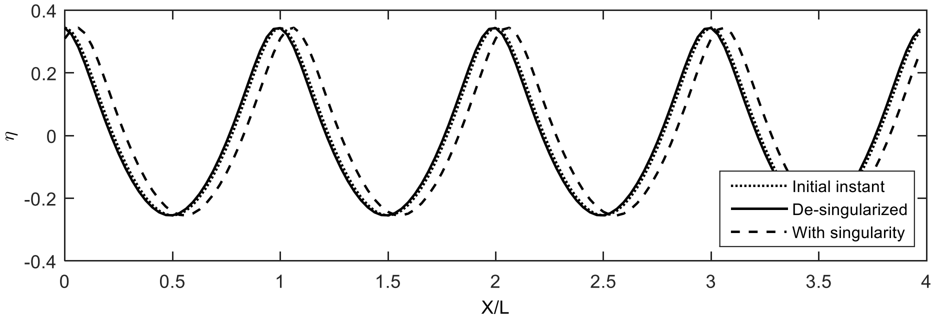

(b) Domain size: $4L \times 2L$

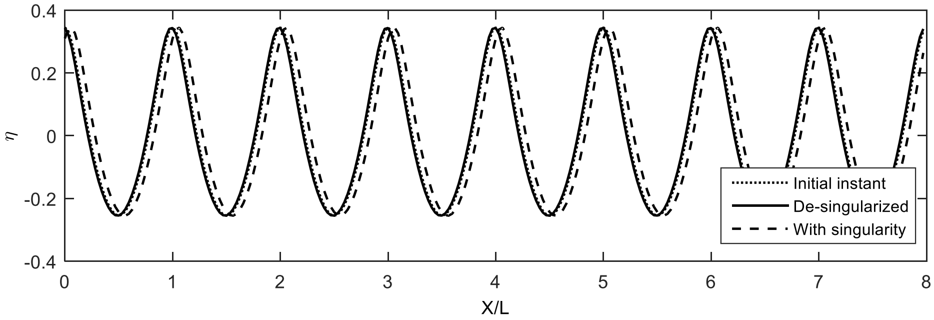

(c) Domain size: $8L \times 2L$

Figure 5.1.4 Profiles of the free surfaces

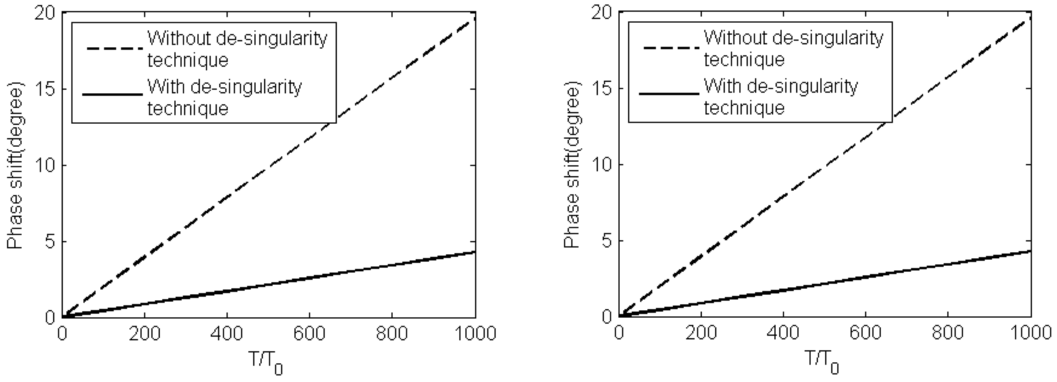

(a) $2L \times 2L$, $Tol_T = 1E-7$ (b) $2L \times 2L$, $Tol_T = 1E-8$

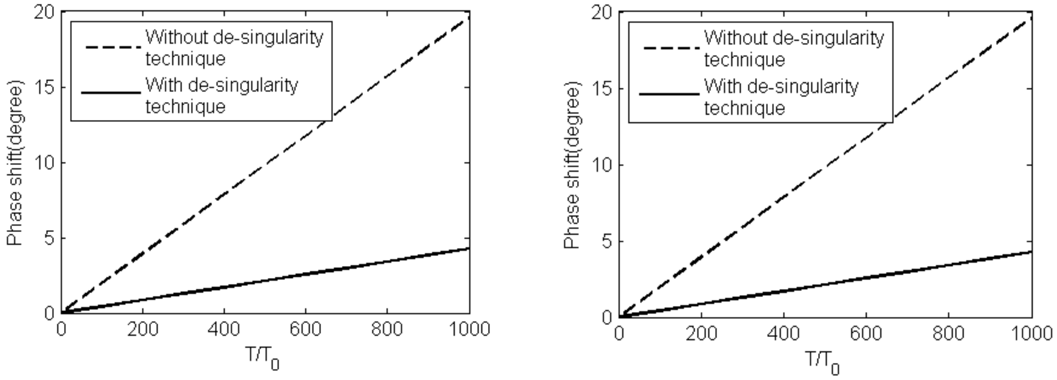

(c) $4L \times 2L$, $Tol_T = 1E-7$ (d) $4L \times 2L$, $Tol_T = 1E-8$

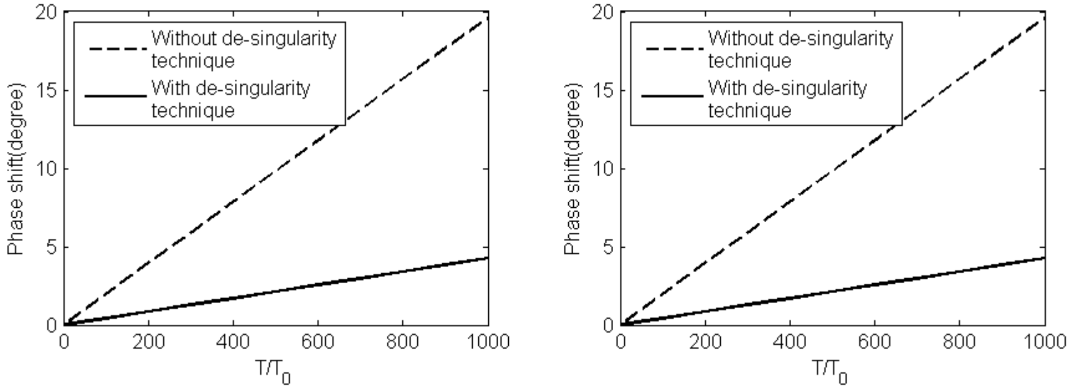

(e) $8L \times 2L$, $Tol_T = 1E-7$ (f) $8L \times 2L$, $Tol_T = 1E-8$

Figure 5.1.5 Variation of the phase shift of wave profiles with time

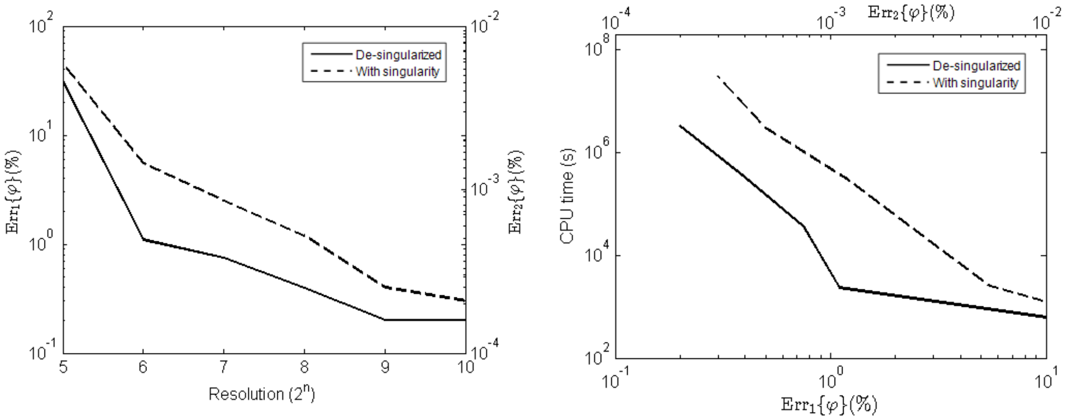

(a) Error against resolution

(b) CPU time against Error

Figure 5.1.6 Results for the case with a domain of $2L \times 2L$ and $\varepsilon = 0.2985$

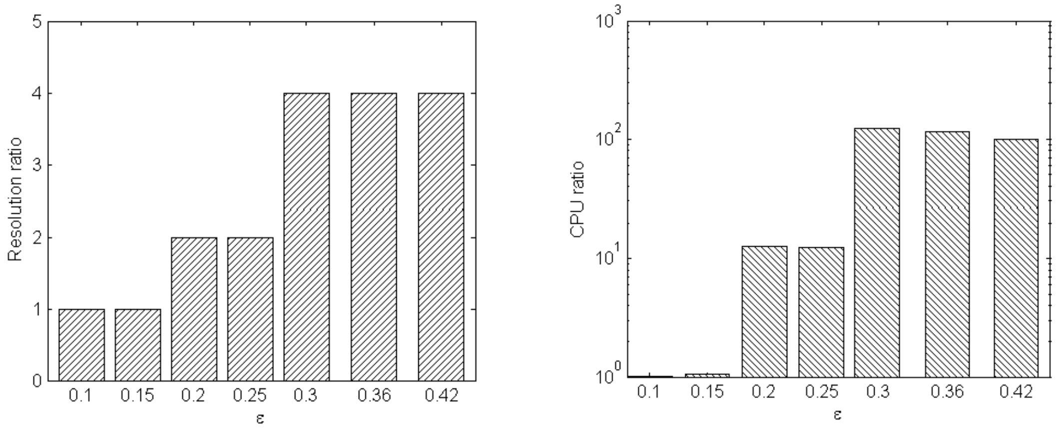

(a) Resolution ratio against steepness

(b) CPU ratio against steepness

Figure 5.1.7 Resolution and CPU ratio to achieve $Err_1 < 2.5\%$ for different values of steepness

5.2 Techniques for Anti-Aliasing (TAA)

In addition to the integration parts discussed in the previous section, one needs to numerically calculate the convolution parts in the spectral method. For this purpose, the discrete Fast Fourier Transform (FFT) or its inverse transform is repeatedly performed on a limited number of *N* points. As well documented, e.g. (Canuto, et al., 1987), the calculation of the convolutions (particularly the higher order ones involving more than two functions, like V_3 and V_4 in Section 3.4.2) in this way suffers aliasing errors when improper resolution is used (Canuto, et al., 1987). The aliasing errors may be theoretically eliminated by using sufficiently high resolution to ensure that the wave component corresponding to the highest frequency or wave number is correctly sampled. However, use of high resolution requires high computational costs. Added to this, it is difficult to predict the highest frequency during the simulation of nonlinear waves because the components of higher frequency are continuously evolving during the simulation due to nonlinearity. Therefore, anti-aliasing techniques are necessary to model nonlinear water waves. As discussed in (Canuto, et al., 1987), there are largely two types of anti-aliasing techniques for general fluid problems: one based on truncation (or padding) and the other based on phase shifting.

In the research for modelling nonlinear water waves, Dommermuth & Yue (1987) dealt with the pseudo-spectral product involving two terms by doubling the width of the spectrum of each term and multiplying in physical domain. Then the spectrum of this product is truncated to the original width after applying Fourier transform. For products involving two or more terms, the multiplication is done successively where each factor is made aliasing-free before multiplied by the next term. Nicholls (1998) and Xu & Guyenne (2009) introduced a filter to remove the aliased components for $|K| > \nu|K|_{max}$ in spectrum domain, where ν is determined by the method consistent with Canuto, et al. (1987). Clamond & Grue (2001) approximated the third order convolution by doubling the spectra in order to remove the aliasing errors (4-half rule). All the techniques used in the cited papers are based on the truncation (or padding) technique. That is perhaps because the technique by using truncation (or padding) is more computationally efficient than that by using phase shifting. Three techniques will be discussed below. All of them are formed by using truncation (or padding).

For the illustration purpose to aid the discussions below, Stokes wave with $\varepsilon = 0.2985$ similar to that Figure 5.1.4 but within a domain of $L \times L$ will be used. Other parameters will be given when necessary. Suppose the resolution of the surface elevation and velocity potential for FFT is N, and the width of their spectrum will be $-N/2 \sim N/2$. In many figures below, the spectra is divided by the Fourier coefficient of $K = 1$, and the quantities in the physical domain are normalized by its maxima.

5.2.1 Anti-aliasing Techniques

TAA1: (2/(I+1)-rule). The spectrum width of the Ith order convolution will be truncated to $N/(I+1)$. This follows exactly the zero-padding method in (Canuto, et al., 1987). For example, in order to estimate $F\{\eta^2 V\}$, which is a part $V_4^{(1)}$ and is the third order convolution, the spectrum of η and V will be truncated to $-32/4 \sim 32/4$ from the range of $-32/2 \sim 32/2$ as shown in Figure 5.2.1(a) for $N = 32$, where the points circled out are padded as zero. Then the product of $\eta^2 V$ is calculated in the physical spatial domain after applying inverse Fourier transform to give both η and V, as shown in Figure 5.2.1 (b) and (c). At last, the product of $\eta^2 V$ is transformed back to spectral space and their spectra $F\{\eta^2 V\}$ are truncated to $-32/4 \sim 32/4$, which is illustrated in Figure 5.2.1 (d). Similarly, to estimate $F\{V\eta^6\}$, which is a part of $V_4^{(3)}$ and is the seventh order convolution. The spectra of η and V are truncated to $-32/8 \sim 32/8$ before calculating $V\eta^6$, as shown in Figure 5.2.1 (e). After the multiplication of the functions in physical space (Figure 5.2.1 (f) and (g)), the spectrum $F\{V\eta^6\}$ is truncated to $-32/8 \sim 32/8$ (Figure 5.2.1 (h)).

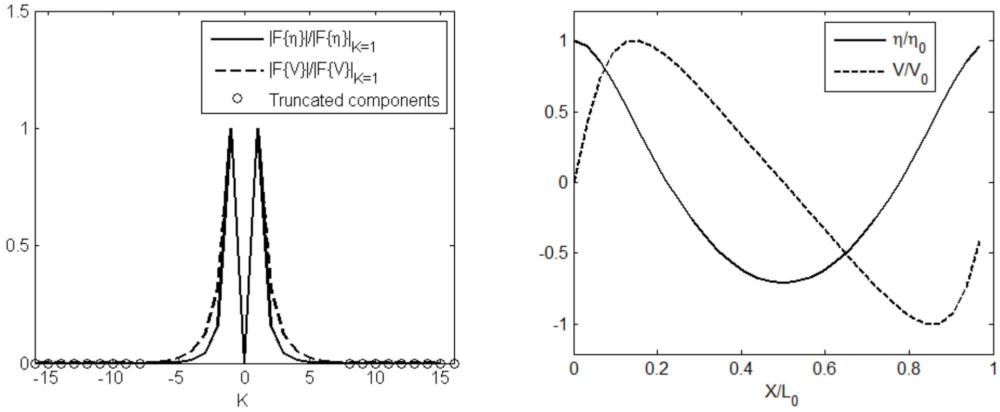

(a) Truncate spectra of η and V

(b) Inverse to physical space

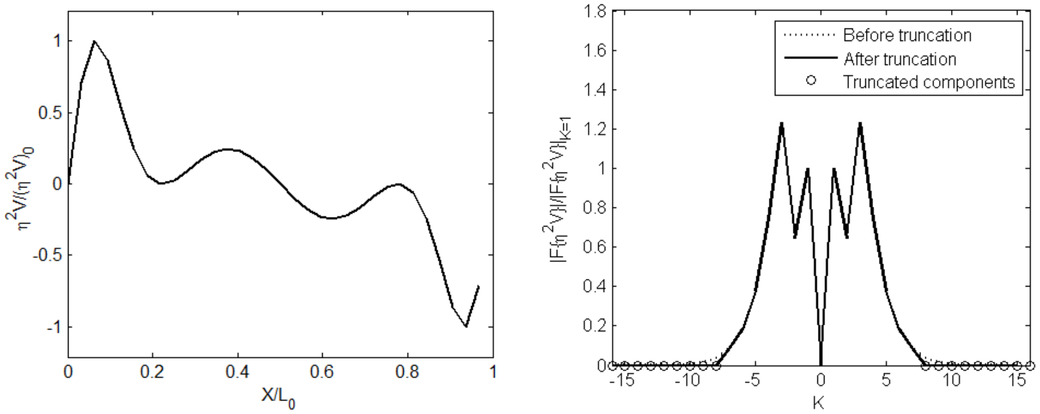

(c) Estimate $\eta^2 V$

(d) Truncate spectrum of $\eta^2 V$

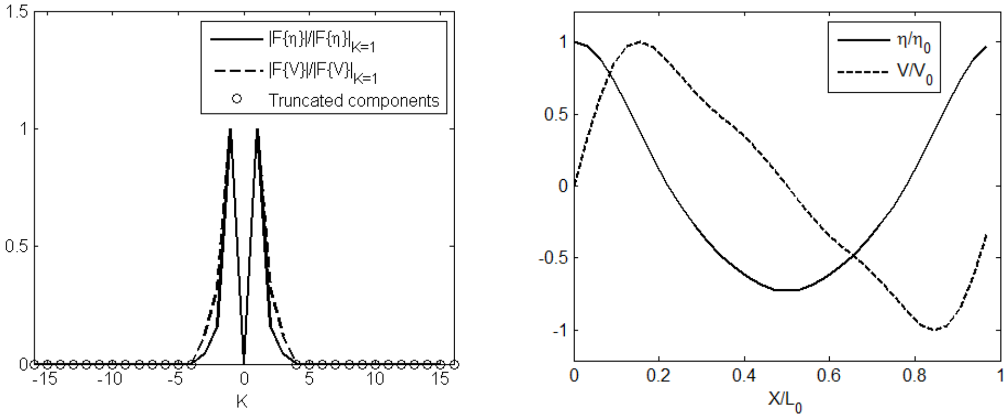

(e) Truncate spectra of η and V

(f) Inverse to physical space

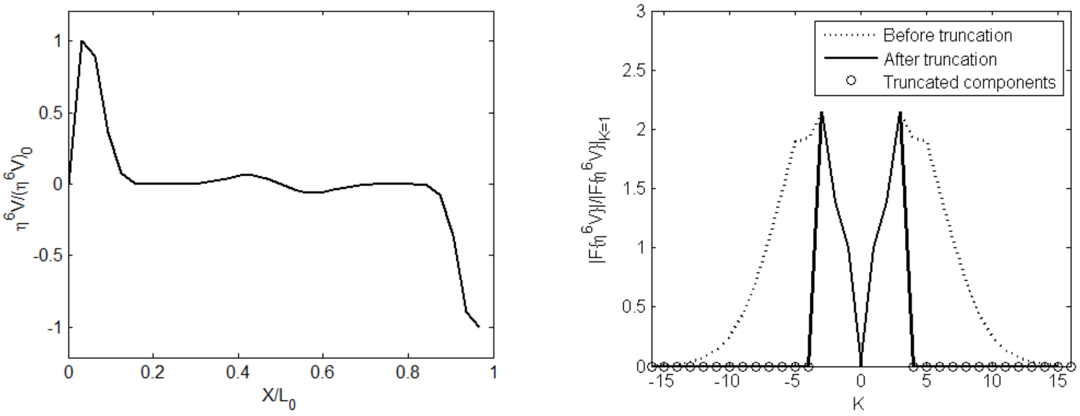

(g) Estimate $\eta^6 V$

(h) Truncate spectrum of $\eta^6 V$

Figure 5.2.1 Illustration of TAA1

TAA2: (Repeated 2/4-rule). This technique was suggested and referred as repeated 4-half rule by Clamond & Grue (2001) and Fructus, et al. (2005). The spectrum width of convolutions of the second and third order are truncated to $-N/4 \sim N/4$. Convolutions of fourth order and higher will be estimated using a repeated 2/4-rule, in which the convolution is broken down into several terms, each one being of lower than the third order. Each individual term is estimated with 2/4-rule. For example, $F\{\eta^3 \nabla\tilde{\phi}\}$ is firstly split into $F\{\eta^3\} * F\{\nabla\tilde{\phi}\}$. Applying the 2/4-rule (same as in TAA1) gives η^3 and $\nabla\tilde{\phi}$ separately (Figure 5.2.2 (a) – (d) and then $\eta^3 \nabla\tilde{\phi}$ (Figure 5.2.2 (e)) in the physical space. After that, $F\{\eta^3 \nabla\tilde{\phi}\}$ is computed by FFT and its spectrum is truncated to $-N/4 \sim N/4$, as shown in Figure 5.2.2 (f).

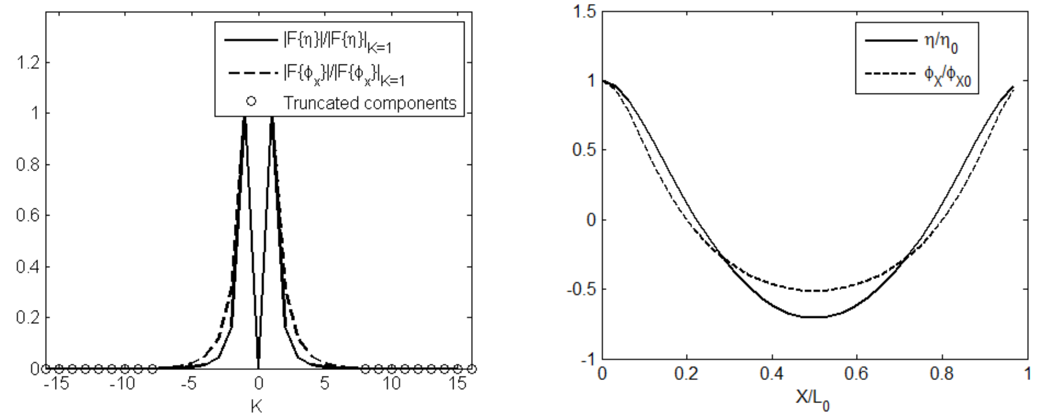

(a) Truncate spectra of η and $\nabla\tilde{\phi}$

(b) Inverse to physical space

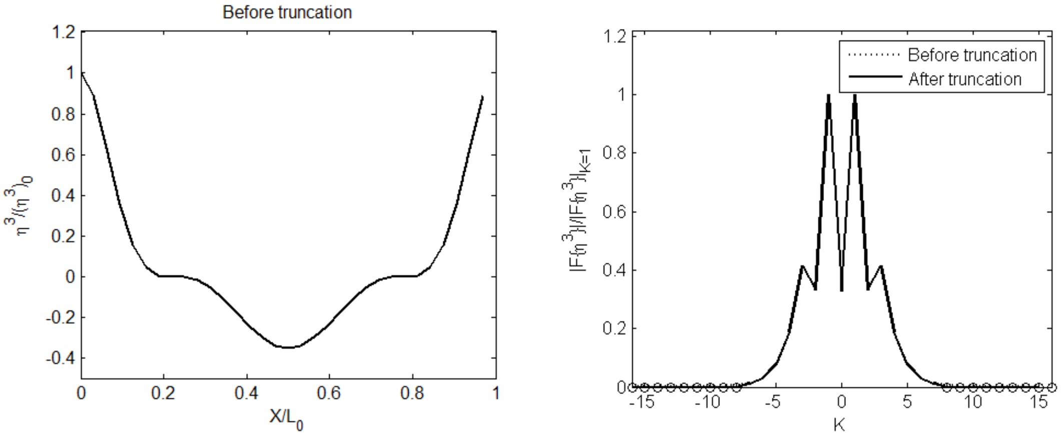

(c) Estimate η^3

(d) Inverse to physical space

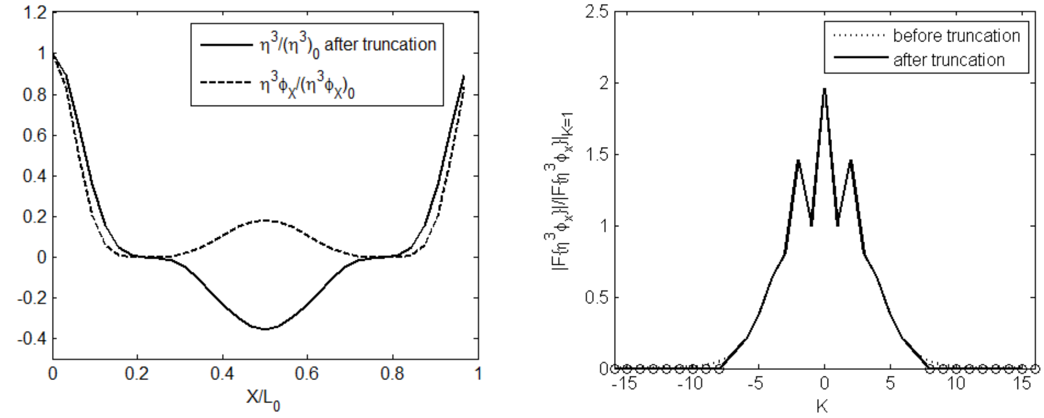

(e) Estimate $\eta^3\nabla\tilde{\phi}$

(f) Truncate spectrum of $\eta^3\nabla\tilde{\phi}$

Figure 5.2.2 Illustration of TAA2

Although this technique may work in some cases, it is found not to be generally accurate. For example, when the technique is applied to evaluate $V_4^{(2)}$ of fifth order convolution for a Stokes wave of $\varepsilon = 0.3$ in a domain of one wave length at the resolution of 2^5, the result in Figure 5.2.3 is obtained, where the solid line is the result obtained by using very high resolution (2^9) for which there should be no aliasing error. It can be seen that TAA2 gives incorrect approximation to $V_4^{(2)}$ at this resolution.

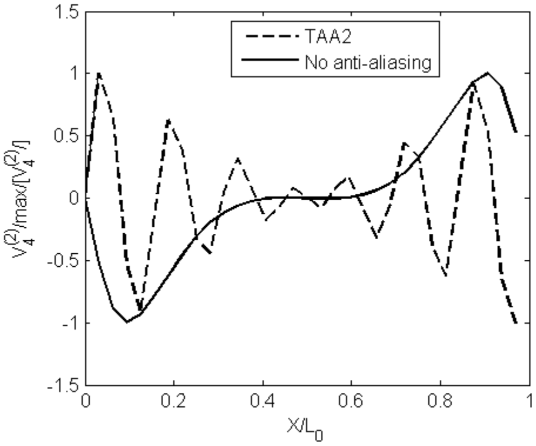

Figure 5.2.3 Profiles of $V_4^{(2)}$

TAA3: (Mixed 2/4-2/8-rule). This technique is suggested by (Wang & Ma, 2015a). For this technique, the convolutions of the second and third order are estimated using the 2/4-rule as in TAA1 and TAA2. The difference lies in dealing with the convolutions of fourth and higher order. To deal with these higher order convolutions, the spectrum of an individual function is padded as zero in the ranges of $-N\sim-N/4$ and $N/4\sim N$, and then they are inversed to the physical domain. The products of the functions are found before transformed into spectral space. The resulting spectrum is truncated to $-N/4\sim N/4$ at last. For instance, to estimate $F\{V\eta^6\}$, the spectrum of V and η is padded as zero except for the range of $-32/4\sim32/4$ within $-32\sim32$ as shown in Figure 5.2.4(a) and (b) for $N = 32$ before they are inversed to physical space (Figure 5.2.4 (c)). Then their product (Figure 5.2.4 (d)) is computed before transforming it to spectral space (Figure 5.2.4 (e)). In the spectral space, the spectrum $F\{V\eta^6\}$ is truncated to $-32/4\sim32/4$ with all other points padded as zero. As this spectrum is truncated from the range of $-32\sim32$ to the range of $-32/4\sim32/4$, it actually follows the 2/8-rule. The principle dealing with the higher order convolutions are similar to that of TAA1 but there are some differences: (1) the spectrum of an individual function covers the range of $-N\sim N$ in this technique rather than $-N/2\sim N/2$ in TAA1; (2) the range of spectrum for all high order (fourth and higher) convolutions is the same but it is different for different order in TAA1 and (3) the nonzero width of the last spectrum is generally larger in TAA3 than in TAA1, which can be found by comparing Figure 5.2.1(h) with Figure 5.2.4 (f).

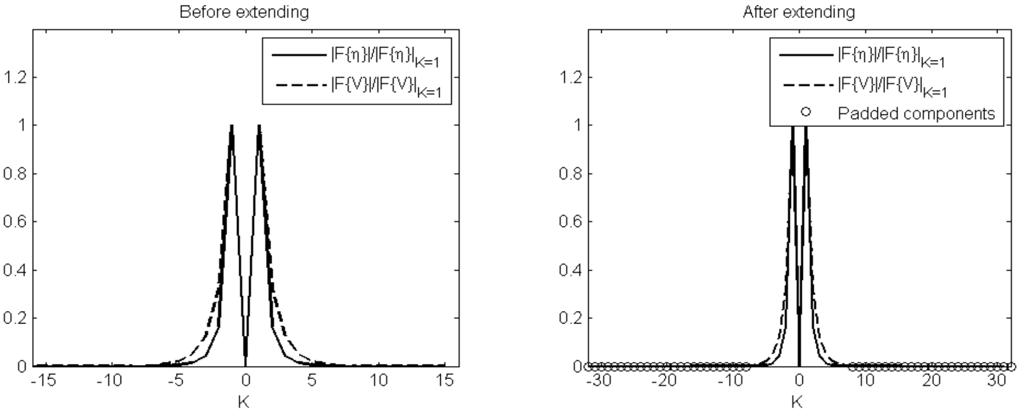

(a) Spectra of η and V

(b) Extend spectra of η and V

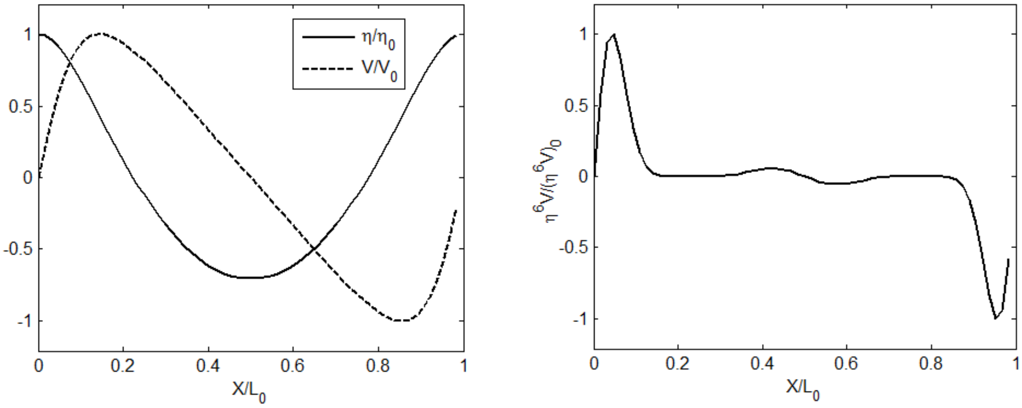

(c) Inverse to physical space

(d) Estimate $V\eta^6$

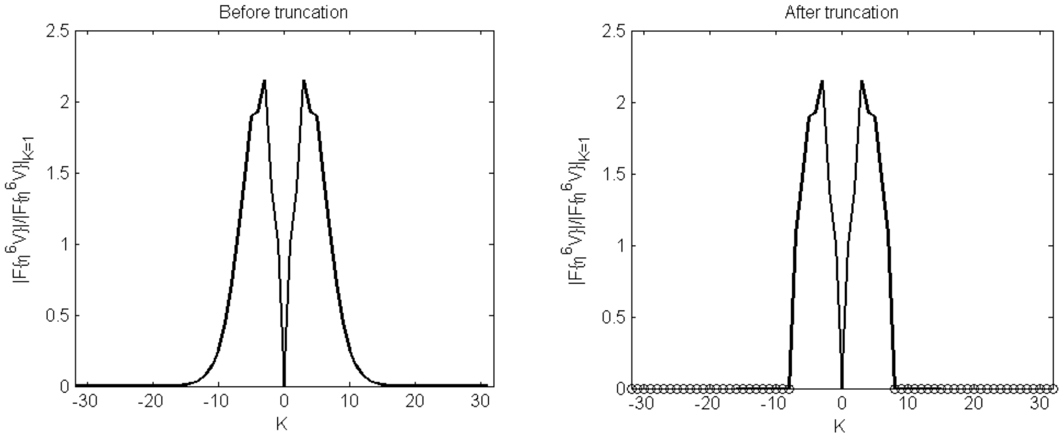

(e) To spectral space

(f) Truncate spectrum of $V\eta^6$

Figure 5.2.4 Illustration of TAA3

5.2.2 Comparisons of different anti-aliasing techniques

In order to show which one of three anti-aliasing techniques yields better results, comparative studies have been carried out and some results are presented and discussed in this sub-section. For this purpose, the convolution parts of V_3 and V_4 for the Stokes waves of different wave steepness within a domain of $L \times L$ at the first time step will be evaluated using the above three anti-aliasing techniques and their results will be compared. The aliasing error will be estimated by

$$Error\{V_3 + V_4\} = \frac{\int \left(\left| V_{3,C}^{(N=2^n)} - V_{3,C}^{(N=2^9)} \right| + \left| V_{4,C}^{(N=2^n)} - V_{4,C}^{(N=2^9)} \right| \right) d\boldsymbol{X}}{\int |V| d\boldsymbol{X}} \tag{5.2.1}$$

where $V_{3,C}^{(N=2^n)}$ and $V_{4,C}^{(N=2^n)}$ are the convolution parts of V_3 and V_4 with resolution of $2^n \times 2^n$ estimated by using one of three anti-aliasing techniques. $V_{3,C}^{(N=2^9)}$ and $V_{4,C}^{(N=2^9)}$ are the convolution parts of V_3 and V_4 computed by using a resolution of $2^9 \times 2^9$, which is tested to be the resolution to eliminate the aliasing error without use of any anti-aliasing technique. The aliasing errors corresponding to three methods are plotted in Figure 5.2.5. It can be seen that the aliasing errors decrease with increase of resolution but they are larger for larger steepness. The TAA3 clearly over-performs relative to the other two techniques for stronger nonlinear waves, such as these with $\varepsilon = 0.3$ and 0.42. In these cases, the error of TAA3 is less than 10^{-6} at the resolution of $2^6 \times 2^6$ but the errors of other two is larger than 10^{-6} at the resolution.

To further demonstrate the fact, Figure 5.2.6(a) presents the minimum resolution required to achieve the results with error less than 10^{-6} by the three different techniques. For the same purpose, Figure 5.2.6 (b) gives the ratio of CPU time corresponding to the three techniques for evaluating the convolution parts of V_3 and V_4 in one time step. The ratio is estimated by dividing the value of the method with TAA1 or TAA2 by that of TAA3. The results clearly indicate that the TAA3 is superior to the others in suppressing the aliasing errors, in particular in estimating the higher order convolutions.

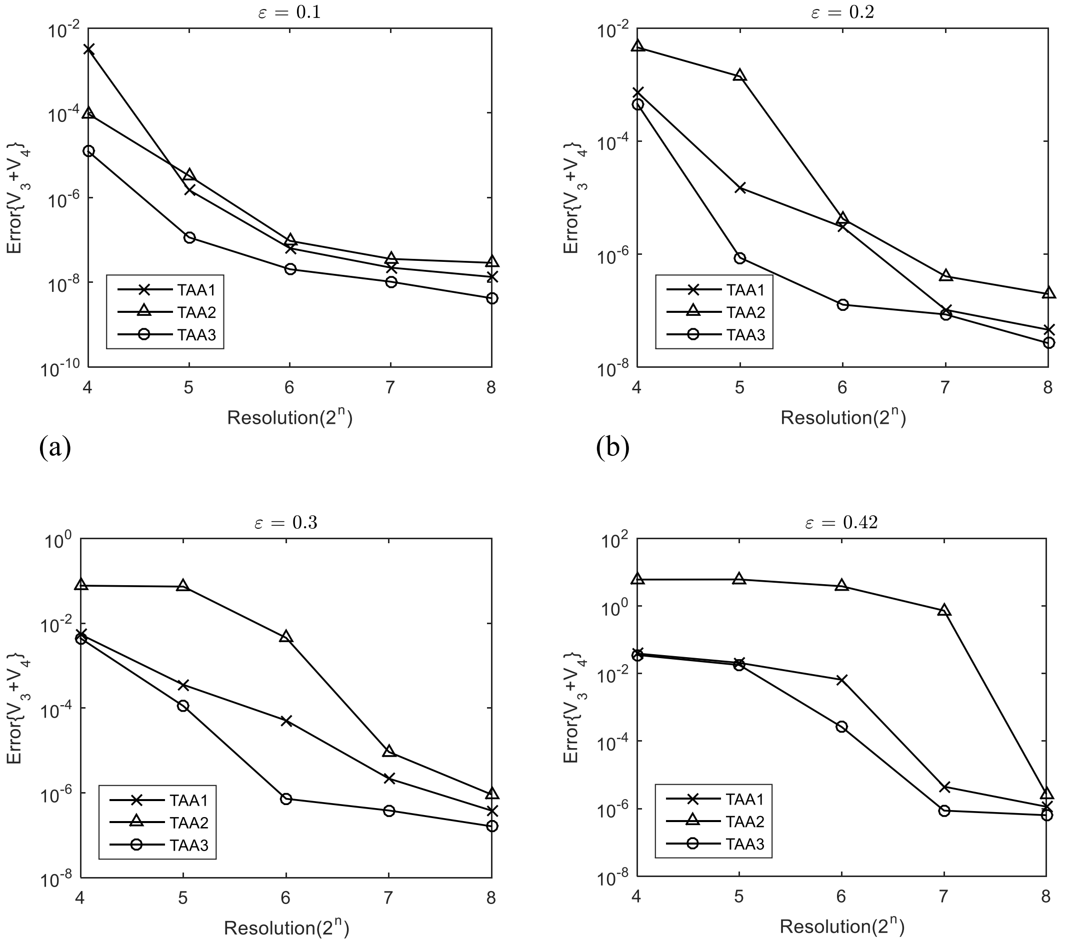

(a) (b)

(c) (d)

Figure 5.2.5 Aliasing error against different resolutions for different steepness

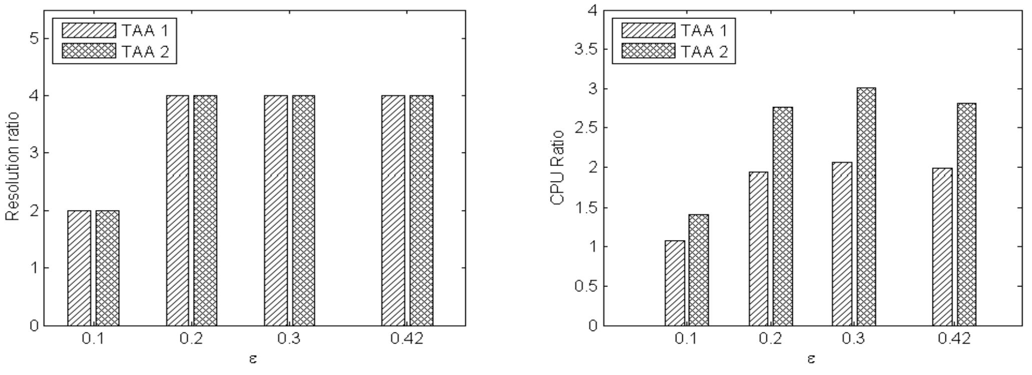

(a) Resolution ratio against steepness (b) CPU ratio against steepness

Figure 5.2.6 Resolution and CPU ratio to achieve $Error\{V_3 + V_4\} < 1E-6$ for different values of steepness

5.3 Techniques for determining the critical surface slope

As indicated in Table 3.4.1, one may use one of three schemes to evaluate the velocity V. Fructus, et al. (2005) used the Scheme 1 while Grue (2010) employed Scheme 2 excluding the estimation of the integral parts. Although more convolution terms need to be evaluated in Scheme 2 than Scheme 1, Scheme 2 is expected to be much more efficient as there is no need of evaluating integral parts. To demonstrate this, the ratio of CPU time taken by Scheme 1 to that of Scheme 2 is plotted in Figure 5.3.1. The results in this figure are obtained by using the two schemes to model the similar waves in Figure 5.1.4 up to a time of $1000T_0$ in a domain of $2L \times 2L$ for different steepness. The resolution is selected such that $Err_1 < 2.5\%$. One can see that Scheme 2 is more than 100 time faster when $\varepsilon \geq 0.25$. It is noted that the numerical results show that $|D|_{max} < 0.5$ for $\varepsilon \leq 0.42$ in the cases associated with Figure 5.3.1. In other words, one can just use Scheme 2 to achieve satisfactory results for cases like these. Note that the sudden drop of CPU ratio for $\varepsilon = 0.36$ is because of the decrease in resolution ratio.

However, it is not always true. This can be understood from the fact that Scheme 2 is derived from Scheme 1 by expanding V_3 and V_4 up to the seventh order (ε^7) as shown in APPENDIX A. Based on this, Scheme 2 should be only accurate when the maximum gradient of the free surface is less than a critical value D_c (D has been defined in section 3.4.2). So far, such a critical value has not been quantified, which will be discussed in the following sections.

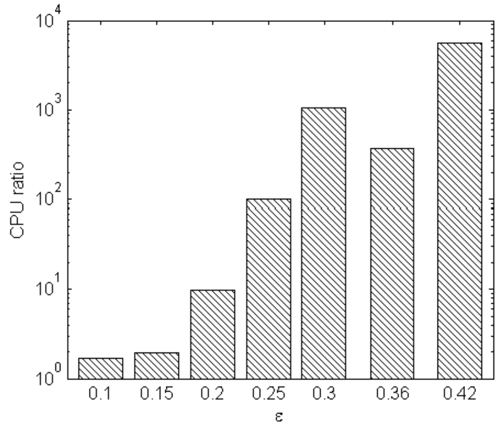

Figure 5.3.1 Ratio of CPU time taken by Scheme 1 to that of Scheme 2 for $\mathrm{Err}_1\{\varphi\} < 2.5\%$

5.3.1 Estimation of magnitude of D_c

As has been noted in section 3.4.2, D represents the local gradient of waves and thus its maximum should have a similar order to the wave steepness ε if the wave does not reach the overturning point. In order to estimate the magnitude of D_c, one may assume that $|D|_{max} \approx \varepsilon$. In addition, the magnitude of D_c must be related to the highest order of differences between Scheme 2 and Scheme 3 or Scheme 1. From Table 3.4.1, the differences come from ignoring $V_{3,I}$ and $V_{4,I}$. From Eq.(3.4.23) and (3.4.24), the leading order of $V_{3,I}$ and $V_{4,I}$ are $O(\varepsilon^8)$ and $O(\varepsilon^9)$ respectively. As the former is one order higher than the latter, the magnitude of D_c may be estimated by using only $V_{3,I}$. To give more specific information about the order of $V_{3,I}$, it has been expanded in APPENDIX A to

$$V_{3,I} = V_3^{(3)} + O(\varepsilon^{10}) \tag{5.3.1}$$

where $V_3^{(3)}$ is given in Equation (A. 8). To be more specific, considering a simple wave described by $\eta = \varepsilon cosX$ and $\tilde{\phi} = \varepsilon sinX$, for which $V = \varepsilon sinX$. For this wave, one obtains, as shown in Equation (A. 17),

$$O(V_{3,I}) \sim O\left(V_3^{(3)}\right) \sim \frac{69}{2560}\varepsilon^8 \sin(2X) \tag{5.3.2}$$

Thus

$$O\left(\frac{V_{3,I}}{V}\right) \sim \frac{69}{2560}\varepsilon^7 \tag{5.3.3}$$

Generally, the error due to ignoring the $V_{3,I}$ and $V_{4,I}$ may be estimated by

$$Error_1\{V\} = \frac{max\left|V_3^{(3)}\right|}{max|V|} \tag{5.3.4}$$

It is clear that the order of $Error_1\{V\}$ is $O(\varepsilon^7)$. For the simple wave, it follows that

$$Error_2\{V\} \sim \frac{\frac{69}{2560}\varepsilon^8}{\varepsilon} = \frac{69}{2560}\varepsilon^7 \approx \frac{69}{2560}|D|_{max}^7 \tag{5.3.5}$$

5.3.2 Values of D_c determined by numerical tests

In this subsection, tests will be carried out to further quantify the critical value D_c. To do so, the error of Scheme 2 is estimated by

$$Error_3\{V\} = \frac{\int\left|V^{(scheme\ 2)} - V^{(scheme\ 3)}\right|dX}{\int\left|V^{(scheme\ 3)}\right|dX} \tag{5.3.6}$$

where $V^{(scheme\ 3)}$ is the profile of the velocity V calculated by using Scheme 3 at an instant, which takes into account of all the terms, and $V^{(scheme\ 2)}$ is the profile of velocity V computed by Scheme 2 at the corresponding instant excluding the integral parts. The simulation is first carried out by using Scheme 3, and the data of V, $\tilde{\phi}$ and η at all time steps are saved in files.

From these data, $|D|_{max}$ is computed for every time step. Then Scheme 2 is employed to estimate the error in Eq.(5.3.6), corresponding to the value of $|D|_{max}$ at each time step. Using the information, one can find the critical value D_c for a specified error. The results for three cases will be presented below.

The first case is about a Stokes wave steepened by a moving pressure on the surface. The initial wave of $\varepsilon = 0.15$ is obtained in the same way as for Figure 5.1.4. The steepness is relatively small initially, but will be steepened by the moving pressure, so that the local maximum surface gradient $|D|_{max}$ will increase gradually and the resulted error can be monitored. The domain covers one wave length ($L \times L$) and is resolved by $2^7 \times 2^7$ points. The duration of the simulation is 5 wave periods (T_0). The pressure distribution on the free surface is specified as

$$p(X,T) = \begin{cases} -p_0 \sin(2\pi T/T_0)\sin(X - CT) & ,\ 0 \le T \le T_0/2 \\ 0 & ,\ T > T_0/2 \end{cases} \tag{5.3.7}$$

where $p_0 = 0.25$ is the amplitude of the pressure and $C = L/T_0$ is the wave phase speed. The wave profiles at some time steps ($T/T_0 = 0.1$, 0.4 and 0.88) obtained by Scheme 3 are shown in Figure 5.3.2(a). It demonstrates that the free surface elevation gradually becomes steeper and steeper. The errors in Eq.(5.3.4), (5.3.5) and (5.3.6) corresponding to the values of $|D|_{max}$ are presented in Figure 5.3.2 (b). It shows that the errors estimated for Scheme 2 using Eq.(5.3.4) and (5.3.6) is less than 2×10^{-4} and does not increases significantly when $|D|_{max} \le 0.5$, while it grows exponentially when $|D|_{max}$ exceeds 0.5. In addition, the errors of Scheme 2 have the same trend as the expression of $\frac{69}{2560}|D|_{max}^7$ in Eq.(5.3.5). Furthermore, the errors estimated by using Eq.(5.3.4) are closely correlated with these of Eq.(5.3.6).

To further show the relationship between the error and $|D|_{max}$, the similar results for $p_0 = 0.22$ and 0.3 are given in Figure 5.3.3(a) and (b), which are consistent with the observation in Figure 5.3.2.

The second case tested is related to a 2D Benjamin-Feir instability (Benjamin & Feir, 1967). To do this test, the wave with $\varepsilon = 0.22$ generated as in Figure 5.1.4 is disturbed by

$$\delta\eta = 0.105\varepsilon cos\left(\frac{9}{8}X - \frac{\pi}{4}\right) + 0.105\varepsilon cos\left(\frac{7}{8}X - \frac{\pi}{4}\right) \tag{5.3.8}$$

The domain covers $8L \times L$ which is resolved by $2^{10} \times 2^7$ points. The duration of the simulation is about 30 wave periods. All the setup parameters are the same as in (Clamond & Grue, 2001). The free surface profiles at $T/T_0 = 0$ and $T/T_0 = 21.34$ obtained by Scheme 3 are shown in Figure 5.3.4(a). The profile at $T/T_0 = 21.34$ from (Clamond & Grue, 2001), denoted by small circles, is also given and has a little visible difference from that calculated by the method of this chapter. The errors of Scheme 2 estimated using Eq.(5.3.6) are less than 2×10^{-4} without significant increase when $|D|_{max} \leq 0.5$, while they grow exponentially when $|D|_{max}$ exceeds 0.5 and agrees quite well with that given by Eq.(5.3.4) and (5.3.5).

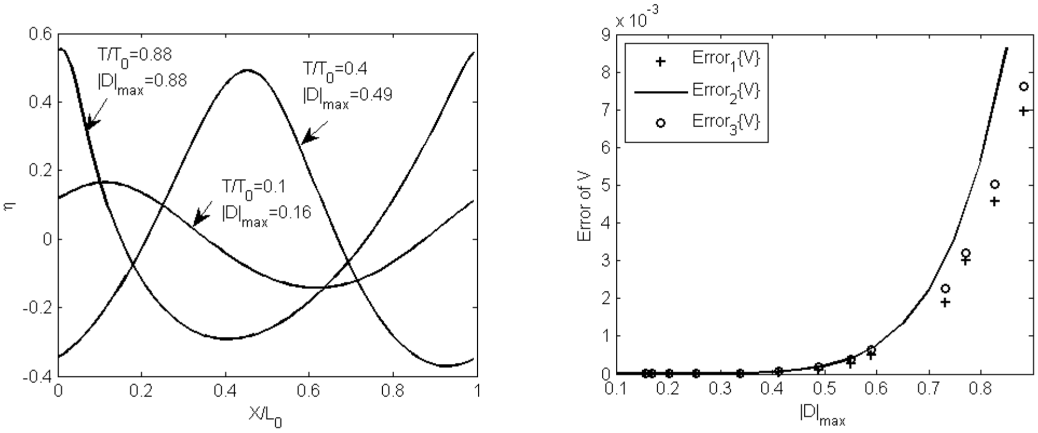

(a) $p_0 = 0.25$ (b) $p_0 = 0.25$

Figure 5.3.2 Wave profiles at different instants (a) and numerical error against maximum gradient (b) for $p_0 = 0.25$

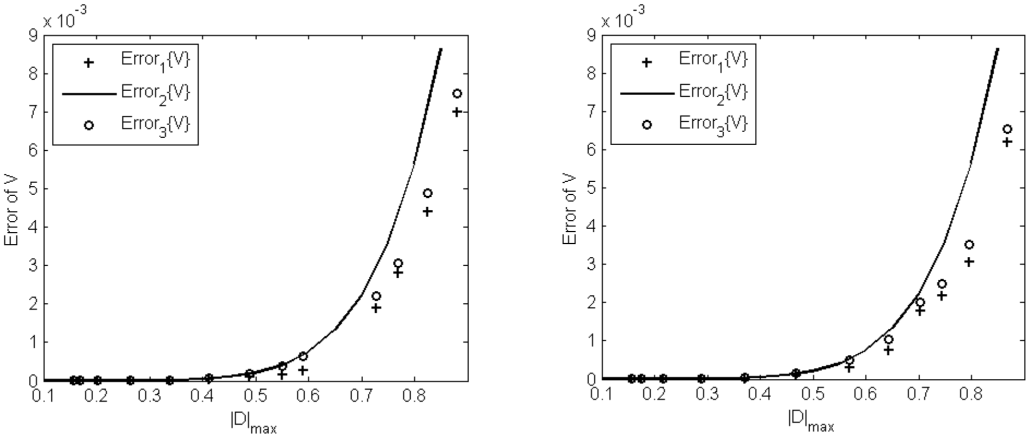

(a) $p_0 = 0.22$ (b) $p_0 = 0.3$

Figure 5.3.3 Numerical error against maximum gradient for different pressure amplitude

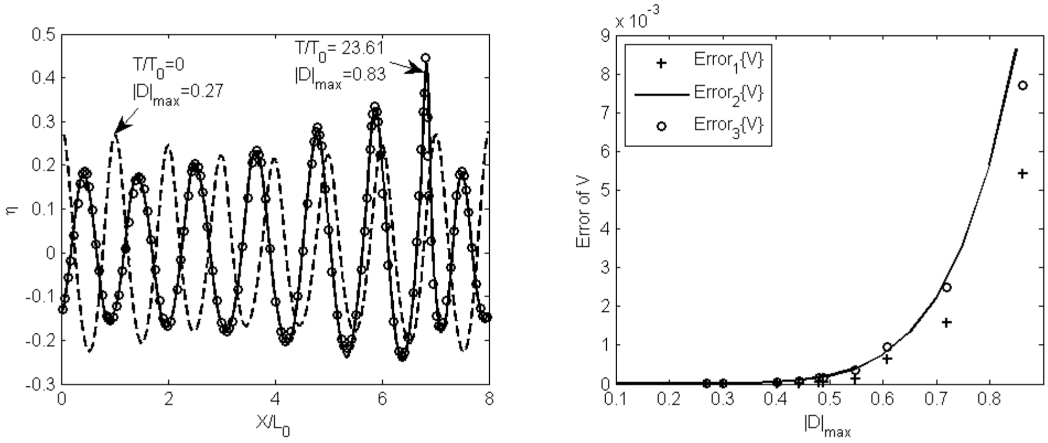

(a) Wave profiles

(b) Error against $|D|_{max}$

Figure 5.3.4 Results for Benjamin-Feir instability

The third case considered is about a wave of $\varepsilon = 0.2985$ generated as in Figure 5.1.4 but perturbed by a directional side-band waves

$$\delta\eta = \frac{0.05\varepsilon}{2}[sin(\boldsymbol{K_1}\cdot\boldsymbol{X}) + sin(\boldsymbol{K_2}\cdot\boldsymbol{X})] \tag{5.3.9}$$

where $\boldsymbol{K_1} = (3/2, 4/3)$ and $\boldsymbol{K_2} = (3/2, -4/3)$. The computational domain covers $2L \times 1.5L$ on transversal and longitudinal direction and is resolved by 2^8×2^8 points. The duration of the simulation is 18 wave periods. During the simulation, the waves grow into horse-shoe pattern eventually at $T/T_0 = 17.8$, as shown in Figure 5.3.5 (a). The error of Scheme 2 is shown on the right in Figure 5.3.5 (b). This again indicates that the error is insignificant when $|D|_{max} \leq 0.5$.

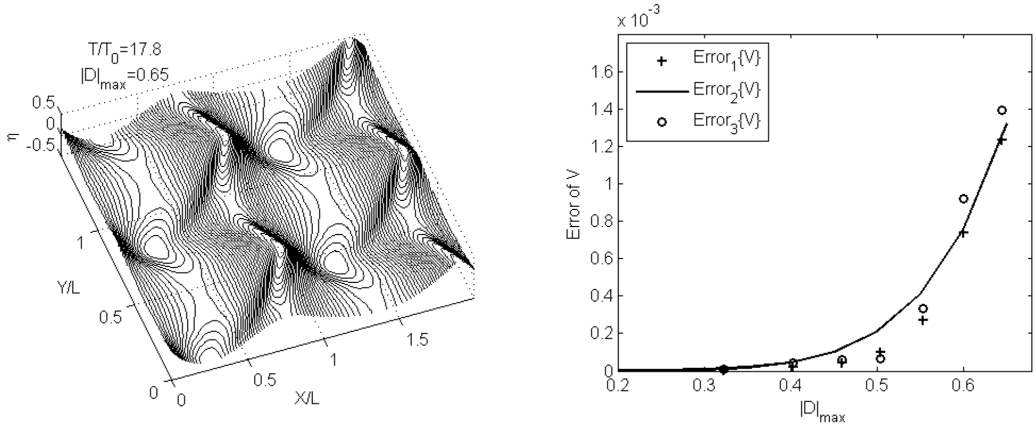

(a) Wave surface snapshot

(b) Error against $|D|_{max}$

Figure 5.3.5 Results for horse-shoe wave pattern

All the above cases for different kinds of wave evidence that one may take 0.5 as the critical value (D_c) if the error of 2×10^{-4} is acceptable, under which Scheme 2 may be applied with ignoring the integral parts in the velocity V. In other words, making $D_c = 0.5$ can guarantee the error due to neglecting the integration part be less than 2×10^{-4}. They evidence also that Eq.(5.3.4) and (5.3.5) give a good estimation to the error of Scheme 2, though the former is derived using a higher order term and the latter using very simple waves. Eq. (5.3.4) is more general than Eq. (5.3.5) as the former is not based on specific waves. In practice, one may take $D_c = 0.5$ or use Eq. (5.3.5) to determine D_c for a specified error. More generally, one may numerically estimate the error by using Eq. (5.3.4). If using this way, the condition of $|D|_{max} \leq D_c$ in flow chart shown in Figure 3.4.2 must be replaced by $Error_1\{V\} \leq Error_c$, where $Error_c$ is the tolerant error.

5.4 Overall efficiency of the ESBI

Up to now, three new techniques have been discussed in section 5.1, 5.2 and 5.3 respectively. They are developed in order to accelerate the computation of the SBI method originally proposed in (Fructus, et al., 2005) and (Grue, 2010). In this section, the overall efficiency of the improved method, which is named as the Enhanced Spectral Boundary Integral (ESBI) method, equipped with the de-singularity technique for weakly singular integrals, the anti-aliasing technique and the mixed scheme (Figure 3.4.2) will be discussed. For this purpose, the convergent properties and CPU time of the method in (Fructus, et al., 2005) and the ESBI will be compared. Both methods are employed to simulate the waves similar to that in Figure 5.3.5 but with different initial steepness, i.e, $\varepsilon = 0.1$, 0.2 and 0.3, respectively. For each of the cases, different resolutions are used, which are $2^5 \times 2^5$, $2^6 \times 2^6$, $2^7 \times 2^7$ and $2^8 \times 2^8$. The simulation is carried out until $T/T_0 = 18$.

For this case, Fructus, et al. (2005) presented a quantitative result of the following ratio for $\varepsilon = 0.2985$

$$\Psi_\epsilon = \frac{|F\{\eta\}|_{(\boldsymbol{K}=(3/2,4/3),T)}}{|F\{\eta\}|_{(\boldsymbol{K}=(1,0),T=0)}} \tag{5.4.1}$$

where $|F\{\eta\}|_{(\boldsymbol{K}=(3/2,4/3),T)}$ is the value of the spectrum at a time T corresponding to the first disturbed term with $\boldsymbol{K} = (3/2, 4/3)$ in Eq.(5.3.9). Their result is re-produced in Figure 5.4.1. A code based on the method in (Fructus, et al., 2005) is also programmed, which will be referred to as the Fructus method and used to compute the same case. Both results are compared with the result from the current enhanced method in the figure. The resolution used for this case is $2^8 \times 2^8$. It can be seen that the present method produces almost the same result as the Fructus method. However, the maximum error between the numerical results calculated here and the data provided by (Fructus, et al., 2005) is about 9.4%, and the error at the end of the simulation is about 0.2%. The main reason would be due to difference in determining of time steps. The specific equation for estimating the error related to the adaptive step, like Eq.(3.4.8), was not given in (Fructus, et al., 2005). The time step may be different if the method for estimating the error is not same as Eq.(3.4.8). Nevertheless, the results by using both the Fructus method and ESBI are consistent with the data in (Fructus, et al., 2005), which indicates that the numerical code for the Fructus method is validated and can be used for comparisons.

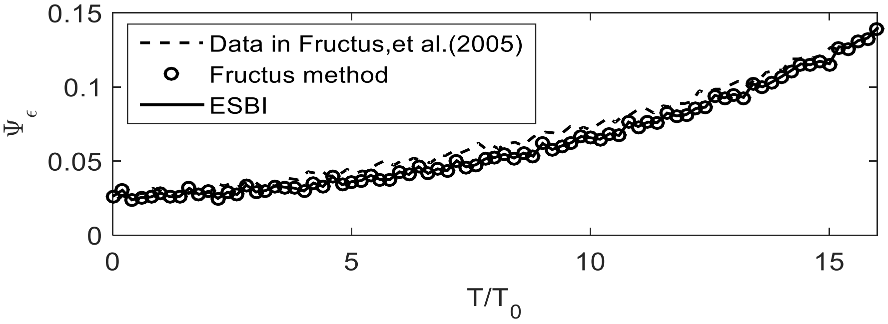

Figure 5.4.1 Evolution of perturbation components of $\boldsymbol{K} = (3/2, 4/3)$

The free surface profiles at three sections ($Y = 3L_0/4$, $X = L_0$ and $X = 4Y/3$) obtained by the code based on the Fructus method and the ESBI are shown in Figure 5.4.2. It shows no visible difference between the methods. Their quantitative difference is of $\int(|\eta_1 - \eta_2|)d\boldsymbol{X}/\int|\eta_2|d\boldsymbol{X} \approx 0.2\%$, where η_1 is the free surface elevation at $T/T_0 = 18$ obtained from the Fructus method and η_2 is that from the ESBI, both for resolution of $2^8 \times 2^8$. This demonstrates that both the methods will produce almost the same results when the resolution is sufficiently high.

However, their convergent rate may be different. To examine this, the error of the wave elevation is defined as

$$Error_2\{\eta\} = \frac{\int(|\eta^{(N=2^n)} - \eta_B|)d\boldsymbol{X}}{\int|\eta_B|d\boldsymbol{X}} \tag{5.4.2}$$

where $\eta^{(N=2^n)}$ is the solution obtained by using a method with resolution $2^n \times 2^n$ at $T/T_0 = 18$ and η_B is the solution with sufficiently high resolution. Here η_B is the benchmark selected as that for Figure 5.3.5, i.e., by using resolution $2^8 \times 2^8$. The errors of two methods corresponding to different initial steepness are plotted in Figure 5.4.3, together with the lines representing $(\Delta X)^s$ where ΔX denotes the element size and s represents the convergent rate. It shows that the convergent rate of the ESBI is closed to the fourth order for all the cases.

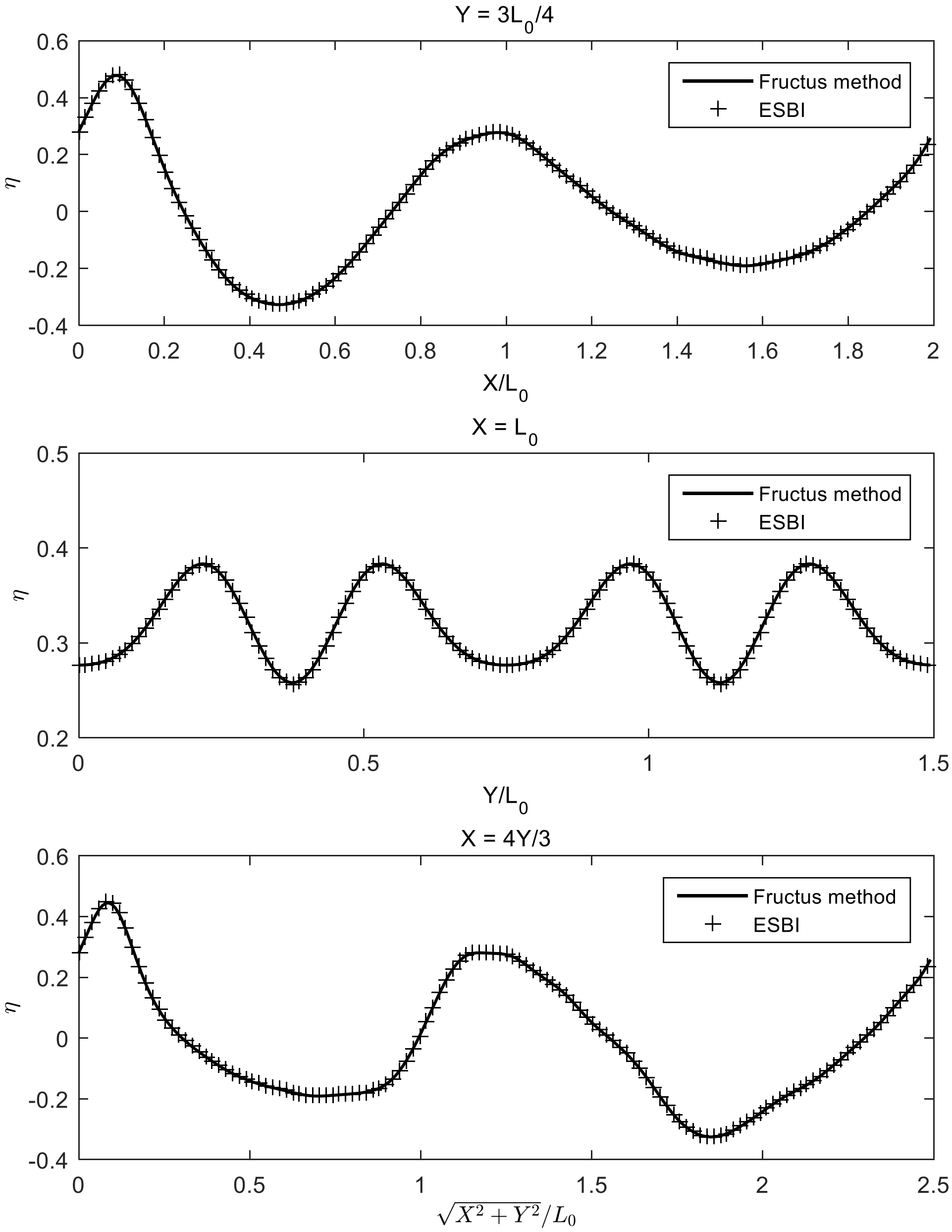

Figure 5.4.2 Free surface profiles at different section for $\varepsilon = 0.3$ at $T/T_0 = 18$

In addition, the CPU time used by the two methods to achieve the results with error less than 0.2% is also investigated. Figure 5.4.4 depicts the ratio of the CPU time used by the Fructus method to that of the ESBI. It indicates that for waves with moderate steepness ($\varepsilon \leq 0.1$), the CPU time of both the methods is similar. When the steepness increases, the advantage of the ESBI over the Fructus method is obvious. For instance, in the case of $\varepsilon = 0.2985$, the ratio is more than 35. Of course, if the requirement on the accuracy is not so high, the CPU time ratio may not be thus large. The wave profiles are examined with different errors. The profiles along the transversal direction corresponding to different error values are shown in Figure 5.4.5. It can be seen that the profile with an error of about 0.6% calculated by Eq.(5.4.2) would be quite different. The error of about 0.2% is needed to be consistent with the benchmark.

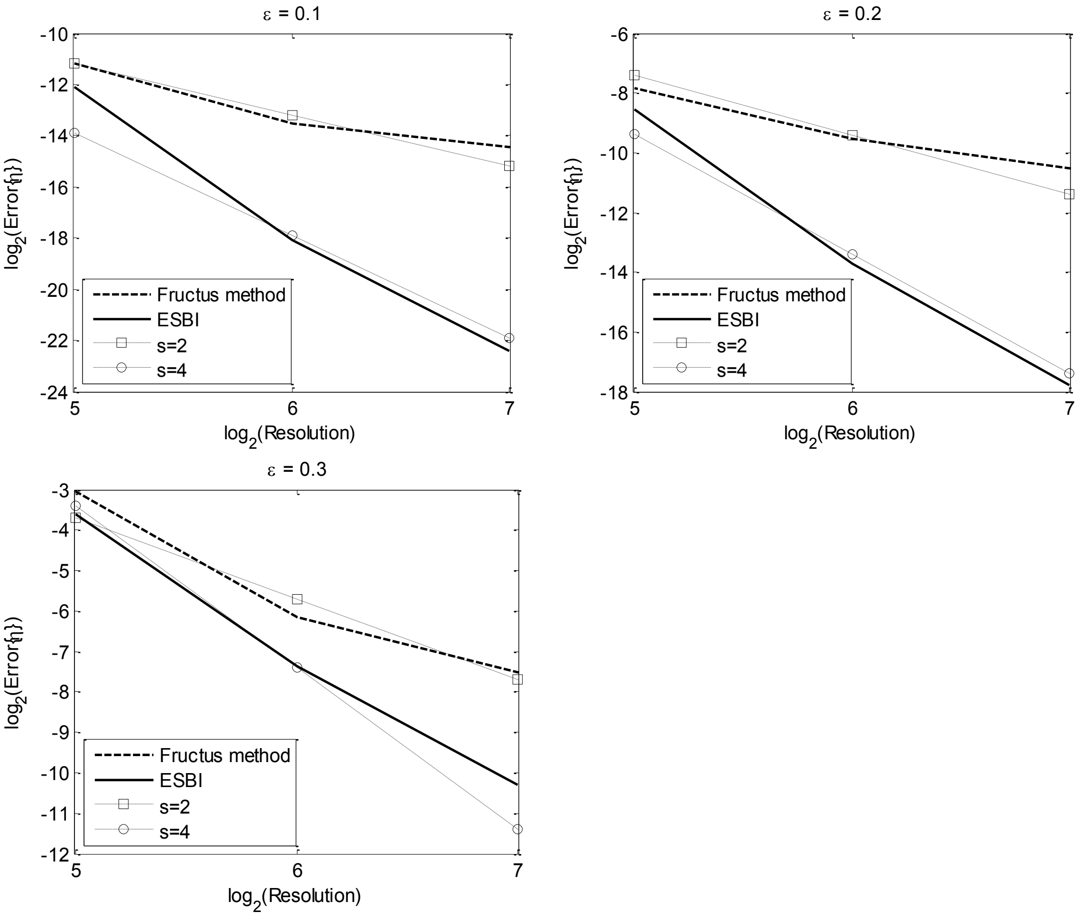

Figure 5.4.3 Convergent rate of Fructus method and ESBI for $\varepsilon = 0.1$, 0.2 and 0.3

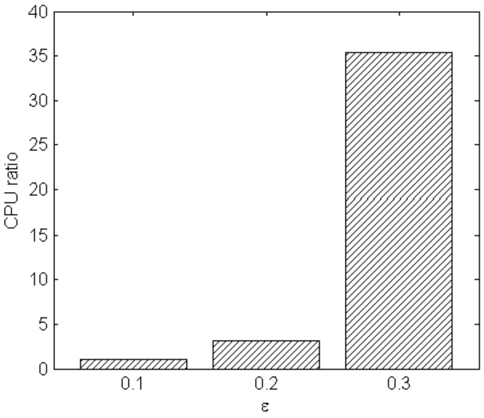

Figure 5.4.4 CPU time ratio against steepness at error less than 0.2%

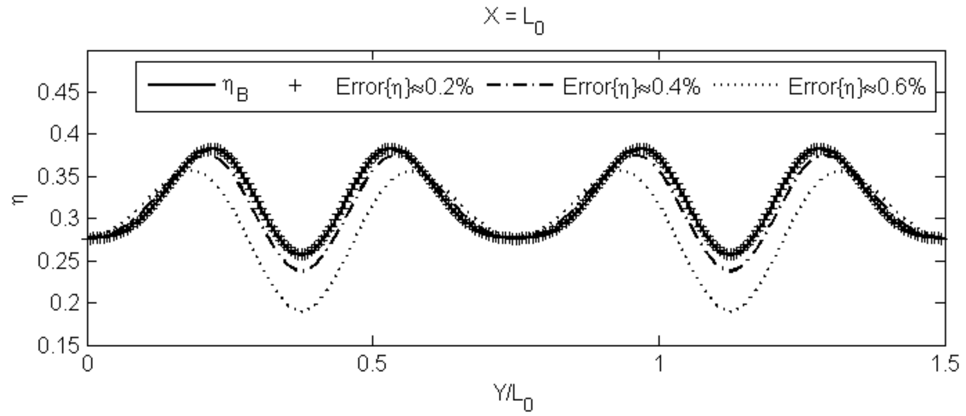

Figure 5.4.5 Profiles corresponding to different errors for $\varepsilon = 0.3$ at $T/T_0 = 18$

5.5 Discussion

This chapter reveals the derivation of the Enhanced Spectral Boundary Integral model, i.e., the ESBI. It is reported that the ESBI has significantly improved the computational efficiency compared with the original method suggested by Fructus, et al. (2005). Based on the numerical tests, the ESBI method equipped with the techniques suggested in this chapter can effectively accelerate the computation, in particular in the cases with strong nonlinearity. In some cases, it has been observed to be more than 35 time faster than the Fructus method.

6 THE HYBRID MODEL

The techniques used to propose the hybrid model are illustrated here, as well as the numerical examples for validating the model.

Table 6.0.1 Short summary of the three models

	ENLSE-5F	QSBI	ESBI
Efficiency	Super-fast. Most efficient among the three models.	Very fast. Efficiency between the ENLSE-5F and ESBI.	Fast. Least efficient among the three models
Accuracy	Accurate for small steepness and narrow spectrum waves. Least accurate among the three models	Accurate for small and moderate steepness waves. Accuracy between the ENLSE-5F and ESBI	Accurate for small, moderate and large steepness waves. Most accurate among the three models

Three models, i.e., ESBI, QSBI and ENLSE-5F, are selected and summarized in Table 6.0.1. The ESBI is the most accurate among the three as it is a fully nonlinear model without ignoring any necessary terms. Although QSBI only gives the solution of vertical velocity to the third order, the boundary conditions and governing equations remain to be fully nonlinear. There will not be significant difference between the ESBI and QSBI when the wave steepness is not high. The ENLSE-5F like other NLSE models is derived from simplified boundary conditions and subjected to limitations on both steepness and spectrum width. So the ENLSE-5F is the least accurate model among all. On the other hand, the ENLSE-5F is the most efficient model. Due to the complexities in solving for the vertical velocity, the QSBI costs more computational efforts than the ENLSE-5F. Furthermore, the involvements of higher order nonlinear parts in solving for the vertical velocity make the ESBI less efficient than the QSBI. In terms of accuracy there is a relation: ESBI > QSBI > ENLSE-5F while ENLSE-5F > QSBI > ESBI in terms of efficiency, where '>' means superior. Based on this, a hybrid method will be formed using the three methods, which is both accurate and efficient, making use of the advantages of the three methods. For this purpose, the three methods (ESBI, QSBI and ENLSE-5F) should be alternatively and automatically employed according to the instantaneous wave information. That is, the simulation of the hybrid method will involve the switching from one model to another. To do so, the following challenges need to be tackled.

a) The conditions need to be found out to determine which model is employed during simulation and when switching to others. This will be discussed in Section 6.2.

b) To employ the three models alternatively, exchanging data from the ENLSE-5F to the QSBI and ESBI is necessary, i.e., the outputs of the ENLSE-5F need to be transformed to the forms accepted by the QSBI and ESBI as their input. The solution obtained from the ENLSE-5F at each time step is the free surface envelope A. To use them as the input for the QSBI and ESBI, the expressions for the free surface elevation and velocity potential in terms of A needs to be derived. This will be discussed in Subsection 6.1.1.

c) On the other hand, in order to exchange data from the QSBI and ESBI to the ENLSE-5F, their outputs need to be transformed to the forms of the input for the ENLSE-5F, which will be resolved in Subsection 6.1.2.

6.1 Relationship between η and A

In order to couple the ENLSE-5F and QSBI/ESBI model, data exchange between these models is a necessary procedure. The outputs of ENLSE-5F at each time step is the space distribution of the complex free surface envelope A. The problem is that the surface elevation η and velocity potential ϕ are analytical expressions of B, which cannot be used directly. In order to prepare the data which could be directly passed to the QSBI/ESBI model, some work needs to be done in advance. On the other hand, the outputs of the QSBI/ESBI model at each time step only include the space distribution of the free surface elevation and velocity potential on the free surface, but A is unknown. In order to pass the data from the QSBI/ESBI model to the ENLSE-5F, A has to be estimated from η by numerical techniques, which will also be presented in the following contexts.

6.1.1 Transformation from A to η and ϕ

As can be seen from equations given previously, the solution of the ENLSE-5F is given in terms of envelop A, but η and ϕ are required to start the QSBI or ESBI. Therefore, there is a need to transform A to η and ϕ when switching from the ENLSE-5F simulation to the QSBI or ESBI simulations. According to Eq.(3.2.1) and (3.2.2), one just needs to estimate the harmonic coefficients A_2, A_3, B, B_1, B_2, B_3 and the term of $\bar{\eta}$. As shown in APPENDIX B, one has

$$A_2 = \frac{1}{2}A^2 - \frac{i}{2}A\frac{\partial A}{\partial X} + \frac{3}{8}A\frac{\partial^2 A}{\partial X^2} + \frac{1}{4}A\frac{\partial^2 A}{\partial Y^2} - \frac{3}{4}\left(\frac{\partial A}{\partial Y}\right)^2 \tag{6.1.1}$$

$$A_3 = \frac{3}{8}A^3 \tag{6.1.2}$$

$$B = F^{-1}\left\{\frac{-i}{\omega}F\left\{A + \frac{3}{8}|A|^2A\right\}\right\} \tag{6.1.3}$$

$$B_2 = -\frac{i}{2}A\frac{\partial^2 A}{\partial Y^2} + \frac{i}{2}\left(\frac{\partial A}{\partial Y}\right)^2 \tag{6.1.4}$$

$$\bar{\phi} = F^{-1}\left\{\frac{i}{2}\frac{\kappa}{K}F\{|A|^2\}\right\} \tag{6.1.5}$$

$$\bar{\eta} = F^{-1}\left\{-i\frac{\kappa}{K}F\left\{real\left(A^*\frac{\partial A}{\partial T}\right)\right\}\right\} - \frac{1}{16}\frac{\partial^2|A|^2}{\partial X^2} - \frac{1}{8}\frac{\partial^2|A|^2}{\partial Y^2} \tag{6.1.6}$$

and $B_3 = 0$. It is worth of noting that Eq.(6.1.3) is different from Hogan's formulation (1985), i.e., $B = -iA + \frac{1}{2}\frac{\partial A}{\partial X}$, which only considers the approximated linear evolution of ϕ and nonlinear effects are neglected. In contrast, Eq. (6.1.3) involves the nonlinear effects up to the third order. Therefore Eq. (6.1.3) is adopted in this study in order to accurately estimate the velocity potential. After all the harmonic coefficients above are evaluated, the surface elevation η and velocity potential ϕ are estimated by using Eq.(3.2.1) and (3.2.2).

6.1.2 Transformation from η to A

When switching the modelling from the QSBI or ESBI simulations to the ENLSE-5F simulations, one needs to obtain the expression for envelop A used for the input to the latter. That means that the spatial solution of the free surface elevation from the QSBI or ESBI is needed to transformed to the envelope A. In order to do so, Eq.(3.2.1) is rewritten as

$$\eta = \bar{\eta} + \eta_1 + \eta_2 + \eta_3 \tag{6.1.7}$$

where

$$\eta_1 = \frac{1}{2}\left(Ae^{i\theta} + c.c.\right),\ \eta_2 = \frac{1}{2}\left(A_2e^{2i\theta} + c.c.\right)$$
$$and\ \ \eta_3 = \frac{1}{2}\left(A_3e^{3i\theta} + c.c.\right) \tag{6.1.8}$$

are the first, second and third harmonics of the free surface elevation, respectively. The relationship between A and η_1 is established (APPENDIX C)

$$A = e^{-i(X-T)}\left(\eta_1 + F^{-1}\{\,sgn(\kappa)F\{\eta_1\}\}\right) \tag{6.1.9}$$

In addition, η_2, η_3 and $\bar{\eta}$ could be estimated with the help of Eq.(6.1.1), (6.1.2) and (6.1.6). However, it is the value of η that is given from the solution of the QSBI or ESBI instead of η_1, η_2, η_3 and $\bar{\eta}$. To overcome this dilemma, iterations are carried out for obtaining the solution A from η, which is graphically illustrated in Figure 6.1.1. It is noted that η and η_1 are in the same order, which are normally much larger than η_2, η_3 and $\bar{\eta}$, and so the iterative procedure starts from $\eta_1 = \eta$.

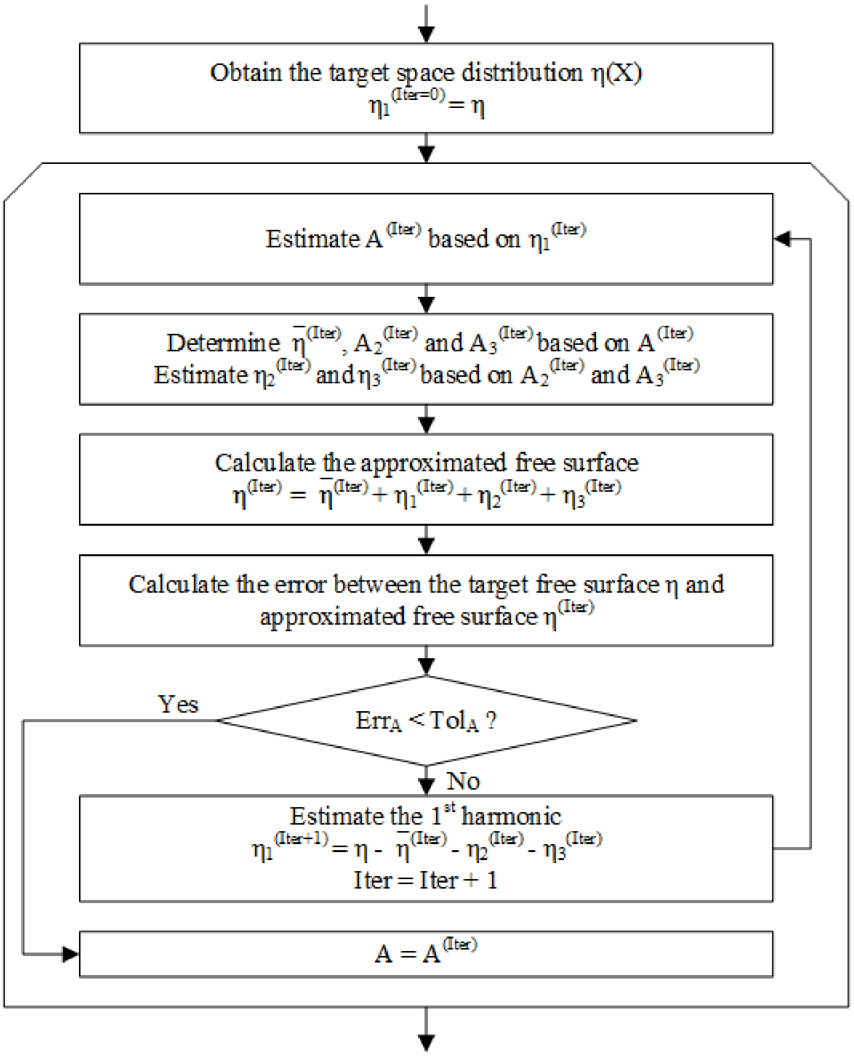

Figure 6.1.1 Flow chart of estimating the envelope A by iterations

The error represents the difference between the target surface η and the approximated surface $\eta^{(Iter)}$ is given as

$$Err_A = \frac{\int \left|\eta - \eta^{(Iter)}\right| d\boldsymbol{X}}{\int |\eta| d\boldsymbol{X}} < Tol_A \tag{6.1.10}$$

It is found that $Tol_A = 10^{-5}$ is enough to give very precise results.

6.2 Methodology for the timing control

In order to form a hybrid method, the three methods — ENLSE-5F, QSBI and ESBI need to be combined. To do so, the key thing is the conditions under which the simulation is switched from one to another. For this purpose, four conditions are introduced:

a) Condition 1: $Err_1 > Tol_1$, $|\eta(T)|_{max} > |\eta(T=0)|_{max}$ and $|\eta(T)|_{max} > |\eta(T - \Delta T)|_{max}$

b) Condition 2: $Err_1 \leq Tol_1$, $|\eta(T)|_{max} \leq |\eta(T=0)|_{max}$ and $|\eta(T)|_{max} \leq |\eta(T - \Delta T)|_{max}$

c) Condition 3: $Err_2 > Tol_2$

d) Condition 4: $Err_2 \leq Tol_2$

where

$$Err_1 = \frac{\max\{|\Psi_3 - \Psi_1|\}}{\max\{|A|\}} \tag{6.2.1}$$

$$Err_2 = \frac{max\left|V_3^{(1)}\right|}{max|V|} \tag{6.2.2}$$

The basic idea of the four conditions aforementioned is to measure the strength of the nonlinearities, i.e., the stronger the waves are, the larger Err_1 and Err_2 are. The first two conditions are used to control the switch between the ENLSE-5F and QSBI. If the waves keeps growing, and finally the steepness is larger than the initial steepness and $Err_1 > Tol_1$, Condition 1 is met and the waves are no longer weakly nonlinear, which means actions should be taken to replace the ENLSE-5F by using the QSBI. Vice versa, if Condition 2 is met, the ENLSE-5F will be recovered. Similarly, the last two conditions are used to control the switch between the QSBI and ESBI. If $Err_2 > Tol_2$, the nonlinearities become so strong that the QSBI should be replaced with the ESBI, and vice versa.

With the four conditions and the formulas for the errors above, the flow chart for the hybrid method is given in Figure 6.2.1. It shows that the procedure starts with ENLSE-5F for waves with small steepness; when Condition 1 is met (the wave being steep enough), FLAG will be assigned to be 2 and so the process will be switched to QSBI in the next time step; after the waves become steeper and so Condition 3 is met, the process will be switched to ESBI in the next time step. During the simulation, if the waves become less steep (or Condition 4 is met), FLAG will be assigned to be 2 from the ESBI and so the process will be switched back to QSBI, then may be to ENLSE-5F if Condition 2 is met. As can be understood, the switch is always through QSBI and there is no direct switch between the ENLSE-5F and the ESBI. It is noted that the process can start from any one of the three methods, as long as the initial value of FLAG is assigned properly. For example, if one knows that the wave spectrum is not narrow-banded and/or the wave steepness is quite large, the initial value of FLAG may be given as 3 and so the process will start from ESBI. Of course, the representation of the initial condition will be different if the starting method is different. Actually, the initial condition is usually given in terms of the free surface elevation and the velocity potential on the free surface as shown in (Wang & Ma, 2015a), which can be employed directly to start QSBI or ESBI. For start with ENLSE-5F, the initial condition information in terms of the free surface elevation and the velocity potential needs to be transformed to the wave envelope in the similar way to that discussed in subsection 6.1.2.

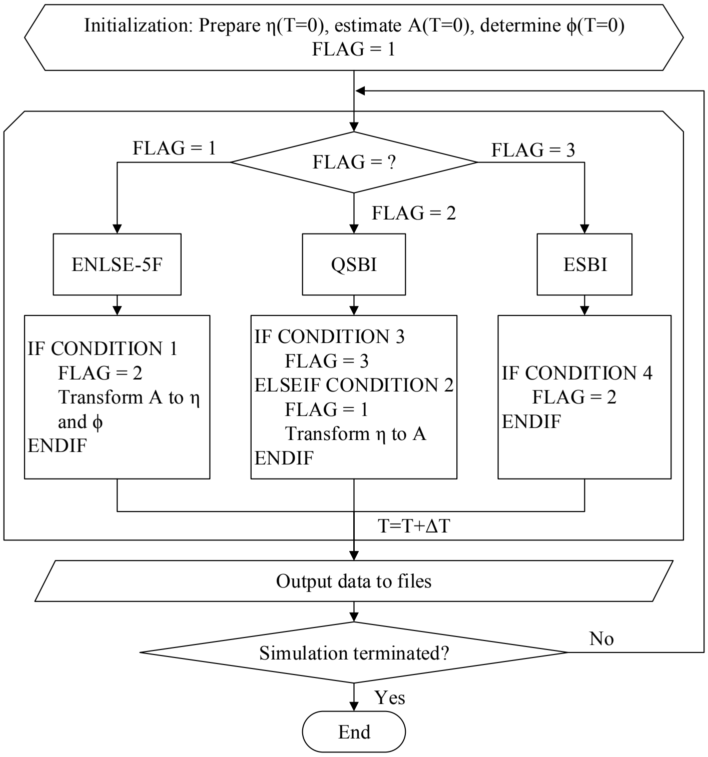

Figure 6.2.1 Flow chart of the numerical scheme for hybrid model

6.3 Effects of Tol_1 and Tol_2 by numerical simulations

In order to control the switch between the three models and guarantee the final results are acceptable, proper values for Tol_1 and Tol_2 need to be specified. Thus this section will discuss how the values for Tol_1 and Tol_2 are determined. For this purpose, numerical simulations of random waves in a two-dimensional domain of $128L_0$ and duration of $1000T_0$ will be performed by using the ENLSE-5F, QSBI and ESBI separately.

Two most frequently used spectra, JONSWAP and Wallops, will be considered. As well known, the JONSWAP spectrum is proposed for developing sea states (Hasselmann, et al., 1973) while the Wallops spectrum is more suitable for fully developed and decaying sea states (Huang, et al., 1981).

The JONSWAP spectrum in dimensionless form is given as (Goda, 2010)

$$S_J(k) = \frac{\alpha_J H_s^2}{2k^3} \exp\left[-\frac{5}{4}\left(\frac{1}{k}\right)^2\right] \gamma^{\exp\left[-\left(\sqrt{k}-1\right)^2/(2\varsigma^2)\ \right]} \tag{6.3.1}$$

where the wave number k has been non-dimensionalized by dividing the peak wave number k_0, $S_J(k)$ by multiplying k_0^5, $\alpha_J = \frac{0.0624(1.094-0.01915 ln\gamma)}{0.23+0.0336\gamma-0.185(1.9+\gamma)^{-1}}$, $\gamma \in [1,9]$ is the peak enhancement factor and

$$\varsigma = \begin{cases} 0.07, & k < 1 \\ 0.09, & k \geq 1 \end{cases}$$

The peak enhancement factor γ controls the width of the spectrum, and the larger γ is.

Meanwhile, the Wallops spectrum is reformulated by Goda (1999) and its dimensionless form follows as

$$S_W(k) = \frac{\alpha_W H_s^2}{2k^{(m+1)/2}} exp\left[-\frac{m}{4k^2}\right] \tag{6.3.2}$$

where $\alpha_W = \frac{0.06238 m^{(m-1)/4}}{4^{(m-5)/4}\Gamma[(m-1)/4]}\left[1 + 0.7458(m+2)^{-1.057}\right]$ and $m \in [5,25]$ is the width parameter. The spectrum becomes narrower when m increases.

To obtain the free surface spatial distribution as the initial condition, linear theory is employed. The linear theory admits that the irregular wave fields are the summation of limited wave components, i.e., Eq.(3.1.7) be replaced with

$$\eta(X,T) = \sum_{j=1}^{J} a_j \cos\left(k_j X - \omega_j T + \varphi_j\right) \tag{6.3.3}$$

where $a_j = \sqrt{2S\left(k_j\right)\Delta k}$, $S(k)$ can be JONSWAP $S_J(k)$, Wallops $S_W(k)$ or other specific spectra, and φ_j is random number evenly distributed in $[0,2\pi)$, k_j and ω_j are the wave number and frequency of the jth component and $\omega_j = \sqrt{k_j}$, J is the total number of the wave components. By using Eq. (6.3.3), the following condition

$$S\left(k_j\right) = \frac{a_j^2}{2\Delta k} \tag{6.3.4}$$

must be satisfied, which ensures that the resulting free surface elevation preserves the shape of the specific spectrum, so that the statistical properties of the spectrum can be well represented by the free surface elevation. One should note that by using Eq. (6.3.3), some randomness of the sea state may be lost, unless sufficiently large number of wave components is adopted, according to Tucker, et al. (1984). However, it can still be used for investigating the effects of Tol_1 and Tol_2, or illustrating the computational efficiency of the hybrid model.

Different combinations of the significant wave height and width parameter are tested based on both the JONSWAP and Wallops spectrum, in order to find proper resolution and tolerance for time marching. The domain covers 128 peak wave lengths and is resolved into 8192 points. The spectrum is discretized by using interval $\Delta k = 2\pi/L_d$ (L_d is the domain length). According to Goda (1999), a cut-off frequency chosen as the 1.5 to 2.0 times the peak frequency, is enough for engineering purpose, which is equivalent to the cut-off wave number $k_{max} = 2.25 \sim 4.0$. It should be noted that by using this cut-off frequency/wave number suggested by Goda (1999), a considerable amount of energy will be neglected when the bandwidth is wide. Thus the cut-off wave number $k_{max} = 8$ is chosen here. The errors of wave elevations will be estimated by

$$Err_\eta = \frac{\int |\eta - \eta_0| d\boldsymbol{X}}{\int |\eta_0| d\boldsymbol{X}} \tag{6.3.5}$$

where η is obtained by using a specific numerical model, and η_0 is the reference solution of wave elevations, which may be analytical solution or evaluated by using a relatively accurate method.

6.3.1 Investigation on effects of Tol_2

Firstly, numerical simulations are carried out based on both JONSWAP and Wallops spectrum with different significant wave heights and spectrum width parameters spanning in the practical range in order to find a proper value for Tol_2. Because this parameter only controls the switch between the QSBI and the ESBI, $FLAG = 2$ and $Tol_1 = 0$ are given during the initialization in the process described in Figure 6.2.1 in all the cases for testing effects of Tol_2.

The simulations are carried out to $1000T_0$ in a two dimensional domain of $128L_0$ for random waves. The errors in the wave elevation are estimated by Eq. (6.3.5), in which η_0 is the free surface at the end of the simulation obtained by only using the ESBI model and η is that obtained by using the hybrid model with different values of Tol_2 specified. The results are presented in Figure 6.3.1. From this figure, one can see that the trend of the error in wave elevations is very similar for the cases with different spectra, different significant wave heights and spectrum widths. It is also seen that for a fixed H_s and spectrum width, the error grows when Tol_2 increases. This is because that the larger value of Tol_2 allows more involvement of the QSBI during the simulation even when the QSBI is not quite accurate at some instance.

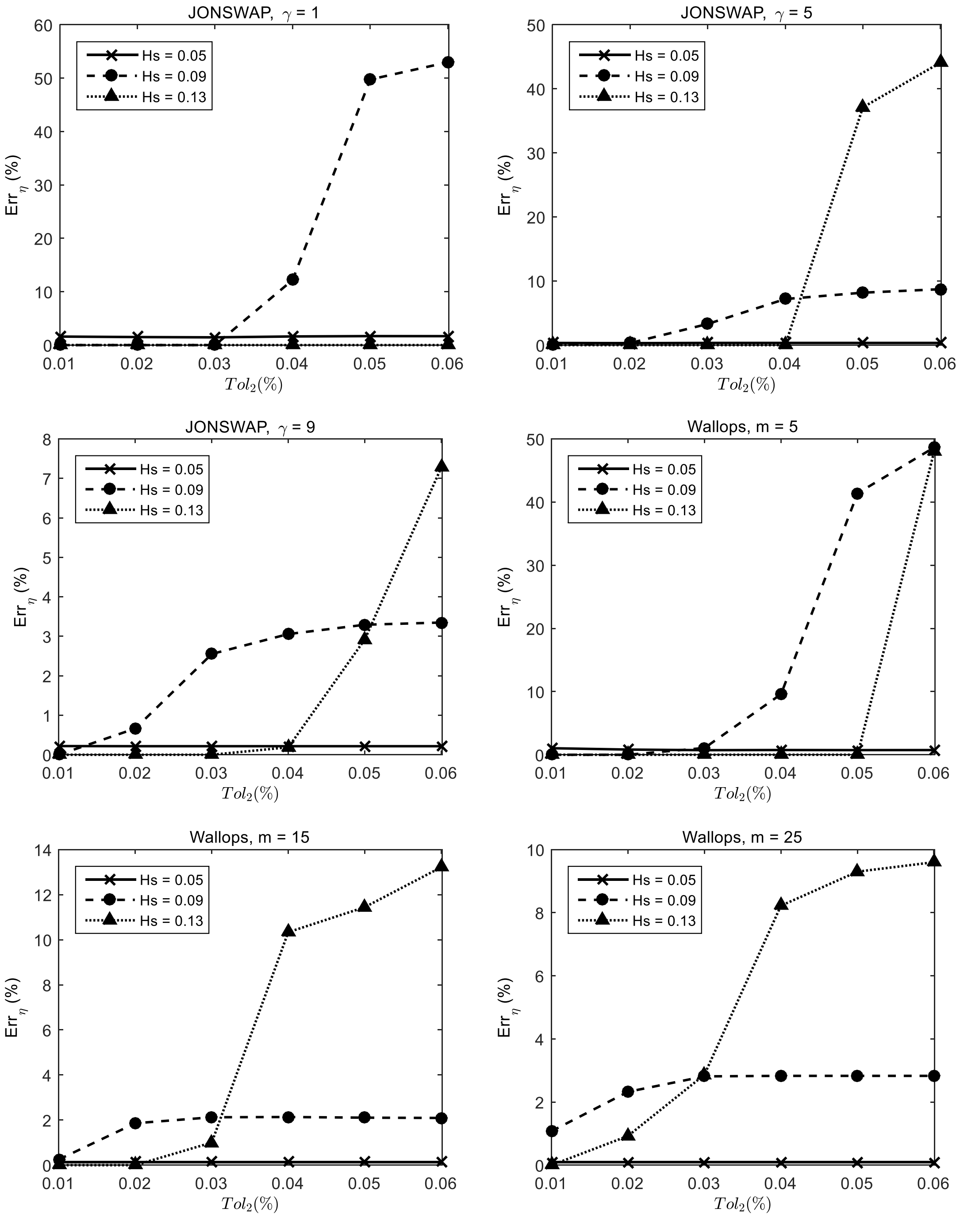

Figure 6.3.1 Err_η against Tol_2

For long time and large scale simulation, the error estimated by Eq. (6.3.5) can be accepted if it is less than 5%. Based on this and also other tests when preparing this chapter, $Err_\eta < 5\%$ is acceptable. Nevertheless, to be conserved and considering that the ENLSE-5F has not been involved yet, one may accept the error (Err_η) of the hybrid model to be not larger than 3% from the point of view of accuracy. On the other hand, it is also expected that the value of Tol_2 is as large as possible. That is because the larger the value of Tol_2 is, the longer the QSBI is involved and so more computational time it saves. By examining all the curves in Figure 6.3.1, one may find that the hybrid model with $Tol_2 \leq 0.03\%$ leads to the error (Err_η) of less than 3% in all the cases with different spectra, different significant wave heights and spectrum widths. Therefore, generally, $Tol_2 = 0.03\%$ will be adopted for controlling the switch between QSBI and ESBI.

6.3.2 Investigation on effects of Tol_1

By using $Tol_2 = 0.03\%$, the numerical tests in 6.3.1 are repeated in order to estimate the appropriate tolerance of Tol_1 to control the switch between the ENLSE-5F and the QSBI. In these tests, all three models are involved in calculating the cases with different values of Tol_1 specified.

The results for the error (Err_η) are shown in Figure 6.3.2. Again, it is found that the trend of the error in wave elevations is very similar for the cases with different parameters, and that for a fixed H_s and spectrum width, the error grows when Tol_1 increases. It is worth noting that for large tolerance, the error corresponding to small steepness is larger than that of large steepness. This is because the ENLSE-5F is involved in the simulation when H_s is small and Tol_1 is large. Large Tol_1 means that ENLSE-5F is involved in stronger nonlinear situations, which leads to more numerical error.

As all three models are involved in these tests, $Err_\eta < 5\%$ may be considered to be acceptable in terms of accuracy and efficiency. By examining Figure 6.3.2, one may find that the condition of $Err_\eta < 5\%$ can be satisfied if $Tol_1 = 0.02\%$. Therefore, 0.02% for Tol_1 can be used for controlling the exchange between the ENLSE-5F and QSBI.

It is worth of noting that the tolerance $Tol_1 = 0.02\%$ and $Tol_2 = 0.03\%$ are obtained based on large numbers of two dimensional (2D) simulations. However, it can be applied to three dimensional (3D) simulations as Eq. (6.2.1) and (6.2.2) can still be used. Next, numerical tests will be carried out to validate the hybrid model for both 2D and 3D simulations by using the tolerances obtained in this section for switching between models.

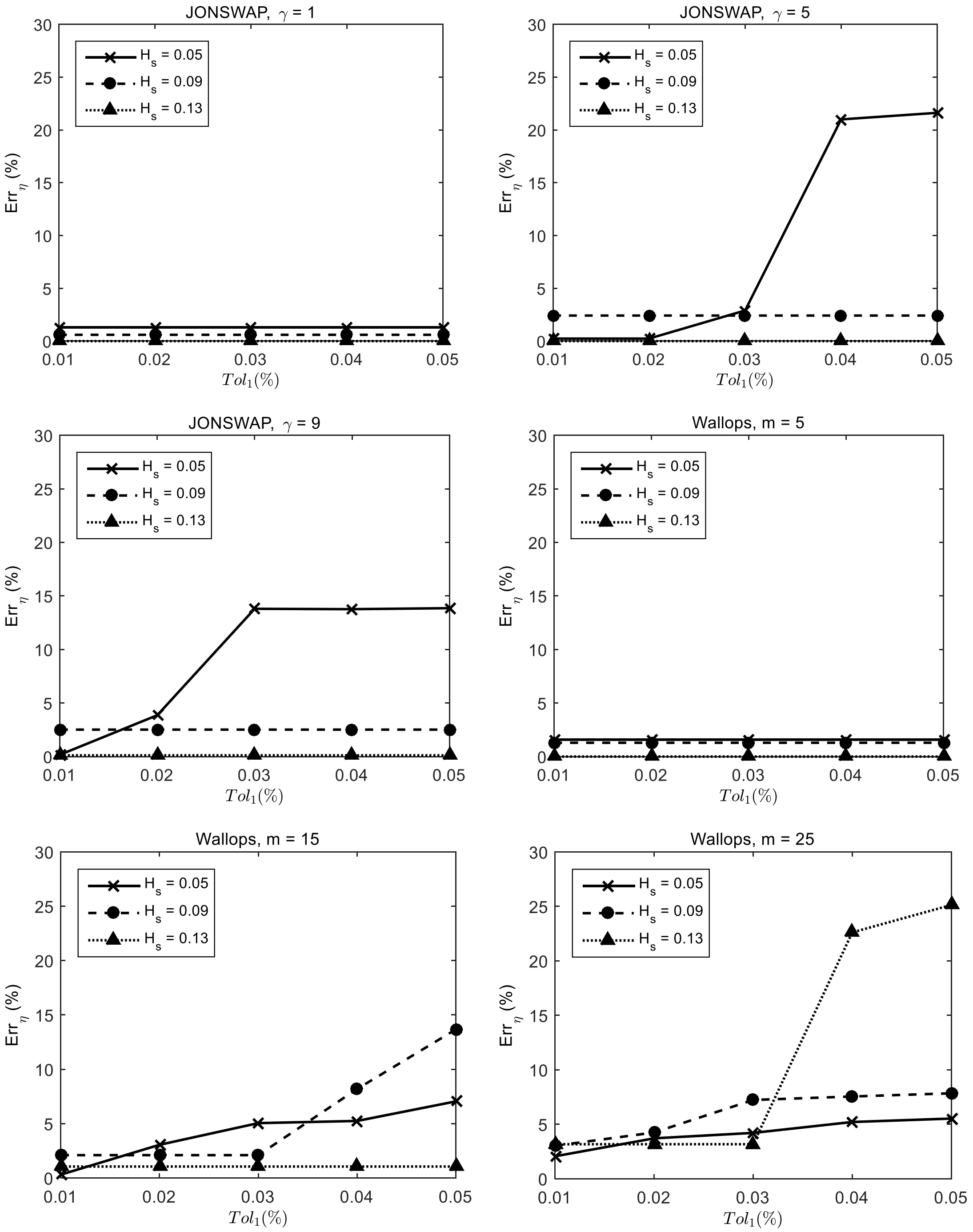

Figure 6.3.2 Err_η against Tol_1

6.4 Validation of the hybrid model

6.4.1 Two dimensional simulations

In order to validate the new hybrid model based on the tolerances determined in the previous two sub-sections, the numerical experiments carried out by Clamond, et al. (2007) is repeated, in which the domain covers 32 Stokes wave lengths and resolved into 32 points per wave length. The initial condition is given by applying

$$A = 0.1\,\mathrm{sech}[0.0354(X - X_c)] \tag{6.4.1}$$

instead of the initialization procedures described in section 6.2, where X_c is the centre of the domain. The other set-ups are the same with those for Figure 6.3.1 and Figure 6.3.2. The free surface profile obtained by using the hybrid model are presented and compared with the results from (Clamond, et al., 2007) in Figure 6.4.1. The agreement between them is very good and the relative difference in the maximum free surface elevation is about 0.65%, which indicates that profiles obtained from the hybrid model is consistent with that from the fully nonlinear method in (Clamond, et al., 2007). Meanwhile, the switch between the models are shown in Figure 6.4.2, where the maximum wave elevation at each time step is plotted with the indicators identifying which model is employed at a time step. One may find that the first 80 periods are taken over by the ENLSE-5F and the ESBI only accounts for the last 25 periods. As the ENLSE-5F uses only negligible computation time, the hybrid model can save more than 60% CPU time compared to that for only using the ESBI method in this case.

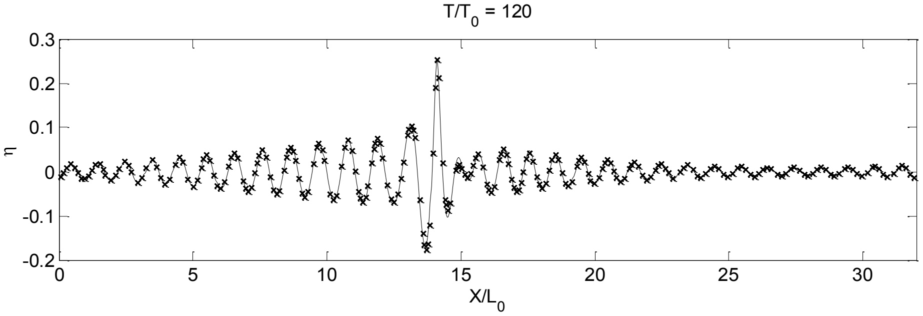

Figure 6.4.1 Free surface at the end of the simulation.

'—': Hybrid method; 'x' Method in Clamond, et al. (2007)

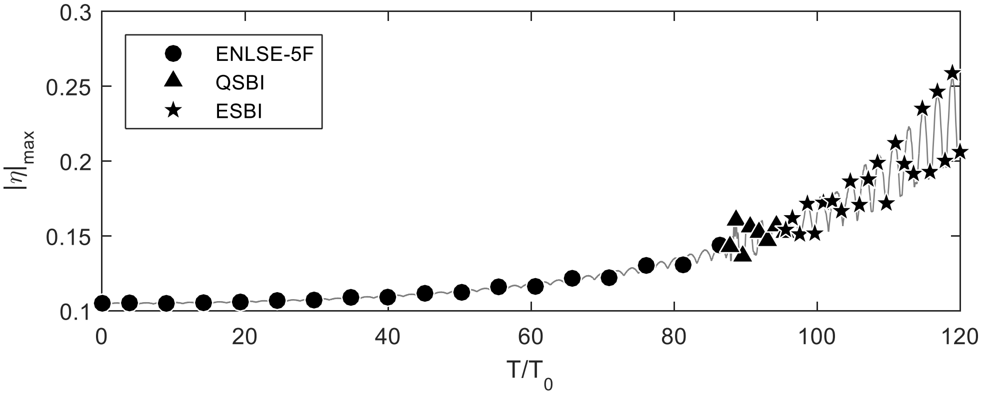

Figure 6.4.2 The exchange between the models. Solid line represents the values of $|\eta|_{max}$

However, in order to validate the present model for large domain and longtime simulations, the results of the hybrid model is also compared with that in (Clamond, et al., 2006), where the domain covers 128 wave lengths and resolved into 4096 points. The initial condition is given by Eq.(4.3.2) and the simulation is carried out to 1500 peak periods and reversed back to the initial stage. The other set-ups are the same with those for Figure 6.3.1 and Figure 6.3.2 and the error of the energy and free surface space distribution at the start and final stage are 1×10^{-3} and 2×10^{-3} respectively. The free surfaces are shown in Figure 6.4.3. The difference between them is almost invisible, with its value at the maximum free surface being about 3.02% occurring at the end of the simulation. The comparison again indicates that the profiles by using the present method and the fully nonlinear method described in (Clamond, et al., 2006) are consistent. In addition, the switch between the models are shown in Figure 6.4.4(a). It is found that after the first extreme wave event, the maximum free surface elevation never drops below the initial status, so that the ENLSE-5F is not involved again in the simulation after the first 100 periods. And the rest of the simulation is completed by the switch between the QSBI and ESBI models. Nevertheless, the about 40% CPU time is saved in this case compared to that using the ESBI model alone. The switch for the backward simulation is also presented in Figure 6.4.4(b), which is symmetric with (a). It further confirms that the numerical technique for controlling the switch between the models is very effective.

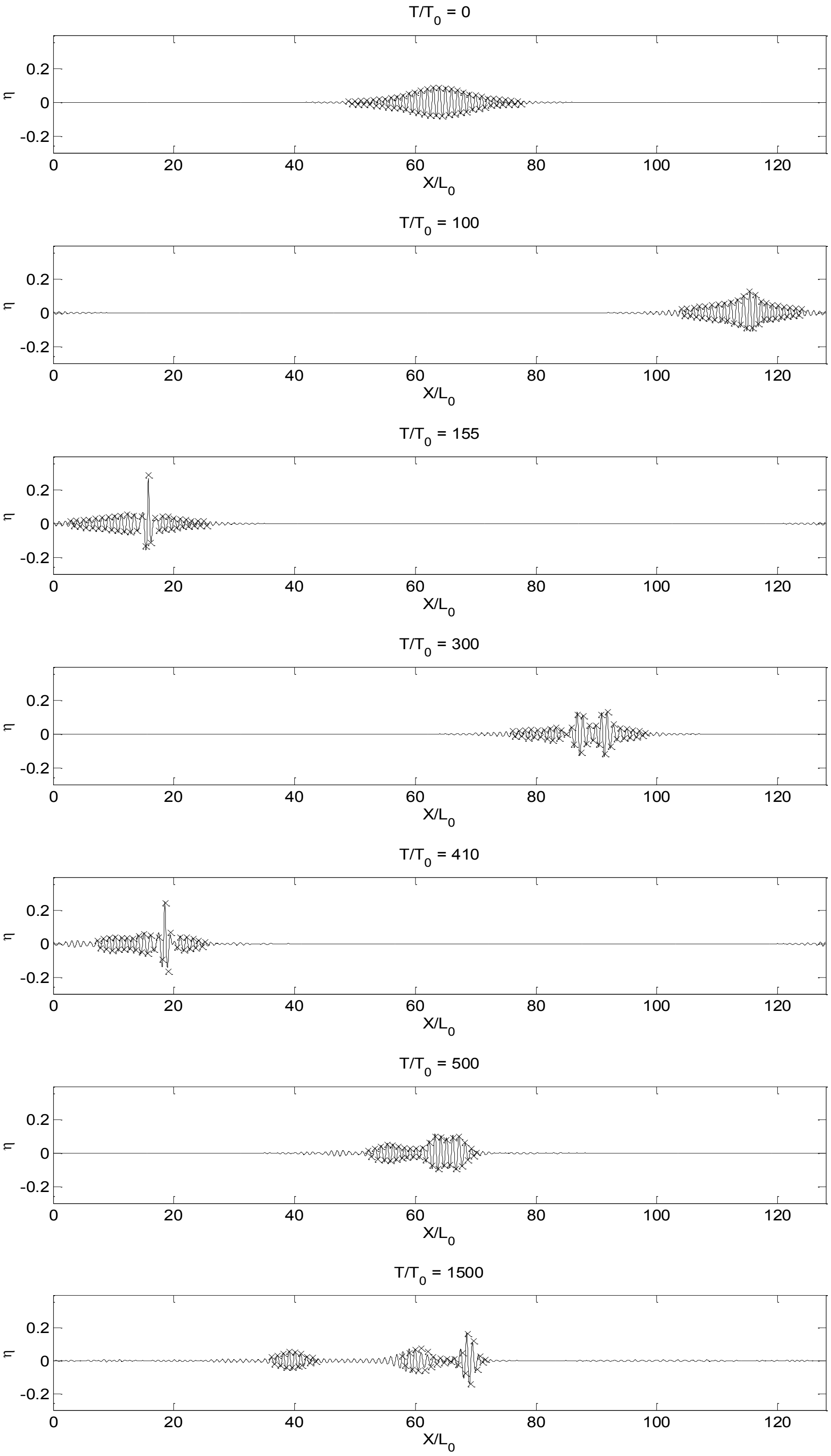

Figure 6.4.3 Free surface at different instant.

'—': Hybrid method; 'x' Method in Clamond, et al. (2006)

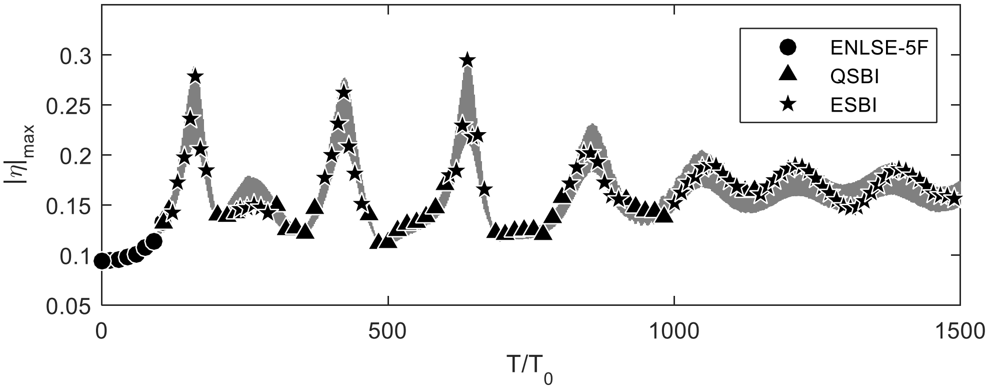

(a) Forward simulation

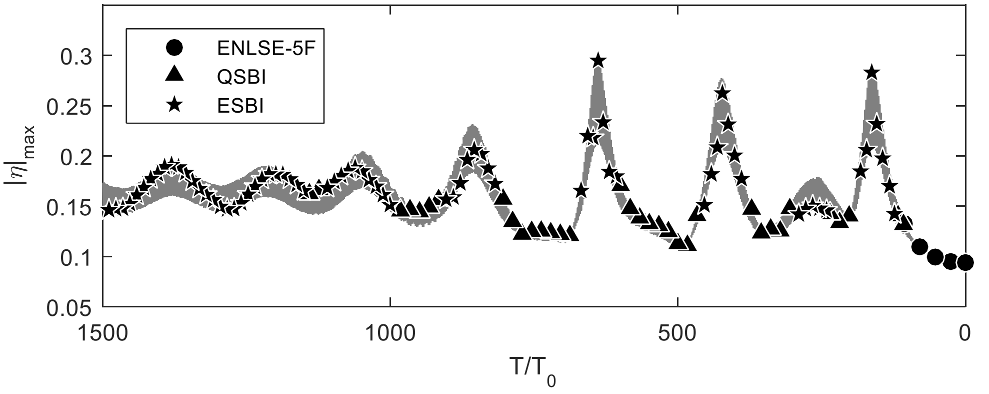

(b) Backward simulation

Figure 6.4.4 The exchange between the models. Solid line represents the values of $|\eta|_{max}$

6.4.2 Three dimensional simulations

Moreover, in order to validate the hybrid model for 3D problems, the numerical tests for directional focusing wave in section 4.3 is repeated with the same setups by using the hybrid model. A back and forth simulation is performed, and the error of the energy and free surface space distribution at the start and final stage are 3×10^{-4} and 1×10^{-4} respectively. The profiles of the free surface along $Y/L_0 = 0$ at the focusing time for both the hybrid model and results in (Bateman, et al., 2001) are shown in Figure 6.4.5, and the error of the maximum surface elevation is about 2.02%, which means that the hybrid model successfully captured the occurrence of the focusing wave in the 3D case.

In order to show the effectiveness of the numerical technique for controlling the switch between models, the maximum free surface elevation against time is shown in Figure 6.4.8 with indicators of each model. It is found that the ENLSE-5F is only involved in the first 1.5 peak periods, while the majority of the simulation is run by QSBI and ESBI. However, it shows that the hybrid model successfully switched from the ENLSE-5F, to QSBI and then ESBI, when the maximum surface becomes larger and larger, in both forward and backward simulations. This case with the parameters in Section 6.3 demonstrates that the hybrid model is also suitable for 3D wave problems.

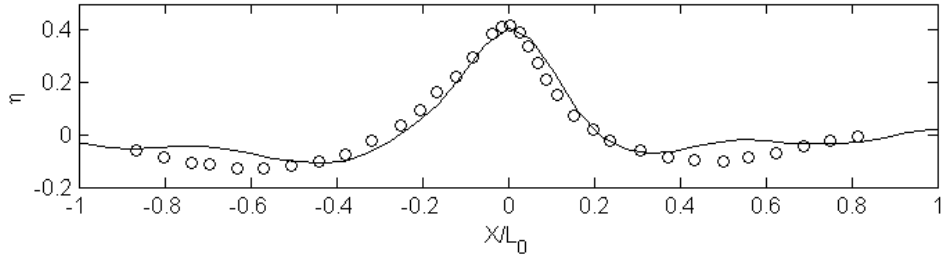

Figure 6.4.5 The Profiles of free surface at $T/T_0 = 7.4$ for focusing wave. '—': Hybrid model; 'o': Fully nonlinear model in (Bateman, et al., 2001)

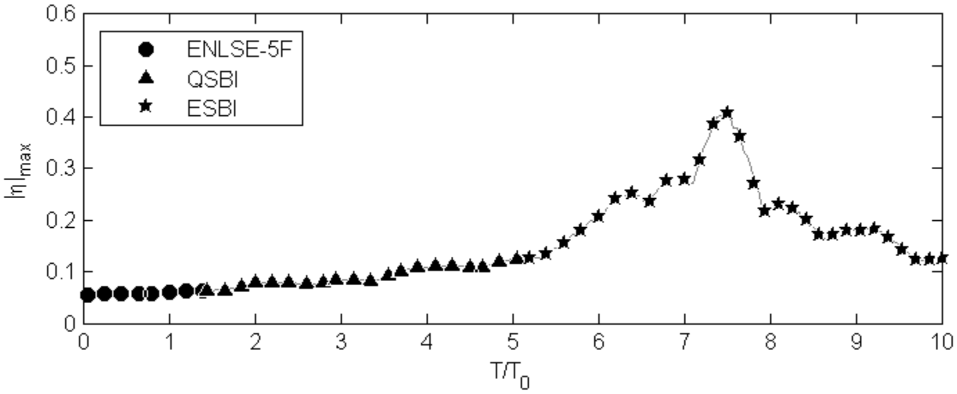

(a) Forward simulation

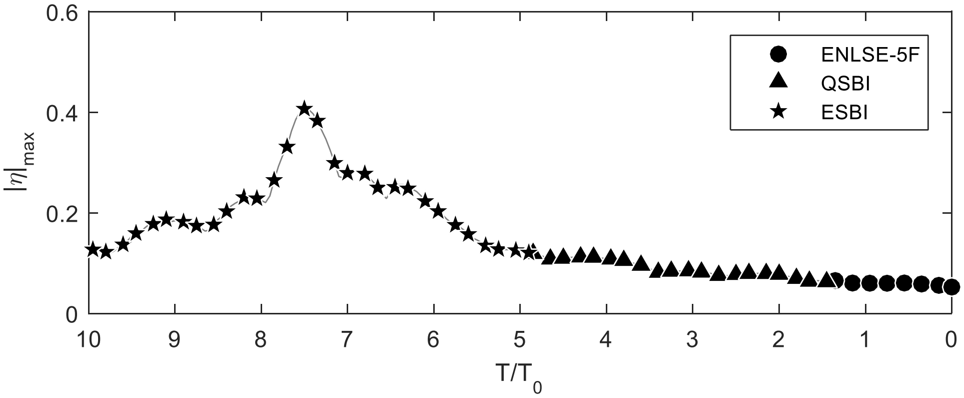

(b) Backward simulation

Figure 6.4.6 The exchange between the models for focusing wave (solid line represents the values of $|\eta|_{max}$)

In addition, a simulation of the crescent wave pattern is also carried out in order to further validate the hybrid model for 3D cases. The test by Fructus et al. (2005) is repeated with the same setups. A uniform Stokes wave train of initial steepness $\varepsilon = 0.1$ is perturbed by directional sidebands

$$\delta\eta = 0.05\sin(1.5X)\cos(1.645Y) \qquad (6.4.2)$$

The domain covers $4L_0 \times 2.43L_0$ and is resolved into 128×128 collocation points, where L_0 is the wave length of Stokes wave. The Stokes wave propagating direction is the peak wave direction which is used to initialize the hybrid model. The duration of the simulation lasts for 1200 Stokes wave periods. The following quantity is introduced to measure the ratio of the amplitude of component $\boldsymbol{K}'$ over the initial Stokes wave amplitude.

$$\Psi_\epsilon(\boldsymbol{K}') = \frac{|F\{\eta\}|_{(\boldsymbol{K}',T)}}{|F\{\eta\}|_{(\boldsymbol{K}=(1,0),T=0)}} \qquad (6.4.3)$$

The results are presented in Figure 6.4.7 for the components of peak wave component $\boldsymbol{K}' = (1,0)$ and perturbation component $\boldsymbol{K}' = (1.5, 1.645)$. It shows that the results obtained by using the hybrid model is highly correlated with that obtained by using the method in (Fructus, et al., 2005) in this 3D case, which again confirms that the tolerance values obtained by using the 2D cases are suitable for the 3D cases. Similar with Figure 6.4.2 and Figure 6.4.4, the switch between the models is shown in Figure 6.4.8, where it is found that the ENLSE-5F is not involved and only the QSBI and ESBI are used during the simulation for this case. And it shows that the hybrid model successfully switched from the QSBI to ESBI when the maximum wave steepness became large, which further confirms that the hybrid model can be used for simulating waves in three dimensions.

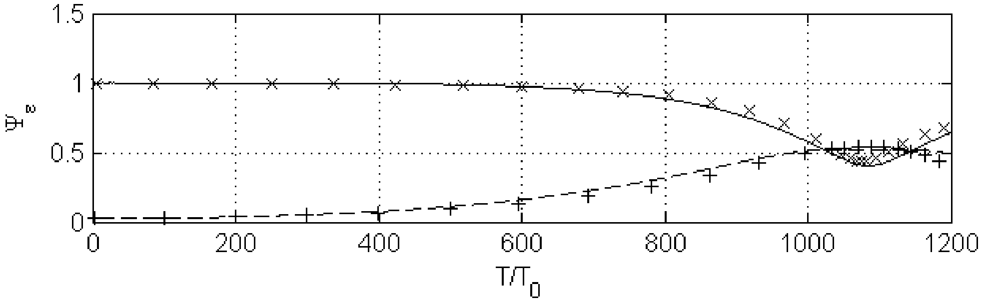

Figure 6.4.7 Evolution of perturbation components and peak wave components for crescent wave: '—' $\boldsymbol{K}' = (1,0)$ by using hybrid model; '--' $\boldsymbol{K}' = (1.5, 1.645)$ by using hybrid model; 'x' $\boldsymbol{K}' = (1,0)$ by using method in (Fructus, et al., 2005); '+' $\boldsymbol{K}' = (1.5, 1.645)$ by using method in (Fructus, et al., 2005)

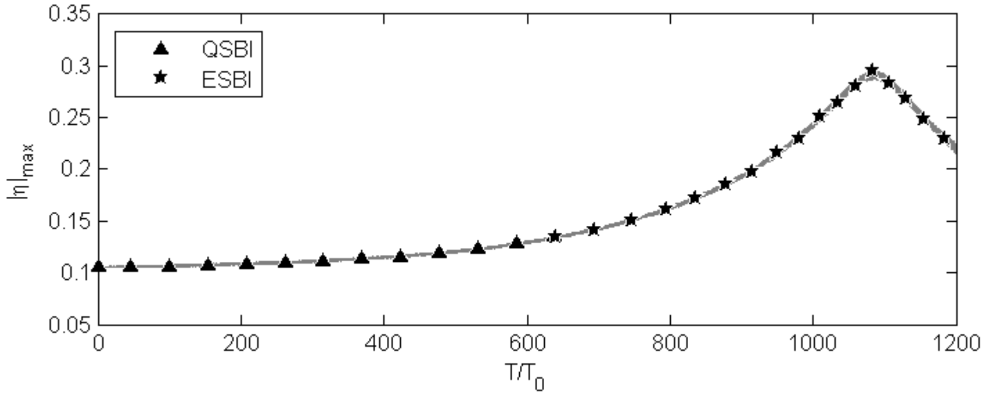

Figure 6.4.8 The exchange between the models for crescent wave. Solid line represents the values of $|\eta|_{max}$

According to Ducrozet et al. (2007), a 3D random sea simulation covering 42×42 peak wave length and lasting for 250 peak wave periods costs10 CPU days on a 3 GHz-Xeon single processor PC based on the fifth order High-order Spectral method. In order to further illustrate the computational efficiency of the present hybrid model, the 3D random wave simulation in (Ducrozet, et al., 2007) and (Docruzet, 2007) is repeated here, i.e., the computational domain, the duration of wave propagation and the resolution in this simulation are all the same as in (Ducrozet, et al., 2007). Also as in (Ducrozet, et al., 2007), the directional wave spectrum is given by

$$S(k,\theta) = S_J(k)G_2(\theta) \tag{6.4.4}$$

where $S_J(k)$ is the JONSWAP spectrum by using Eq.(6.3.1), $H_s = 0.28$, $\gamma = 3.3$, and the spreading function follows as

$$G_2(\theta) = \begin{cases} \frac{2}{\pi}\cos^2(\theta), & |\theta| \le \frac{\pi}{2} \\ 0, & |\theta| > \frac{\pi}{2} \end{cases} \tag{6.4.5}$$

The free surface elevation is outputted every peak period and it is shown in Figure 6.4.9 for that at $T/T_0 = 250$. The statistics of the free surface elevation at $T/T_0 = 200$ is compared with the same experiment in (Docruzet, 2007), which is shown in Figure 6.4.10. It indicates that the hybrid model gives consistent statistical results with the HOS method in (Ducrozet, et al., 2007) and (Docruzet, 2007). The simulation here is performed by using a single core on a workstation equipped with Intel(R) Xeon(R) CPU E5620@2.4GHz. It is found that only the QSBI and ESBI are involved in the simulation. The total CPU time costed by the hybrid method is 11.9 hours, which is only about 1/20 of the CPU time reported by Docrozet et al. (2007). In addition, the clock speed of the processor used here is slower than that used by Docrozet et al. (2007) , which means that the CPU time of the hybrid method can be further shortened if using higher performance computer. However, as the efficiency of the CPU does not only depend on its clock speed, such a big difference can also be exaggerated. Nevertheless, it is difficult to carry out the simulation on the same platform with Docrozet et al. (2007) in order to compare the efficiency. It is also noted that it is impossible to directly compare the wave elevation with Docrozet et al. (2007), because the phase of each wave component is assigned randomly in both simulations. Since the agreement of the surface probability distribution is observed, the hybrid model is validated and can be used to simulate 3D random waves.

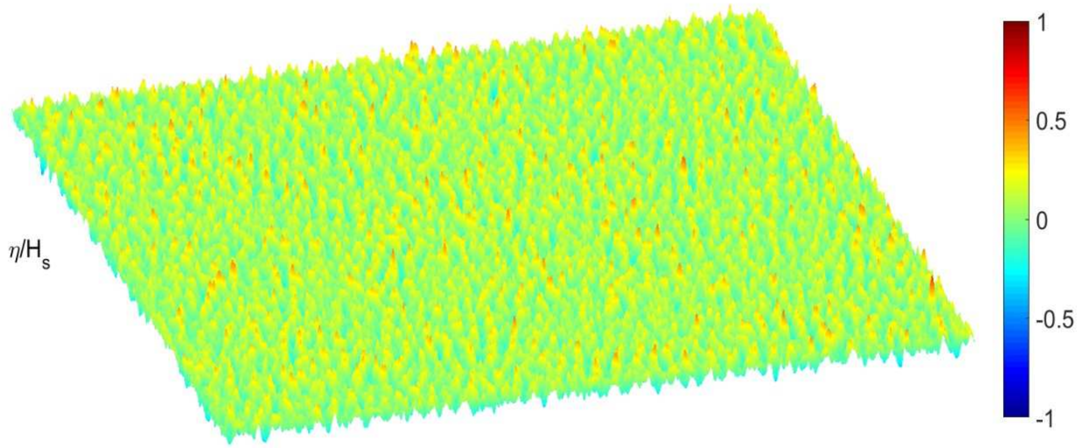

Figure 6.4.9 Free surface elevation at $T/T_0 = 250$

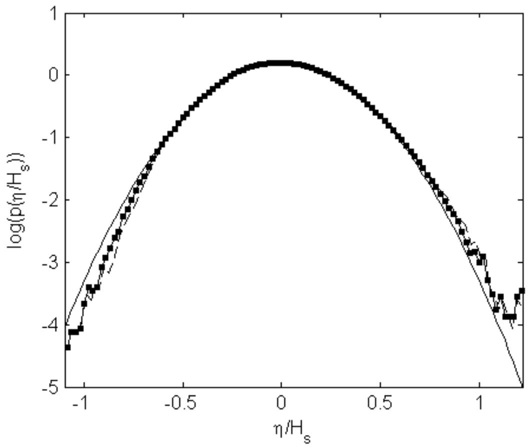

Figure 6.4.10 Probability distribution of the free surface elevation at $T/T_0 = 200$. '—' Gaussian distribution; '---' Results in (Docruzet, 2007); '—■' Results by using hybrid model

6.5 Discussion

This chapter presents a hybrid model for simulating rogue waves in random seas on a large spatial and time scale. The coupling algorithm between the ENLSE-5F (the Fifth Order Enhanced Nonlinear Schrödinger Equation based on Fourier transform), QSBI (Quasi Spectral Boundary Integral) and ESBI (Enhanced Spectral Boundary Integral) methods is then suggested with the techniques for data transfer. The tolerances for controlling the switch between the three models are investigated through numerical tests on the cases corresponding to different spectra (Wallops and JONSWAP spectra) with a wide range of parameters. The hybrid model is then validated based on the published results, which reveals that the techniques for coupling these three models are effective. And the results obtained by using the hybrid model are satisfactory in comparison with that in the literatures. For 3D random waves, the simulation of the same case as that in (Ducrozet, et al., 2007) is also carried out, it is found that the CPU time costed by the hybrid method is only about 1/20 of that reported by Ducrozet, et al. (2007). More numerical examples for large scale random wave simulations by using the hybrid model will be presented in chapter 7, in order to illustrate its computational efficiency.

7 NUMERICAL SIMULATION OF ROGUE WAVES IN RANDOM SEAS

Efforts have been made to obtain the ENLSE-5F and the ESBI, which together with the QSBI are used to propose the hybrid model. In this chapter, the newly proposed hybrid model will be adopted to simulate random seas on large time and space scale, in which rogue waves are embedded. Its computational efficiency will be tested against the fully nonlinear ESBI. Before that, attention should also be paid to techniques of embedding rogue waves in random sea for testing the performance of the hybrid method in various scenarios. That is because real rogue waves are unpredictable and could happen at arbitrary time and location, and so directly testing on them may not be able to check the performance of the hybrid model in various scenarios.

This chapter is organized in the following way: The numerical technique for embedding rogue waves in random background will be discussed in section 7.1, and validations based on linear theory are also presented; Numerical tests will be carried out in order to illustrate the overall efficiency of the hybrid model in section 7.2.

7.1 Techniques to embed rogue waves

Since the main target of the hybrid model is to provide an efficient way to simulate rogue waves in random seas on a large time and space scale, simulations will be mainly focused on the cases with tailored rogue waves embedded in random background. A short review about the techniques for embedding rogue waves in random seas are presented in APPENDIX D.

7.1.1 Basic formulations

7.1.1.1 Formulations for generating single rogue wave

According to Kriebel & Alsina (2000), the free surface can be split into the focusing part η_T and the random part η_R, i.e.,

$$\begin{aligned}\dot{\eta}(X,T) &= \eta_T + \eta_R \\ &= \sum_{j=1}^{J} a_{Tj}\cos\left(k_jX - \omega_jT + \varphi_{Tj}\right) \\ &\quad + \sum_{j=1}^{J} a_{Rj}\cos\left(k_jX - \omega_jT + \varphi_{Rj}\right)\end{aligned} \tag{7.1.1}$$

where φ_{Rj} is the random phase, $\varphi_{Tj} = -k_jX_f + \omega_jT_f$ is the phase of the focusing part, X_f and T_f are the focusing location and time respectively, $a_{Rj} = \sqrt{2P_RS(k_j)\Delta k}$ and $a_{Tj} = \sqrt{2P_TS(k_j)\Delta k}$ are the amplitudes for the random and focusing part respectively, P_R and P_T denote the energy ratio for each part, and $P_R + P_T = 1$. Equivalently, Eq.(7.1.1) can also be reformulated as

$$\dot{\eta}(X,T) = \sum_{j=1}^{J} \sqrt{a_j^2 + 2a_{Tj}a_{Rj}\cos\left(\varphi_{Tj} - \varphi_{Rj}\right)}\cos\left(k_jX - \omega_jT + \varphi_j\right) \tag{7.1.2}$$

where $\theta_j = \arctan\left[\frac{a_{Rj}\sin(\varphi_{Rj}) + a_{Tj}\sin(\varphi_{Tj})}{a_{Rj}\cos(\varphi_{Rj}) + a_{Tj}\cos(\varphi_{Tj})}\right]$.

It is obvious that the spectrum corresponding to Eq.(7.1.2), i.e., $S'(k_j) = \left[a_j^2 + 2a_{Tj}a_{Rj}\cos\left(\varphi_{Tj} - \varphi_{Rj}\right)\right]/2\Delta k \neq S(k_j)$, unless $\varphi_{Tj} = \varphi_{Rj}$, which is impossible because φ_{Rj} is random and φ_{Tj} is deliberately assigned. It means that by using Eq.(7.1.1), condition of Eq. (6.3.4) is not met thus the shape of the corresponding spectrum will not be identical to the specific spectrum, due to the involvement of numerical errors. This is not desirable for numerical simulation as aforementioned.

In order to eliminate the involved numerical errors and reserve the shape of the specific spectrum, a correction term is introduced in Eq.(7.1.1), and the free surface elevation could be written as

$$\ddot{\eta}(X,T) = \eta_T + \eta_R + \eta_C = \sum_{j=1}^{J} a_j\cos\left(k_jX - \omega_jT + \theta_j\right) \tag{7.1.3}$$

where $a_j = \sqrt{2S(k_j)\Delta k}$ and the correction part $\eta_C = \ddot{\eta} - \dot{\eta}$. It is reported that the random oscillation in the spectrum introduced by using Kriebel & Alsina's method (2000) can be effectively avoided by using Eq.(7.1.3). In order to tailor a rogue wave of specified height, the amount of the energy for the focusing part, i.e., P_T, can be adjusted by small increment. The larger P_T is, the higher the resulted rogue wave is. Thus iterations are needed until the tailored rogue wave height meets the requirements.

7.1.1.2 Formulations for generating multiple rogue waves

Since sometimes rogue waves appear in groups, e.g., the well-known three sisters (Kharif, et al., 2009), techniques for generating multiple focusing wave are worth being studied. Based on the method by Kriebel & Alsina (2000), if one wants to embed several rogue waves in random background, Eq.(7.1.1) can be slightly modified as

$$\begin{aligned}\dot{\eta}'(X,T) &= \eta'_T + \eta'_R \\ &= \sum_{m=1}^{M}\sum_{j=1}^{J} a'_{Tjm}\cos\left(k_jX - \omega_jT + \varphi'_{Tjm}\right) \\ &\quad + \sum_{j=1}^{J} a'_{Rj}\cos\left(k_jX - \omega_jT + \varphi'_{Rj}\right)\end{aligned} \tag{7.1.4}$$

where M is the amount of rogue waves to be embedded, $a'_{Rj} = \sqrt{P_R}a_j$ and $a'_{Tjm} = \sqrt{P_{Tm}}a_j$ are the amplitudes, $P_R + \sum_{m=1}^{M} P_{Tm} = 1$, P_{Tm} is the energy percentage for the mth rogue wave, φ'_{Rj} is the random phase, $\varphi'_{Tjm} = -k_jX_{fm} + \omega_jT_{fm}$, X_{fm} and T_{fm} are the focusing location and time for the mth rogue wave respectively. By using Eq.(7.1.4), spurious oscillation is inevitably involved in the specific spectrum, which is not desirable.

Similar to Eq.(7.1.3), a correction term can also be introduced to Eq.(7.1.4), in order to eliminate the numerical errors involved. The corrected equation for generating amount of M rogue waves is given as

$$\ddot{\eta}''(X,T) = \sum_{j=1}^{J} a_j\cos\left(k_jX - \omega_jT + \theta'_j\right) \tag{7.1.5}$$

where the phase is estimated through the formulation $\theta'_j = \arctan\left[\frac{a'_{Rj}\sin\left(\varphi'_{Rj}\right)+\sum_{m=1}^{M} a'_{Tjm}\sin\left(\varphi'_{Tjm}\right)}{a'_{Rj}\cos\left(\varphi'_{Rj}\right)+\sum_{m=1}^{M} a'_{Tjm}\cos\left(\varphi'_{Tjm}\right)}\right]$. By using this equation, the spurious fluctuations in the spectrum will be effectively eliminated.

To use Eq. (7.1.3) or (7.1.5) as the initial condition for the ESBI or QSBI model, the velocity potential is required, which can be obtained through Eq.(3.1.8).

7.1.2 Validations based on linear theory

In order to illustrate the effectiveness of the improved method for embedding rogue waves in random seas, numerical tests are carried out in this section. For the sake of proving that the new technique can preserve the shape of the specific spectrum, tests based on the linear theory is enough. Second order nonlinear effects have already been discussed in (Wang, et al., 2015), however, which is not the subject of this study therefore will be not further investigated.

7.1.2.1 Tests based on empirical spectrum

In order to show that the new technique has advantages over the original method by Kriebel & Alsina (2000) on reserving the spectrum shape, an example is given here. The domain covers 128 peak wave lengths and is resolved into 8192 points. The JONSWAP spectrum in terms of wave number is adopted and discretized by using interval $\Delta k = 2\pi/L_d$ (L_d is the domain length), $\gamma = 3$ and the cut-off wave number $k_{max} = 4$, which covers the normal range for practical use (Goda, 1999). By making $P_T = 20\%$, the free surface spatial distribution at focusing time is described in Figure 7.1.1 (a). It shows that the rogue wave height differs significantly from each other by using Eq.(7.1.1) and Eq. (7.1.3). This is due to the existence of the additional correction term in Eq.(7.1.3), which slightly modifies the free surface in comparison with Eq.(7.1.1). However, one can always generate the rogue wave of requiring height by adjusting the value of P_T as long as $P_T \leq 1$. That means to obtain a rogue wave with larger height, one just needs a higher value of P_T. Next, the observed spectrum of the free surface by using Eq.(7.1.1) and Eq.(7.1.3) are obtained and compared. The free surface spatial distribution is analyzed and FFT is adopted to estimate the spectrum. Results are presented in Figure 7.1.1 (b), in which it is found the observed spectrum by using Eq.(7.1.3) is identical to the specified spectrum, while that obtained by using Eq.(7.1.1) fluctuates significantly. In addition, the total spectral energy is also estimated by using trapezium rule and the error of that by using Eq.(7.1.1) is about 3%, which is unacceptable for engineering practices.

One may argue that such fluctuations could be artificially removed through smoothing technique. Thus the spectrum from the case adopting the original technique is smoothed 100 times using a five-point smoothing technique (Longuet-Higgins & Cokelet, 1976), as shown in Figure 7.1.2. Although the smoothed spectrum seems to be less fluctuated, the shape of the smoothed spectrum is visibly different from the specified one around the spectral peak. The difference between the smoothed spectra by using Eq.(7.1.1) without the correction and the original spectrum may deliver a misleading signal that there is an energy transfer between harmonics due to nonlinearity.

Therefore, compared with the original method by Kriebel & Alsina (2000), the improved method, i.e., Eq.(7.1.3), can effectively remove the spurious fluctuations in spectrum. In order to generate rogue waves in random background as well as reserving the shape of the specified spectrum, the improved method, i.e., Eq.(7.1.3), should be employed.

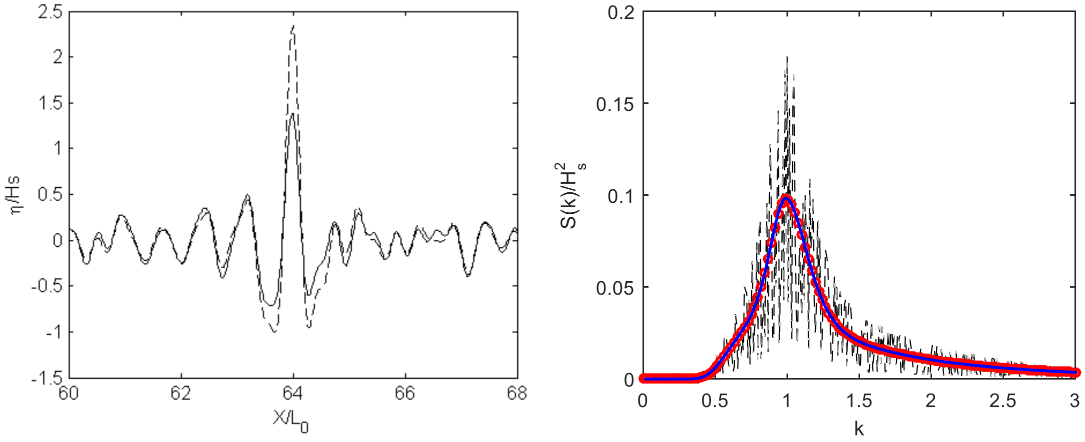

(a) (b)

Figure 7.1.1 Free surface and observed spectra based on the JONSWAP spectrum.

(a) Free surface elevation: '---' by using Eq.(7.1.1), '—' by using Eq.(7.1.3); (b) Observed spectrum: Blue '—' specified spectrum, '---' by using Eq.(7.1.1), Red 'o' by using Eq. (7.1.3)

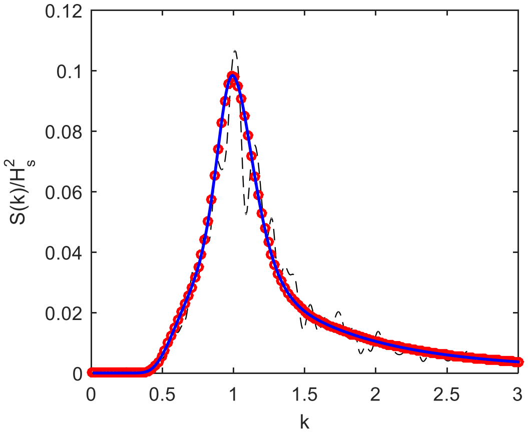

Figure 7.1.2 Observed spectra based on the JONSWAP spectrum: Blue '—' specified spectrum, '---' by using Eq.(7.1.1) after smooth, Red 'o' by using Eq. (7.1.3)

7.1.2.2 Tests based on Gaussian process

Nevertheless, as pointed out by Tucker, et al. (1984), some statistical property will be lost if the amplitude of each component is calculated by letting $a_j = \sqrt{2S(k_j)\Delta k}$, i.e., the variance of the variance of each run will be underestimated. Instead, the amplitude should be given stochastically. However, it should be noted that the improved method, i.e., Eq.(7.1.3), works well for any specified spectrum. To address this point, the JONSWAP spectrum is now replaced with that based on a real Gaussian distribution suggested by Tucker, et al. (1984), and the procedures for Figure 7.1.1 are repeated. The free surface is presented in Figure 7.1.3(a), which is similar to Figure 7.1.1(a). It is worth of noting that even though the JONSWAP spectrum is replaced with that representing the Gaussian process, the observed spectrum by using Eq.(7.1.1) still brings in significant fluctuation, as indicated in Figure 7.1.1(b). While it shows perfect consistence between the specified spectrum and that obtained by using Eq.(7.1.3). In addition, it is found that the spectral energy of the observed spectrum obtained by using Eq.(7.1.1) produces error about 3.1% compared with the specified one, which is unacceptable. This further illustrate the effectiveness of the improved method, i.e., Eq.(7.1.3), for embedding rogue waves in random sea. In addition, it also shows that the improved method is able to reserve the spectral shape no matter the spectrum is specified by using empirical forms, such JONSWAP etc., or following the Gaussian distribution, such as that suggested by Tucker, et al. (1984).

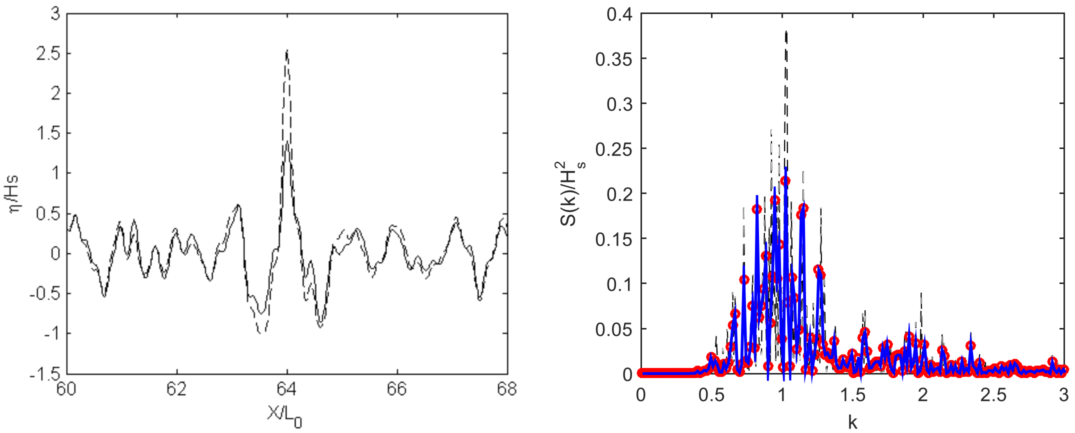

(a) (b)

Figure 7.1.3 Free surface and observed spectra based on the Gaussian distribution. (a) Free surface elevation: '---' by using Eq. (7.1.1), '—' by using Eq. (7.1.3); (b) Observed spectrum: Blue '—' specified spectrum, '---' by using Eq.(7.1.1), Red 'o' by using Eq. (7.1.3)

7.1.2.3 Tests based on CNW theory

Furthermore, to show the effectiveness of the present improved method, the CNW approach (Taylor, et al., 1997) is also adopted here for validation. A rogue wave of crest height $1.5H_s$ is generated by using the CNW approach. The same experimental condition as Figure 7.1.1 is applied for the present method. The spectrum corresponding to the CNW is obtained by using FFT. Then the random sea state embedded with rogue wave is reconstructed by using Eq.(7.1.3) based on the spectrum corresponding to the CNW, where $P_T = 20\%$ is employed (chosen randomly). The free surface are presented in Figure 7.1.4(a). It shows that the rogue wave height by using both the methods are comparable, though the random background waves are totally different. Whereas the percentage of the energy for the focusing part is adjustable by using the present method, the rogue wave height can always be tailored to desired height. Thus, to generate a rogue wave with a same height of that based on the CNW is not difficult. Meanwhile, through comparing the spectra in Figure 7.1.4 (b), it is found that there is good agreement between the present method and CNW. This further confirms that the current technique for embedding rogue waves in random background can perfectly preserve the spectral shape, in spite of what the specified spectrum looks like.

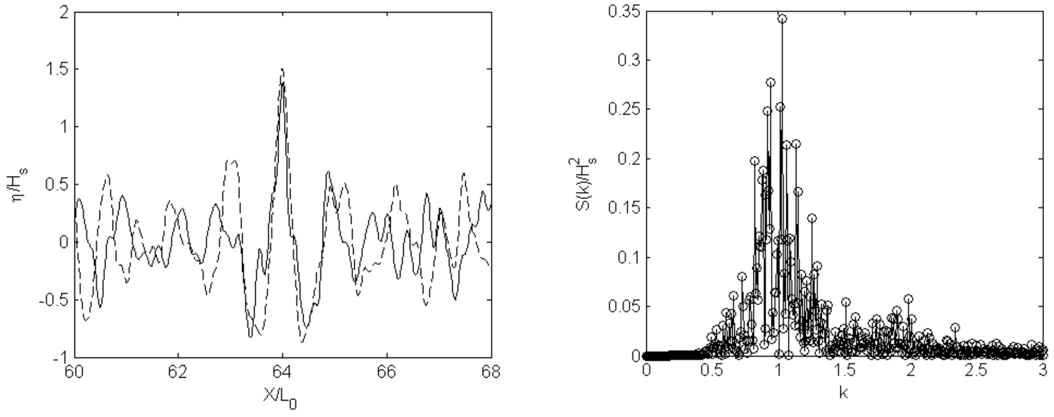

(a) (b)

Figure 7.1.4 Free surface and observed spectra based on the CNW.

(a) Free surface elevation: '---' by using CNW, '—' by using Eq. (7.1.3); (b) Observed spectrum: '—' by using CNW, 'o' by using Eq. (7.1.3)

7.1.2.4 Tests on generating multiple rogue waves

In this section, the effectiveness of Eq.(7.1.5) for generating multiple rogue waves are investigated. Two and three rogue waves on spatial scale are generated simultaneously by using the same set-ups for Figure 7.1.1, and $P_{Tm} = 20\%$ is employed. The original method, i.e., Eq. (7.1.4), is also adopted for comparison. The free surface profiles at focusing time and the corresponding spectra are displayed in Figure 7.1.5. The rogue wave profiles of the twins and triplets are shown in Figure 7.1.5(a) and (c) respectively, which indicate that multiple rogue waves are successfully generated by using both the methods, although the rogue wave height obtained by using Eq.(7.1.5) is shown slightly smaller than that by using Eq.(7.1.4). However, through comparing the spectra, as indicated in Figure 7.1.5(b) and (d), it is found that the original method by using Eq.(7.1.4) brings in significant fluctuations, while the new technique by using Eq.(7.1.5) is able to perfectly reserve the specified spectral shape.

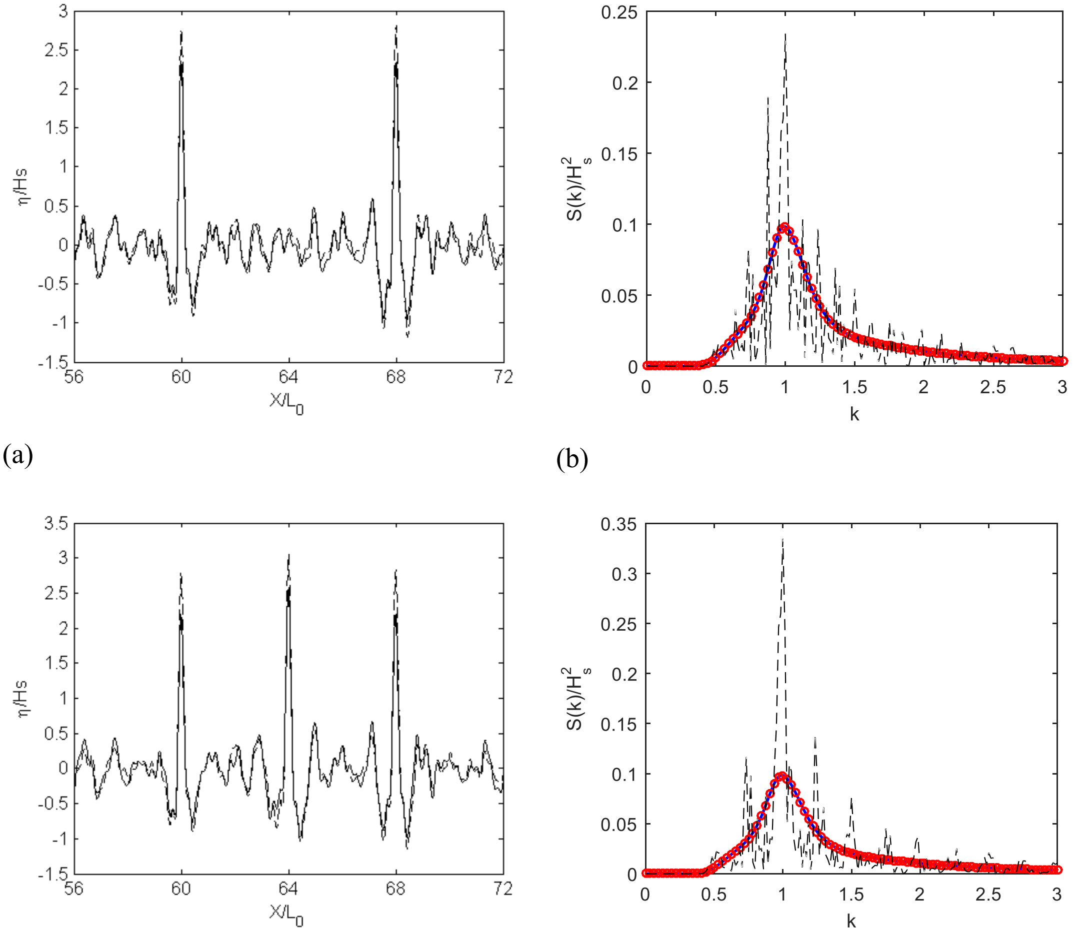

(a) (b)

(c) (d)

Figure 7.1.5 Free surface and observed spectra for multiple rogue waves tests.

(a) Free surface elevation: '---' by using Eq. (7.1.4), '—' by using Eq. (7.1.5); (b) Observed spectrum: Blue '—' specified spectrum, '---' by using Eq. (7.1.4), Red 'o' by using Eq. (7.1.5)

7.1.3 Discussion

In this subsection, an improved technique for generating rogue waves in random sea is suggested. The effectiveness of the improved technique is investigated by numerical tests using the linear theory. The investigations suggest that the improved technique can effectively retain the features of the specified wave spectrum and remove spurious fluctuations in the existing method. Therefore, this method will be adopted in the following study to generate the initial condition for the numerical simulations. It is worth of noting that the method suggested by

Tucker, et al. (1984) for generating random waves will not be employed in this study. The reason is that the author is not trying to address the statistics of random seas, but to illustrate the computational efficiency of the hybrid model. According to Tucker, et al. (1984), it is acceptable for this purpose in such situations. Next, further numerical tests will be carried out in order to illustrate the overall efficiency of the hybrid model proposed in chapter 6. Details are presented in the next section.

7.2 Discussions on the overall performance of the hybrid model

In this section, more numerical examples will be tested on the new hybrid model with $Tol_1 = 0.02\%$ and $Tol_2 = 0.03\%$, which are determined in 6.3.

The CPU ratio is introduced that is the CPU time of the ESBI divided by that of the hybrid model. All the simulations are implemented on the same workstation equipped with the Intel Xeon E5-2630 v2 (Intel Corporation, Santa Clara, CA, USA) of 2.6GHz processor. Pre-tests have been carried out based on the JONSWAP spectrum with $H_s = 0.13$, $\gamma = 5$ without embedding rogue waves, and it takes the ESBI 10638s ~ 3h, the QSBI 5404s ~ 1.5h (about a half of CPU time for ESBI), while the ENLSE-5F only 734s ~ 12min (only 7% of CPU time for ESBI), to finish one sea state simulation ($1000T_0$) covering $128L_0$ domain by a resolution of 2^6 per L_0 independently. For such a strong nonlinear case, it takes the hybrid model about the same time with the ESBI, due to that only the ESBI is involved during the computation.

7.2.1 Different rogue wave height

Next, the significant wave height keeps unchanged, i.e., $H_s = 0.05$, and test on different rogue wave heights, i.e., $2H_s$, $3H_s$ and $4H_s$. The basic set-ups are the same with that for Figure 6.3.1 and Figure 6.3.2. The errors of the free surface together with the CPU ratios are presented in Figure 7.2.1 for the cases with different spectrum and different parameters.

It shows that the errors obtained by using both the JONSWAP and Wallops spectrum with different width parameters are less than 5%, which confirms that the values for the Tol_1 and Tol_2 controlling the switch between the models are appropriate for the cases with different embedded rogue waves. It can be seen from Figure 7.2.1(b) that the CPU time ratio is approximately 1.9 in all cases with the JONSWAP spectrum, except for the cases with $2H_s{\sim}3H_s$ and $\gamma = 9$. That is because the ENLSE-5F is only involved in these cases with the rogue wave heights of $2H_s{\sim}3H_s$ and $\gamma = 9$ but not in other cases. When the ENLSE-5F is not involved, the calculation is switched only between the QSBI and ESBI models. As indicated above, the QSBI use about a half of CPU time used by ESBI, which implies that the QSBI are implemented in most of time steps for the cases except for these with $2H_s \sim 3H_s$ and $\gamma = 9$. When the ENLSE-5F is involved, the CPU time ratio can reach to 2.6, slightly better than other cases, indicating that the ENLSE-5F is not involved in a large number of steps.

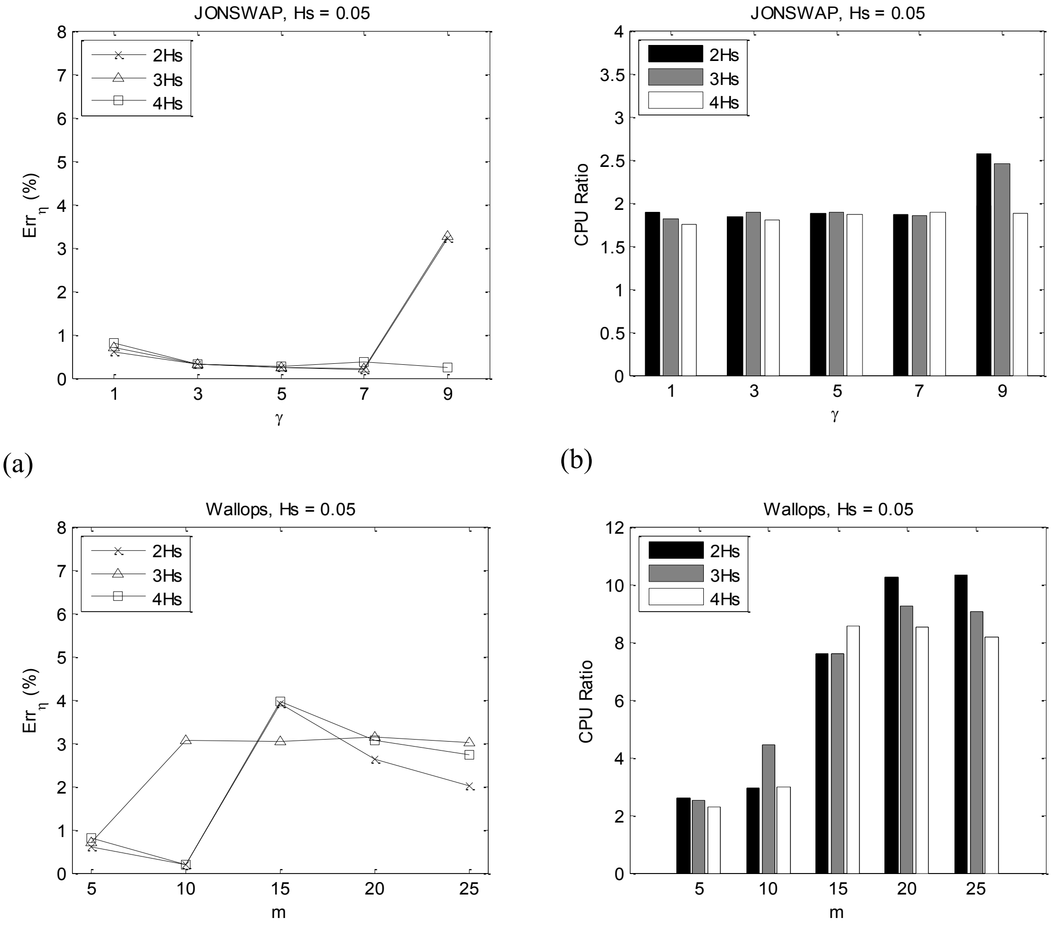

(a) (b)

(c) (d)

Figure 7.2.1 Err_η and CPU ratio (CPU time of ESBI/CPU time of hybrid model) for the cases with different rogue wave heights

On the other hand, for the simulations based on the Wallops spectrum, the story is different in particular when $m > 10$. In these cases, the CPU time is more than 8 or even 10, Figure 7.2.1(d), implying that the new hybrid method is very much more efficient than the ESBI only. When $m \leq 10$, the ratio is not so high, though it is larger than 2.

In order to illustrate how the models switch during the simulation, Figure 7.2.2 is presented in a similar way to that for Figure 6.4.2 and Figure 6.4.4. It shows that in some case, the process starts with ENLSE-5F, then goes to QSBI and ESBI, ending with QSBI, e.g., Figure 7.2.2(a).

In some other cases, the process starts with ENLSE-5F, then goes to QSBI and ESBI, ending with ENLSE-5F, e.g., Figure 7.2.2(f). The various scenarios illustrated in Figure 7.2.2 demonstrated that the automatic switch between the three models works well.

Furthermore, the profiles with the rogue wave height of $4H_s$ at focusing time and location are shown in Figure 7.2.3. It is found that the results obtained by using the hybrid model are almost identical with that obtained by only using the ESBI. However, the hybrid model significantly save the CPU time with different degree as indicated above.

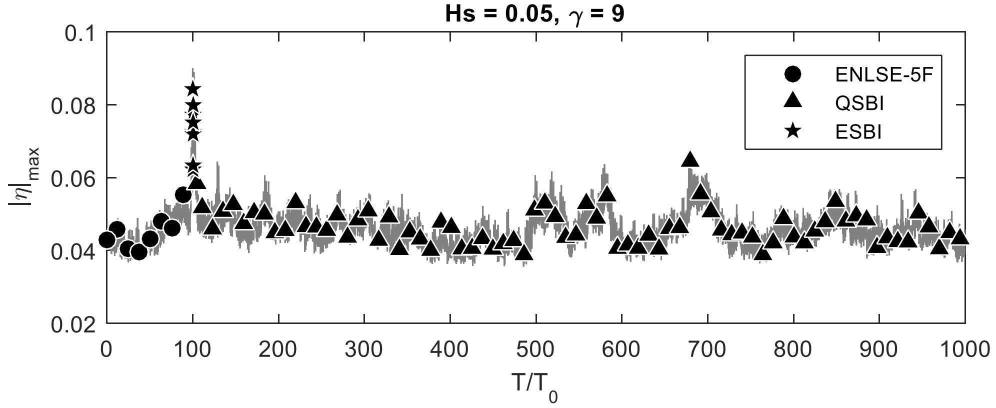

(a): $2H_s$

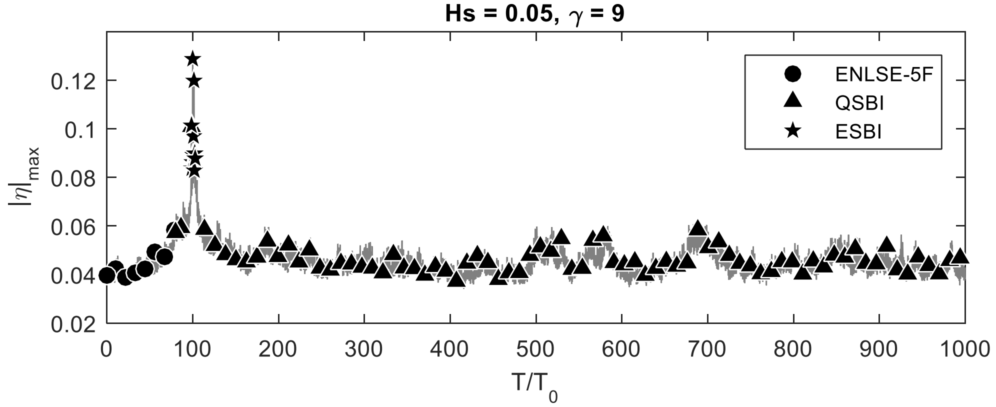

(b): $3H_s$

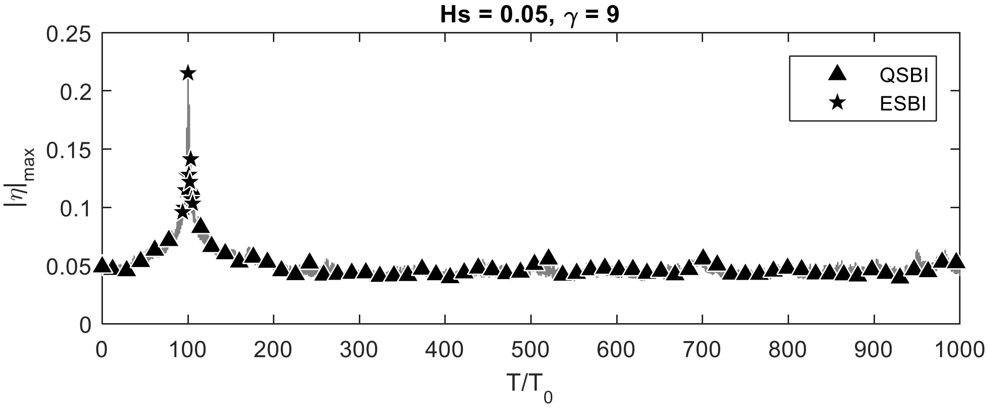

(c): $4H_s$

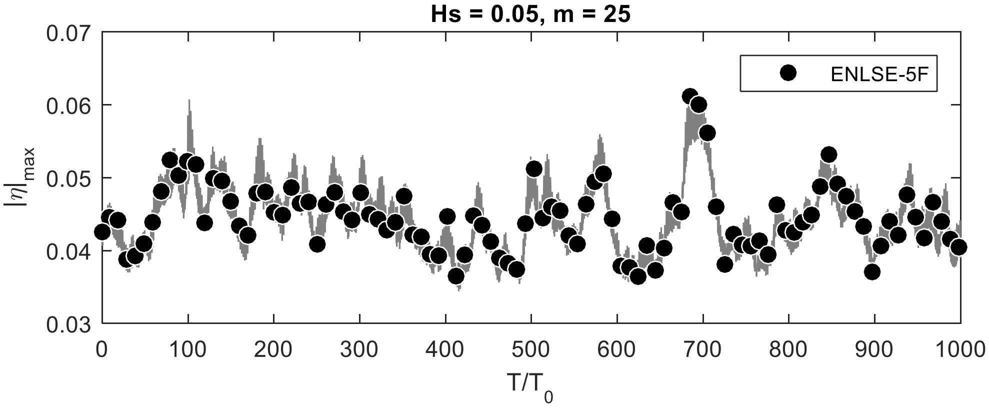

(d): $2H_s$

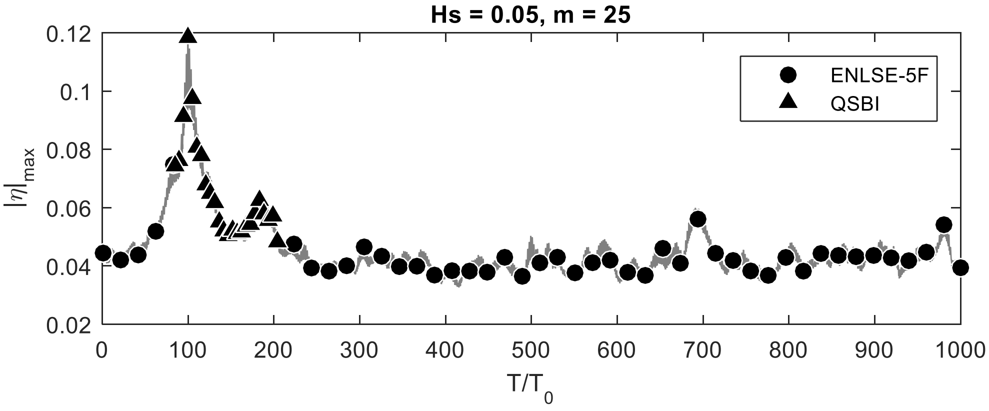

(e): $3H_s$

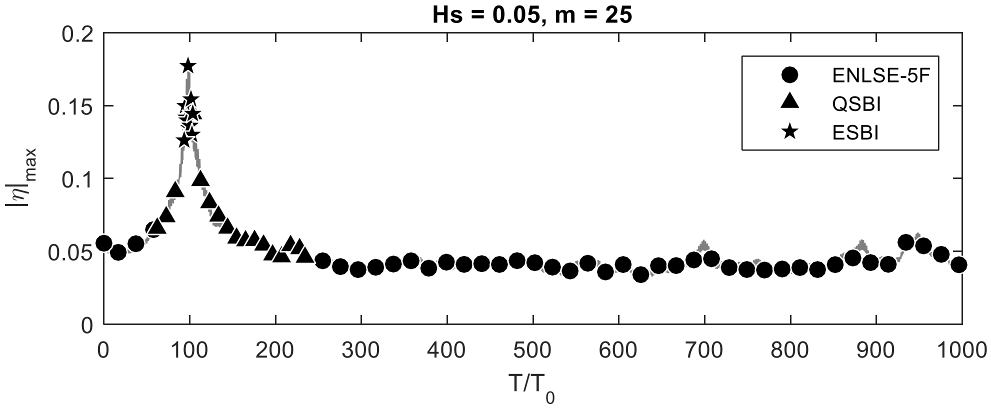

(f): $4H_s$

Figure 7.2.2 The exchange between models for the cases with different rogue wave heights

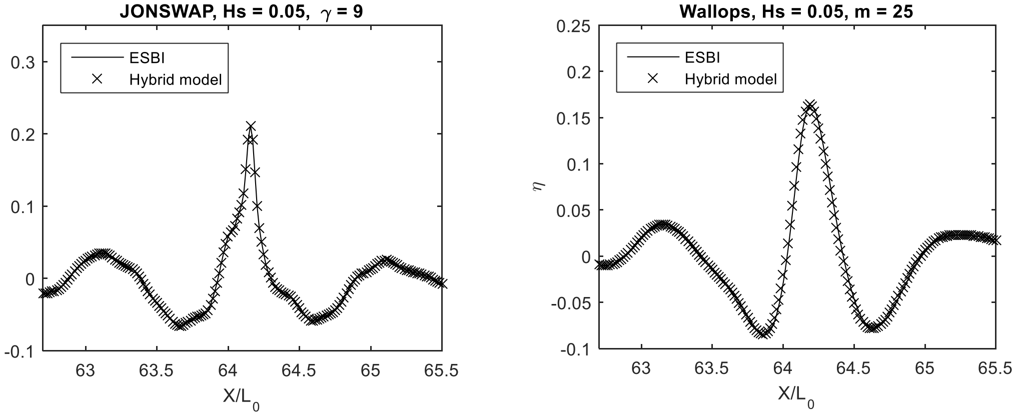

(a) (b)

Figure 7.2.3 The profiles of the rogue wave with height of $4H_s$for the cases with different rogue wave heights

7.2.2 Different numbers of rogue waves on temporal scale

However, there are possibilities that more than one rogue wave event happen during one sea state (Kharif, et al., 2009). Therefore, cases with different amount of rogue wave events on temporal scale are investigated in this section. In addition to one rogue wave event $T_f/T_0 = 100$, cases of two rogue wave events $T_f/T_0 = 100\&500$ and three rogue wave events $T_f/T_0 = 100\&500\&900$ are studied by using the same set-ups with that for Figure 6.3.1 and Figure 6.3.2. The rogue wave height is fixed to $3H_s$ as there will not be energy left to generate the random background if three successive rogue wave higher than $3H_s$ are generated by using the method explained in (Wang, et al., 2015) and section 7.1. Similarly, the errors and CPU ratios are presented in Figure 7.2.4.

As shown in Figure 7.2.4 (a) and (c), the errors for all the cases considered in this section are less than 5%, which again confirms effectiveness of the values of Tol_1 and Tol_2 for controlling the switching in the cases with different amount of rogue waves on temporal scale.

It is shown in Figure 7.2.4 (b) that for the simulations based on the JONSWAP spectrum, the maximum CPU ratio appears for the case $T_f/T_0 = 100$ with $\gamma = 9$, which is approximately 2.5. This is because of the involvement of the ENLSE-5F for a small amount of time steps and QSBI for the most of that in the simulation by using the hybrid model. Besides, another two cases of $T_f/T_0 = 100\&500$ and $T_f/T_0 = 100\&500\&900$ with $\gamma = 1$ are mostly taken over by the ESBI, so that the CPU ratio is approximately 1.2, but a little higher than 1 due to the involvement of the QSBI. Apart from the case above, the CPU ratios of the rest cases are almost the same, say 1.8~2, due to that the majority of the time steps during the simulation by using the hybrid model are taken over by the QSBI.

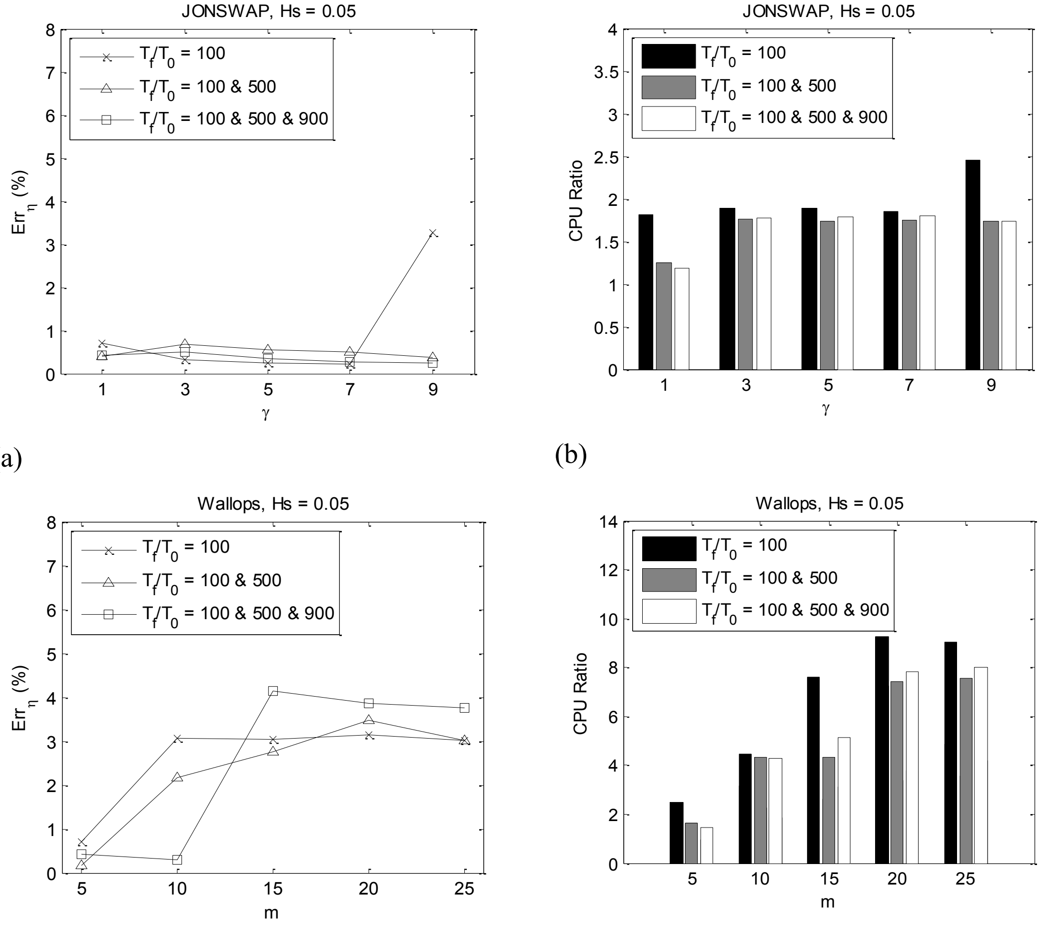

(a)

(b)

(c)

(d)

Figure 7.2.4 Err_η and CPU ratio (CPU time of ESBI/CPU time of hybrid model) : different rogue wave number on temporal scale

While on the other hand, for the simulations based on the Wallops spectrum, the CPU ratios are all larger than 4 except the cases with $m = 5$, which are however approximately 2. Roughly speaking, the CPU ratio increases when the spectrum becomes narrower (m increases). Among all, the most efficient case is the one that rogue wave only occurs once at $T_f/T_0 = 100$ with $m = 20$, which leads to the CPU ratio of 9.2.

In addition, in order to examine how the hybrid model switching between each model for the numerical examples in this section, similar graphs with Figure 6.4.2 and Figure 6.4.4 are presented in Figure 7.2.5. It shows that for the cases based on the JONSWAP spectrum, the hybrid model can effectively switch from QSBI to ESBI, and then back to QSBI during each occurrence of rogue wave, e.g., Figure 7.2.5 (a)(b); While for that based on the Wallops spectrum, the hybrid model starts with ENLSE-5F, then to QSBI and/or ESBI, and switches back to with ENLSE-5F before the end of the simulations, e.g., Figure 7.2.5 (c)(d). It reveals that the numerical techniques for controlling the automatic switch between the three models is very effective.

Furthermore, in order to show that the hybrid model successfully captured the movement of the free surface when rogue waves occur, the free surface elevation at focusing time and location for the case $T_f/T_0 = 100\&500\&900$, are shown in Figure 7.2.6. It is seen that no visible difference can be observed between the results obtained by using the hybrid model and the ESBI, which indicates that the hybrid model is very accurate.

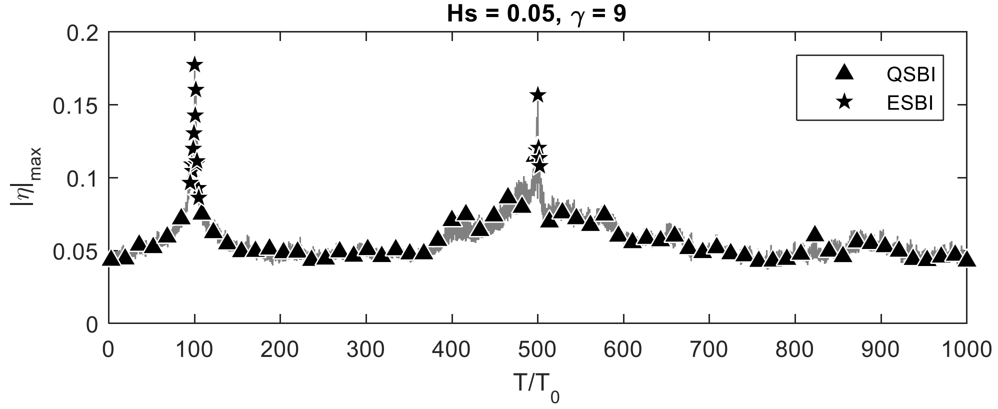

(a): $T_f/T_0 = 100\&500$

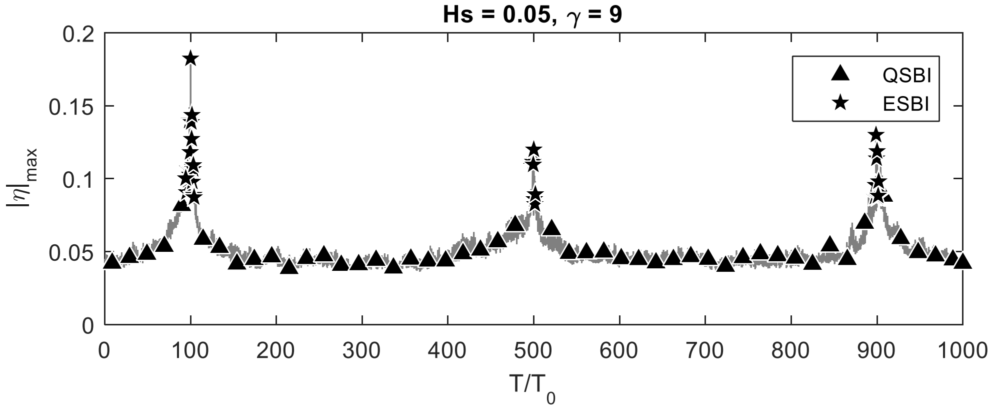

(b): $T_f/T_0 = 100\&500\&900$

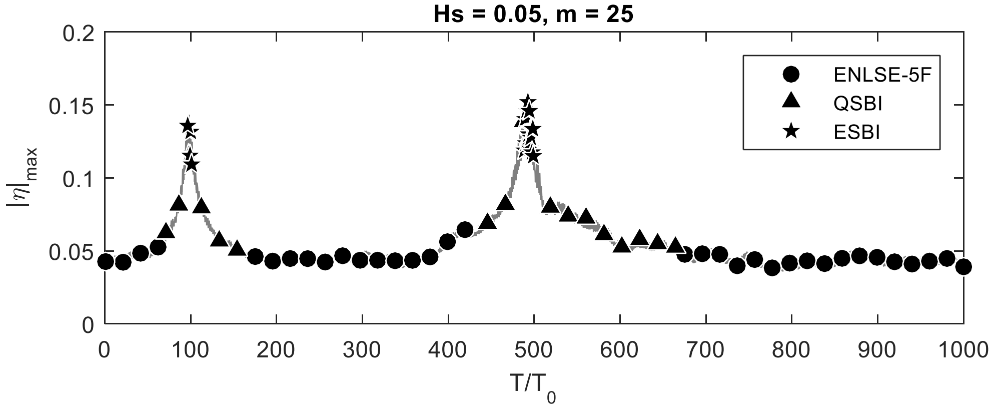

(c): $T_f/T_0 = 100\&500$

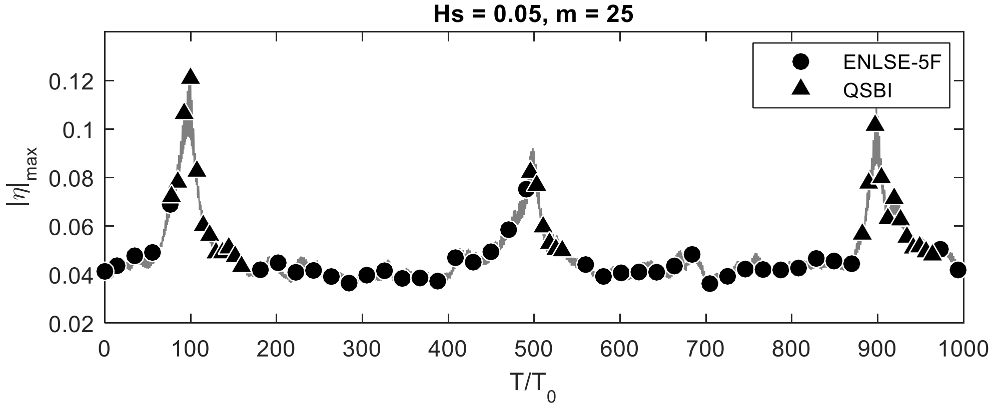

(d): $T_f/T_0 = 100\&500\&900$

Figure 7.2.5 Maximum wave elevations with indicator which model is used for the cases of different numbers of rogue waves in time domain

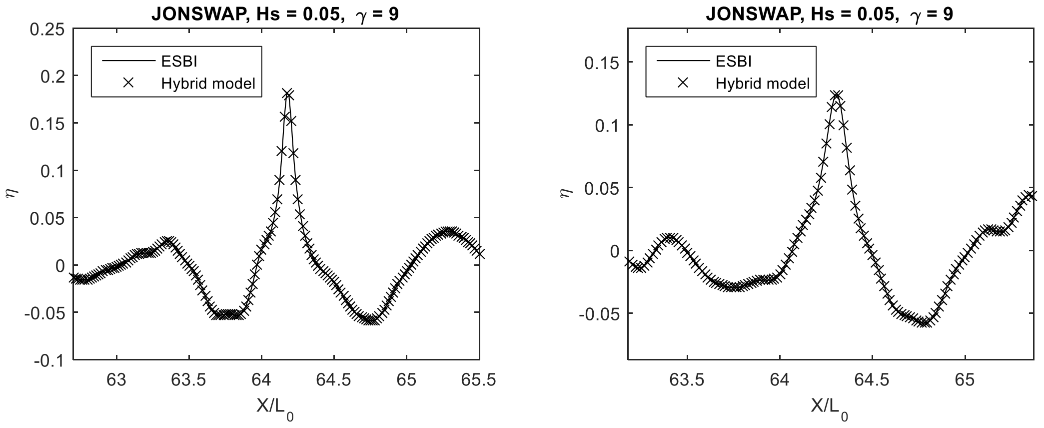

(a): $T/T_0 = 100$

(b): $T/T_0 = 500$

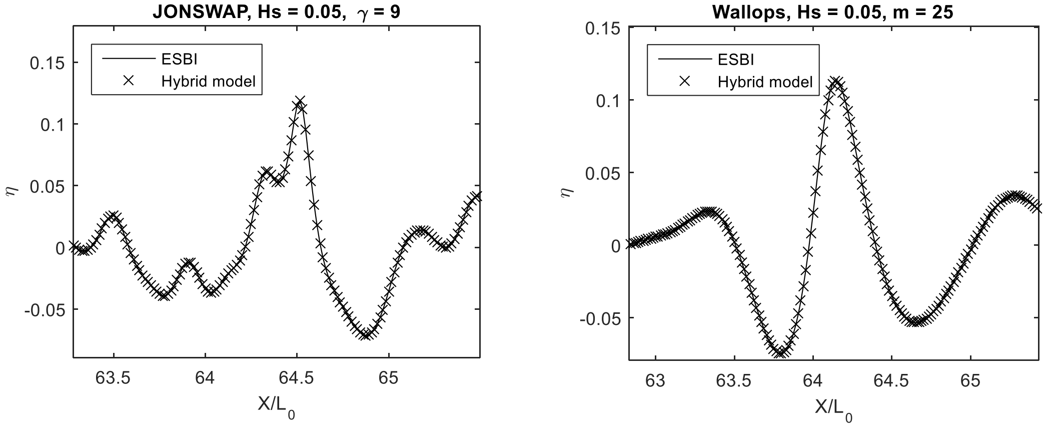

(c): $T/T_0 = 900$

(d): $T/T_0 = 100$

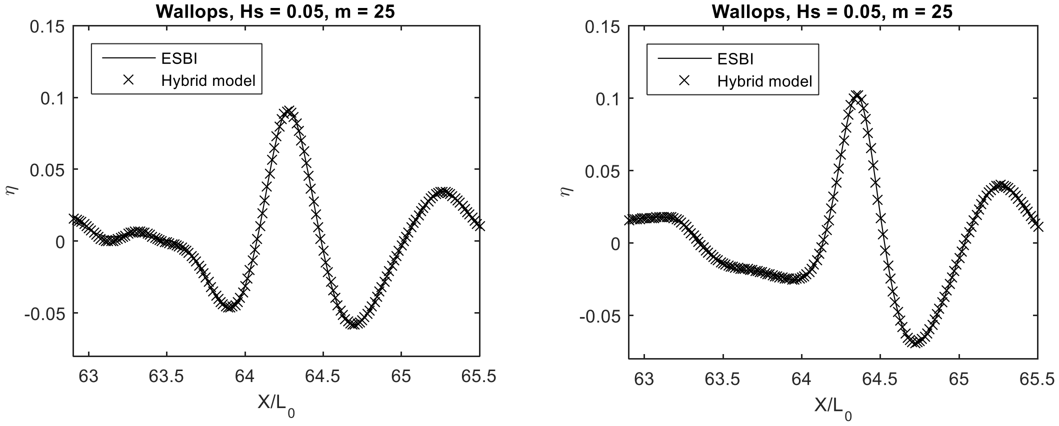

(e): $T/T_0 = 500$

(f): $T/T_0 = 900$

Figure 7.2.6 The profiles of the rogue waves for the cases of different numbers of rogue waves in time domain

7.2.3 Different numbers of rogue waves on space scale

Moreover, there are possibilities that several rogue waves can occur simultaneously but at different locations (Kharif, et al., 2009). Thus in this section, different numbers of rogue waves are generated at $T_f/T_0 = 100$, but at different locations. In addition to the case in which a single rogue wave occurs at $X_f/L_0 = 64$, two more cases of the twins occur at $X_f/L_0 = 32\&64$ and the triplets at $X_f/L_0 = 32\&64\&96$ are investigated. As aforementioned, the rogue wave height is fixed to $3H_s$ as there will not be energy left to generate the random background if three rogue wave higher than $3H_s$ are generated at the same time by using the method explained in (Wang, et al., 2015) and section 7.1. The basic set-ups are the same with that for Figure 6.3.1 and Figure 6.3.2. Again, the errors and the CPU ratios are shown in Figure 7.2.7.

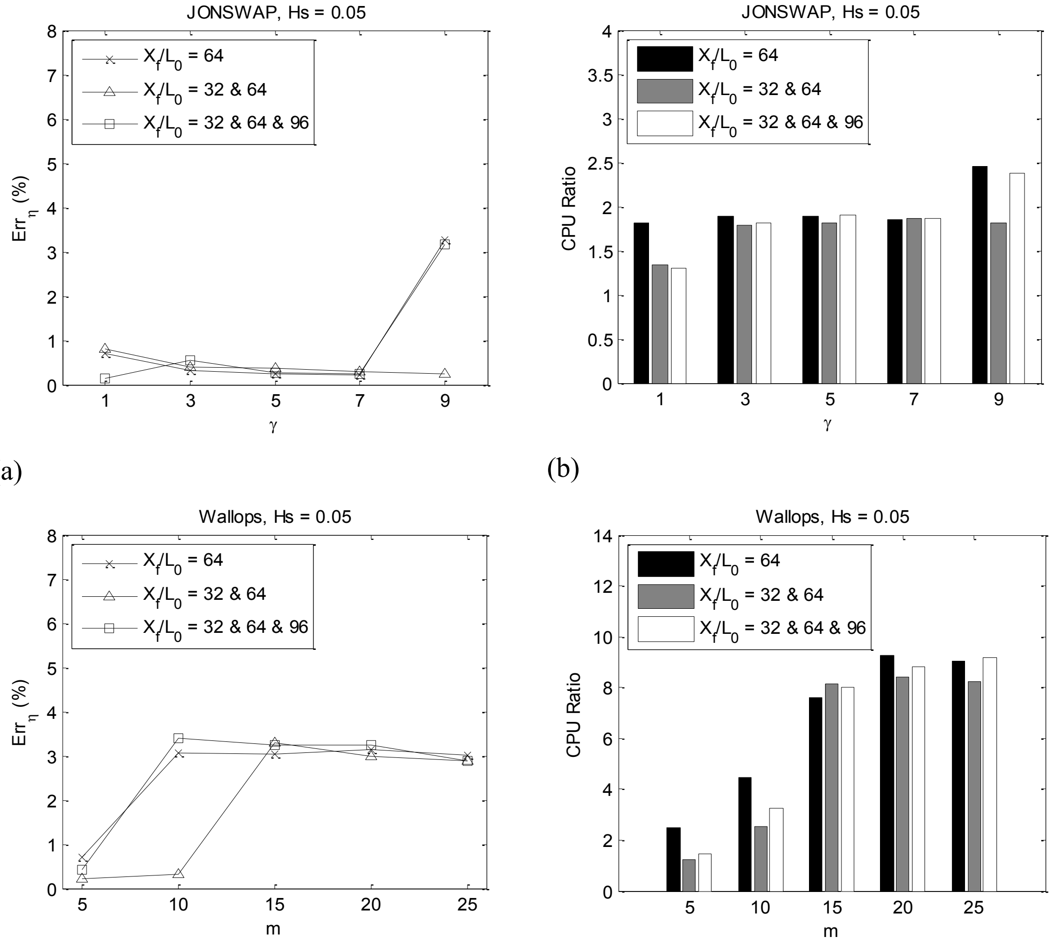

(a) (b)

(c) (d)

Figure 7.2.7 Err_η and CPU ratio (CPU time of ESBI/CPU time of hybrid model) for the cases of different amount of rogue waves on spatial scale

It is seen again that errors of all simulations considered in this section are less than 5%, which confirms that the values for the Tol_1 and Tol_2 controlling the switch between the models are appropriate for the cases with different embedded rogue waves on spatial scale.

According to Figure 7.2.7 (b), for the simulations based on the JONSWAP spectrum, the CPU ratios reach the highest, i.e., nearly 2.4~2.5, only for the cases $X_f/L_0 = 64$ and $X_f/L_0 = 32\&64\&96$ with $\gamma = 9$, due to the involvement of ENLSE-5F for a limited time steps and QSBI for the most of it. While for the cases $X_f/L_0 = 32\&64$ and $X_f/L_0 = 32\&64\&96$ with $\gamma = 1$, the majority of the duration is taken over by the ESBI, so that the computational efficiency of the hybrid model is comparable with the ESBI model, which leads to the CPU ratios approximated equal to 1.3~1.4. Apart from these cases, the majority of the duration is taken over by the QSBI, thus the CPU ratios are identically equal to 1.8, which indicates that the hybrid model still saves almost half the CPU time than the ESBI.

Meanwhile, the situations are totally different for the simulations based on the Wallops spectrum, as shown in Figure 7.2.7(d), especially when $m \geq 10$, the hybrid model is at least 8 times faster than the ESBI. In spite of the case $X_f/L_0 = 32\&64$ and $X_f/L_0 = 32\&64\&96$ with $m = 5$, in which the CPU ratios are between 1~1.5 due to that ESBI takes over the majority of the simulation, the rest of the cases are 2.5~4.5 times faster than the ESBI. So that the hybrid model is again proved to be more computational efficient than the ESBI.

The similar graphs with Figure 6.4.2 and Figure 6.4.4 are also presented in Figure 7.2.8, in order to illustrate the effectiveness of the numerical techniques for controlling the switch between each model. It shows that the hybrid model starts with the QSBI and switch to ESBI, then back to QSBI before the end of the simulation in Figure 7.2.8(a). Otherwise, the hybrid model begins with ENLSE-5F, switching to QSBI and/or ESBI when rogue waves occur, then ends with ENLSE-5F or QSBI, e.g., Figure 7.2.8(b)-(d). The various situations shown in Figure 7.2.8 indicate that the hybrid model can effectively switch between each model according to the intensity of the nonlinearities in order to achieve the highest computational efficiency. It is also worth of noting that only one extreme maximum free surface is observed in each case, due to that the rogue waves occur at the same time. Thus, it could be easily concluded that the switch is not affected by the numbers of the rogue waves happen at the same time, because the coupling scheme is carried out on the temporal scale.

Additionally, the free surface profiles at each focusing location for the case $X_f/L_0 = 32\&64\&96$ are shown in Figure 7.2.9. Although the fully focusing is not achieved at $X_f/L_0 = 96$ based on the Wallops spectrum in Figure 7.2.9(b), rogue waves are observed at the rest locations. And most importantly, the results obtained by using the hybrid model is consistent with that obtained by using the ESBI, which implies that the hybrid model has successfully captured the movement of the free surface, compared with the ESBI.

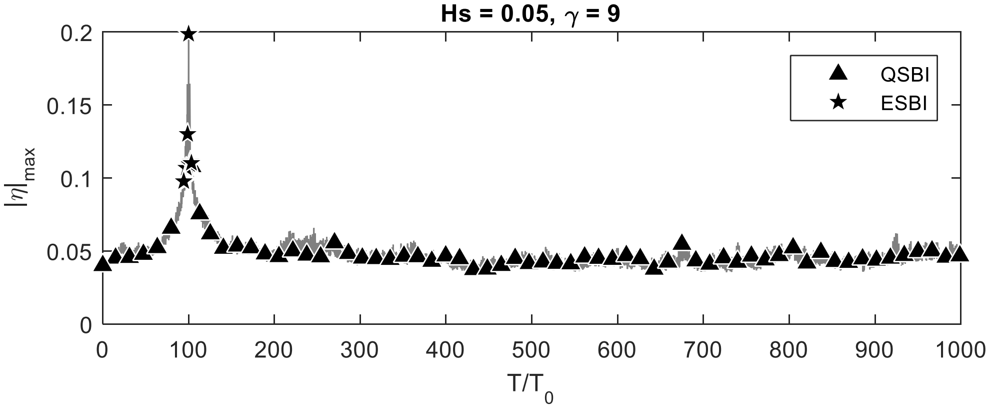

(a): $X_f/L_0 = 32\&64$

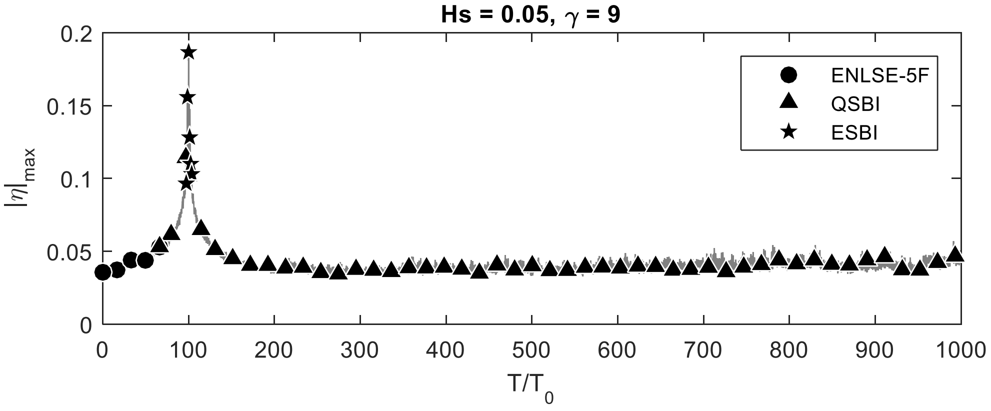

(b): $X_f/L_0 = 32\&64\&96$

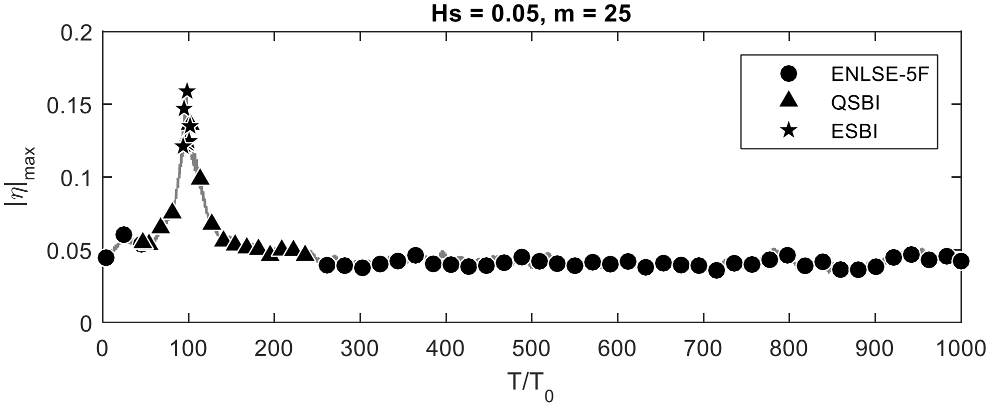

(c): $X_f/L_0 = 32\&64$

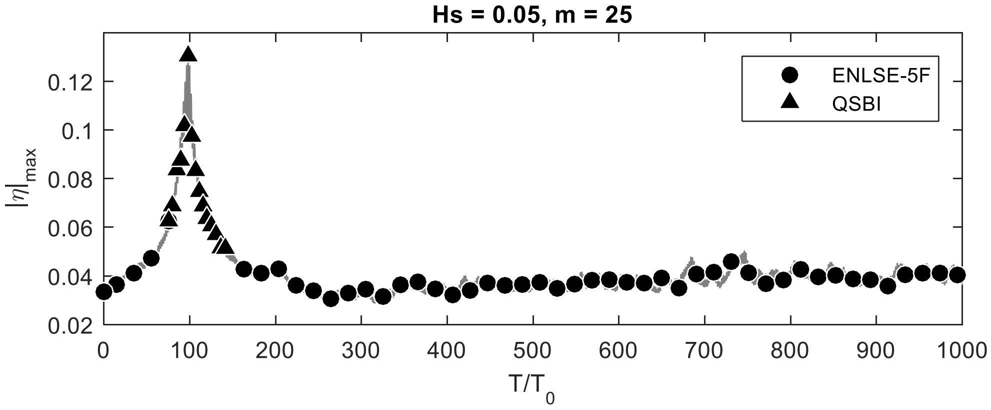

(d): $X_f/L_0 = 32\&64\&96$

Figure 7.2.8 Maximum wave elevations with indicator which model is used for the cases of different numbers of rogue waves in spatial domain

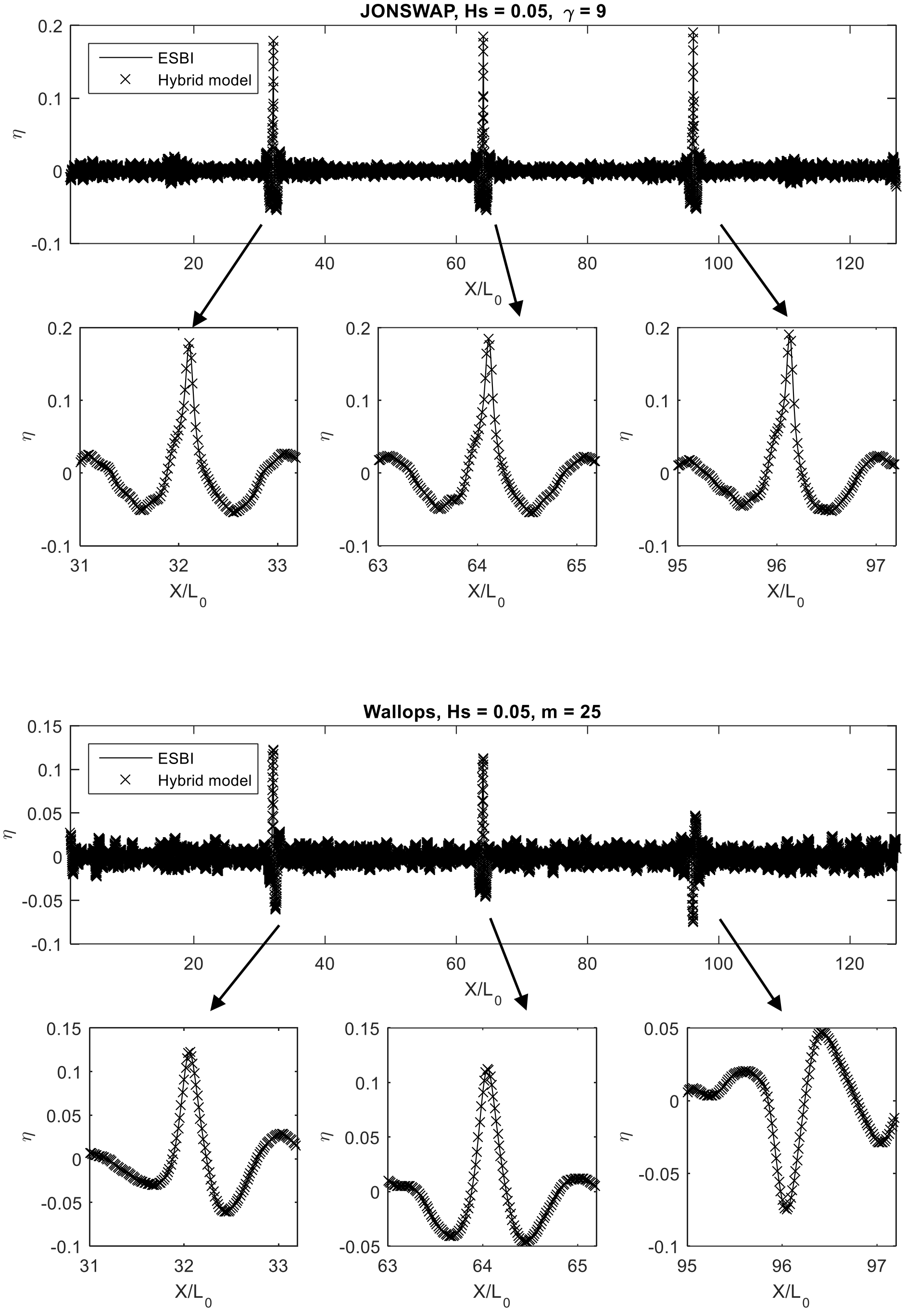

(a)

(b)

Figure 7.2.9 The profiles of the rogue waves for the cases of different numbers of rogue waves in spatial domain

7.3 Discussion

In this chapter, an improved technique for embedding rogue waves in random background is suggested and validated based on linear theory. The investigations suggest that the improved technique can effectively retain the features of the specified wave spectrum and remove spurious fluctuations in the original method by Kriebel & Alsina (2000). Then various cases are carried out to investigate the effectiveness of the new hybrid method, which include one rogue wave, two rogue waves and three rogue waves in time domain and in spatial domain based on two popular wave spectra – Wallops and JONSWAP spectra. The results show that for the same level of accuracy, the hybrid model significantly improved the computational efficiency, especially when the spectrum is narrow. In some cases, the hybrid model is more than 10 times faster than just using the ESBI method. For example, in the case $H_s = 0.05$ & $m = 25$ based on the Wallops spectrum embedded with a rogue wave of $2H_s$, the ESBI requires $2.8h$ while the hybrid model only need $16min$ to finish the simulation. The numerical simulations of random waves presented here aim to illustrate the computational efficiency of the hybrid model. To investigate statistics of random seas, the method suggested by Tucker, et al. (1984) should be used to generate the initial condition.

8 CONCLUSIONS AND RECOMMENDATIONS

8.1 Conclusions

In this thesis, a hybrid model coupling the ENLSE-5F, QSBI and ESBI is proposed to allow simulations of rogue waves in random deep sea on large space and time scales. The numerical implementation is very fast due to the application of the FFT. The instantaneous free surface spatial distribution is obtained at every time step in the Cartesian coordinate system by an Eulerian scheme, which means the free surface is a single valued function at a fixed location. It means that the current hybrid model cannot deal with wave overturning or breaking, more particularly, the scheme breaks at such points.

The most distinguishing feature of this hybrid model is that it is able to switch automatically between the three models, i.e., the ENLSE-5F, QSBI and ESBI, according to the local intensity of the nonlinearities. Techniques are developed to couple these models. When the wave steepness is mild and the nonlinearities are weak, the ENLSE-5F is adopted, which significantly accelerates the simulation. Meanwhile, if rogue waves start to occur, or the nonlinearities become relatively stronger, the QSBI will take over the simulation. In that case, the numerical simulation is still more efficient than by using the ESBI alone. Otherwise, if the waves are violent and the nonlinearities become very strong, the ESBI will be employed eventually. The converse also holds, after occurrence of the rogue waves, the sea state returns back to mild. Thus the ESBI will be replaced with the QSBI, and then by the ENLSE-5F again.

To be more specific, the contributions of this work are summarized as follows.

1) Based on the Higher Order Dysthe Equation suggested by Debsarma & Das (2005), the linear operator is replaced with the exact linear solution and thus the ENLSE-5H is proposed. This equation is based on the Hilbert transform and needs special techniques to deal with the Cauchy integral involved. To simplify computations, an equivalent formulation is obtained, i.e., the ENLSE-5F, which is based on the Fourier transform and easier to be solved numerically compared to its counterpart. The benefit of the ENLSE-5F is that the Hilbert transform is now replaced with the Fourier transform, and no need to estimating the Cauchy integral any more. In addition, FFT could be adopted to perform the Fourier transform, which is in accordance with the numerical implementation of the QSBI and ESBI model. Thus it makes the coupling procedure more straight forward.

2) The ESBI method is developed based on the original SBI method developed by Fructus, et al. (2005) and Grue (2010). In the SBI, the Neumann operator was introduced and expressed in terms of the free surface and the velocity potential. The kinematic and dynamic boundary conditions were reformulated into the skew-symmetric form after applying the Fourier transform. The free surface and velocity potential are updated through integrating the equations with respect to time, which requires the velocity on the free surface. The velocity on the free surface is decomposed into convolution parts and integration parts. Convolution parts are evaluated by FFT, and the integration parts have kernels decaying quickly along the distance between the source and field points but their integrands are weakly singular. The basic formulations are the same between the SBI and ESBI, except some numerical techniques are introduced in ESBI to improve the computational efficiency. The distinguishing features of the ESBI in chapter 5 include (a) A de-singularity technique is proposed to accelerate efficiently evaluating the integrals with weak singularity; (b) An anti-aliasing technique is developed to overcome the aliasing problem associated with Fourier Transform or Inverse Fourier Transform with a limited resolution; and (c) a technique for determining a critical value of the free surface slope, under which the integrals can be neglected so that the estimation of the vertical velocity only depends on FFT. These features significantly accelerate the computation, in particular when waves are strongly nonlinear. It is reported that in some cases, e.g., Figure 5.3.5, the ESBI is approximately 35 times faster than the SBI.

3) After review and compare the existing potential models, ENLSE-5F, QSBI and the ESBI are deliberately selected to be coupled. Firstly, techniques are developed to exchange data between those models, i.e., the transformation from A to η and ϕ, and transformation from η to A. Basic formulations are obtained and numerical procedures are suggested. Subsequently, numerical investigations are carried out in order to determine Tol_1 and Tol_2, which is the key to control the exchange between those models while guarantees the accuracy of the simulation is acceptable. Based on that, the hybrid model is validated, and the consistence between the numerical results obtained by using the hybrid model with that in the publications indicates the numerical techniques for coupling those models work very well. More evidence are provided in section 7.2 to illustrate the improvement on the computational efficiency. It is reported that the hybrid model suggested here could be 10 times faster than by using the ESBI alone in some cases.

8.2 Recommendations

Although hybrid model and the guidance for selecting the proper wave model are suggested in this thesis, there are still some questions unsolved, which will be left to future work.

1) In this thesis, the velocity potential for the QSBI and ESBI models is obtained by assuming it is a solution of the Schrödinger type equation, whereas the fully nonlinear solution of the velocity potential has not been proposed. This assumption will be problematic when the wave steepness is large due to that higher order nonlinear terms should be considered if the nonlinearities are strong. It is recommended that the fully nonlinear solution of the velocity potential can be estimated supposed that the free surface elevation is given.

2) At this stage, only deep water situation is considered. However, wave dynamics near shore is also a very important subject. The sea bed can significantly affect the evolution of near shore waves groups. It is also one of the most important factors to account for the rogue wave occurrence. Therefore, the hybrid model is suggested to be extended to finite water depth, including variable depth and moving depth. This can be accomplished by coupling the NLSE (Hasimoto & Ono, 1972) for constant depth or NLSE (Mei, 1983) for variable depth with fully nonlinear model.

3) This thesis only considers the evolution of the surface waves, however, the wave-structure interaction is another interesting and important topic in engineering practice. In order to make sure the marine structures are able to withstand hostile wave conditions, the wave force acting on the structure and the resulted responses should be examined. However, the present model is limited to such applications due to the difficulties in dealing with the discontinuous free surface. Thus, new numerical techniques should be introduced to overcome this problem.

4) In the present study, the effects of current is not involved. Nevertheless, the characteristics of random waves could be significantly changed if encountered with current. In addition, the opposing current also increases the possibility of the rogue wave occurrence. So wave-current interaction is also strongly recommended to be considered in the hybrid model. However, due to that only periodical boundary condition is allowed by using the hybrid model, the current cannot be modelled easily. This is because the velocity potential will not satisfy this boundary condition due to the existence of the current. Thus, the hybrid model should be extended to non-periodical situations by introducing new numerical techniques.

5) Additionally, due to the limitation of potential wave theory, breaking waves cannot be simulated. Thus the present hybrid model is only capable for simulating non-breaking waves. Once wave breaking occurs, the model collapses either. However, this dynamic feature can be captured by using the NS model. Thus, this hybrid model can be extended to involve the NS model in order to handle the local post-breaking stage.

6) Last but not least, a fast numerical technique for calculating wave kinematics inside of the fluid body is also of great interests. For example, by estimating the velocity and acceleration on

the wetted surface, forces on the structures can be calculated, which can be used for analyzing the responses of the structures under wave actions. Therefore such a numerical technique is very useful for engineering practices.

APPENDIX A

Equation (3.4.14) is re-written as

$$F\{V_3\} = \frac{K}{2\pi}F\left\{\int_{S_0} \tilde{\phi}'\left[1-(1+D^2)^{-3/2}\right]\nabla'\cdot\left[(\eta'-\eta)\nabla'\frac{1}{R}\right]d\boldsymbol{X}'\right\} \tag{A. 1}$$

The term involving in the local gradient is expanded in the Taylor series

$$1-(1+D^2)^{-3/2} = \frac{3}{2}D^2 - \frac{15}{8}D^4 + \frac{35}{16}D^6 \ldots \tag{A. 2}$$

Using it, V_3 becomes

$$\begin{aligned} F\{V_3\} = \frac{K}{2\pi}F\Bigg\{&\frac{3}{2}\int \tilde{\phi}'D^2\nabla'\cdot\left[(\eta'-\eta)\nabla'\frac{1}{R}\right]d\boldsymbol{X}' \\ &-\frac{15}{8}\int \tilde{\phi}'D^4\nabla'\cdot\left[(\eta'-\eta)\nabla'\frac{1}{R}\right]d\boldsymbol{X}' \\ &+\int \tilde{\phi}'\left[1-(1+D^2)^{-3/2}-\frac{3}{2}D^2+\frac{15}{8}D^4\right]\nabla' \\ &\cdot\left[(\eta'-\eta)\nabla'\frac{1}{R}\right]d\boldsymbol{X}'\Bigg\} \\ &= F\left\{V_3^{(1)}\right\} + F\left\{V_3^{(2)}\right\} + F\{V_{3,I}\} \end{aligned} \tag{A. 3}$$

where

$$\begin{aligned} F\left\{V_3^{(1)}\right\} = -\frac{K}{6}\Big[&Ki\boldsymbol{K}\cdot F\{\eta^3\nabla\tilde{\phi}\} - 3F\left\{\eta F^{-1}\left\{Ki\boldsymbol{K}\cdot F\{\eta^2\nabla\tilde{\phi}\}\right\}\right\} \\ &+ 3F\left\{\eta^2 F^{-1}\left\{Ki\boldsymbol{K}\cdot F\{\eta\nabla\tilde{\phi}\}\right\}\right\} \\ &+ F\left\{\eta^3 F^{-1}\left\{K^3 F\{\tilde{\phi}\}\right\}\right\}\Big] \end{aligned} \tag{A. 4}$$

and

$$\begin{aligned} F\left\{V_3^{(2)}\right\} = -\frac{K}{120}\Big[&\boldsymbol{iK}K^3\cdot F\{\eta^5\nabla\tilde{\phi}\} - 5F\left\{\eta F^{-1}\left\{\boldsymbol{iK}K^3\cdot F\{\eta^4\nabla\tilde{\phi}\}\right\}\right\} \\ &+ 10F\left\{\eta^2 F^{-1}\left\{\boldsymbol{iK}K^3\cdot F\{\eta^3\nabla\tilde{\phi}\}\right\}\right\} \\ &- 10F\left\{\eta^3 F^{-1}\left\{\boldsymbol{iK}K^3\cdot F\{\eta^2\nabla\tilde{\phi}\}\right\}\right\} \\ &+ 5F\left\{\eta^4 F^{-1}\left\{\boldsymbol{iK}K^3\cdot F\{\eta\nabla\tilde{\phi}\}\right\}\right\} \\ &+ F\left\{\eta^5 F^{-1}\left\{K^5 F\{\tilde{\phi}\}\right\}\right\}\Big] \end{aligned} \tag{A. 5}$$

Both Equations ((A. 4) and ((A. 5) differ from these by Grue (2010), though it can be proven that they are equivalent. The corresponding equations in Grue (2010) contain 7 and 11 terms in $V_3^{(1)}$ and $V_3^{(2)}$, respectively. Therefore the equations above need less calculation.

In order to estimate the leading order of $V_{3,I}$, the expansion goes further to the eighth order convolution

$$
\begin{aligned}
F\{V_{3,I}\} = \frac{K}{2\pi} F\Bigg\{ & \frac{35}{16}\int \tilde{\phi}'\nabla'\cdot\left[(\eta'-\eta)\nabla'\frac{1}{R}\right] D^6 d\boldsymbol{X}' \\
& + \int \tilde{\phi}'\left[1-(1+D^2)^{-3/2}-\frac{3}{2}D^2+\frac{15}{8}D^4-\frac{35}{16}D^6\right]\nabla' \\
& \cdot\left[(\eta'-\eta)\nabla'\frac{1}{R}\right] d\boldsymbol{X}'\Bigg\} \qquad \text{(A. 6)} \\
= F\left\{V_3^{(3)}\right\} + \frac{K}{2\pi}F\Bigg\{ & \int \tilde{\phi}'\left[1-(1+D^2)^{-3/2}-\frac{3}{2}D^2+\frac{15}{8}D^4-\frac{35}{16}D^6\right]\nabla' \\
& \cdot\left[(\eta'-\eta)\nabla'\frac{1}{R}\right] d\boldsymbol{X}'\Bigg\}
\end{aligned}
$$

where

$$
\begin{aligned}
F\left\{V_3^{(3)}\right\} &= \frac{K}{2\pi}F\left\{\frac{35}{16}\int \tilde{\phi}'\nabla'\cdot\left[(\eta'-\eta)\nabla'\frac{1}{R}\right] D^6 d\boldsymbol{X}'\right\} \\
&= -\frac{K}{5040}\Big[i\boldsymbol{K}K^5\cdot F\{\eta^7\nabla\tilde{\phi}\} - 7F\left\{\eta F^{-1}\left\{i\boldsymbol{K}K^5\cdot F\{\eta^6\nabla\tilde{\phi}\}\right\}\right\} \\
&\quad + 21F\left\{\eta^2F^{-1}\left\{i\boldsymbol{K}K^5\cdot F\{\eta^5\nabla\tilde{\phi}\}\right\}\right\} \\
&\quad - 35F\left\{\eta^3F^{-1}\left\{i\boldsymbol{K}K^5\cdot F\{\eta^4\nabla\tilde{\phi}\}\right\}\right\} \qquad \text{(A. 7)} \\
&\quad + 35F\left\{\eta^4F^{-1}\left\{i\boldsymbol{K}K^5\cdot F\{\eta^3\nabla\tilde{\phi}\}\right\}\right\} \\
&\quad - 21F\left\{\eta^5F^{-1}\left\{i\boldsymbol{K}K^5\cdot F\{\eta^2\nabla\tilde{\phi}\}\right\}\right\} \\
&\quad + 7F\left\{\eta^6F^{-1}\left\{i\boldsymbol{K}K^5\cdot F\{\eta\nabla\tilde{\phi}\}\right\}\right\} + F\left\{\eta^7F^{-1}\left\{K^7F\{\tilde{\phi}\}\right\}\right\}\Big]
\end{aligned}
$$

Therefore

$$
\begin{aligned}
V_3^{(3)} = -\frac{1}{5040} F^{-1}\Big\{ & i\boldsymbol{K}K^6 \cdot F\{\eta^7 \nabla \tilde{\phi}\} - 7KF\Big\{\eta F^{-1}\Big\{i\boldsymbol{K}K^5 \cdot F\{\eta^6 \nabla \tilde{\phi}\}\Big\}\Big\} \\
& + 21KF\Big\{\eta^2 F^{-1}\Big\{i\boldsymbol{K}K^5 \cdot F\{\eta^5 \nabla \tilde{\phi}\}\Big\}\Big\} \\
& - 35KF\Big\{\eta^3 F^{-1}\Big\{i\boldsymbol{K}K^5 \cdot F\{\eta^4 \nabla \tilde{\phi}\}\Big\}\Big\} \\
& + 35KF\Big\{\eta^4 F^{-1}\Big\{i\boldsymbol{K}K^5 \cdot F\{\eta^3 \nabla \tilde{\phi}\}\Big\}\Big\} \\
& - 21KF\Big\{\eta^5 F^{-1}\Big\{i\boldsymbol{K}K^5 \cdot F\{\eta^2 \nabla \tilde{\phi}\}\Big\}\Big\} \\
& + 7KF\Big\{\eta^6 F^{-1}\Big\{i\boldsymbol{K}K^5 \cdot F\{\eta \nabla \tilde{\phi}\}\Big\}\Big\} \\
& + KF\Big\{\eta^7 F^{-1}\Big\{K^7 F\{\tilde{\phi}\}\Big\}\Big\}\Big\}
\end{aligned}
\qquad (\text{A. }8)
$$

For $\eta = \varepsilon cosX$, $\tilde{\phi} = \varepsilon sinX$ and $V = \varepsilon sinX$, one can obtain

$$
\begin{aligned}
& F^{-1}\Big\{K^6 F\{\nabla \cdot (\eta^7 \nabla \tilde{\phi})\}\Big\} \\
& = -8\varepsilon^8 \frac{1}{128}[8^6 \sin(8X) + 6^7 \sin(6X) + 14 \times 4^6 \sin(4X) + 14 \\
& \qquad \times 2^6 \sin(2X)]
\end{aligned}
\qquad (\text{A. }9)
$$

$$
\begin{aligned}
& F^{-1}\Big\{-7KF\Big\{\eta F^{-1}\Big\{K^5 F\{\nabla \cdot (\eta^6 \nabla \tilde{\phi})\}\Big\}\Big\}\Big\} \\
& = 7^2 \varepsilon^8 \frac{1}{128}[8 \times 7^5 \sin(8X) + 6(7^5 + 5^6) \sin(6X) + 4(5^6 + 3^7) \sin(4X) \\
& \qquad + 2(3^7 + 5) \sin(2X)]
\end{aligned}
\qquad (\text{A. }10)
$$

$$
\begin{aligned}
& F^{-1}\Big\{21KF\Big\{\eta F^{-1}\Big\{K^5 F\{\nabla \cdot (\eta^6 \nabla \tilde{\phi})\}\Big\}\Big\}\Big\} \\
& = -6\varepsilon^6 \frac{21}{128}[6^5 \times 8 \sin(8X) + 6(2 \times 6^5 + 4^6) \sin(6X) \\
& \qquad + 4(6^5 + 2 \times 4^6 + 5 \times 2^5)\sin(4X) \\
& \qquad + 2(4^6 + 5 \times 2^6) \sin(2X)]
\end{aligned}
\qquad (\text{A. }11)
$$

$$
\begin{aligned}
& F^{-1}\Big\{-35KF\Big\{\eta^3 F^{-1}\Big\{K^5 F\{\nabla \cdot (\eta^4 \nabla \tilde{\phi})\}\Big\}\Big\}\Big\} \\
& = 5\varepsilon^5 \frac{35}{128}[8 \times 5^5 \sin(8X) + 6(3 \times 5^5 + 3^6) \sin(6X) \\
& \qquad + 4(3 \times 5^5 + 3 \times 3^6 + 2)\sin(4X) \\
& \qquad + 2(5^5 + 3 \times 3^6 + 4) \sin(2X)]
\end{aligned}
\qquad (\text{A. }12)
$$

$$
F^{-1}\Big\{35KF\Big\{\eta^4 F^{-1}\Big\{K^5 F\{\nabla \cdot (\eta^3 \nabla \tilde{\phi})\}\Big\}\Big\}\Big\} \qquad (\text{A. }13)
$$

$$
\begin{aligned}
&= -4\varepsilon^{8}\frac{35}{128}[8\times 4^{5}\sin(8X) + 6(4^{6}+2^{6})\sin(6X) \\
&\qquad + 4(6\times 4^{5} + 4\times 2^{6})\sin(4X) + 2(4^{6}+5\times 2^{6})\sin(2X)]
\end{aligned}
$$

$$
\begin{aligned}
&F^{-1}\left\{-21KF\left\{\eta^{5}F^{-1}\left\{K^{5}F\{\nabla\cdot\left(\eta^{2}\nabla\tilde{\phi}\right)\}\right\}\right\}\right\} \\
&= 3\varepsilon^{8}\frac{21}{128}[8\times 3^{5}\sin(8X) + 6(5\times 3^{5}+1)\sin(6X) \\
&\qquad + 4(10\times 3^{5}+4)\sin(4X) + 2(9\times 3^{5}+5)\sin(2X)]
\end{aligned}
\tag{A. 14}
$$

$$
\begin{aligned}
&F^{-1}\left\{7KF\left\{\eta^{6}F^{-1}\left\{K^{5}F\{\nabla\cdot\left(\eta\nabla\tilde{\phi}\right)\}\right\}\right\}\right\} \\
&= -2^{5}\varepsilon^{8}\frac{7}{64}(8\sin(8X) + 6^{2}\sin(6X) + 14\times 4\sin(4X) + 14\times 2\sin(2X))
\end{aligned}
\tag{A. 15}
$$

$$
\begin{aligned}
&F^{-1}\left\{KF\left\{\eta^{7}F^{-1}\left\{K^{7}F\{\tilde{\phi}\}\right\}\right\}\right\} \\
&= \varepsilon^{8}\frac{1}{128}(8\sin(8X) + 36\sin(6X) + 56\sin(4X) + 28\sin(2X))
\end{aligned}
\tag{A. 16}
$$

Therefore, the summation of the terms above gives

$$
\begin{aligned}
V_{3}^{(3)} &= -\frac{1}{5040}\frac{\varepsilon^{8}}{128}[-17388\sin(2X) + 3024\sin(4X) - 12\sin(6X)] \\
&\sim \frac{69}{2560}\varepsilon^{8}\sin(2X)
\end{aligned}
\tag{A. 17}
$$

Similarly, the local gradient term of V_4 in Eq.(3.4.17),

$$
V_{4} = F^{-1}\left\{\frac{K}{2\pi}F\left\{\int_{S_0}\frac{V'}{R}\left(1-\frac{1}{\sqrt{1+D^{2}}}\right)d\boldsymbol{X}'\right\}\right\}
\tag{A. 18}
$$

can also be expanded in the Taylor series

$$
1-\frac{1}{\sqrt{1+D^{2}}} = \frac{1}{2}D^{2} - \frac{3}{8}D^{4} + \frac{5}{16}D^{6} + \cdots
\tag{A. 19}
$$

Then this integration of V_4 could be rewritten as

$$
\begin{aligned}
F\{V_{4}\} &= \frac{K}{2\pi}F\left\{\int\frac{V'}{R}\frac{1}{2}D^{2}d\boldsymbol{X}' - \int\frac{V'}{R}\frac{3}{8}D^{4}d\boldsymbol{X}' + \int\frac{V'}{R}\frac{5}{16}D^{6}d\boldsymbol{X}'\right. \\
&\qquad \left. + \int\frac{V'}{R}\left(1-\frac{1}{\sqrt{1+D^{2}}} - \frac{1}{2}D^{2} + \frac{3}{8}D^{4} - \frac{5}{16}D^{6}\right)d\boldsymbol{X}'\right\} \\
&= F\left\{V_{4}^{(1)}\right\} + F\left\{V_{4}^{(2)}\right\} + F\left\{V_{4}^{(3)}\right\} + F\{V_{4,I}\}
\end{aligned}
\tag{A. 20}
$$

where

$$
\begin{aligned}
F\left\{V_{4}^{(1)}\right\} = -\frac{K}{2}&\left[KF\{\eta^{2}V\} - 2F\left\{\eta F^{-1}\{KF\{\eta V\}\}\right\}\right. \\
&\left. + F\left\{\eta^{2}F^{-1}\{KF\{V\}\}\right\}\right]
\end{aligned}
\tag{A. 21}
$$

$$F\left\{V_4^{(2)}\right\} = -\frac{K}{24}\Big[K^3F\{V\eta^4\} - 4F\left\{\eta F^{-1}\{K^3F\{V\eta^3\}\}\right\}$$
$$+ 6F\left\{\eta^2F^{-1}\{K^3F\{V\eta^2\}\}\right\} \tag{A. 22}$$
$$- 4F\left\{\eta^3F^{-1}\{K^3F\{V\eta\}\}\right\} + F\left\{\eta^4F^{-1}\{K^3F\{V\}\}\right\}\Big]$$

$$F\left\{V_4^{(3)}\right\} = \frac{-K}{720}\Big[K^5F\{V\eta^6\} - 6F\left\{\eta F^{-1}\left\{K^5F\{V\eta^5\}\right\}\right\}$$
$$+ 15F\left\{\eta^2F^{-1}\left\{K^5F\{V\eta^4\}\right\}\right\}$$
$$- 20F\left\{\eta^3F^{-1}\left\{K^5F\{V\eta^3\}\right\}\right\} \tag{A. 23}$$
$$+ 15F\left\{\eta^4F^{-1}\left\{K^5F\{V\eta^2\}\right\}\right\}$$
$$- 6F\left\{\eta^5F^{-1}\left\{K^5F\{V\eta\}\right\}\right\} + F\left\{\eta^6F^{-1}\left\{K^5F\{V\}\right\}\right\}\Big]$$

$F\left\{V_4^{(1)}\right\}$ is the same as that in Fructus, et al. (2005). The other two, corresponding to the fifth and seventh order convolutions are consistent with these in Grue (2010). The evaluation of V_4 is implicit due to the involvement of V and needs to be determined by iterations.

APPENDIX B

Trulsen & Dysth (1996) have given the coefficients for each harmonic of the surface elevation and velocity potential, corresponding to the first kind of NLSE in terms of B, i.e., Eq. (3.2.13)-(3.2.17). However, since the ENLSE-5F in this study is an equation in terms of A, the solution by using Eq. (3.2.13)-(3.2.17) is not straightforward. According to Hogan's substitution (Hogan, 1985), i.e., $B = -iA + \frac{1}{2}\frac{\partial A}{\partial X}$, replace which into the expression for each harmonic coefficient and keep the appearance to the third order, then one has for Eq.(3.2.14)

$$A_2 = \frac{1}{2}A^2 - \frac{i}{2}A\frac{\partial A}{\partial X} + \frac{3}{8}A\frac{\partial^2 A}{\partial X^2} + \frac{1}{4}A\frac{\partial^2 A}{\partial Y^2} - \frac{3}{4}\left(\frac{\partial A}{\partial Y}\right)^2 \qquad \text{(B. 1)}$$

For Eq.(3.2.15)

$$A_3 = -\frac{3i}{8}B^3 = -\frac{3i}{8}\left(-A^2 - iA\frac{\partial A}{\partial X}\right)\left(-iA + \frac{1}{2}\frac{\partial A}{\partial X}\right) \approx \frac{3}{8}A^3 \qquad \text{(B. 2)}$$

For Eq.(3.2.17), where

$$|B|^2 = \left(-iA + \frac{1}{2}A_X\right)\left(iA^* + \frac{1}{2}A_X^*\right) \approx |A|^2 - \frac{i}{2}AA_X^* + \frac{i}{2}A^*A_X \qquad \text{(B. 3)}$$

Substitute Eq.(B. 3) and Eq.(3.2.9) into Eq.(3.2.17) and neglecting higher order terms

$$\bar{\eta} = F^{-1}\left\{-i\frac{\kappa}{K}F\{real(A^*A_T)\}\right\} - \frac{1}{16}\frac{\partial^2|A|^2}{\partial X^2} - \frac{1}{8}\frac{\partial^2|A|^2}{\partial Y^2} \qquad \text{(B. 4)}$$

Now all the harmonic coefficients are obtained for transforming A to η, next the coefficients for transforming A to ϕ will be introduced. Since $\bar{\phi}$ has already been obtained as given by Eq.(3.2.9), and $B_3 = 0$, the first harmonic coefficient B and second harmonic coefficient B_2 remain unknown, which will be formulated.

Based on the NLSE of first kind to the third order (Zakharov, 1968), i.e.,

$$\frac{1}{2}\frac{\partial B}{\partial X} + \frac{i}{8}\frac{\partial^2 B}{\partial X^2} - \frac{1}{16}\frac{\partial^3 B}{\partial X^3} = -\frac{\partial B}{\partial T} - \frac{i}{2}|B|^2B \qquad \text{(B. 5)}$$

substitute which into Eq.(3.2.13), one has

$$A = iB - \frac{\partial B}{\partial T} - \frac{3\mathrm{i}}{8}|B|^2B \qquad \text{(B. 6)}$$

This expression is consistent with Mei's deduction (Mei, 1983). Meanwhile, the exact linear solution admits

$$\frac{\partial B}{\partial T} = F^{-1}\{i(1-\omega)F\{B\}\} \qquad \text{(B. 7)}$$

substitute which into Eq.(B. 6),

$$A = iB + F^{-1}\{i(\omega - 1)F\{B\}\} - \frac{3\mathrm{i}}{8}|B|^2B = F^{-1}\{i\omega F\{B\}\} - \frac{3\mathrm{i}}{8}|B|^2B \tag{B. 8}$$

Re-arrange Eq.(B. 8)

$$F^{-1}\{i\omega F\{B\}\} = A + \frac{3i}{8}|B|^2B \approx A + \frac{3}{8}|A|^2A \tag{B. 9}$$

and make B explicit

$$B = F^{-1}\left\{\frac{-i}{\omega}F\left\{A + \frac{3}{8}|A|^2A\right\}\right\} \tag{B. 10}$$

Now the first harmonic coefficient B for velocity potential is obtained. Similarly, the second harmonic coefficient for the velocity potential can be reformulated as

$$B_2 = -\frac{i}{2}A\frac{\partial^2 A}{\partial Y^2} + \frac{i}{2}\left(\frac{\partial A}{\partial Y}\right)^2 \tag{B. 11}$$

APPENDIX C

It is known that

$$\eta_1 = \frac{1}{2}\left[Ae^{i(X-T)} + c.c.\right] \tag{C. 1}$$

The 1st harmonic could also be described as the summation of various components

$$\eta_1 = \sum_{j=1}^{N/2} \frac{1}{2}\left(\Lambda_j e^{iK_jX} + c.c.\right) \tag{C. 2}$$

Assume $\Lambda_j = p_j + iq_j$, where p and q are real functions of X, then

$$\eta_1 = \sum_{j=1}^{N/2} \frac{1}{2}\left(\Lambda_j e^{iK_jX} + c.c.\right) = \sum_{j=1}^{N/2}\left(p_i \cos\left(K_jX\right) + q_i \sin\left(K_jX\right)\right) \tag{C. 3}$$

Applying 1D Hilbert transform $\hbar\{\eta_1(X)\} = \frac{1}{\pi}\int_{-\infty}^{\infty} \frac{\eta_1(X')}{X'-X} dX'$ to η_1 gives

$$\hbar\{\eta_1\} = \sum_{j=1}^{N/2}\left(-p_i \sin\left(K_jX\right) + q_i \cos\left(K_jX\right)\right) \tag{C. 4}$$

Therefore

$$\begin{aligned} \sum_{j=1}^{N/2} \Lambda_j e^{iK_jX} = \sum_{j=1}^{N/2} &\Big[p_i \cos\left(K_jX\right) + q_i \sin\left(K_jX\right) \\ &- i\left(-p_i \sin\left(K_jX\right) + q_i \cos\left(K_jX\right)\right)\Big] = \eta_1 - i\hbar\{\eta_1\} \\ &= Ae^{i(X-T)} \end{aligned} \tag{C. 5}$$

Thus

$$A = e^{-i(X-T)}\left(\eta_1 - i\hbar\{\eta_1\}\right) \tag{C. 6}$$

Note that $\hbar\{\eta_1\} = F^{-1}\{i\, sgn(\kappa) F\{\eta_1\}\}$, then the equation above becomes

$$\begin{aligned} A &= e^{-i(X-T)}\left(\eta_1 - iF^{-1}\{i\, sgn(\kappa) F\{\eta_1\}\}\right) \\ &= e^{-i(X-T)}\left(\eta_1 + F^{-1}\{sgn(\kappa) F\{\eta_1\}\}\right) \end{aligned} \tag{C. 7}$$

APPENDIX D

Many experimental and numerical investigations have been carried out to study the rogue wave generation and propagation (Ma, 2008b; Adcock & Yan, 2010; Adcock, et al., 2011), their interaction with wind (Touboul, et al., 2006; Yan & Ma, 2011) and current (Touboul, et al., 2007; Wu & Yao, 2004; Yan, et al., 2010). In most of the studies, the rogue waves are generated by using spatial-temporal focusing approach, which often targets that the entire wave energy is fully focused at the same time and the same location. Such studies significantly contribute to the wave kinematics and dynamics associated with the giant wave during a short window of time near its occurrence, but do not reflect the real situation that the observed rogue waves are always embedded with the random waves, formed from random sea states following the statistic behavior of random sea. It has been reported that the rogue wave generated in such a way shows an unrealistic sea state, which is out of the range of values in any filed observations of rogue waves (Kriebel & Alsina, 2000). Alternatively, a direct random sea simulation may well reflect the statistical feature of field observation of rogue waves. Nevertheless, it may need a long duration covering $10^3 \sim 10^5$ individual waves to observe the occurrence of rogue waves, which usually have exceedance probabilities ranging from 10^{-3} to 10^{-5} (Adcock & Taylor, 2014). More importantly, the occurrence of the rogue waves generated in this way is random and unpredictable in a time domain numerical simulation or experiment.

In order to constrain the occurrence of a rogue wave in a limited space during a predictable timeframe, Taylor, et al. (1997) proposed a Constrained NewWave (CNW) theory using a linear Gaussian random process, which assembles both the random and the deterministic quantities in order to achieve (1) both the mean and the covariance of the random process to realize a random sea are identical to the leading order terms in both the exact solution of the expected profile around the maximum of height by Lindgren (1970) and the NewWave theory; and (2) In the region of constraint, the local variances is minimized so that it is as deterministic as possible to approximate asymptotic forms of extreme wave profiles that are indistinguishable from a purely random occurrence of that particular crest. The ensemble statistics of the constrained realization by this approach matches those of purely random occurrences of large waves. Clauss & Steinhagen (2000) developed a Sequential Quadratic Programming method to optimize the location and time instant of the maximum crest in space and time domain respectively for the purpose of re-producing an expected asymmetric wave profile. They considered a random phase spectrum, which is routinely ignored in Gaussian random wave model, and concluded that the random character of the optimized sea state is not completely lost. Funke & Mansard (1982), Zou & Kim (2000) and Kim (2008) suggested a method to deform the largest crest/trough wave in order to produce an asymmetric profile of the free surface in a constrained region of a random time history, which was obtained through specifying random phases. However, one drawback of these methods is that a targeted local wave profile or a tailored time history, as the constrained condition, must be specified. Such constrain is very variable and may not be easily deterministically obtained prior to the numerical prediction. In addition, a stationary wave spectrum is usually considered by using the above approaches. This means that the local and rapid spectral changes following the evolution of large ocean waves cannot be fully considered during the locally constraint process (Baldock, et al., 1996; Gibson & Swan, 2007).

In addition to the methods mentioned above, Kriebel & Alsina (2000) developed another approach to generate rogue waves in random seas. Attributing to the success in generating temporal-spatial focusing extreme wave in laboratory or numerical investigations (Baldock, et al., 1996), Kriebel & Alsina (2000) proposed to divide the specified spectrum into two parts: the phases of wave components in one part (referred to as the focusing part) are carefully assigned leading to a spatial-temporal focusing wave group; those of the second part (referred to as the random part) are randomly assigned to form the random background. This approach acknowledges the fact that not all wave energy is focused at the same location. This approach does not need a pre-determined local wave profile or tailored time history to constrain the occurrence of the rogue wave. As a result, it may be more feasible to investigate the nonlinear evolution of the rogue waves and to explore the variation of the wave profile following the occurrence of the rogue waves. The experimental investigation by Kriebel & Alsina (2000) demonstrated that a spatial-temporal focus of 15% spectral wave energy (the remaining part still behaves as a random sea) may lead to the occurrence of the rogue waves in a realistic sea, i.e. the highest wave height is about 2.24 H_s (the largest wave amplitude reaches 1.18 H_s) and the probability distribution of wave amplitudes largely follows the Rayleigh distribution with an abnormality representing the occurrence of the rogue wave.

Unlike the CNW theory, Kriebel & Alsina's approach (2000), as well as the Sequential Quadratic Programming method by Clauss & Steinhagen (2000), the local crest/trough distortion method by Funke & Mansard (1982) and Zou & Kim (2000) adopted deterministic wave amplitudes and random phase spectra. In such a way, some randomness of the sea state may be lost, unless sufficiently large number of wave components is adopted, according to Tucker, et al. (1984). Nevertheless, it may be practical for deterministic or short-term statistic studies. It is also worth noting that there is not limit in Kriebel & Alsina's approach (2000) on specifying the wave amplitudes and the number of wave components. The randomness of the real sea state may be largely reserved through introducing random wave amplitudes or increasing the number of wave components.

However, the linear analysis indicates that the approach developed by Kriebel & Alsina (2000) numerically modifies the spectral density distribution unless the phases of the random part satisfying a certain condition. This typically results in a significantly random fluctuation of the spectral density distribution. Unlike the random oscillation observed in the Gaussian random process, e.g. the CNW theory, the random fluctuation in the Kriebel & Alsina's approach (2000) is not physical but numerical due to improperly assembling the random and focusing parts. It may be smoothed numerically with undesirable energy loss. To overcome the problem, Wang, et al. (2015) improved this method through introducing a correction term when assembling the random and the focusing parts, which is adopted in this study.

APPENDIX E

The author's publications by the date of submitting this thesis are listed below:

[1] Wang, J. & Ma, Q. W., 2015a. Numerical techniques on improving computational efficiency of Spectral Boundary Integral Method. *International Journal for Numerical Methods in Engineering,* 102(10), pp. 1638-1669.

[2] Wang, J. & Ma, Q. W., 2015b. Numerical Investigation on Limitation of Boussinesq Equation for Generating Focusing Waves. *Procedia Engineering,* Volume 126, pp. 597-601.

[3] Wang, J., Yan, S. & Ma, Q. W., 2015. An Improved Technique to Generate Rogue Waves in Random Sea. *Computer Modeling in Engineering & Sciences,* 106(4), pp. 263-289.

[4] Wang, J., Ma, Q. W. & Yan, S., 2015. A hybrid model for simulating rogue waves in random seas on a large time and space scale. *Journal of Computational Physics.* (In press)

REFERENCES

Abbott, M. B., McCowan, A. D. & Warren, I. R., 1984. Accuracy of short-wave numerical models. *Journal of Hydraulic Engineering,* 110(10), pp. 1287-1301.

Adcock, T. A. A. & Taylor, P. H., 2009. Focusing of unidirectional wave groups on deep water: an approximate nonlinear Schrödinger equation-based model. *Proceedings of the Royal Society of London A: Mathematical, Physical and Engineering Sciences,* 465(2110), pp. 3083-3102.

Adcock, T. A. A. & Taylor, P. H., 2014. The physics of anomalous ('rogue') ocean waves. *Reports on Progress in Physics,* 77(10), p. 105901.

Adcock, T. A. A., Taylor, P. H., Yan, S., Ma, Q. W., & Janssen, P. A. E. M., 2011. Did the Draupner wave occur in a crossing sea?. *Proceedings of the Royal Society of London A: Mathematical, Physical and Engineering Sciences,* 467(2134), pp. 3004-3021.

Adcock, T. A. A. & Yan, S., 2010. The focusing of uni-directional Gaussian wave-groups in finite depth: an approximate NLSE based approach. *ASME 2010 29th International Conference on Ocean, Offshore and Arctic Engineering,* Issue American Society of Mechanical Engineers, pp. 569-576.

Agnon, Y., Madsen, P. A. & Schäffer, H. A., 1999. A new approach to high-order Boussinesq models. *Journal of Fluid Mechanics,* Volume 399, pp. 319-333.

Airy, G. B., 1845. *Tides and waves.* London: Encyclopaeida Metropolitana.

Alber, I., 1978. The effects of randomness on the stability of two-dimensional surface wavetrains. *Proceedings of the Royal Society of London A: Mathematical, Physical and Engineering Sciences,* 363(1715), pp. 525-546.

Baker, G. R., Meiron, D. I. & Orszag, S. A., 1982. Generalized vortex methods for free-surface flow problems. *Journal of Fluid Mechanics,* Volume 123, pp. 477-501.

Baldock, T. E., Swan, C. & Taylor, P. H., 1996. A Laboratory Study of Nonlinear Surface Waves on Water. *Philosophical Transactions of the Royal Society of London A: Mathematical, Physical and Engineering Sciences,* 354(1707), pp. 649-676.

Bateman, W. J. D., Swan, C. & Taylor, P. H., 2001. On the efficient numerical simulation of directionally spread surface water waves. *J. Comput. Phys.,* Volume 174, pp. 277-305.

Beck, R. F. & Liapis, S., 1987. Transient motions of floating bodies at zero forward speed. *Journal of Ship Research,* 31(3), pp. 164-176.

Benjamin, T. B., Bona, J. L. & Mahony, J. J., 1972. Model equations for long waves in nonlinear dispersive systems. *Philosophical Transactions of the Royal Society of London A: Mathematical, Physical and Engineering Sciences,* 272(1220), pp. 47-78.

Benjamin, T. B. & Feir, J. E., 1967. The disintegration of wave trains on deep water Part 1. Theory. *J. Fluid Mech.,* Volume 2, pp. 417-430.

Benjamin, T. B. & Hasselmann, K., 1967. Instability of periodic wavetrains in nonlinear dispersive systems. *Proceedings of the Royal Society of London A: Mathematical, Physical and Engineering Sciences,* 299(1456), pp. 59-76.

Benney, D. J. & Roskes, G. J., 1969. Wave instabilities. *Studies in Applied Mathematics,* Volume 48, pp. 377-385.

Boo, S. Y., Kim, C. H. & Kim, M. H., 1994. A numerical wave tank for nonlinear irregular waves by 3-D higher order boundary element method. *International Journal of Offshore and Polar Engineering (ISOPE-94-04-4-265),* 4(4).

Boussinesq, J., 1871. Théorie de l'intumescence liquide, applelée onde solitaire ou de translation, se propageant dans un canal rectangulaire. *Comptes Rendus de l'Academie des Sciences,* Volume 72, pp. 755-759.

Brandini, C. & Grilli, S. T., 2001a. *Modeling of freak wave generation in a three-dimensional NWT.* Stavanger, Norway, Proc. 11th Intl Offshore and Polar Engng Conf., pp.124-131.

Brandini, C. & Grilli, S. T., 2001b. *Three-dimensional wave focusing in fully nonlinear wave models.* San Francisco, USA, Proc. 4th Intl Symp. on Ocean Wave Measurement and Analysis, pp.1102-1111.

Brinch-Nielsen, U. & Jonsson, I. G., 1986. Fourth order evolution equations and stability analysis for Stokes waves on arbitrary water depth. *Wave Motion,* 8(5), pp. 455-472.

Byatt-Smith, J. G. B. & Longuet-Higgins, M. S., 1976. On the speed and profile of steep solitary waves. *Proceedings of the Royal Society of London A: Mathematical, Physical and Engineering Sciences,* 350(1661), pp. 175-189.

Canuto, C., Haussaini, M. Y., Quarteroni, A. & Zang, Z. A., 1987. *Spectral Methods in Fluid Dynamics.* Berlin: Springer-Verlag.

Celebi, M. S., Kim, M. H. & Beck, R. F., 1998. Fully nonlinear three-dimensional numerical wave tank simulations. *Journal of Ship Research,* Volume 42, pp. 33-45.

Chappelear, J. E., 1961. Direct Numerical Calculation of Nonlinear Ocean Waves. *J. Geophys. Res.,* 66(2), pp. 501-508.

Chau, F. P. & Eatock-Taylor, R., 1992. Second-order wave diffraction by a vertical cylinder. *Journal of Fluid Mechanics,* Volume 240, pp. 571-599.

Chen, Q., 2006. Fully nonlinear Boussinesq-type equations for waves and currents over porous beds. *Journal of Engineering Mechanics,* 132(2), pp. 220-230.

Chen, Q., Kirby, J. T., Dalrymple, R. A., Kennedy, A. B., & Chawla, A., 2000. Boussinesq modeling of wave transformation, breaking, and runup. II: 2D. *Journal of Waterway, Port, Coastal, and Ocean Engineering,* 126(1), pp. 48-56.

Chu, V. H. & Mei, C. C., 1970. On slowly-varying Stokes waves. *Journal of Fluid Mechanics,* 41(4), pp. 873-887.

Chu, V. H. & Mei, C. C., 1971. The non-linear evolution of Stokes waves in deep water. *Journal of Fluid Mechanics,* 47(2), pp. 337-351.

Clamond, D., 2003. Cnoidal-type surface waves in deep water. *Journal of Fluid Mechanics,* Volume 489, pp. 101-120.

Clamond, D. & Dutykh, D., 2013. Fast accurate computation of the fully nonlinear solitary surface gravity waves. *Computers & Fluids,* Volume 84, pp. 35-38.

Clamond, D., Francius, M., Grue, J. & Kharif, C., 2006. Long time interaction of envelope solitons and freak wave formations. *European Journal of Mechanics B/Fluids,* Volume 25, pp. 536-553.

Clamond, D., Fructus, D. & Grue, J., 2007. A note on time integrators in water-wave simulations. *Journal of Engineering Mathematics,* Volume 58, pp. 149-156.

Clamond, D., Fructus, D., Grue, J. & Kristiansen, O., 2005. An efficient model for three-dimensional surface wave simulations. Part II: Generation and absorption. *Journal of Computational Physics,* Volume 205, pp. 686-705.

Clamond, D. & Grue, J., 2001. A fast method for fully nonlinear water-wave computations. *J. Fluid Mech.,* Volume 447, pp. 337-355.

Clauss, G. F., Schmittner, C. E. & Stuck, R., 2005. *Numerical Wave Tank: Simulation of Extreme Waves for the Investigation of Structural Responses.* Halkidiki, Greece, 24th International Conference on Offshore Mechanics and Arctic Engineering, pp. 785-792.

Clauss, G. F. & Steinhagen, U., 1999. *Numerical simulation of nonlinear transient waves and its validation by laboratory data.* Brest, France, Proc. 9th Inernational Offshore and Polar Engineering Conference, pp.368-375.

Clauss, G. F. & Steinhagen, U., 2000. *Optimization of Transient Design Waves in Random Sea.* Seatle, USA, The Tenth International Offshore and Polar Engineering Conference, pp. 229-236.

Cokelet, E. D., 1977a. Breaking waves. *Nature,* Volume 267, pp. 769-774.

Cokelet, E. D., 1977b. Steep gravity waves in water of arbitrary uniform depth. *Philosophical Transactions of the Royal Society of London A: Mathematical, Physical and Engineering Sciences,* 286(1335), pp. 183-230.

Craig, W., Guyenne, P. & Sulem, C., 2012. Hamiltonian higher-order nonlinear Schrödinger equations for broader-banded waves on deep water. *European Journal of Mechanics-B/Fluids,* Volume 32, pp. 22-31.

Craig, W. & Sulem, C., 1993. Numerical simulation of gravity waves. *J. Comput. Phys.,* Volume 108, pp. 73-83.

Cui, C., Zhang, N., Guo, C. & Fang, Z., 2011. Impact of water depth variation on simulated freak waves and their time-frequency energy spectrum. *Acta Oceanologica Sinica,* 33(6), pp. 173-179.

Cui, C., Zhang, N., Yu, Y. & Li, J., 2012. Numerical study on the effects of uneven bottom topography on freak waves. *Ocean Engineering,* Volume 54, pp. 132-141.

Dalzell, J. F., 1999. A note on finite depth second-order wave-wave interactions. *Applied Ocean Research,* Volume 21, pp. 105-111.

Dao, M. H., Xu, H., Chan, E. S. & Tkalich, P., 2011. Numerical modelling of extreme waves by Smoothed Particle Hydrodynamics. *Nat. Hazards Earth Syst. Sci.,* Volume 11, pp. 419-429.

Davey, A. & Stewartson, K., 1974. On three-dimensional packets of surface waves. *Proc. R. Soc. Lond. A,* Volume 388, pp. 101-110.

Dean, R. G., 1965. Stream Function Representation of Nonlinear Ocean Waves. *J. Geophys. Res.,* 70(18), pp. 4561-4572.

Dean, R. G., 1974. *Evaluation and development of water wave theories for engineering application (Vol. 2),* Gainesville, Florida, USA: US Coastal Engineering Research Center.

Debsarma, S. & Das, K. P., 2005. A higher-order nonlinear evolution equation for broader bandwidth gravity waves in deep water. *Physics of Fluids,* 14(104101), pp. 1-8.

Dias, F. & Kharif, C., 1999. Nonlinear gravity and capillary-gravity waves. *Annual review of fluid mechanics,* 31(1), pp. 301-346.

Dingemans, M., 1973. *Water waves over an uneven bottom: a discussion of long wave equations,* Delft, The Netherlands: Technical Report R729, part2, Delft Hydraulics.

Docruzet, G., 2007. *Modélisation des processus non-linéaires de génération et de propagation d'états de mer par une approche spectrale (Doctoral dissertation).* Ecole Centrale de Nantes: Université de Nantes.

Dold, J. W., 1992. An efficient surface-integral algorithm applied to unsteady gravity waves. *Journal of Computational Physics,* Volume 103, pp. 90-115.

Dommermuth, D. G. & Yue, D. K., 1988. *The nonlinear three-dimensional waves generated by a moving surface disturbance.* Berkeley, California, Proceedings of the 17th Symposium on Naval Hydrodynamics, pp.59-71.

Dommermuth, D. & Yue, D., 1987. A high-order spectral method for the study of nonlinear gravity waves. *J. Fluid Mech.,* Volume 184, pp. 267-288.

Dormand, J. R. & Pince, P. J., 1980. A family of embedded Runge-Kutta formulae. *Journal of Computational and Applied Mathematics,* 6(1), pp. 19-26.

Ducrozet, G., Bonnefoy, E., Touze, D. L. & Ferrant, P., 2007. 3-D HOS simulation of extreme waves in open seas. *Nat. Hazards Earth Syst. Sci.,* Volume 7, pp. 109-122.

Dysthe, K. B., 1979. Note on a modification to the nonlinear Schrödinger equation for application to deep water waves. *Proc. R. Soc. Lond. A,* Volume 369, pp. 105-114.

Dysthe, K. B., Socquet-Juglard, H., Trulsen, K., Krogstad, H. E., & Liu, J., 2005. *"Freak" waves and large-scale simulations of surface gravity waves.* Honolulu, Hawaii, In Proc..

Dysthe, K. B., Trulsen, K., Krogstad, H. & Socquet-Juglard, H., 2003. Evolution of a narrow-band spectrum of random surface gravity waves. *Journal of Fluid Mechanics,* Volume 478, pp. 1-10.

Eatock-Taylor, R. & Huang, J. B., 1997. Semi-analytical formulation for second-order diffraction by a vertical cylinder in bichromatic waves. *Journal of fluids and structures,* 11(5), pp. 465-484.

Enet, F., 2006. *Tsunami generation by under water landslides. PhD thesis.* Kingston, Rhode Island, USA: Department of Ocean Engineering, University of Rhode Island.

Fedele, F., 2015. On the kurtosis of deep-water gravity waves. *Journal of Fluid Mechanics,* Volume 782, pp. 25-36.

Fenton, J. D., 1972. A ninth-order solution for the solitary wave. *J. Fluid Mech.,* Volume 53, pp. 257-271.

Fenton, J. D., 1979. A high-order cnoidal wave theory. *Journal of Fluid Mechanics,* 94(1), pp. 129-161.

Fenton, J. D., 1985. A fifth-order Stokes theory for steady waves. *Journal of Waterway Port Coastal and Ocean Engineering,* 111(2), pp. 216-234.

Fenton, J. D., 1988. The numerical solution of steady water wave problems. *Comp. Geosci.,* 14(3), pp. 357-368.

Fenton, J. D., 1990. Nonlinear wave theories. *The Sea,* 9(1), pp. 3-25.

Fenton, J. D. & Gardiner-Garden, R. S., 1982. Rapidly-convergent methods for evaluating elliptic integrals and theta and elliptic functions. *Australian Mathematical Society, Journal, Series B-Applied Mathematics,* Volume 24, pp. 47-58.

Ferrant, P., 1996. *Simulation of strongly nonlinear wave generation and wave-body interactions using a fully nonlinear MEL model.* Trondheim,Norway, Proc. 21st Symp. on Naval Hydrodynamics, pp.93-108.

Ferrant, P., Gentaz, L., Monroy, C., Luquet, R., Ducrozet, G., Alessandrini, B., Jacquin, E. &

Drouet, A., 2008. *Recent adcances towards the viscous flow simulation of ships manoeuvering in waves.* Jeju, Korea, Proc. of 23rd International Workshop on Water Waves and Floating Bodies.

Ferrant, P., Touze, D. L. & Pelletier, K., 2003. Non-linear time-domain models for irregular wave diffraction about offshore structures. *International Journal for Numerical Methods in Fluids,* 43(10-11), pp. 1257-1277.

Fochesato, C., Grilli, S. T. & Dias, F., 2007. Numerical modeling of extreme rogue waves generated by directional energy focusing. *Wave Motion,* Volume 44, pp. 395-416.

Forristall, G. Z., 2000. Wave crest distributions: Observations and second-order theory. *Journal of Physical Oceanography,* 30(8), pp. 1931-1943.

Forristall, G. Z., 2005. *Understanding rogue waves: Are new physics really necessary?.* Honolulu, Hawaii, Proceedings of the 14th Aha Hulikoá Hawaiian Winter Workshop on Rogue Waves, pp.29-35.

Fructus, D., Clamond, D., Grue, J. & Kristiansen, O., 2005. An efficient model for three-dimensional surface wave simulations Part I: Free space problems. *Journal of Computational Physics,* Volume 205, pp. 665-685.

Fructus, D. & Grue, J., 2007. An explicit method for the nonlinear interaction between water waves and variable and moving bottom topography. *Journal of Computational Physics,* 222(2), pp. 720-739.

Fructus, D., Kharif, C., Francius, M., Kristiansen, Ø., Clamond, D. & Grue, J., 2005. Dynamics of crescent water wave patterns. *Journal of Fluid Mechanics,* Volume 537, pp. 155-186.

Funke, E. & Mansard, E., 1982. The control of wave asymmetries in random waves. *Coastal Engineering Proceedings,* 1(18), pp. 725-744.

Gentaz, L., Luquet, R., Alissanderini, B. & Ferrant, P., 2004. *Numerical simulation of the 3D viscous flow around a vertical cylinder in non-linear waves using an explicit incident wave model.* Vancouver, Canada, ASME 2004 23rd International Conference on Offshore Mechanics and Arctic Engineering, pp. 157-163.

Gibbs, R. H. & Taylor, P. H., 2005. Formation of walls of water in 'fully'nonlinear simulations. *Applied Ocean Research,* 27(3), pp. 142-157.

Gibson, R. & Swan, C., 2007. The evolution of large ocean waves: the role of local and rapid spectral changes. *Proceedings of the Royal Society of London A: Mathematical, Physical and Engineering Sciences,* 463(2077), pp. 21-48.

Gibson, R., Swan, C. & Tromans, P., 2007. Fully nonlinear statistics of wave crest elevation calculated using a spectral response surface method: Applications to unidirectional sea states.

Journal of physical oceanography, 37(1), pp. 3-15.

Goda, Y., 1999. A comparative review on the functional forms of directional wave spectrum. *Coastal Engineering Journal,* 41(1), pp. 1-20.

Goda, Y., 2010. *Random Seas and Design of Maritime Structures.* Singapore: World Scientific.

Gramstad, O. & Trulsen, K., 2011. Fourth-order coupled nonlinear Schrödinger equations for gravity waves on deep water. *Physics of Fluids ,* 23(6), p. 062102.

Gramstad, O. & Trulsen, K., 2011. Hamiltonian form of the modified nonlinear Schrödinger equation for gravity waves on arbitrary depth. *Journal of Fluid Mechanics,* Volume 670, pp. 404-426.

Grice, J. R., Taylor, P. H. & Eatock-Taylor, R., 2015. Second-order statistics and 'designer'waves for violent free-surface motion around multi-column structures. *Philosophical Transactions of the Royal Society of London A: Mathematical, Physical and Engineering Sciences,* 373(2033), p. 20140113.

Grilli, S. T., Guyenne, P. & Dias, F., 2001. A fully non-linear model for three-dimensional overturning waves over an arbitrary bottom. *International Journal for Numerical Methods in Fluids,* Volume 35, pp. 829-867.

Grilli, S. T., Harris, J. & Greene, N., 2008. *Modeling of wave-induced sediment transport around obstacles.* Hamburg, Germany, Proceeding of 32nd International Coastal Engineering Conference, pp.1638-1650.

Grilli, S. T. & Horrillo, J., 1997. Numerical generation and absorption of fully nonlinear periodic waves. *Journal of Engineering Mechanics,* 123(10), pp. 1060-1069.

Grilli, S. T., Skourup, J. & Svendsen, I. A., 1989. An efficient boundary element method for nonlinear water waves. *Engineering analysis with boundary elements,* Volume 6, pp. 97-107.

Grilli, S. T. & Subramanya, R., 1996. Numerical modeling of wave breaking induced by fixed or moving boundaries. *Computational Mechanics,* 17(6), pp. 374-391.

Grilli, S. T., Vogelmann, S. & Watts, P., 2002. Development of a three-dimensional numerical wave tank for modelling tsunami generation by underwater landslides. *Engne Anal. Bound. Elem.,* Volume 26, pp. 301-313.

Grimshaw, R., 1971. The solitary wave in water of variable depth. Part 2. *J. Fluid Mech.,* Volume 46, pp. 611-622.

Grimshaw, R. & Annenkov, S., 2011. Water wave packets over variable depth. *Studies in Applied Mathematics,* 126(4), pp. 409-427.

Grue, J., 2005. *A nonlinear model for surface waves interacting with a surface-piercing cylinder.* Longyearbyen, Norway, Proc. 20th Int. Workshop on Water Waves and Floating Bodies.

Grue, J., 2010. Computation formulas by FFT of the nonlinear orbital velocity in three-dimensional surface wave fields. *J. Eng. Math.,* Volume 67, pp. 55-69.

Grue, J., 2015. Nonlinear interfacial wave formation in three dimensions. *Journal of Fluid Mechanics,* Volume 767, pp. 735-762.

Grue, J., Pelinovsky, E. N., Fructus, D., Talipova, T. & Kharif, C., 2008. Formation of undular bores and solitary waves in the Strait of Malacca caused by the 26 December 2004 Indian Ocean tsunami. *Journal of Geophysical Research: Oceans,* 113(C5), pp. 1-14.

Guyenne, P., Grilli, S. T. & Dias, F., 2000. *Numerical modelling of fully nonlinear three-dimensional overturning waves over arbitrary bottom.* Sydney, Australia, Proc. 27th Intl Conf. on Coastal Engng, pp.417-428.

Harlow, F. H. & Welch, J. E., 1965. Numerical Calculation of Time-Dependent Viscous Incompressible Flow of Fluid with Free Surface. *Physics of Fluids (1958-1988),* Volume 8, pp. 2182-2189.

Harris, J. C. & Grilli, S. T., 2010. *Coupling of NWT and Large-eddy Simulation for Wave-induced Sediment Transport.* Beijing, China, The Twentieth International Offshore and Polar Engineering Conference, pp.578-585.

Harris, J. C. & Grilli, S. T., 2012. A perturbation approach to large eddy simulation of wave-induced bottom boundary layer flows. *International Journal for Numerical Methods in Fluids,* 68(12), pp. 1574-1604.

Hasimoto, H. & Ono, H., 1972. Nonlinear modulation of gravity waves. *Journal of the Physical Society of Japan,* Volume 33, pp. 805-811.

Hasselmann, K., 1962. On the non-linear energy transfer in a gravity-wave spectrum. Part I: General theory.. *J. Fluid Mech.,* Volume 12, pp. 481-500.

Hasselmann, K., Barnett, T. P., Bouws, E., Carlson, H., Cartwright, D. E., Enke, K., Ewing, J. A., Gienapp, H., Hasselmann, D. E., Kruseman, P. & Meerburg, A., 1973. *Measurements of wind-wave growth and swell decay during the joint north sea wave project (JONSWAP),* Hamburg: Deutsches Hydrographisches.

Heinze, C., 2003. *Nonlinear hydrodynamic effects on fixed and oscillating structures in waves (PhD thesis).* Oxford: Department of Engineering Science, Oxford University.

Henderson, K. L., Peregrine, D. H. & Dold, J. W., 1999. Unsteady water wave modulations: fully nonlinear solutions and comparison with the nonlienar Schrodinger equation. *Wave motion,* 29(4), pp. 341-361.

Hirt, C. W. & Nichols, B. D., 1981. Volume of fluid (VOF) method for the dynamics of free boundaries. *Journal of Computational Physics,* 39(1), pp. 201-225.

Hogan, S. J., 1985. The fourth-order evolution equation for deep-water gravity-capillary waves. *Proc. R. Soc. Lond. A,* Volume 402, pp. 359-372.

Huang, J. B. & Eatock-Taylor, R., 1996. Semi-analytical solution for second-order wave diffraction by a truncated circular cylinder in monochromatic waves. *Journal of Fluid Mechanics,* Volume 319, pp. 171-196.

Huang, N. E., Long, S. R., Tung, C. C., Yuen, Y. & Bliven, L. F., 1981. A unified two-parameter wave spectral model for a general sea state. *J. Fluid Mech. ,* Volume 112, pp. 203-224.

Hunter, J. K. & Vanden-Broeck, J. M., 1983. Solitary and periodic gravity—capillary waves of finite amplitude. *Journal of Fluid Mechanics,* Volume 134, pp. 205-219.

Hu, P., Wu, G. X. & Ma, Q. W., 2002. Numerical simulation of nonlinear wave radiation by a moving vertical cylinder. *Ocean Engineering,* 29(14), pp. 1733-1750.

Hu, Z., Tang, W., Xue, H. & Zhang, X., 2015. Numerical study of Rogue waves as nonlinear Schrödinger breather solutions under finite water depth. *Wave Motion,* Volume 52, pp. 81-90.

Isaacson, M. & Cheung, K., 1991. Second order wave diffraction around two-dimensional bodies by time-domain method. *Applied Ocean Research,* 13(4), pp. 175-186.

Isaacson, M. & Cheung, K. F., 1992. Time-domain second-order wave diffraction in three dimensions. *Journal of waterway, port, coastal, and ocean engineering,* 118(5), pp. 496-516.

Janssen, P. A. E. M., 1983. On a fourth-order envelope equation for deep-water waves. *J. Fluid Mech.,* Volume 126, pp. 1-11.

Janssen, P. A. E. M., 2009. On some consequences of the canonical transformation in the Hamiltonian theory of water waves. *Journal of Fluid Mechanics,* Volume 637, pp. 1-44.

Jassen, C. F., Grilli, S. T. & Krafczyk, M., 2010. *Modeling of wave breaking and wave-structure interactions by coupling of fully nonlinear potential flow and lattice-Boltzmann models.* Beijing, China, The Twentieth International Offshore and Polar Engineering Conference, pp.686-693.

Johnson, R., 1976. On the modulation of water waves on shear flows. *Proceedings of the Royal Society of London A: Mathematical, Physical and Engineering Sciences,* 347(1651), pp. 537-546.

Johnson, R., 1997. *A modern introduction to the mathematical theory of water waves.* Cambridge: Cambridge University Press.

Kadomtsev, B. B. & Petviashvili, V. I., 1970. On the stability of solitary waves in weakly dispersive media. *Soviet Physics,* Volume 15, pp. 539-541.

Kakutani, T., 1971. Effect of an Uneven Bottom on Gravity Waves. *J. Phy. Soc. Japan,* Volume 30, pp. 272-276.

Kashiwagi, M. & Ohwatari, Y., 2002. *First-and second-order water waves around an array of* *floating vertical cylinders.* Cambridge, UK, 17th International Workshop on Water Waves and Floating Bodies.

Kelvin, L., 1887. On the waves produced by a single impulse in water of any depth, or in a dispersive medium. *Proceedings of the Royal Society of London. Ser. A.,* Volume 42, pp. 80-85.

Kennedy, A. B., Chen, Q., Kirby, J. T. & Dalrymple, R. A., 2000. Boussinesq modeling of wave transformation, breaking, and runup. I: 1D. *Journal of Waterway, Port, Coastal, and Ocean Engineering,* 126(1), pp. 39-47.

Kennedy, A. B., Kirby, J. T., Chen, Q. & Dalrymple, R. A., 2001. Boussinesq-type equations with improved nonlinear performance. *Wave Motion,* 33(3), pp. 225-243.

Kharif, C., Pelinovsky, E. & Slunyaev, A., 2009. *Rogue Waves in the Ocean.* Berlin Heidelberg: Springer-Verlag.

Kim, C. H., 2008. *Nonlinear Waves and Offshore Structure.* Singapore: World Scientific Publishing Co. Pte. Ltd.

Kirby, J. T. & Vengayil, P., 1988. Nonresonant and resonant reflection of long waves in varying channels. *Journal of Geophysical Research,* 93(C9), pp. 10782-10796.

Kit, E. & Shemer, L., 2002. Spatial versions of the Zakharov and Dysthe evolution equations for deep-water gravity waves. *Journal of Fluid Mechanics,* Volume 450, pp. 201-205.

Komen, G. J., Cavaleri, L., Donelan, M., Hasselmann, K., Hasselmann, S. and Janssen, P.A.E.M., 1996. *Dynamics and modeling of ocean waves.* New York: Cambridge University Press.

Korteweg, D. J. & DE Vries, G., 1895. On the change of form of long waves advancing in a rectangular cannal, and on a new type of long stationary waves. *Phil. Mag.*, Volume 39: 422-443.

Kriebel, D., 1990. Nonlinear wave interaction with a vertical circular cylinder. Part I: Diffraction theory. *Ocean Engineering,* 17(4), pp. 345-377.

Kriebel, D., 1992. Nonlinear wave interaction with a vertical circular cylinder. Part II: Wave run-up. *Ocean Engineering,* 19(1), pp. 75-99.

Kriebel, D. L. & Alsina, M. V., 2000. *Simulation of Extreme Waves in a Background Random Sea.* Seatle, USA, The Tenth International Offshore and Polar Engineering Conference, pp.31-37.

Laitone, E. V., 1960. The second approximation to cnoidal and solitary waves. *Journal of Fluid Mechanics,* 9(3), pp. 430-444.

Lake, B. M., Yuen, H. C., Rungaldier, H. & Ferguson, W. E., 1977. Nonlinear deep-water waves: theory and experiment. Part 2. Evolution of a continuous wave train. *Journal of Fluid Mechanics,* 83(1), pp. 49-74.

Lamb, H., 1916. *Hydrodynamics (Fourth Edition).* Cambridge: Cambrige University Press.

Lavrenov, I. V., 2003. *Wind-Waves in Oceans: Dynamics and Numerical Simulations.* Berlin: Springer.

Le Méhauté, B., 1976. *An Introduction to Hydrodynamics and Water Waves.* Berlin: Springer Berlin Heidelberg.

Lee, C. & Newman, J., 2006. *WAMIT (R) User Manual Version 6.4S.* Chestnut Hill, MA, USA: WAMIT, Inc..

Lighthill, M., 1979. Waves and hydrodynamic loading. *Proc. 2nd Int. Conf. on Behaviour of Offshore Structures,* Volume 1, pp. 1-40.

Lindgren, G., 1970. Some properties of a normal process near a local maximum. *The Annals of Mathematical Statistics,* pp. 1870-1883.

Liu, P. C., 2007. A chronology of freauqe wave encounters. *Geofizika,* 24(1), pp. 57-70.

Liu, Y., Dommermuth, D. G. & Yue, D. K., 1992. A high-order spectral method for nonlinear wave–body interactions. *Journal of fluid Mechanics,* Volume 245, pp. 115-136.

Liu, Y. & Yue, D. K., 1998. On generalized Bragg scattering of surface waves by bottom ripples. *Journal of Fluid Mechanics,* Volume 356, pp. 297-326.

Lo, E. & Mei, C. C., 1985. A numerical study of water-wave modulation based on a higher-order nonlinear Schrödinger equation. *J. Fluid Mech.,* Volume 150, pp. 395-416.

Long, R. R., 1956. Solitary waves in the one-and two-fluid systems. *Tellus A,* 8(4).

Longuet-Higgins, M. S., 1963. The effect of non-linearities on statistical distributions in the theory of sea waves. *J. Fluid Mech.,* Volume 17, pp. 459-480.

Longuet-Higgins, M. S., 1976. On the nonlinear transfer of energy in the peak of a gravity-wave spectrum: a simplified model. *Proceedings of the Royal Society of London A: Mathematical, Physical and Engineering Sciences,* 347(1650), pp. 311-328.

Longuet-Higgins, M. S. & Cokelet, E. D., 1976. The deformation of steep surface waves on water. I. A numerical method of computation. *Pro. R. Soc. Lond. A.,* Volume 350, pp. 1-26.

Longuet-Higgins, M. S. & Fenton, J. D., 1974. On the mass, momentum, energy and circulation of a solitary wave. II. *Proceedings of the Royal Society of London A: Mathematical, Physical and Engineering Sciences,* 340(1623), pp. 471-493.

Longuet-Higgins, M. S. & Stewart, R. W., 1962. Radiation stress and mass transport in gravity waves, with application to "surf beats". *Journal of Fluid Mechanics,* 13(4), pp. 481-504.

Longuet-Higgins, M. S. & Stewart, R. W., 1964. Radiation stresses in water waves; a physical discussion, with applications. *Deep Sea Research and Oceanographic Abstracts,* 11(4), pp. 529-

56.

Lukomsky, V. P., Gandzha, I. S. & Lukomsky, D. V., 2002a. Steep sharp-crested gravity waves on deep water. *Physical review letters,* 89(16), p. 164502.

Lukomsky, V. P., Gandzha, I. S. & Lukomsky, D. V., 2002b. Computational analysis of the almost-highest waves on deep water. *Computer physics communications,* 147(1), pp. 548-551.

Luquet, R., Alessanderini, B., Ferrant, P. & Gentaz, L., 2004. *Simulation of the viscous flow past a ship in waves using the SWENSE approach.* St John's, Newfoundland, Canada, Proc. 24th ONR Symposium on Naval Hydrodynamics.

Luquet, R., Ferrant, P., Alessandrini, B., Ducrozet, G. & Gentaz, L., 2007. *Simulation of a TLP in waves using the SWENSE scheme.* Lisbon, Portugal, Proc. of the 17th International Offshore and Polar Engineering Conference, pp.1916-1923.

Luquet, R., Jacquin, E., Guillerm, P. E., Gentaz, L., Ferrant, P., & ALESSANDRINI, X., 2005. *RANSE with free surface computations around fixed and free DTMB 5415 model in still water and in waves.* Tokyo, Japan, Proceeding of CFD Workshop.

Lynett, P. J. & Liu, P. L. F., 2004. Linear analysis of the multi-layer model. *Coastal Engineering,* Volume 51, pp. 439-454.

Madsen, P. A., Bingham, H. B. & Liu, H., 2002. A new Boussinesq method for fully nonlinear waves from shallow to deep water. *Journal of Fluid Mechanics,* Volume 462, pp. 1-30.

Madsen, P. A., Bingham, H. B. & Schäffer, H. A., 2003. Boussinesq-type formulations for fully nonlinear and extremely dispersive water waves: derivation and analysis. *Proc. R. Soc. Lond. A,* 459(2033), pp. 1075-1104.

Madsen, P. A. & Fuhrman, D. R., 2010. High-Order Boussinesq-Type Modelling of Nonlinear Wave Phenomena in Deep and Shallow Water. In: *Adcances in Numerical Simulation of Nonlinear Water Waves.* Singagpore: World Scienticif Publishing Co. Pte. Ltd., pp. 245-286.

Madsen, P. A., Murray, R. & Sørensen, O. R., 1991. A new form of the Boussinesq equations with improved linear dispersion characteristics. *Coastal engineering,* 15(4), pp. 371-388.

Madsen, P. A. & Schäffer, H. A., 1998. Higher–order Boussinesq–type equations for surface gravity waves: derivation and analysis. *Philosophical Transactions of the Royal Society of London A: Mathematical, Physical and Engineering Sciences,* 356(1749), pp. 3123-3181.

Madsen, P. A. & Sørensen, O. R., 1992. A new form of the Boussinesq equations with improved linear dispersion characteristics. Part 2. A slowly-varying bathymetry. *Coastal engineering,* 18(3), pp. 183-204.

Malenica, S., Eatock-Taylor, R. & Huang, J. B., 1999. Second-order water wave diffraction by an array of vertical cylinders. *Journal of Fluid Mechanics,* Volume 390, pp. 349-373.

Ma, Q. W., 1998. *Numerical simulation of nonliear interaction between structures and steep waves (PhD Thesis).* London: Department of Mechanical Enginieering, University College London, UK.

Ma, Q. W., 2008a. A new meshless interpolation scheme for MLPG_R method. *Computer Modeling in Engineering & Sciences,* 23(2), pp. 75-90.

Ma, Q. W., 2008b. Numerical generation of freak waves using MLPG_R and QALE-FEM methods. *Computer Modeling In Engineering And Sciences,* 667(1), pp. 1-12.

Ma, Q. W., 2010. *Advances in numerical simulation of nonlinear water waves.* Singapore: World Scientific.

Ma, Q. W., Wu, G. X. & Eatock-Taylor, R., 1997. *Finite element analysis of non-linear transient waves in a three dimensional long tank.* Carry-le-Rouet, France, 12th International Workshop on Water Waves and Floating Bodies.

Ma, Q. W., Wu, G. X. & Eatock-Taylor, R., 2001a. Finite element simulation of fully non-linear interaction between vertical cylinders and steep waves. Part 1: Methodology and numerical procedure. *Int. J. Numer. Meth. Fluids,* Volume 36, pp. 265-285.

Ma, Q. W., Wu, G. X. & Eatock-Taylor, R., 2001b. Finite element simulation of fully non-linear interaction between vertical cylinders and steep waves. Part 2: Numerical results and validation. *Int. J. Numer. Meth. Fluids,* Volume 36, pp. 287-308.

Ma, Q. W. & Yan, S., 2006. Quasi ALE finite element method for nonlinear water waves. *Journal of Computational Physics,* Volume 212, pp. 52-72.

Ma, Q. W. & Yan, S., 2009. QALE-FEM for numerical modelling of non-linear interaction between 3D moored floating bodies and steep waves. *International journal for numerical methods in engineering,* 78(6), pp. 713-756.

Ma, Q. W. & Zhou, J. T., 2009. MLPG_R method for numerical simulation of 2D breaking waves. *Computer Modeling in Engineering & Sciences,* 43(3), pp. 277-304.

Ma, Y. C., 1979. The perturbed plane-wave solution of the cubic Schrödinger equation. *Studies in Applied Mathematics,* Volume 60, pp. 43-58.

McCowan, A. D., 1987. *The range of application of Boussinesq type numerical short wave models.* Lausanne, Switzerland, Proceeding of 22nd IAHR World Congress.

McCowan, J., 1891. VII. On the solitary wave. *The London, Edinburgh, and Dublin Philosophical Magazine and Journal of Science,* 32(194), pp. 45-58.

McLean, J., 1982a. Instabilities of finite-amplitude water waves. *Journal of Fluid Mechanics,* Volume 114, pp. 315-330.

McLean, J., 1982b. Instabilities of finite-amplitude gravity waves on water of finite depth.

Journal of Fluid Mechanics, Volume 114, pp. 331-341.

McLean, J., Ma, Y. C., Martin, D. U., Saffman, P. G. & Yuen, H. C., 1981. Three-dimensional instability of finite-amplitude water waves. *Physical Review Letters,* 46(13), pp. 817-821.

Mei, C. C., 1983. *The applied dynamics of ocean surface waves.* New York: Wiley.

Mei, C. C., Stiassinie, M. & Yue, D. K. P., 2005. *Theory and applications of ocean surface waves. Part 1: Linear Aspects.* Singapore: World Scientific.

Mei, C. C. & Le Méhauté, B., 1966. Note on the equations of long waves over an uneven bottom. *J. Geophys. Res.,* Volume 71, pp. 393-400.

Miles, J. W., 1980. Solitary waves. *Annual review of fluid mechanics,* 12(1), pp. 11-43.

Miles, J. W., 1981. The Korteweg-de Vries equation: a historical essay. *Journal of fluid mechanics,* Volume 106, pp. 131-147.

Molin, B., 1979. Second-order diffraction loads upon three-dimensional bodies. *Applied Ocean Research,* 1(4), pp. 197-202.

Monkmeyer, P. L., 1970. A higher order theory for symmetrical gravity waves. *Coastal Engineering Proceedings,* 1(12), pp. 543-561.

Monroy, C., Ducrozet, G., Bonnefoy, F., Babarit, A., Gentaz, L. & Ferrant, P., 2011. *RANS simulations of CALM buoy in regular and irregular seas using SWENSE method.* Beijing, China, Proceeding of The Twentieth International Offshore and Polar Engineering Conference, pp. 678-686.

Monroy, C., Ducrozet, G., Roux de Reilhac, P., Gentaz, L., Ferrant, P. & Alessandrini, B., 2009. *RANS simulations of ship motions in regular and irregular head seas using the SWENSE method.* Osaka, Japan, Proceeding of The 19th International Offshore and Polar Engineering Conference, pp. 6-14.

Narayanaswamy, M., Crespo, A. J. C., Gomes-Gesteira, M. & Dalrymple, R. A., 2010. SPHysic-FUNWAVE hybrid model for coastal wave propagation. *Journal of Hydaulic Research,* Volume 48, pp. 85-93.

New, A. L., McIver, P. & Peregrine, D. H., 1985. Computations of overturning waves. *J. Fluid Mech.,* Volume 150, pp. 233-251.

Nicholls, D. P., 1998. Traveling Water Waves: Spectral Continuation Methods with Parallel Implementation. *Journal of Computational Physics,* 143(1), pp. 224-240.

Nicholls, D. P. & Reitich, F., 2001a. A new approach to analyticity of Dirichlet-Neumann operators. *Proc. Royal Soc. Edin. A,* 131(6), pp. 1411-1433.

Nicholls, D. P. & Reitich, F., 2001b. Stability of high-order perturbative methods for the computation of Dirichlet-Neumann operators. *J. Comput. Phys.,* 170(1), pp. 276-298.

Nikolkina, I. & Didenkulova, I., 2012. Catalogue of rogue waves reported in media in 2006-2010. *Natural hazards,* 61(3), pp. 989-1006.

Ning, D. Z., Zang, J., Liu, S.X., Eatock-Taylor, R., Teng, B. & Taylor, P. H., 2009. Free-surface evolution and wave kinematics for nonlinear uni-directional focused wave groups. *Ocean Engineering,* 36(15), pp. 1226-1243.

Nwatchok, S., Biouele, C., Zobo, B. & Nkomom, T., 2011. Application of Zakharov equation in three dimensions to deep water gravity waves. *International Journal of the Physical Sciences,* Volume 6, pp. 7447-7455.

Nwogu, O., 1993. Alternative form of Boussinesq equations for nearshore wave propagation. *Journal of waterway, port, coastal, and ocean engineering,* 119(6), p. 618–638.

Nwogu, O. & Demirbilek, Z., 2004. Numerical modeling of ship-induced currents in confined waterways. *Proc. 29th Int. Conf. on Coastal Engineering,* pp. 256-268.

Onorato, M., Osborne, A. R., Serio, M. & Bertone, S., 2001. Freak waves in random oceanic sea states. *Physical review letters,* 86(25), pp. 5831-5834.

Onorato, M., Osborne, A. R., Serio, M., Cavaleri, L., Brandini, C. & Stansberg, C. T., 2002. Freely decaying weak turbulence for sea surface gravity waves. *Physical review letters,* 89(14), p. 144501.

Onorato, M., Osborne, A. R., Serio, M., Cavaleri, L., Brandini, C. & Stansberg, C. T., 2006. Extreme waves, modulational instability and second order theory: wave flume experiments on irregular waves. *European Journal of Mechanics-B/Fluids,* 25(5), pp. 586-601.

Onorato, M., Proment, D. & Toffoli, A., 2011. Triggering rogue waves in opposing currents. *Phys. Rev. Lett.,* 107(18), pp. 184502-184507.

Osborne, A., 2001. The random and deterministic dynamics of 'rogue waves' in unidirectional, deep-water wave trains. *Marine structures,* 14(3), pp. 275-293.

Pelinovsky, E. & Sergeeva, A., 2006. Numerical modeling of the KdV random wave field. *European Journal of Mechanics B/Fluids,* Volume 25, pp. 425-434.

Peregrine, D. H., 1967. Long waves on a beach. *Journal of fluid mechanics,* 27(4), pp. 815-827.

Peregrine, D. H., 1983. Water waves, nonlinear Schrödinger equations and their solutions. *The Journal of the Australian Mathematical Society. Series B. Applied Mathematics,* 25(1), pp. 16-43.

Phillips, O. M., 1960. On the dynamics of unsteady gravity waves of finite amplitude. Part 1. The elementary interactions. *Journal of Fluid Mechanics,* 9(2), pp. 193-217.

Phillips, O. M., 1981. Wave interactions - the evolution of an idea. *Journal of Fluid Mechanics,* Volume 106, pp. 215-227.

Pinkster, J. A., 1980. *Low frequency second order wave exciting forces on floating structures (PhD thesis).* TU Delft: Delft University of Technology.

Piterbarg, V., 2012. *Asymptotic methods in the theory of Gaussian processes and fields (Vol. 148).* USA: American Mathematical Soc..

Rahman, M., 1984. Wave diffraction by large offshore structures: an exact second-order theory. *Applied Ocean Research,* 6(2), pp. 90-100.

Ransley, E., Hann, M., Greaves, D. M., Raby, A. & Simmonds, D., 2013. *Numerical and physical modeling of extreme waves at Wave Hub.* Plymouth, UK, Proceedings 12th International Coastal Symposium, pp. 1645-1650.

Rayleigh, L., 1876. On waves. *Phil. Mag,* 1(5), pp. 257-279.

Rienecker, M. M. & Fenton, J. D., 1981. A Fourier approximation method for steady water waves. *Journal of Fluid Mechanics,* Volume 104, pp. 119-137.

Rosemurgy, W., Edmund, D., Maki, K. & Beck, R., 2012. *A velocity decomposition approach for steady free-surface flow.* Gothenbug, Sweden, Proceeding of the 29th Symposium on Naval Hydrodynamics, pp.1-21.

Rudman, M. & Cleary, P. W., 2013. Rogue wave impact on a tension leg platform: The effect of wave incidence angle and mooring line tension. *Ocean Engineering,* Volume 61, pp. 123-138.

Russell, J. S., 1845. *Report on Waves: Made to the Meetings of the British Association in 1842-43.* London: Richard And John E. Taylor.

Rygg, O. B., 1988. Nonlinear refraction-diffraction of surface waves in intermediate and shallow water. *Coastal Engineering,* 12(3), pp. 191-211.

Schäffer, H. A., 2008. Comparison of Dirichlet–Neumann operator expansions for nonlinear surface gravity waves. *Coastal Engineering,* 55(4), pp. 288-294.

Schäffer, H. A. & Madsen, P. A., 1995. Further enhancements of Boussinesq-type equations. *Coastal Engineering,* 26(1), pp. 1-14.

Schober, C. & Calini, A., 2008. Rogue Waves in Higher Order Nonlinear Schrödinger Models. In: E. Pelinovsky & C. Kharif, *Extreme Ocean Waves.* Berlin: Springer Netherlands, pp. 31-51.

Schwartz, L. W., 1974. Computer extension and analytic continuation of Stokes' expansion for gravity waves. *Journal of Fluid Mechanics,* 62(3), pp. 553-578.

Schwartz, L. W. & Vanden-Broeck, J. M., 1979. Numerical solution of the exact equations for capillary–gravity waves. *Journal of Fluid Mechanics,* 95(1), pp. 119-139.

Sharma, J. N. & Dean, R. G., 1981. Second-order directional seas and associated wave forces. *Society of Petroleum Engineers Journal,* 21(1), pp. 129-140.

Sharma, J. N. & Dean, R. G., 1979. *Development and evaluation of a procedure for simulating* *a random directional second order sea surface and associated wave forces.* Newark, USA: University of Delaware.

Shemer, L., Sergeeva, A. & Sunyaev, A., 2010. Applicability of envelope model equations for simulation of narrow-spectrum unidirectional random wave field evolution: Experimental validation. *Physics of Fluids,* Volume 22, pp. 016601 1-9.

Shi, F., Kirby, J. T. & Tehranirad, B., 2012. *FUNWAVE-TVD. Fully Nonlinear Boussinesq Wave Model with TVD Solver. Documentation and User's Manual,* Newark, Delaware: Center for Applied Coastal Research, University of Delaware.

Sitanggang, K. I. & Lynett, P. J., 2009. Multi-scale simulation with a hybrid Boussinesq-RANS hydrodynamic model. *International journal for numerical methods in fluids,* 62(9), pp. 1013-1046.

Skourup, J., Ottensen Hansen , N. & Andreasen, K., 1996. Non-Gaussian Extreme Waves in the Central North Sea. *Proc. Offshore Mechanics and Arctic Engineering Conf.,* Volume I-A, pp. 25-32.

Slunyaev, A., Pelinovsky, E., Sergeeva, A., Chabchoub, A., Hoffmann, N., Onorato, M. & Akhmediev, N., 2013. Super rogue waves in simulations based on weakly nonlinear and fully nonlinear hydrodynamic equations. *Physical Review E,* 88(1), p. 012909.

Slunyaev, A. V., 2005. A high-order nonlinear envelope equation for gravity waves in finite-depth water. *Journal of Experimental and Theoretical Physics,* 101(5), pp. 926-941.

Solisz, W. & Hudspeth, R., 1993. Complete second-order solution for water waves generated in wave flumes. *Journal of Fluids and Structures,* 7(3), pp. 253-268.

Sriram, V., Ma, Q. W. & Schlurmann, T., 2012. *Numerical simulation of breaking waves using hybrid coupling of FNPT and NS solvers.* Rhodes, Greece, Proceedings of the 22nd international offshore and polar engineering conference, pp.1118-1124.

Sriram, V., Sannasiraj, S. A. & Sundar, V. J., 2006. Simulation of 2-D nonlinear waves using finite element method with cubic spline approximation. *Journal of Fluids and Structures,* 22(5), pp. 663-681.

Stewartson, K., 1977. On the resonant interaction between a surface wave and a weak surface current. *Mathematika,* 24(1), pp. 37-49.

Stiassnie, M., 1984. Note on the modified nonlinear Schrödinger equation for deep water waves. *Wave Motion,* Volume 6, pp. 431-433.

Stoker, J. J., 2011. *Water waves: The mathematical theory with applications.* New York: John Wiley & Sons.

Stokes, G. G., 1847. On the theory of oscillatary waves. In: *Mathematical and Physical Papers.*

London: Cambridge University Press.

Sung, H. G. & Grilli, S. T., 2005. *Numerical Modeling of Nonlinear Surface Waves caused by Surface Effect Ships Dynamics and Kinematics.* Seoul, South Korea, The Proceedings of the 15th International Offshore and Polar Engineering Conference, pp. 124-131.

Sung, H. G. & Grilli, S. T., 2006. *Combined Eulerian-Lagrangian or Pseudo-Lagrangian, Descriptions of Waves Caused by an Adcancing Free Surface Distrubance.* San Francisco, California, The Proceedings of the 16th International Offshore and Polar Engineering Conference, pp. 487-494.

Sung, H. G. & Grilli, S. T., 2008. BEM Computations of 3-D Fully Nonlinear Free Surface Flows Caused by Advancing Surface Disturbances. *Intl. J. Offshore and Polar Engng,* 18(4), pp. 292-301.

Tanaka, M., 1986. The stability of solitary waves. *Physics of Fluids,* Volume 29, pp. 650-655.

Taylor, P. H., Jonathan, P. & Harland, L. A., 1997. Time domain simulation of jack-up dynamics with the extremes of a Gaussian process. *Journal of Vibration and Acoustics,* 119(4), pp. 624-628.

Cavaleri, L., Alves, J. H., Ardhuin, F., Babanin, A., Banner, M., Belibassakis, K., Benoit, M., Donelan, M., Groeneweg, J., Herbers, T. H. C. & Hwang, P., 2007. Wave modelling - The state of the art. *Progress in Oceanography,* 75(4), pp. 603-674.

Thomas, R., Kharif, C. & Manna, M., 2012. A nonlinear Schrödinger equation for water waves on finite depth with constant vorticity. *Physics of Fluids,* 24(12), p. 127102.

Toffoli, A., Gramstad, O., Trulsen, K., Monbaliu, J., Bitner-Gregersen, E. & Onorato, M., 2010. Evolution of weakly nonlinear random directional waves: laboratory experiments and numerical simulations. *Journal of Fluid Mechanics,* Volume 664, pp. 313-336.

Toffoli, A., Monbaliu, J., Onorato, M., Osborne, A.R., Babanin, A.V. and Bitner-Gregersen, E., 2006. Second-Order Theory and Setup in Surface Gravity Waves: A Comparison with Experimental Data. *Journal of Physical Oceanography,* Volume 37, pp. 2726-2739.

Tong, R. P., 1997. A new approach to modelling an unsteady free surface in boundary integral methods with application to bubble-structure interactions. *Math. Compt. Simul.,* Volume 44, pp. 415-426.

Touboul, J., Giovanangeli, J. P., Kharif, C. & Pelinovsky, E., 2006. Freak waves under the action of wind: experiments and simulations. *European Journal Mechanics B/Fluid,* Volume 25, pp. 662-676.

Touboul, J., Pelinovsky, E. & Kharif, C., 2007. Nonlinear focusing wave group on current. *Journal of Korean Society of Coastal and Ocean Engineers,* Volume 19, pp. 222-227.

Trulsen, K. & Dysthe, K. B., 1996. A modified nonlinear Schrödinger equation for broader bandwidth gravity waves on deep water. *Wave motion,* Volume 24, pp. 281-298.

Trulsen, K. & Dysthe, K. B., 1997. Frequency downshift in three-dimensional wave trains in a deep basin. *Journal of Fluid Mechanics,* Volume 352, pp. 359-373.

Trulsen, K., Gudmestad, O. & Velarde, M., 2001. The nonlinear Schrödinger method for water wave kinematics on finite depth. *Wave motion,* 33(4), pp. 379-395.

Trulsen, K., Kliakhandler, I., Dysthe, K. B. & Velarde, M. G., 2000. On weakly nonlinear modulation of waves on deep water. *Physics of Fluids,* 12(10), pp. 2432-2437.

Trulsen, K., Stansberg, C. & Velarde, M., 1999. Laboratory evidence of three-dimensional frequency downshift of waves in a long tank. *Physics of Fluids,* 11(1), pp. 235-237.

Tsai, W. T. & Yue, D. K., 1996. Computation of nonlinear free-surface flows. *Annual review of fluid mechanics,* 28(1), pp. 249-278.

Tucker, M., Challenor, P. & Carter, D., 1984. Numerical simulation of a random sea: a common error and its effect upon wave group statistics. *Applied ocean research,* 6(2), pp. 118-122.

Turnbull, M. S., Borthwick, A. G. L. & Eatock-Taylor, R., 2003. Wave–structure interaction using coupled structured–unstructured finite element meshes. *Applied ocean research,* 25(2), pp. 63-77.

Ursell, F., 1953. The long wave paradox in the theory of gravity waves. *Proc. Camb. Phil. Soc,* Volume 49, pp. 685-694.

Vastano, A. C. J. & Mungall, J. C. H., 1976. *Theory of waves and surges which propagate the length of a horizontal rectangular canal, imparting to the fluid contained within the canal velocities that are sensibly the same from the top to the bottom [English translation of Boussinesq(1872)].* s.l.:College of Geosciences, Texas A&M Univ. Rep. 76-2-T.

Vinje, T. & Brevig, P., 1981. Numerical simulation of breaking waves. *Advances in Water resources,* 4(2), pp. 77-82.

Vitanov, N., Chabchoub, A. & Hoffmann, N., 2013. Deep-Water Waves: on the Nonlinear Schrödinger Equation and its Solutions. *Journal of Theoretical and Applied Mechanics,* 43(2), pp. 43-54.

Wang, C. Z. & Khoo, B. C., 2005. Finite element analysis of two-dimensional nonlinear sloshing problems in random excitations. *Ocean Engineering,* 32(2), pp. 107-133.

Wang, C. Z. & Wu, G. X., 2006. An unstructured-mesh-based finite element simulation of wave interactions with non-wall-sided bodies. *Journal of fluids and structures,* 22(4), pp. 441-461.

Wang, C. Z. & Wu, G. X., 2007. Time domain analysis of second-order wave diffraction by an array of vertical cylinders. *Journal of Fluids and Structures,* 23(4), pp. 605-631.

Wang, C. Z., Wu, G. X. & Drake, K. R., 2007. Interactions between nonlinear water waves and non-wall-sided 3D structures. *Ocean engineering,* 34(8), pp. 1182-1196.

Wang, J. & Ma, Q. W., 2015a. Numerical techniques on improving computational efficiency of Spectral Boundary Integral Method. *International Journal for Numerical Methods in Engineering,* 102(10), pp. 1638-1669.

Wang, J. & Ma, Q. W., 2015b. Numerical Investigation on Limitation of Boussinesq Equation for Generating Focusing Waves. *Procedia Engineering,* Volume 126, pp. 597-601.

Wang, J., Ma, Q. W. & Yan, S., 2015. A hybrid model for simulating rogue waves in random seas on a large time and space scale. *Journal of Computational Physics (In press).*

Wang, J., Yan, S. & Ma, Q. W., 2015. An Improved Technique to Generate Rogue Waves in Random Sea. *Computer Modeling in Engineering & Sciences,* 106(4), pp. 263-289.

Wei, G. & Kirby, J. T., 1995. Time-dependent numerical code for extended Boussinesq equations. *Journal of Waterway, Port, Coastal, and Ocean Engineering,* 121(5), pp. 251-261.

Wei, G., Kirby, J. T., Grilli, S. T. & Subramanya, R., 1995. A fully nonlinear Boussinesq model for suface waves. Part 1. Highly nonlinear unsteady waves. *J. Fluid Mech.,* Volume 294, pp. 71-92.

West, B., Brueckner, K. A., Janda, R. S., Milder, D. M., & Milton, R. L., 1978. A new numerical method for surface hydrodynamics. *Journal of Geophysical Research: Oceans,* 92(C11), pp. 11803-11824..

Westhuis, J. H. & Andonowati, A. J., 1998. *Applying the finite element method in numerically solving the two dimensional free-surface water wave equations.* Hermans, Netherlands, Proc. 13th Int. Workshop on Water Waves and Floating Bodies, pp.171-174.

Whitham, G. B., 1965. Non-Linear Dispersive Waves. *Proceedings of the Royal Society of London A: Mathematical, Physical and Engineering Sciences,* 283(1393), pp. 238-261.

Whitham, G. B., 1967. Non-linear dispersion of water waves. *Journal of Fluid Mechanics,* 27(2), pp. 399-412.

Whitham, G. B., 1974. *Linear and Nonlinear Waves.* New York: Wiley-interscience.

Witting, J. M., 1975. On the highest and other solitary waves. *SIAM Journal on Applied Mathematics,* 28(3), pp. 700-719.

Witting, J. M., 1984. A unified model for the evolution nonlinear water waves. *Journal of Computational Physics,* 56(2), pp. 203-236.

Wu, C. H. & Yao, A., 2004. Laboratory measurements of limiting freak waves on current. *Journal of Geophysical Research: Oceans,* 109(C12).

Wu, G., 2004. *Direct Simulation and Deterministic Prediction of Large-scale Nonlinear Ocean*

Wave-field (PhD Thesis). Cambridge, USA: Massachusetts Institute of Technology.

Wu, G., Liu, Y. & Yue, D. K., 2005. *Studying rogue waves using large-scale direct phase-resolved simulations.* Honolulu, Hawaii, Proc. 14th 'Aha Huliko'a Winter Workshop, Rogue Waves, pp. 101-107.

Wu, G., Liu, Y. & Yue, D. K., 2006. A note on stabilizing the Benjamin–Feir instability. *Journal of Fluid Mechanics,* Volume 556, pp. 45-54.

Wu, G. X., 1991. On the second order wave reflection and transmission by a horizontal cylinder. *Applied ocean research,* 13(2), pp. 58-62.

Wu, G. X. & Eatock-Taylor, R., 1994. Finite element analysis of two dimensional non-linear transient water waves. *Appl. Ocean Res.,* Volume 16, pp. 363-372.

Wu, G. X. & Eatock-Taylor, R., 1995. Time stepping solution of the two dimensional non-linear wave radiation problem. *Ocean Eng.,* Volume 22, pp. 785-798.

Wu, G. X. & Hu, Z. Z., 2004. Simulation of nonlinear interactions between waves and floating bodies through a finite-element-based numerical tank. *Proceedings of the Royal Society of London A: Mathematical, Physical and Engineering Sciences,* 460(2050), pp. 2797-2817.

Wu, G. X., Ma, Q. W. & Eatock-Taylor, R., 1995. *Nonlinear wave loading on a floating body.* Oxford, UK, Proceedings of the 10th International Workshop on Water Waves and Floating Bodies.

Wu, G. X., Ma, Q. W. & Eatock-Taylor, R., 1996. *Analysis of interactions between nonlinear waves and bodies by domain decomposition.* Trondheim, Norway, ONR 21st Symposium on Naval Hydrodynamics, pp. 110-119.

Wu, G. X., Ma, Q. W. & Eatock-Taylor, R., 1998. Numerical simulation of sloshing waves in a 3D tank based on a finite element method. *Applied Ocean Research,* 20(6), pp. 337-355.

Wu, T. Y., 2001. A unified theory for modeling water waves. *Advances in applied mechanics,* Volume 37, pp. 2-89.

Xiao, W., 2013. *Study of directional ocean wavefield evolution and rogue wave occurrence using large-scale phase-resolved nonlinear simulations (Doctoral dissertation).* Cambridge, United States: Massachusetts Institute of Technology.

Xiao, W., Liu, Y., Wu, G. & Yue, D. K. P., 2013. Rogue wave occurrence and dynamics by direct simulations of nonlinear wave-field evolution. *J. Fluid Mech.,* Volume 720, pp. 357-392.

Xue, M., Xü, H., Liu, Y. & Yue, D. K., 2001. Computations of fully nonlinear three-dimensional wave–wave and wave–body interactions. Part 1. Dynamics of steep three-dimensional waves. *Journal of Fluid Mechanics,* Volume 438, pp. 11-39.

Xü, H. & Yue, D. K., 1992. *Computations of fully nonlinear three-dimensional water waves.*

Seoul, Korea, Proc. 19th Symp. on Naval Hydrodynamics.

Xu, L. & Guyenne, P., 2009. Numerical simulation of three-dimensional nonlinear water waves. *Journal of Computational Physics,* 228(22), pp. 8446-8466.

Xu, Y., Xia, X. & Wang, J., 2012. Calculation and approximation of the cnoidal function in cnoidal wave theory. *Computers & Fluids,* Volume 68, pp. 244-247.

Yan, S., 2006. Numerical simulation on nonlinear response of moored floating structures to steep waves. *PhD thesis. School of Engineering and Mathematical Sciences. City University London.*

Yan, S. & Ma, Q. W., 2009. Nonlinear simulation of 3-D freak waves using a fast numerical method. *International Journal of Offshore and Polar Engineering,* 19(3), pp. 168-175.

Yan, S. & Ma, Q. W., 2010. QALE-FEM for modelling 3D overturning waves. *International Journal for Numerical Methods in Fluids,* 63(6), pp. 743-768.

Yan, S. & Ma, Q. W., 2011. Improved model for air pressure due to wind on 2D freak waves in finite depth. *European Journal Mechanics B/Fluid,* Volume 30, pp. 1-11.

Yan, S. & Ma, Q. W., 2014. *Sensitivity Investigation on Wave Dynamics with Thin-Walled Moonpool.* Busan, Korea, The Twenty-fourth International Ocean and Polar Engineering Conference.

Yan, S., Ma, Q. W. & Adcock, T. A. A., 2010. *Investigation of freak waves on uniform current.* Harbin, Proc. 25th Int Workshop on Water Waves and Floating Bodies.

Yan, S., Zhou, J. T., Ma, Q. W., Wang, J., Zheng, Y. & Wazni, B., 2013. *Fully Nonlinear Simulation of Tsunami Wave Impacts on Onshore Structures.* Alaska, USA, The Twenty-third International Offshore and Polar Engineering Conference.

Yuen, H. C. & Ferguson, W. E., 1978. Relationship between Benjamin-Feir instability and recurrence in the nonlinear Schrödinger equation. *Physics of Fluids,* 21(8), pp. 1275-1278.

Yuen, H. C. & Lake, B. M., 1982. Nonlinear dynamics of deep-water gravity waves. *Adv. Appl. Mech,* 22(67), p. 229.

Zakharov, V. E., 1968. Stability of periodic waves of finite amplitude on the surface of a deep fluid. *Sov. Phys. J. Appl. Mech. Tech. Phys,* Volume 9, pp. 86-94.

Zakharov, V. E. & Shabat, A. B., 1972. Exact theory of two-dimensional self-focussing and one-dimensional self-modulation of waves in nonlinear media. *Soviet Physics JETP,* 34(1), pp. 62-69.

Zhang, Y., Zhang, N. & Pei, Y., 2007. *Numerical simulation and mechanism analysis of freak waves in random ocean sea states.* Lisbon, Portugal, The Proceedings of the 17th International Offshore and Polar Engineering Conference, pp. 1806-1810.

Zhao, X. & Hu, C., 2012. Numerical and experimental study on a 2-D floating body under extreme wave conditions. *Applied Ocean Research,* Volume 35, pp. 1-13.

Zhao, X., Hu, C. & Sun, Z., 2010. Numerical simulation of extreme wave generation using VOF method. *Journal of Hydrodynamics,* 22(4), pp. 466-477.

Zhu, Q., Liu, Y., Tjavaras, A. A., Triantafyllou, M. S. & Yue, D. K. P., 1999. Mechanics of nonlinear short-wave generation by a moored near-surface buoy. *Journal of Fluid Mechanics,* Volume 381, pp. 305-335.

Zou, J. & Kim, C. H., 2000. *Generation of Strongly Asymmetric Wave in Random Seaway.* Seattle, Proceeding of The Tenth International Offshore and Polar Engineering Conference, pp. 95-102.

Zou, Z. L., 1999. Higher order Boussinesq equations. *Ocean Engineering,* 26(8), pp. 767-792.

Zou, Z. L., 2000. A new form of higher order Boussinesq equations. *Ocean Engineering,* 27(5), pp. 557-575.